NATIONAL CENTRE FOR NUCLEAR RESEARCH

DOCTORAL THESIS

The fundamental metallicity relation through cosmic time: from $z \sim 0$ to $z \sim 1$

Author:
Francesco PISTIS

Supervisor:
Agnieszka POLLO
Auxiliary supervisor:
Daniela VERGANI

A thesis submitted in fulfillment of the requirements
for the degree of Doctor of Philosophy

in the

Astrophysics division (BP4)

NATIONAL
CENTRE
FOR NUCLEAR
RESEARCH
ŚWIERK

June 19, 2023

Declaration of Authorship

I, Francesco PISTIS, declare that this thesis titled, "The fundamental metallicity relation through cosmic time: from $z \sim 0$ to $z \sim 1$" and the work presented in it are my own. I confirm that:

- This work was done wholly or mainly while in candidature for a research degree at the National Centre for Nuclear Research.
- Where any part of this thesis has previously been submitted for a degree or any other qualification at the National Centre for Nuclear Research or any other institution, this has been clearly stated.
- Where I have consulted the published work of others, this is always clearly attributed.
- Where I have quoted from the work of others, the source is always given. With the exception of such quotations, this thesis is entirely my own work.
- I have acknowledged all main sources of help.
- Where the thesis is based on work done by myself jointly with others, I have made clear exactly what was done by others and what I have contributed myself.

Signed:

Date:

"We are made of the same substance as the sky and the cosmos. We are stardust."

Margherita Hack

NATIONAL CENTRE FOR NUCLEAR RESEARCH

Abstract

The fundamental metallicity relation through cosmic time: from $z \sim 0$ to $z \sim 1$

Francesco PISTIS

Stars are responsible for creating heavy elements in the Universe both during their lifetime and at the moment of their death. By studying metallicity (the abundance of heavy elements relative to hydrogen), we can infer information on the evolutionary history of galaxies. The metallicity is affected by various processes, for example, the infall of pristine gas, the outflow of metal-rich gas, and stellar feedback. These processes shape important relationships between the metallicity and other physical properties of galaxies. An important relation is the so-called fundamental metallicity relation (FMR) which defines a 3D surface based on the stellar mass ($M_\star$), star formation rate (SFR), and metallicity for star-forming galaxies.

This Ph.D. work focuses on comparing FMR at different redshifts. In this work, we used data from the Sloan Digital Sky Survey (SDSS) in the local Universe (at redshift $z \sim 0$) and the VIMOS Public Extragalactic Redshift Survey (VIPERS) up to redshift $z \sim 0.8$. VIPERS allows us to increase significantly the statistical sample size with respect to the previous works, up to several thousand observations within redshift $0.48 < z < 0.8$.

In order to have consistent spectral measurements between the samples, we re-measured the VIPERS galaxy spectra with the Penalized PiXel-Fitting (pPXF) fitting code. pPXF allows us to fit separately the stellar and gas component of the spectra to extract the stellar and gas kinematics, as well as the stellar population of stars and galaxies. The separate fit of the stellar continuum and gas emission allows a better measure of the lines' properties. We also paid particular attention to computing consistently all the properties defining the FMR in both samples taken into consideration.

Initially, we homogenized the sample by analyzing different biases that may arise from the data selection (method of selection of star-forming galaxies, signal-to-noise selection, selection on the quality of spectra) and observations (intrinsic luminosity evolution of galaxies, the fraction of blue galaxies). We found that the analysis can be particularly biased by a high signal-to-noise threshold applied specifically on the emission line [O III] λ4959. However, projecting the FMR on planes defined by the combination of the $M_\star$ and SFR greatly reduces the effects of biases. After correcting for the biases mentioned above, we reduce the difference of the FMR between the samples to ~ 0.1 dex, which is comparable to the average scatter in the metallicity of the populations of both samples.

We then proceed to study how different methods of comparison can affect the interpretation of the differences between the different datasets. We compared the low and intermediate redshift samples via a set of parametric and non-parametric methods. The parametric methods are based on studying the different projections of the FMR. In order to compare specific physical properties at different redshifts, we build three control-sample by cross-matching the VIPERS and the SDSS according to the physical properties of interest — i.e. ($M_\star$-SFR), galaxy mass function, and relative distance from the star-forming main sequence. The non-parametric method is based on studying the metallicity-relative sSFR (specific SFR, defined as the ratio SFR/$M_\star$) relation. The relative sSFR is defined based on a normalization of the sSFR. The choice of normalization allows for the comparison of specific properties between the samples. Using both families of methods we find a statistically significant difference between the FMR and its projections for low and intermediate redshift, increasing with $M_\star$. This study results in the first observational evidence for an evolution of the FMR up to median $z \sim 0.63$ with a significance of $\sim 3\,\langle\sigma_{\mathrm{med}}\rangle_{\mathrm{VIPERS}}$.

Finally, in the last part of the work (which will be a subject of future more detailed analysis), we try to select sub-populations and outliers based on the FMR by applying machine learning algorithms to the low and intermediate redshift samples. The goal of this part is to look for footprints left by galaxy evolution or environmental effects on the surface of the FMR. We initially apply the principal component analysis to reduce the dimensionality of the problem by projecting the data in a 2D space with the highest variance. In this 2D space, we apply the K-means clustering algorithm to group galaxies into sub-populations, and the local outlier factor to find the outliers. Despite the fact we do not observe big differences from the point of view of galaxy evolution between the sub-populations, the outliers can be divided into smaller groups according to their distance from the star-forming main sequence and having broad (equivalent width ratio [O III] $\lambda5007/\mathrm{H}\beta > 1$) or narrow (equivalent width ratio [O III] $\lambda5007/\mathrm{H}\beta \leq 1$) lines. These groups of outliers will be the subject of future more detailed analysis.

NATIONAL CENTRE FOR NUCLEAR RESEARCH

Streszczenie

The fundamental metallicity relation through cosmic time: from $z \sim 0$ to $z \sim 1$

Francesco PISTIS

Gwiazdy są odpowiedzialne za tworzenie ciężkich pierwiastków we Wszechświecie zarówno podczas swojego życia, jak i w momencie śmierci. Badając metaliczność (obfitość pierwiastków ciężkich w stosunku do wodoru), możemy uzyskać informacje na temat historii ewolucji galaktyk. Na metaliczność wpływają różne procesy, na przykład napływ czystego gazu, wypływ gazu bogatego w metale i gwiezdne sprzężenie zwrotne. Procesy te kształtują ważne zależności między metalicznością a innymi właściwościami fizycznymi galaktyk. Ważną relacją jest tak zwana podstawowa relacja metaliczności (FMR), która definiuje trójwymiarową powierzchnię opartą na masie gwiazdowej ($M_\star$), tempie formowania się gwiazd (SFR) i metaliczności dla galaktyk gwiazdotwórczych.

Niniejsza praca doktorska koncentruje się na porównaniu FMR przy różnych przesunięciach ku czerwieni. W tej pracy wykorzystaliśmy dane z katalogu Sloan Digital Sky Survey (SDSS) w lokalnym Wszechświecie (przy przesunięciu ku czerwieni $z \sim 0$) oraz VIMOS Public Extragalactic Redshift Survey (VIPERS) do przesunięcia ku czerwieni $z \sim 0,8$. VIPERS pozwala nam znacznie zwiększyć rozmiar próbki statystycznej w stosunku do wcześniejszych prac, do kilku tysięcy galaktyk w zakresie przesunięcia ku czerwieni $0,48 < z < 0,8$.

Aby uzyskać spójne pomiary własności widm między próbkami, ponownie przeanalizowaliśmy katalog widm VIPERS za pomocą kodu Penalized PiXel-Fitting (pPXF). pPXF pozwala nam dopasować oddzielnie składnik gwiazdowy i gazowy widma, aby wyodrębnić kinematykę gwiazd i gazu, a także populację gwiazd i galaktyk. Oddzielne dopasowanie kontinuum gwiazdowego i emisji gazu pozwala lepiej zmierzyć właściwości linii. Zwróciliśmy również szczególną uwagę na spójne dla obu katalogów obliczenie wszystkich właściwości fizycznych galaktyk definiujących FMR.

Początkowo zhomogenizowaliśmy próbkę, analizując różne odchylenia, które mogą wynikać z selekcji danych (metoda selekcji galaktyk gwiazdotwórczych, selekcja sygnału do szumu, selekcja jakości widm) i obserwacji (wewnętrzna ewolucja jasności galaktyk, frakcja niebieskich galaktyk). Stwierdziliśmy, że najsilniejsze obciążenie dla analizy może wiązać się z różnicami progu sygnału do szumu linii widmowych, w szczególności w przypadku linii emisyjnej [O III] λ4959. Jednak rzutowanie FMR na płaszczyzny zdefiniowane na podstawie kombinacji $M_\star$ i SFR znacznie zmniejsza wpływ zaburzeń. Biorąc pod uwagę odchylenia, różnica między FMR mierzonym dla obu katalogów daje się zredukować o $\sim 0,1$ dex, co odpowiada średniemu rozrzutowi metaliczności populacji galaktyk w obu katalogach.

Następnie zbadaliśmy, w jaki sposób różne metody porównania mogą wpływać na interpretację danych. Porównaliśmy próbki o niskim i pośrednim przesunięciu ku czerwieni w katalogach SDSS i VIPERS za pomocą metody parametrycznej i metody nieparametrycznej. Pierwsza metoda polega na badaniu różnych projekcji FMR. W celu porównania konkretnych właściwości fizycznych przy różnych przesunięciach ku czerwieni, zbudowaliśmy trzy próbki kontrolne poprzez dopasowanie

krzyżowe interesujących nas właściwości fizycznych — właściwości fizycznych ($M_\star$-SFR), funkcji masy galaktyk i względnej odległości od głównego ciągu gwiazdotwórczego galaktyk. Ta ostatnia metoda polega na zbadaniu relacji metaliczność-względny sSFR (specyficzny SFR, zdefiniowany jako stosunek SFR/$M_\star$). Względny sSFR jest normalizacją sSFR. Wybór normalizacji pozwala na porównanie określonych właściwości między próbkami. Zastosowanie obu metod pozwoliło na konsystentną detekcję różnicy FMR pomiędzy niskim (SDSS) i pośrednim (VIPERS) przesunięciem ku czerwieni, rosnącej wraz ze wzrostem $M_\star$. Wynikiem tej pracy jest zatem pierwszy w literaturze obserwacyjny pomiar ewolucji FMR pomiędzy $z \sim 0.63$ a $z \sim 0$ z istotnością $\sim 3 \langle\sigma_{\rm med}\rangle_{\rm VIPERS}$.

Wreszcie w ostatniej części pracy (która będzie przedmiotem przyszłej bardziej szczegółowej analizy), staramy się wybrać subpopulacje i wartości odstające na podstawie FMR, stosując algorytmy uczenia maszynowego do próbek o niskim i pośrednim przesunięciu ku czerwieni. Celem tej części pracy jest poszukiwanie śladów pozostawionych przez ewolucję galaktyk lub efekty środowiskowe na powierzchni FMR. Początkowo stosujemy analizę głównych składowych FMR (metodą PCA, ang. Principal Component Analysis), aby zmniejszyć wymiarowość problemu poprzez rzutowanie danych na przestrzeń 2D o największej wariancji. W tej przestrzeni 2D stosujemy algorytm klasteryzacji K-średnich (ang. K-means), aby pogrupować galaktyki w subpopulacje, oraz lokalny czynnik odstający, aby znaleźć wartości odstające. Pomimo faktu, że nie obserwujemy dużych różnic z punktu widzenia ewolucji galaktyk między subpopulacjami, galaktyki odstające można podzielić na mniejsze grupy w zależności od ich odległości od głównej sekwencji gwiazdotwórczej galaktyk (ang. galaxy main sequence) i posiadania szerokich (równoważny stosunek szerokości [O III] $\lambda5007/{\rm H}\beta > 1$) lub wąskich (równoważny stosunek szerokości [O III] $\lambda5007/{\rm H}\beta \leq 1$) linii. Ich szczegółowe własności będą przedmiotem dalszych badań.

Acknowledgements

I want to express my genuine gratitude to my parents for their unwavering support and love throughout my journey. However, they couldn't witness the conclusion of this adventure. I also want to thank my siblings, Paola and Nicola, for taking care of our parents during their illness while I was abroad. They did this without burdening me and also supported me in my studies. I am truly grateful for their altruism. Moreover, I am grateful to my extended family for their support and care after my parents passed away.

I am thankful for the enduring friendship of Federica and Matteo. They have been a valuable source of assistance and encouragement, not only in my personal life but also in my academic life.

I would like to express my appreciation to my colleagues at the doctoral school who have helped me grow both personally and professionally. I would like to give special thanks to Misha and Gabriele, with whom I started and shared this journey together.

Finally, I would like to express my gratitude to my supervisor, Dr. Agnieszka Pollo, for entrusting me with the opportunity to pursue a Ph.D. when I was on the threshold of giving up. Additionally, I appreciate her support during personal issues. Similarly, I extend my appreciation to my co-supervisor, Dr. Daniela Vergani, for her invaluable assistance in enhancing my research.

Contents

List of Figures

List of Tables

To my parents, in loving memory.

Scientific output

Publications as the first author:

- F. Pistis et al. (July 2022). The fundamental metallicity relation from SDSS ($z \sim 0$) to VIPERS ($z \sim 0.7$). Data selection or evolution. A&A 663, A162, A162. DOI: `10.1051/0004-6361/202142430`. arXiv: `2206.02458 [astro-ph.GA]`
- F. Pistis et al. (2023a). A comparative study of the fundamental metallicity relation. The impact of methodology on its observed evolution. A&A submitted
- F. Pistis et al. (2023b). Galaxy evolution footprint on the fundamental metallicity relation. A machine learning approach. in prep.

Publications as co-author:

- M. Figueira et al. (Nov. 2022). SFR estimations from $z = 0$ to $z = 0.9$. A comparison of SFR calibrators for star-forming galaxies. A&A 667, A29, A29. DOI: `10.1051/0004-6361/202141701`. arXiv: `2209.04390 [astro-ph.GA]`
- W. J. Pearson et al. (2023). Influence of star-forming galaxy selection on the galaxy main sequence. A&A submitted
- M. Hamed et al. (2023a). Decoding the IRX-β dust attenuation relation in star-forming galaxies at intermediate redshift. A&A submitted
- G. Riccio et al. (2023). X-ray luminosity - star formation rate scaling relation: constraints from the eROSITA Final Equatorial Depth Survey (eFEDS). A&A submitted

Introduction

Extragalactic sources have been known since ancient times (although nobody knew they were extragalactic). In the sky, there are three extragalactic sources visible to the naked eye, Andromeda galaxy (M31) in the northern celestial hemisphere, Small and Large Magellanic Clouds in the southern celestial hemisphere. With the use of telescopes, many star clusters and nebulae were cataloged during the 18th and 19th centuries as part of the Milky Way. The advent of larger and more advanced telescopes allowed us to resolve their structures and study their properties.

In the 20th century, Edwin Hubble studying M31 found the presence of Cepheids stars. The Cepheids are variable stars whose pulsation period is well-related to the absolute magnitude, as discovered by Henrietta Leavitt. Hubble was then able to measure the distance of M31 and other sources proving for the first time that these sources were external to the Milky Way. In this way, the field of studies on extragalactic astronomy was born more or less a century ago.

This Ph.D. thesis focuses on the chemical evolution of galaxies. Specifically, we focus on the relation between the mass content in stars of galaxies (stellar mass, $M_\star$), the amount of gas converted into stars per year (star formation rate, SFR), and the relative abundance of heavy elements to the hydrogen (metallicity), the so-called fundamental metallicity relation (FMR). The core of the thesis is the comparison of galaxies from the local Universe — maximum redshift $z \sim 0.2$ with a lookback time of 2.4 Gyr — from the Sloan Digital Sky Survey (SDSS) and galaxies from at intermediate redshift — maximum redshift $z \sim 0.8$ with a lookback time of 6.3 Gyr — from the VIMOS Public Extragalactic Redshift Survey (VIPERS)

In view of that, the Ph.D. work presented in this Thesis revolves around the following three main themes: (i) how biases introduced by data selection and observations can affect the comparison of the FMR at different redshift; (ii) the impact of methodology on the observed evolution of the FMR at different redshift (iii) and the search for footprints left by the galaxy evolution on the FMR. The Thesis is organized into six Chapters.

Chapter 1 provides a review of the state-of-art of the main relations between galaxy properties. In particular, we focus on the star-forming main sequence, the mass-metallicity relation, and the FMR. In this chapter, we also provide some open questions on the FMR and its evolution. The work presented in the following chapters of this Thesis will give an answer to some of these open questions.

Chapter 2 focuses on the definition of the physical properties of galaxies and their measurements. Specifically on the properties of interest for the study of the FMR: $M_\star$, SFR, and metallicity.

Chapter 3 provides the steps of the data selection. In this chapter, we also provide descriptions of the estimations of the physical properties.

Chapter 4 describes how different biases introduced by data selection (different diagram selections, cut on the signal to noise of emission lines, quality of the spectra) and observations (evolution of the luminosity of galaxies with redshift and the fraction of blue galaxies) affect the comparison of samples at different redshifts. In this chapter, we compare the FMR in the local Universe and at intermediate redshift with and without taking into account these biases.

Chapter 5 reviews different methods to compare galaxies at different redshifts. In particular, we analyze two families of methods: i) a parametric method that consists of the study of the FMR projections into 2D spaces; and ii) a non-parametric method that consists of the study of the normalized-sSFR[1]-metallicity relation in different $M_\star$ bins. Choosing different normalizations allows us to study different aspects of the FMR.

Chapter 6 describes the search of footprints left by galaxy evolution on the FMR. In this part of the Thesis, we make use of machine learning algorithms to define clusters of galaxies and outliers from the point of view of the FMR

Finally, we summarize the main results from our work in Chapter 7 and we report the future prospective in Chapter 8.

---

[1] Specific SFR, defined as the ratio between SFR and $M_\star$

CHAPTER 1

Island universes

This chapter describes the state-of-art on extragalactic observations, focusing on galaxy formation (Sect. 1.1), galaxy evolution (Sect. 1.2), and the description of the main relations between galaxy properties of interest for this work, such as the star-forming main sequence (Sect. 1.3), the mass-metallicity relation (Sect. 1.4), and the fundamental metallicity relation (Sect. 1.5). Finally, we report the questions still open about the fundamental metallicity relation (Sect. 1.6), pointing out the goal and the contribution of this Ph.D. Thesis.

1.1 Galaxy formation

The study of galaxy formation tries to answer the problem of how the Universe is as we observe it today. The cosmic web (Cautun et al., 2014; Elbers et al., 2023; Neyrinck et al., 2018) connects the galaxies in the largest structure in the Universe, unlike the early Universe that emerged from an extremely uniform and homogeneous state.

The comic microwave background (CMB, discovered by Penzias et al., 1965), was the first evidence of an extremely uniform and homogeneous state of the early Universe. Successive missions (e.g. the Wilkinson Microwave Anisotropy Probe, WMAP, from NASA and the Planck mission from ESA, Bennett et al., 2013; Planck Collaboration et al., 2014) Figure 1.1 shows the CMB measurements made by WMAP and Planck missions.

How do we pass from a uniform and homogeneous Universe to the structure we see today? The models of galaxy formation can be divided into two families: i)

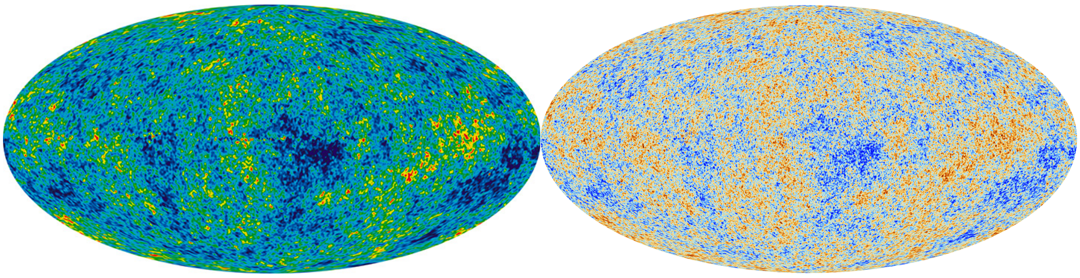

Figure 1.1: Cosmic microwave background (CMB) as seen from the WMAP (left, Bennett et al., 2013) and Planck (right, Planck Collaboration et al., 2014) missions.

top-down theories where galaxies form starting as a single uniform collapse of a gas cloud (Eggen et al., 1962); ii) bottom-up theory, also called hierarchical model, where the matter started to collapse into smaller clumps (mass on the order of globular clusters), and then many of these clumps merged to form galaxies (White et al., 1978).

The top-down theories assume a matter distribution in the early Universe as clumps mainly composed of dark matter. Interacting gravitationally with each other, these clumps acquire angular momentum. As the baryonic matter cools down, it collapses towards the central part of these clumps of dark matter. Conserving the angular momentum. the matter near the center accelerates its rotation forming a tight disk. Once the disk cools down, the gas is no more gravitationally stable. The cloud, at this point, splits into smaller clouds of gas which can form stars. Dark matter cannot dissipate energy since it interacts only by gravitational force it cannot dissipate energy. In this way, dark matter remains distributed outside the disk in what is known as the dark halo (Searle et al., 1978). The top-down theories have difficulties to predict the observation of stars located outside the disk.

The hierarchical model (see Fig. 1.2) results in disk-like distributions of baryonic matter with dark matter distributed to form the halo, as in the top-down theory. The hierarchical model predicts a larger number of small galaxies than large ones, matching the observations (Bell et al., 2003). It is still unclear what stops the contraction. Models of disk galaxies formation have difficulties to reproduce the rotation speed and size of disk galaxies. The radiation of bright newborn stars (Qu et al., 2017) and active galactic nucleus (Menci et al., 2006; Taylor et al., 2016, AGN,) can slow the contraction of a forming disk.

1.2 Galaxy evolution

We can see a galaxy as a system in communication with its environment (both gas and nearby galaxies, Fig. 1.3; Maiolino et al., 2019). When pristine gas falls into a galaxy, it triggers the formation of new stars. These stars process the interstellar medium (ISM), creating heavy elements which are released during their evolution or death. The metallicity of the ISM is measured by the relative abundance of heavy elements compared to hydrogen. Different generations of stars recycle the ISM multiple times, creating and destroying dust and heavy elements. The presence of an AGN at the center of a galaxy can impact the evolution of the ISM by heating or removing gas through winds. This can lead the galaxy towards a quenching event. The chemical evolution of a galaxy is closely connected to its stellar evolution, and studying it provides valuable insights into these processes.

To understand how galaxies evolve, different models have been developed considering consider all processes within a cosmological framework (Dayal et al., 2018; Matteucci, 2012; Naab et al., 2017; Silk et al., 2014; Silk et al., 2012; Somerville et al., 2015). When creating a model, the first issue to address is maintaining a low star formation "efficiency" (SFE), as only a small portion of baryons are transformed into stars. Galaxies have a smaller amount of baryons compared to the overall average in the cosmos, and this fraction increases with mass up to a halo mass of around $10^{12} M_{\odot}$ (Baldry et al., 2008; Papastergis et al., 2012). To prevent accretion or remove baryons from galaxies, a mechanism is necessary.

There are ways to limit star formation in a galaxy. One method involves putting the gas into a state that is not available for star formation, such as a highly turbulent or hot state. Another way is to prevent further gas accretion, which cuts off the fuel needed for sustainable and prolonged star formation. Supernovae (SNe), radiation

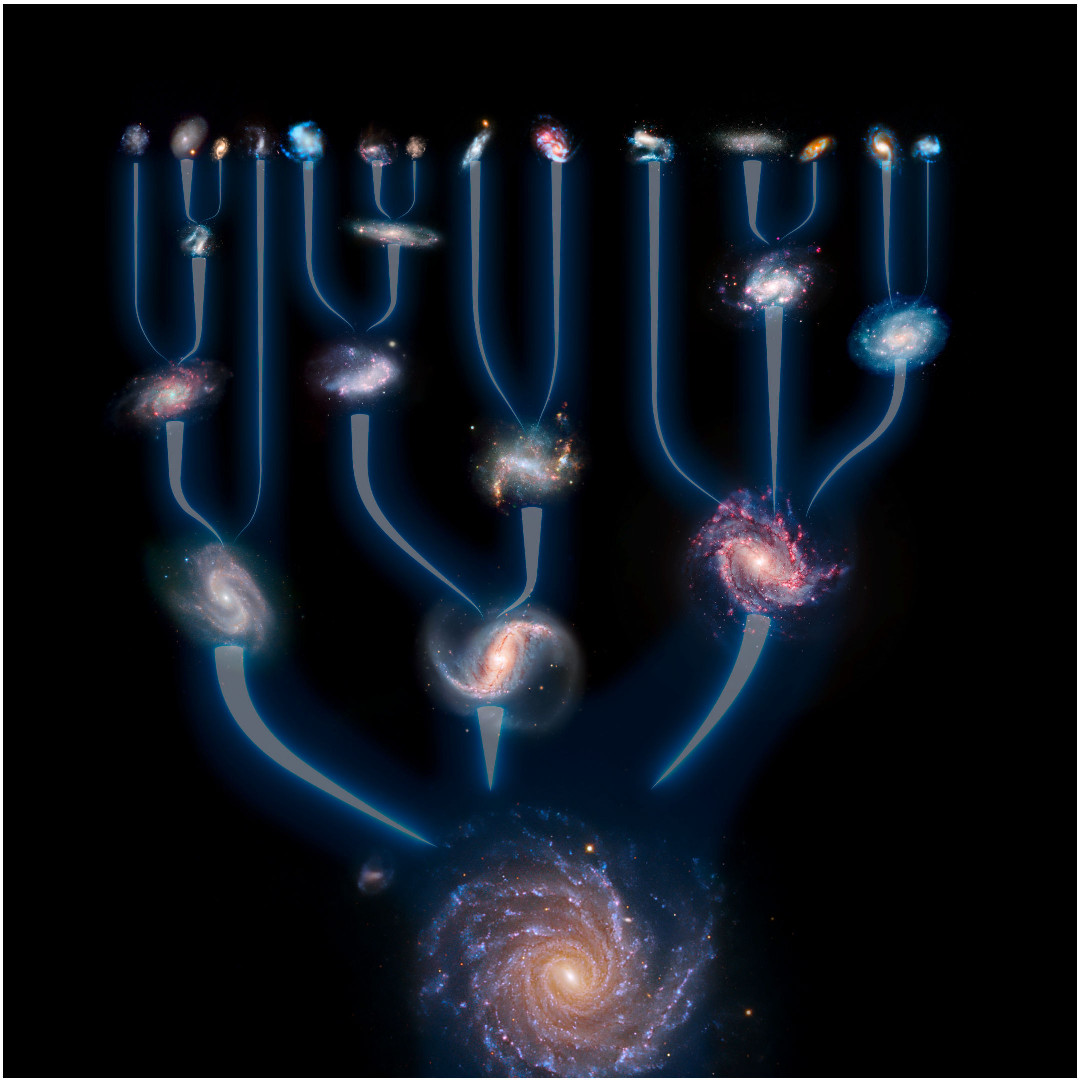

Figure 1.2: Scheme of galaxies formation according to the hierarchical model (bottom-up). Credits: ESO/L. Calçada (`https://www.eso.org/public/belgium-nl/images/1016-galaxy_formation_merger/`).

from young stars, AGN, and ram-pressure removal due to interaction with the intracluster medium (ICM) can cause this feedback. These models are defined by a few critical parameters.

- SFE, the measurement of the number of stars formed per unit time per unit gas mass, is defined as

  $$\epsilon = \frac{\mathrm{SFR}}{M_{\mathrm{gas}}}, \tag{1.1}$$

  where the SFR is the star formation rate. The SFE is opposite to the gas "depletion time", which is the time it takes for star formation to convert all gas into stars without gas accretion and with a constant SFR. However, the SFR cannot remain constant if there is no gas accretion. The differential equation that describes the closed-box model shows that the SFR must decline exponentially:

  $$\mathrm{SFR} = -\frac{\mathrm{d}M_{\mathrm{gas}}}{\mathrm{dt}} = \epsilon M_{\mathrm{gas}}. \tag{1.2}$$

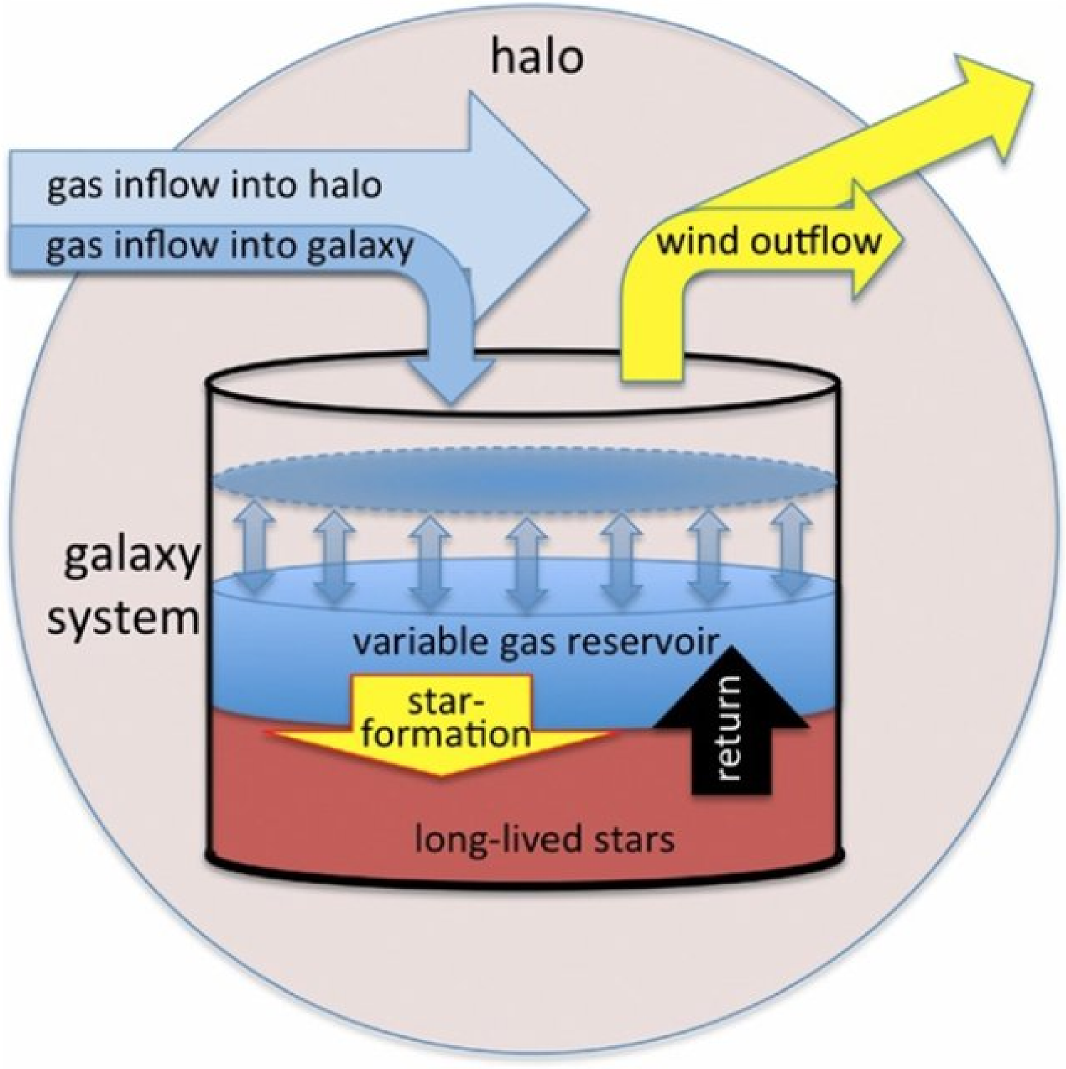

Figure 1.3: Scheme of the communication between a galaxy and its environment. Credits: Lilly et al. (2013).

The depletion time is the time taken for the SFR to decrease to $1/e$ of its initial value, and it is related to the SFR's e-folding time. The Schmidt-Kennicutt relation (the original relation has a slope equal to 1.4, Kennicutt et al., 2012) assumes that the SFE is constant and not affected by gas mass or surface density, which results in a linear relationship.

- The outflow mass loading factor, i.e., the ratio between mass outflow rate and star formation rate

$$\eta = \frac{\dot{M}_{\text{outfl}}}{SFR}. \tag{1.3}$$

Outflows in star-forming (SF) galaxies are typically attributed to SNe and radiation pressure from stars. The loading factor, denoted by η, is commonly observed to be around one (Fluetsch et al., 2019; Heckman et al., 2015; Steidel et al., 2010). It is predicted that the loading factor will have an inverse relationship with the galaxy's mass due to its stronger gravitational well. However, the presence of an AGN (Cicone et al., 2014; Fluetsch et al., 2019) can significantly increase the loading factor η. It is important to distinguish between gas that

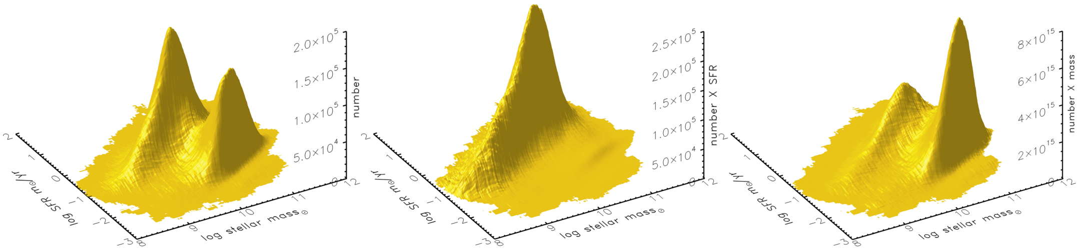

Figure 1.4: 3D distribution of the number of galaxies (left), weighted by SFR (middle), and weighted by $M_\star$ in the SFR-$M_\star$ plane. Credits: Renzini et al. (2015).

falls back into the galaxy and gas that leaves the halo, as the latter may only be re-accreted over long timescales. The outflowing gas's chemical composition is usually assumed to be similar to the average metallicity of the ISM within the galaxy.

- The rate of gas inflow is crucial in regulating how galaxies evolve. It is commonly accepted that the rate of gas inflow is proportional to the SFR of the galaxy. This simplifies the equations used to describe the galaxy's evolution and chemical enrichment. However, there is no physical evidence linking the SFR to the gas inflow. Assuming that the accretion rate is proportional to the SFR, as shown in Eqs. 1.1-1.3, implies that the gas mass and SFR will decrease exponentially over time, meaning that galaxies cannot follow the observed SF main sequence (MS Brinchmann et al., 2004; Daddi et al., 2007; Schreiber et al., 2015; Speagle et al., 2014; Whitaker et al., 2012) relationship between mass and SFR. It is only correct to assume that the inflow rate is proportional to the SFR in a perfect equilibrium scenario where the inflow rate is precisely balanced by the SFR and outflow rate. It is generally assumed that the inflow gas is chemically pristine.

1.3 The star-forming main sequence

In SF galaxies, there is a strong correlation between the SFR and $M_\star$, which is referred to as the MS (Brinchmann et al., 2004; Elbaz et al., 2007; Noeske et al., 2007). Figure 1.4 displays the 3D distribution of galaxies in the SFR-$M_\star$ plane, based on data from the Sloan Digital Sky Survey (SDSS) DR7 release (Abazajian et al., 2009). The distribution reveals two clear peaks. However, when the number of galaxies is weighted by the SFR, there is a single peak, where the majority of the SFR is concentrated. On the other hand, when weighted by $M_\star$, the distribution still shows two peaks. The bulk of $M_\star$ is found in the region of passive galaxies, while only a small percentage of the mass is attributed to active galaxies.

The scatter around the MS is the result of variation of the infalling matter into galaxies and epochs of bursty star-formation (Abramson et al., 2014; Matthee et al., 2019; Mitra et al., 2017; Tacchella et al., 2016). This scatter is consistently measured to be between 0.2–0.3 dex, regardless of the mass of the galaxy, and has remained consistent throughout the history of the universe (Kurczynski et al., 2016; Speagle et al., 2014; Tomczak et al., 2016; Whitaker et al., 2012). This consistency is due to the steady growth of mass in all galaxies, through similar and gradual star formation processes, happening during all cosmic times (Lee et al., 2015).

In the literature, two shapes of the MS are described:

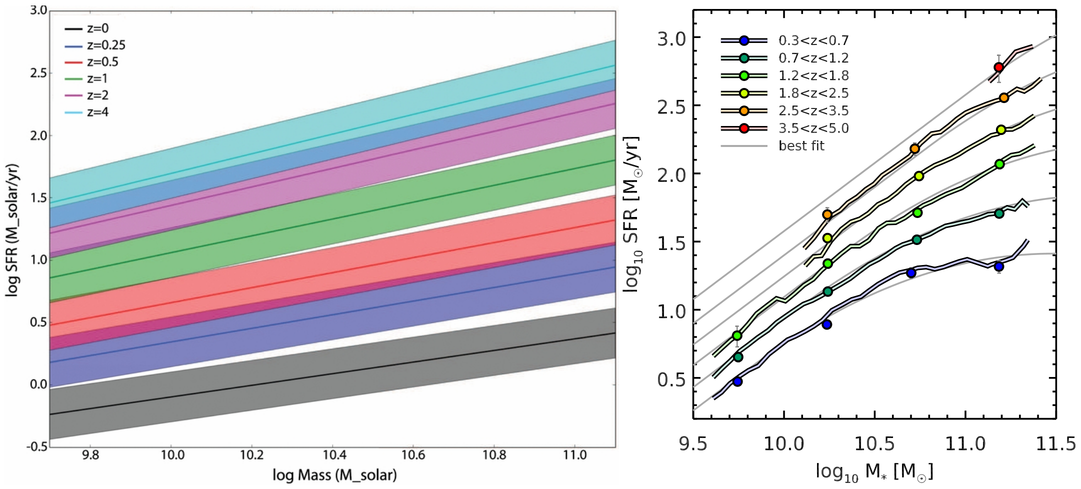

Figure 1.5: Evolution of the MS. Left panel) simple power law (Credits: Speagle et al., 2014). Right panel) MS with turnover at high mass (Credits: Schreiber et al., 2015)

i) simple power law of the form $\log \mathrm{SFR} \propto \log M_\star$ at all $M_\star$ (Pearson et al., 2018; Speagle et al., 2014);

ii) MS with a turnover at high mass with the relation becoming shallower at higher masses (Lee et al., 2015; Popesso et al., 2019, 2023; Schreiber et al., 2015; Tomczak et al., 2016; Whitaker et al., 2012).

The variation in the shape of the MS of galaxies is attributed to the criteria used to select SF galaxies. When SF galaxies are selected with stricter criteria, the MS exhibits a weaker turnover at high masses (Johnston et al., 2015). Contrarily, less strict criteria result in a stronger turnover. The SFR tracer and the tracer of the MS itself (mean, mode or median) used also contribute to the observed turnover (Popesso et al., 2019).

The MS slope, or the low mass MS when a turnover is present, is found to be in the range 0.4–1.0 (Fig. 1.5, Pearson et al., 2018; Popesso et al., 2023; Schreiber et al., 2015; Tomczak et al., 2016; Whitaker et al., 2014). The slope has been seen to reduce with redshift in some studies (e.g., Randriamampandry et al., 2020), while it is observed to increase in others (e.g., Pearson et al., 2018; Speagle et al., 2014). Normalization also evolves with redshift (Fig. 1.5, Pearson et al., 2018; Popesso et al., 2023; Schreiber et al., 2015; Speagle et al., 2014; Tomczak et al., 2016). The increase in SFR with redshift is expected to depend on the amount of cool gas available which reduces with redshift (Dunne et al., 2011; Genzel et al., 2015; Kokorev et al., 2021; Scoville et al., 2016; Tacconi et al., 2010). This, associated with the SFR per dust mass either being constant or increasing with redshift (Scoville et al., 2016; Tacconi et al., 2010), implies an increase in SFR and normalization of the MS with redshift.

1.4 The mass-metallicity relation

Various integrated properties of galaxies have been found to have scaling relations with their gas phase and stellar metallicities. These relations are observed in both active SF and quiescent galaxies and can provide insight into their evolution. The formation and evolution of galaxies are influenced by several factors, such as halo mass and environment, which can affect the metallicity through its dependence on the star formation history (SFH), gas accretion, merging, and gas outflow (Maiolino

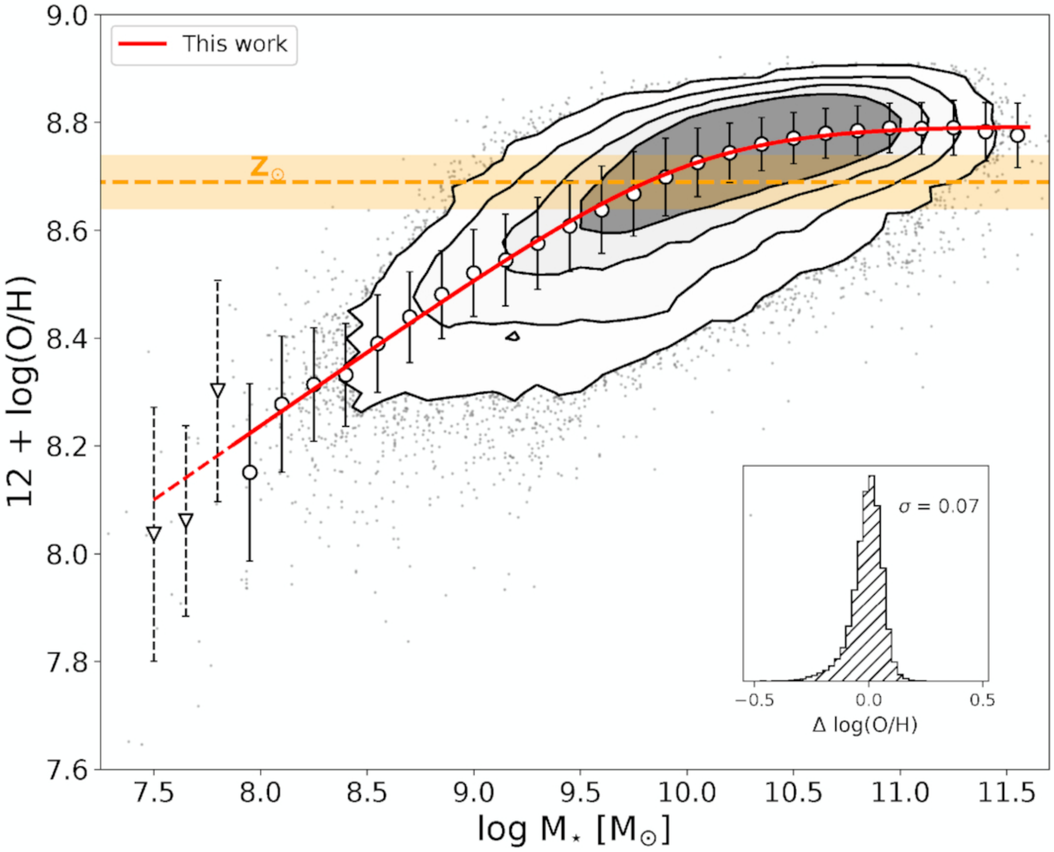

Figure 1.6: Mass–metallicity relation (MZR) for the SF sample based on SDSS galaxies. Credits: Curti et al., 2020

et al., 2019). The focus of this Ph.D. work will be on exploring the scaling relations for gas-phase metallicity.

Researchers first measured the ISM metallicity dependency on mass in galaxies of the Local Group (Peimbert et al., 1970). The first observation of the Mass-Metallicity Relation (MZR) — which illustrates the correlation between chemical abundance and total mass — was conducted on a small sample of local, SF galaxies, such as irregulars and blue-compact dwarfs (Lequeux et al., 1979), as a dependence of chemical abundance on total (dynamical[1]) mass. The correlation was confirmed by other studies (Kinman et al., 1981; Pagel et al., 1981; Talent, 1981). These same studies have also found an anti-correlation between metallicity and gas fraction, which is driven by the anti-correlation between mass and gas fraction (Peeples et al., 2014; Rodrigues et al., 2012).

The statistical significance of the MZR studies has significantly increased with the observation via the SDSS survey. With the use of SDSS spectra, more than 100 000 galaxies were measured for the main optical lines (Curti et al., 2020; Lian et al., 2015; Mannucci et al., 2010; Pérez-Montero et al., 2013; Tremonti et al., 2004). The scatter around the MZR for SDSS data is roughly 0.1 dex (Mannucci et al., 2010; Tremonti et al., 2004), which is slightly larger than the uncertainty on the measurement of metallicity. The MZR is observed in the mass range of approximately $\sim 10^7\ M_\odot$ to $\sim 10^{12}\ M_\odot$ (Curti et al., 2020; Haurberg et al., 2013, 2015; Lee et al., 2006; Mannucci et al., 2010; Pilyugin et al., 2013; Skillman et al., 1988; Tremonti et al., 2004; van Zee

---

[1] Total mass derived by the kinematic properties of a galaxy.

et al., 2006), with a steep dependence at low $M_\star$ up to $\sim 10^{10}\ M_\odot$, where it flattens out at higher $M_\star$.

Different driving mechanisms can explain the existence and the shape of the MZR:

i) The MZR is influenced by feedback (Brooks et al., 2007; Garnett, 2002). In starburst galaxies, SNe commonly produce outflows (Heckman, 2002; Heckman et al., 2017; Law et al., 2007; Martin et al., 2012; Steidel et al., 2010; Weiner et al., 2009). Interestingly, these outflows have higher metallicities than the Interstellar Medium (ISM) of the host galaxies (Chisholm et al., 2018) and are efficient in removing metal-enriched gas from low-mass galaxies into the circumgalactic medium (CGM) and intergalactic medium (IGM) (Chisholm et al., 2018; Tremonti et al., 2004; Tumlinson et al., 2011). This phenomenon has been documented by Chisholm and is expected to have implications on the origin of metals in the universe, as studied by Tremonti, Tumlinson, and Chisholm.

ii) High-mass galaxies evolve faster and earlier, at higher redshift, than low-mass galaxies (the so-called "downsizing", Cowie et al., 1996; Somerville et al., 2015). Consequently, high-mass galaxies convert a larger fraction of gas into stars and metals reaching higher metallicities (Maiolino et al., 2008; Zahid et al., 2011a). The MZR results in an evolutionary sequence when interpreted from the point of view of downsizing.

iii) The early-stage evolution of low-mass galaxies and their larger gas fraction (Erb et al., 2006b; Lagos et al., 2016a; Rodrigues et al., 2012) might be connected to the continuous infall of metal-poor gas, which reduces the metallicity increasing, at the same time, the SFR.

iv) The shape of the initial mass function (IMF) at high mass might depend on galaxy mass, introducing systematic changes in the average stellar yields and in the rate of metal enrichment (Köppen et al., 2007; Lian et al., 2018a; Mollá et al., 2015; Trager et al., 2000; Vincenzo et al., 2016).

v) The metallicity of the infalling gas, recycled from different stellar generations, might be larger for larger mass galaxies (Brook et al., 2014; Ma et al., 2016).

The MZR is influenced by various factors such as feedback from stars and AGNs, chemical yields, the metal content of the outflowing gas in relation to the parent galaxy's ISM, the amount of metal that gets re-absorbed by the galaxy, and the evolution of the SFR (Maiolino et al., 2019). Some of these parameters are degenerate. The measurements of metallicity help to break these degeneracies. By comparing, for example, the stellar and gas MZRs, only two scenarios reproduce both relations as well as the MS (Lian et al., 2018b):

i) strong outflows remove a large fraction of the metals;

ii) a steeper IMF describes the early stages of galaxy formation.

In order to track the MZR's changes over time, it is necessary a large number of spectra. However, only high signal-to-noise ratio (S/N) spectra can provide accurate measurements of metallicities for both the stellar population and gas phase when using "strong-line"[2] calibrations (see Sect. 2.5, Maiolino et al., 2019).

---

[2] Strong-line diagnostic related with lines that are not possible to calibrate empirically through the direct method because the required data are not available.

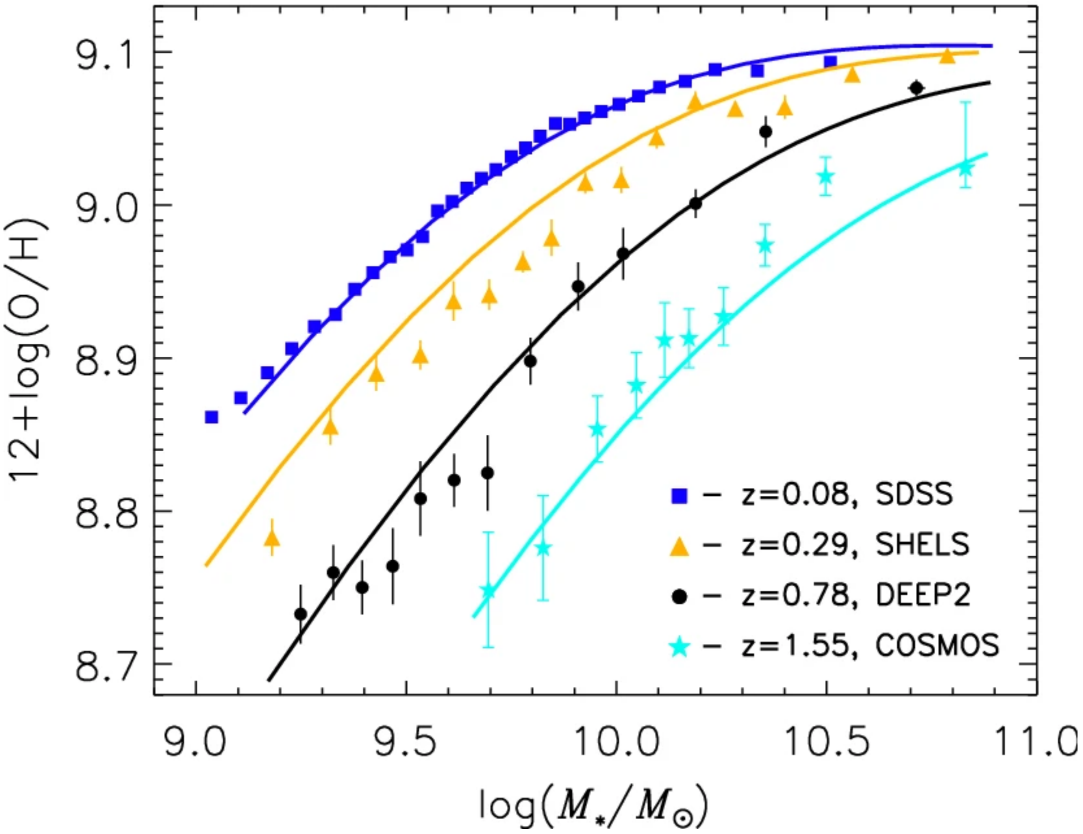

Figure 1.7: MZR evolution with redshift up to $z = 1.55$. The plot shows the MZR for $z = 0.08$ (blue), $z = 0.29$ (yellow), $z = 0.78$ (black), and $z = 1.55$ (cyan). Credits: Zahid et al. (2014b).

The MZR has been studied up to a redshift of $z \sim 3.5$. This is the point where the primary optical lines fall within the near-infrared bands. The MZR indicates a consistent decrease in metallicity with increasing redshift, meaning that at a given mass, the amount of metals observed decreases (see Fig. 1.7). High-mass galaxies progress rapidly and attain their current metallicity at around $z \sim 1$, a chemical form of downsizing (Maiolino et al., 2019). Conversely, low-mass galaxies display a swift evolution of the MZR as redshift changes.

Many studies have been conducted using optical spectroscopy to examine the evolution at intermediate redshifts ($z \leq 1.5$, Contini et al., 2002; Cowie et al., 2008; Cresci et al., 2012; Guo et al., 2016; Hoyos et al., 2005; Kobulnicky et al., 2003, 2004; Maier et al., 2004, 2005, 2006; Moustakas et al., 2011; Nakajima et al., 2013; Pérez et al., 2016; Pérez-Montero et al., 2013; Savaglio et al., 2005; Suzuki et al., 2017; Zahid et al., 2011b; Zahid et al., 2013). However, to further investigate higher redshifts, near-infrared spectroscopy is necessary. In the near-infrared part of the spectrum, the sky background is much brighter, the atmosphere has reduced transmission, and the spectrographs have technological limits compared to optical ones. This makes it more difficult to obtain useful spectra, especially for galaxies with higher SFR. Despite these difficulties, some studies have been conducted at $z \sim 2$ (Bian et al., 2017; Cullen et al., 2014a; Erb et al., 2006a, 2010; Finkelstein et al., 2011; Onodera et al., 2015; Sanders et al., 2015, 2016, 2018; Steidel et al., 2014; Wuyts et al., 2012, 2014; Zahid et al., 2014a) and $z \sim 3$ (Belli et al., 2013; Maier et al., 2014; Maiolino et al., 2008; Mannucci et al., 2009; Onodera et al., 2016; Troncoso et al., 2014) by stacking several galaxies to detect the faintest lines needed to estimate metallicity. However, stacking spectra introduces more uncertainties, such as choosing which galaxies to stack, how to perform the stacking, and accounting for possible non-linear effects. (Maiolino et al., 2019).

To understand the details of the evolution it is important to take into account the different methodologies used:

i) At high redshift, each survey allows access to a limited number of diagnostics to use as metallicity indicators, introducing scatters and systematics among different surveys (Kewley et al., 2008). Moreover, different results can be achieved using different line rations of the same calibration (Brown et al., 2016). It is also unclear if there is significant evolution with the redshift of the calibrations. This evolution can be caused by different conditions of the SF regions (in terms of the ionization parameter), ionizing spectra, density, pressure, and N/O ratio. These effects can differ for different methods (Kashino et al., 2017; Kewley et al., 2013a,b, 2015; Shapley et al., 2015; Steidel et al., 2014; Strom et al., 2018).

ii) The method to measure $M_\star$ (and SFR) affects the results (Cresci et al., 2019; Yates et al., 2012).

iii) The selection of galaxies affects the results, especially when selecting via the flux of metallicity-sensitive lines, such as [O III] λ5007 (Izotov et al., 2015; Izotov et al., 2011; Xia et al., 2012) the results can be biased towards lower or higher metallicities.

iv) A similar effect is given by using an S/N cut on the flux of the line used to measure the metallicity. Metallicity-dependent selection effects can be introduced using an S/N threshold equal to 3–5 on all the lines (Yates et al., 2012). These biases are difficult to trace (Cresci et al., 2019; Salim et al., 2014). The inverse approach selects via a high S/N threshold only for emission lines that are directly related to SFR but are less sensitive on metallicity, e.g., Hα and Hβ, resulting in a more SFR-selected sample (Mannucci et al., 2010). The studied samples are usually not mass or volume selected in both cases.

v) In surveys with observations via fibers, the spectra are usually observed within a fixed aperture independent of the galaxy distance. The presence of radial metallicity gradients together with the observation strategy introduces fake correlations of metallicity with distance and galaxy size. These fake correlations are not easy to estimate and correct (Curti et al., 2020; Mannucci et al., 2010; Salim et al., 2014).

vi) The metallicity dependence on SFR and other galaxy properties (e.g., size and surface density) affects the shape and evolution of the observed MZR via the selection of galaxies in terms of luminosity and redshift range. These effects can explain (Cresci et al., 2019) the differences shown in literature (Steidel et al., 2014; Wuyts et al., 2014).

Regardless of these biases, the observed MZR evolves with redshift (see Fig. 1.7), especially at $z > 1$. The evolution is observed as a metallicity decrease with redshift at a given $M_\star$ with a rate that depends on redshift and $M_\star$.

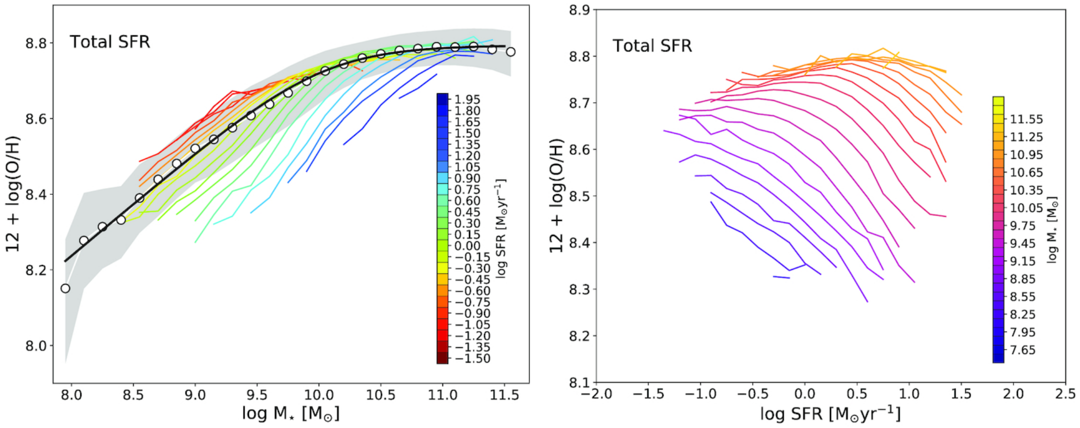

Figure 1.8: Evidence for the fundamental metallicity relation (FMR). Left panel: MZR in bins of SFR. Right panel: SFR-metallicity relation in bins of $M_\star$. Credits: Curti et al. (2020).

1.5 The fundamental metallicity relation

Once a good precision of the measurements was achieved, proof for dependencies of metallicity on other galaxy properties emerged (Maiolino et al., 2019). Among all, correlations of

i) the metallicity residuals from the MZR with galaxy color, ellipticity, and central mass(Tremonti et al., 2004);

ii) the MZR shape on galaxy size (Hoopes et al., 2007);

iii) the MZR on SFR at a given mass (Ellison et al., 2008a);

were reported. A new relationship called the Fundamental Metallicity Relation (FMR, Mannucci et al., 2010) has been introduced to connect the $M_\star$, metallicity, and SFR. The purpose of this is to reduce the scatter in metallicity around the median relationship in the local universe to about 0.05 dex, which is consistent with the level of uncertainty in measuring metallicity. This relationship shows that metallicity decreases as SFR and the specific SFR (sSFR, defined as the ratio of SFR to $M_\star$) at a given mass. More SF galaxies show lower metallicities than more passive ones for a given mass (see Fig.1.8)

Despite the evolution of the MZR, the FMR does not show any evolution up to $z = 2.5$ (see Fig.1.7, Mannucci et al., 2010). The metallicity residual with respect to the FMR defined in the local universe (Mannucci et al., 2010) of all the data at $z < 2.5$ available (Epinat et al., 2009; Erb et al., 2006a; Förster Schreiber et al., 2009; Law et al., 2009; Lehnert et al., 2009; Liu et al., 2008; Savaglio et al., 2005; Shapley et al., 2005; Wright et al., 2009) are consistent with zero. Only data at higher redshifts (Maiolino et al., 2008; Mannucci et al., 2009) shows a bigger residual, with a difference of about 0.06 dex.

As for the MZR, also the shape of the FMR (see Fig. 1.10) depends on different factors, especially on how galaxies and how $M_\star$, SFR, and metallicity are estimated. Various shapes have been suggested for the FMR, including those proposed (Brisbin et al., 2012; Hunt et al., 2012; Lara-López et al., 2010; Mannucci et al., 2010; Nakajima et al., 2014; Yates et al., 2012). When determining metallicity via "direct" methods that rely on the T_e measurement, the FMR demonstrates a stronger correlation with

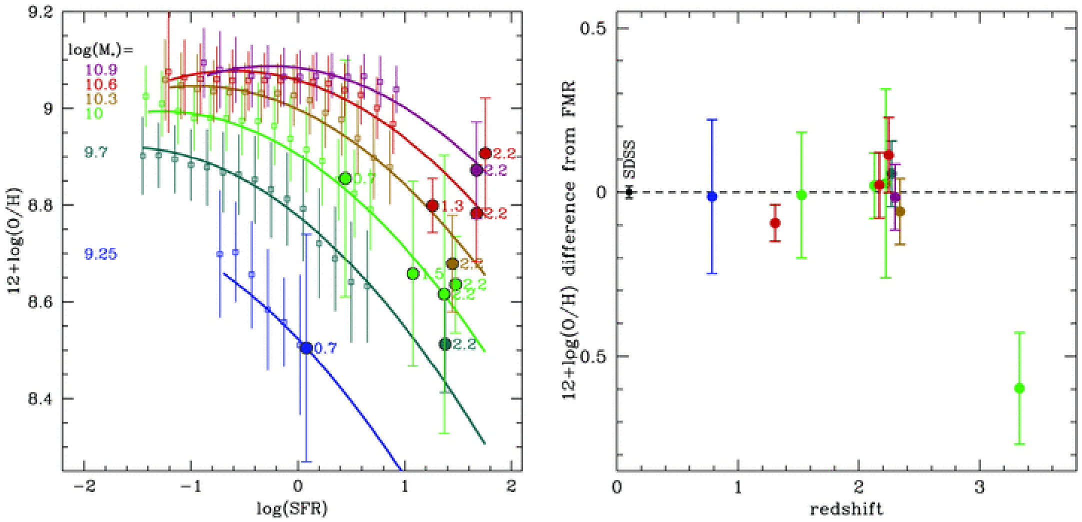

Figure 1.9: Evolution of the metallicity-SFR relation (left panel) and the metallicity residuals from the FMR (right panel) for galaxies at different redshifts. The local definition of the FMR is consistent with all the samples up to $z = 2.5$. Metallicities lower by ~ 0.6 dex are observed at $z \sim 3.3$. Credits: Mannucci et al. (2010).

the SFR (Andrews et al., 2013). To measure T_e, auroral lines must be detected, even in SDSS observations, and the stacking of spectra based on $M_\star$ and SFR is necessary, assuming that metallicity is linked only to these two parameters (Maiolino et al., 2019). A distinct T_e-calibration was established (Curti et al., 2017) by stacking spectra based on their similarities (i.e., identical [O II] $\lambda3727/\text{H}\beta$ and [O III] $\lambda5007/\text{H}\beta$ ratios) rather than physical properties. The usage of different metallicity calibrations, SFR estimations, and dependence on galaxy size, as well as considering the SFR distance from the MS, further impact the FMR (Cresci et al., 2019; Salim et al., 2014; Telford et al., 2016).

The origin of the FMR is still discussed. Several explanations have been proposed to explain the dependence of the metallicity on both $M_\star$ and SFR:

i) a varying SFE to describe the metallicity dependence on SFR and galaxy size (Ellison et al., 2008a);

ii) SFR feedback from infalling metal-poor gas (the infall supply the ISM with metal-poor gas, lowering the metallicity, increasing at the same time the fuel of the star formation Mannucci et al., 2010).

The FMR is the result of the important role of cold gas accretion in galaxy evolution. Gas-equilibrium models can describe and explain the FMR. Some models (Lilly et al., 2013) do not predict any evolution of the FMR because base the equilibrium on basic physical properties resulting stable across cosmic time. Other models (Davè et al., 2011) predict a slow evolution with redshift due to the continuous enrichment of the CGM. It is not possible at the moment to distinguish between these two scenarios (Sanders et al., 2018) because of the limited precision of the observational results.

Studies using hydrodynamical simulations (De Rossi et al., 2018; De Rossi et al., 2017; Lagos et al., 2016a; Lagos et al., 2016b) have confirmed the observed FMR. These simulations suggest that key factors in reproducing the observations are the properties of stellar and AGN feedback, as well as the relationship between star formation and metallicity. Additionally, the IllustrisTNG simulation (Torrey et al.,

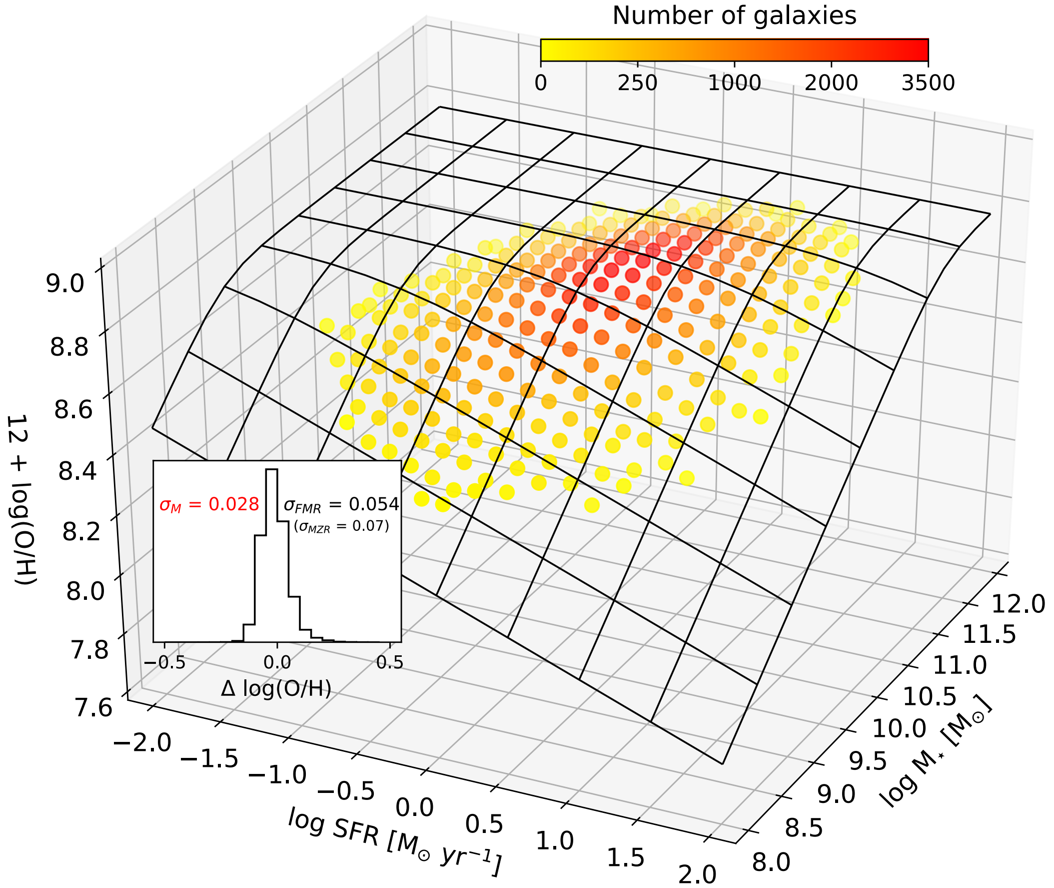

‘

Figure 1.10: Visualization of the 3D shape of the FMR, color-coded by the number of galaxies in each bin. The histogram shows the metallicity dispersion of individual galaxies around the surface. Credits: Curti et al. (2020).

2018) has successfully reproduced the FMR at high redshift. This is believed to be due to the similar timescales of SFR and metallicity evolution.

The presence of evolution, or lack of it, of the FMR has been studied both observationally and theoretically. The local FMR agrees with metallicities at $z \sim 1$ in many studies (Calabrò et al., 2017; Cresci et al., 2012; Henry et al., 2013a,b; Maier et al., 2015a; Maier et al., 2015b; Stott et al., 2013; Yabe et al., 2012, 2014) and at $z \sim 2$ (Belli et al., 2013; Hirschauer et al., 2018; Kacprzak et al., 2016; Nakajima et al., 2012, 2014; Salim et al., 2015; Sanders et al., 2018; Wuyts et al., 2016). Some studies confirm the SFR-metallicity relation, but with a weaker dependence or with some evolution with respect to the local FMR (Cullen et al., 2014b; Grasshorn Gebhardt et al., 2016; Niino, 2012; Pérez-Montero et al., 2013; Salim et al., 2015; Wu et al., 2016; Zahid et al., 2014a).

The SFR-metallicity relation is not found in some studies at high redshift (Onodera et al., 2015; Sanders et al., 2015; Steidel et al., 2014; Wuyts et al., 2012, 2014, 2016; Yabe et al., 2014, 2015). There are mainly two problems when comparing the metallicity properties of distant galaxies with the local (SDSS) FMR:

i) Is the local FMR able to predict the average metallicity of a galaxy sample with a given average $M_\star$ and average SFR?

ii) Is it possible to detect the metallicity dependence on the SFR in the high-redshift sample as in the local universe?

The local FMR is still able to predict the average metallicity (Cresci et al., 2019) of the galaxies of the sample quoted above where the SFR-metallicity relation is missing. Some works describe the detection of the SFR-metallicity relation also at high redshift (Kacprzak et al., 2016; Kashino et al., 2017; Salim et al., 2015; Sanders et al., 2018; Zahid et al., 2014a) finding an anti-correlation between metallicity and SFR at $z \sim 2$.

Table 1.1: Samples used in different studies of the FMR.

Survey	Reference	z	Sample size
SDDS	1	0.07 – 0.30	141 825
Collection	1	0.5 – 2.5	182
LSD, AMAZE	1	3 – 4	16
zCOSMOS	2	0.2 – 0.8	334
SDSS	3	0.005 – 0.25	177 071
MOSDEF	4	$\sim$ 2.3	87
zCOSMOS	5	05 – 0.9	39
KBSS	6	$\sim$ 2.3	130
eBOSS	7	0.6 – 0.9	35
CALIFA	8	0.005 – 0.03	612
SDSS-IV MANGA	8	0.03 – 0.17	2730
SDSS	9	0.027 – 0.3	153 452
SDSS	10	0.005 – 0.2	68 942
SDSS	11	0.027 – 0.27	156 018
VIPERS	11	0.5 – 0.8	**4 772**
SDSS	12, 13	0.027 – 0.27	155 931
VIPERS	12, 13	0.5 – 0.8	**6 222**

References. (1) Mannucci et al. (2010); (2) Cresci et al. (2012); (3) Yates et al. (2012); (4) Sanders et al. (2015); (5) Maier et al. (2015b); (6) Salim et al. (2015); (7) Gao et al. (2018); (8) Cresci et al. (2019); (9) Curti et al. (2020); (10) Bustamante et al. (2020); (11) Pistis et al. (2022); (12) Pistis et al. (2023a); (13) Pistis et al. (2023b).

1.6 Open questions

The comparison of galaxy samples at different redshifts involves many difficulties, including:

i) fundamentality of the FMR or byproduct of more underlying relations;

ii) different selection effects (e.g., survey limit, S/N of spectra Pistis et al., 2022);

iii) different rest-frame observed;

iv) different selection criteria for SF galaxies and estimation of metallicity;

v) different metallicity calibrators based on different sets of emission lines or different methodology of calibration (Kewley et al., 2008);

vi) small samples available at higher z (as seen from Table 1.1);

vii) different methods of selecting galaxies for comparison;

viii) different methods of comparison (to be addressed in this study).

In this Ph.D. Thesis, we focus to answer three of these open questions:

i) the effects of biases introduced by data selection and survey limits on the FMR (see Chapter 4, Pistis et al., 2022);

ii) the effects of the methods of comparison on the conclusion about the FMR evolution (see Chapter 5, Pistis et al., 2023a);

iii) the search for footprints left over the FMR by galaxy evolution or environment and outliers in the FMR (see Chapter 6, Pistis et al., 2023b).

Thus, the main goal of this thesis is the application of the largest presently available spectroscopic galaxy catalogs up to $z \sim 0.8$ in order to find out if the FMR is indeed fundamental, i.e. if it does - or does not - evolve, along with the development of a set of methods and tests which can be then applied in the future, yet larger datasets.

CHAPTER 2

How to measure galaxies?

This chapter describes the state-of-art on extragalactic observations, focusing on photometric surveys (Sect. 2.1), spectroscopic surveys (Sect. 2.2), and how to measure the main properties such as $M_\star$ (Sect. 2.3), SFR (Sect. 2.4), and metallicity (Sect. 2.5).

2.1 Photometric surveys

Photometry is a technic by which the flux of photons is measured in a range of wavelengths (bandwidth) called filters. In Figure 2.1 are reported the filters for the SDSS and the MegaCam, the wide-field optical imaging facility at the Canada-France-Hawaii Telescope (CFHT). The integrated observation of the source in a relatively wide bandwidth allows us to reduce the observational time, reducing the exposure time. This improves efficiency and allows us to gather data more quickly.

Observing the same source in a wide range of filters, we can build the so-called Spectral Energy Distribution (SED, see Fig. 2.2). The SED is the plot of the brightness or flux density (i.e., power) versus the frequency or wavelength and it is used to classify astronomical sources. Different bandwidths probe different properties of the observed galaxy:

i) in the ultraviolet (UV) wavelengths, we observe directly the young stars having information directly information about the SFR;

ii) in the visible and near-infrared (NIR) wavelengths, we observe evolved stars having information about the $M_\star$;

iii) in the mid-infrared (MIR) wavelengths, we observe the dust and the Polycyclic Aromatic Hydrocarbons (PAHs) having information about the metallicity;

iv) in the far-infrared (FIR), we observe the hot dust having information about the hidden SFR;

v) in the sub-mm, we observe the cold dust having information about the dust mass.

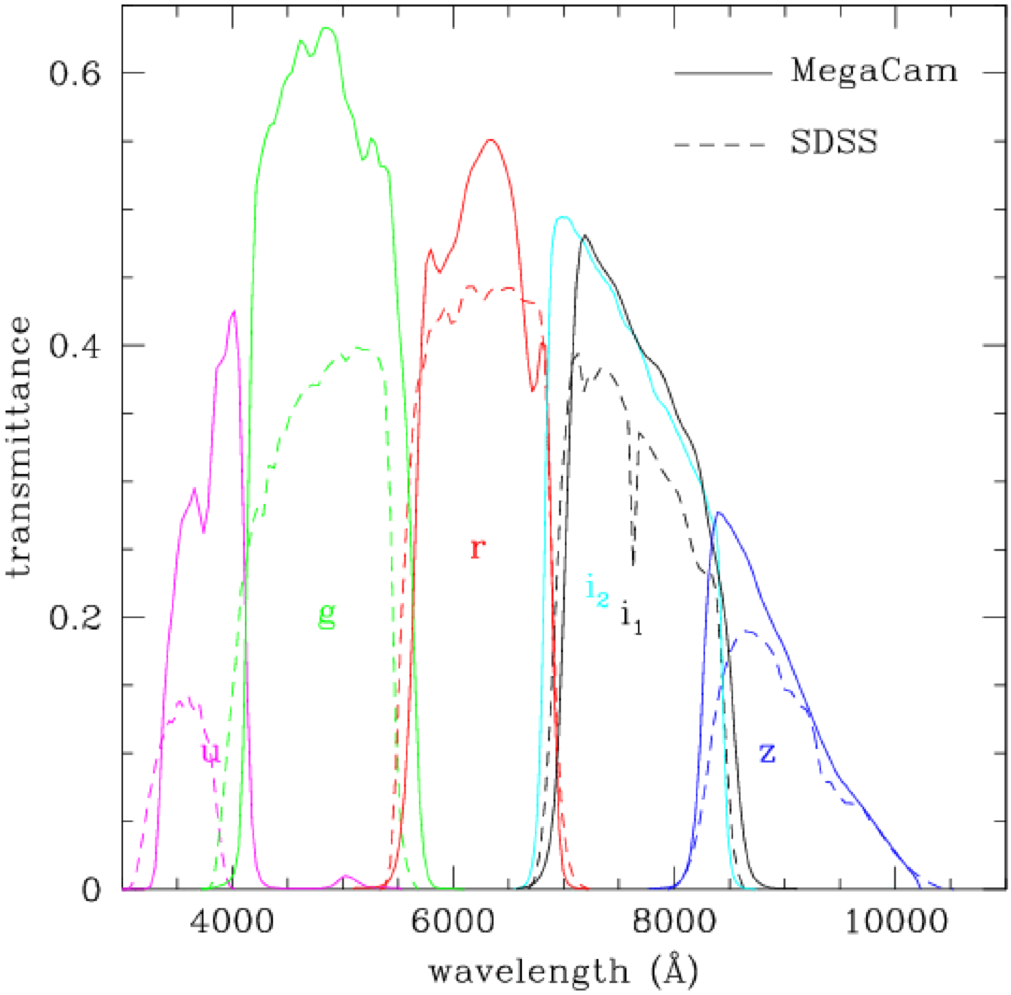

Figure 2.1: Comparison of the filters used in the SDSS and CFHTLS (MegaCam) surveys. Credits: Canadian Astronomy Data Centre (https://www.cadc-ccda.hia-iha.nrc-cnrc.gc.ca/en/megapipe/docs/filtold.html).

2.2 Spectroscopic surveys

Observing a galaxy through a spectrograph, we can study the photon flux in a small range of wavelengths. For example, SDSS observed the spectra of galaxies between 3 800 Å and 9 200 Å, while the VIMOS Public Extragalactic Redshift Survey (VIPERS) measured the spectra between 5 500 Å and 9 500 Å. Figure 2.3 shows different types of spectra according to the light-matter interactions that represent. Observing directly a hot and dense light source, e.g. stars and galaxies, we observe a continuous spectrum containing all wavelengths in a certain range. Stars and galaxies emit light that travels in all directions and interacts with the matter in space. If we observe the emitted light through a gas cloud, the matter composing the cloud absorbs part of the light. The absorption is a selective process, the wavelengths absorbed depend on what elements compose the cloud. The absorption spectrum shows dark lines corresponding to the wavelengths absorbed by the gas. The gas cloud gets heated up while absorbing the light leading to an excitation state of the atoms and molecules within the gas. The energy surplus is then emitted again in the form of light. The spectrum of this emitted

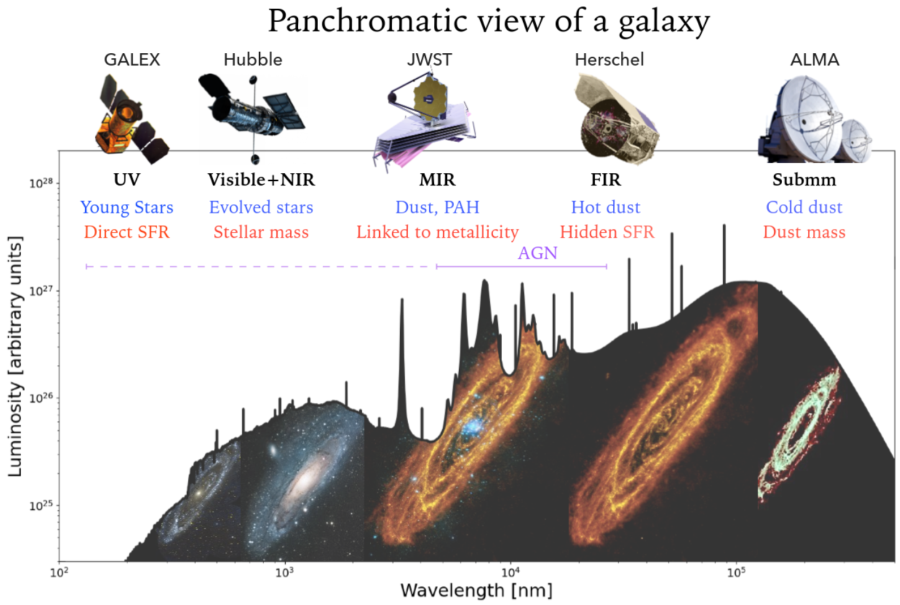

Figure 2.2: Spectral Energy Distribution (SED) built with observations from ultraviolet (UV) to sub-millimeter (sub-mm) wavelengths. Credits: M. Hamed

light by the hot gas cloud depends on its temperature, density, and composition. The spectra of a cloud with and without a background light source are the negatives of each other. We can derive information about the chemical composition of the light sources from their spectra.

2.3 Measure the stellar mass

The measure of $M_\star$ is fundamental to understanding the formation of galaxies. The estimating of $M_\star$ is a powerful probe to identify the stellar population that can be compared to theoretical predictions. The $M_\star$ can be only derived by observation making different work hypotheses and assuming different models.

Single stellar population[1] (SSP) models (Bruzual et al., 2003; Maraston et al., 2011) are integrated with models of the star formation history (SFH) and chemical evolution of model galaxies to reproduce the observed SEDs. This procedure is complicated by the need to assume an initial mass function (IMF, Baldry et al., 2003; Chabrier, 2003; Kroupa, 2001; Salpeter, 1955) and the dust attenuation (Calzetti et al., 2000; Lo Faro et al., 2017). The SEDs are usually built upon broad-band photometry. Different assumptions made during the fitting procedure affect the estimation of the $M_\star$ (Conroy et al., 2009; Ilbert et al., 2010; Marchesini et al., 2009; Michałowski et al., 2012; Moustakas et al., 2013; Papovich et al., 2001; Wuyts et al., 2007).

SED fitting codes commonly used are:

i) *LePhare*[2] (Arnouts et al., 1999; Ilbert et al., 2006a): code to estimate the photometric redshift and to perform SED fitting up to FIR. The physical parameters and uncertainties are based on *PÉGASE* (Programme d'Étude des GAlaxies par synthèse Évolutive, Fioc et al., 1997; Fioc et al., 1999, 2019) and SSP models (Bruzual et al., 2003).

---

[1] Assuming that all the stars are formed from the same gas cloud, at the same time (same age) and same chemical composition (metallicity).

[2] http://www.cfht.hawaii.edu/~arnouts/lephare.html

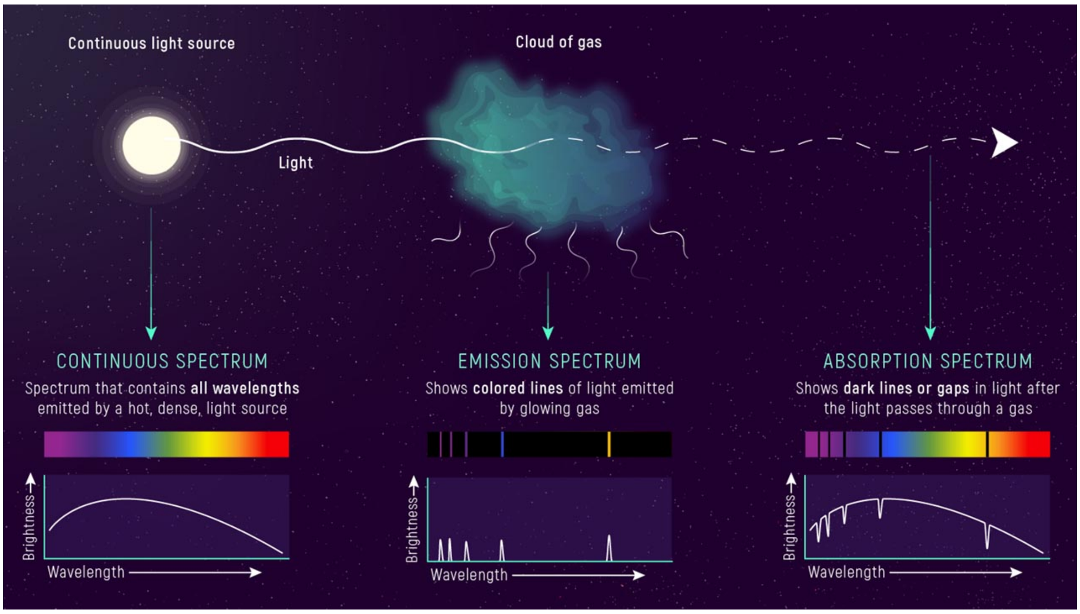

Figure 2.3: Different types of spectra: continuous, emission, and absorption. Credits: Webb Space Telescope (`https://webbtelescope.org/contents/media/images/01F8GF8DK2PRY4FP9DA2XPQC8S`).

ii) *HYPERZMASS* (modified version of the photometric redshift code *HYPERZ*[3], Bolzonella et al., 2000a, 2010): fit of the photometric catalog with magnitudes computed from SED templates. The templates can be built via different stellar libraries (Bruzual et al., 2003; Maraston, 2005), IMF (Chabrier, 2003; Kroupa, 2001; Salpeter, 1955), the dust attenuation is modeled using the Calzetti's law (Calzetti et al., 2000). When the spectroscopic redshift is measured, it is possible to compare the observed and template fluxes at a fixed $z = z_{\text{spec}}$, providing the best-fit SED minimizing the chi-squared χ^2.

iii) *FIREFLY*[4] (a full spectral fitting code, Wilkinson et al., 2017): fit made via minimization of the χ^2 to derive the properties of the stellar system (observed galaxy or star cluster spectra, or simulated spectra). The code fits the spectroscopic data with a combination of single-burst stellar population models. *FIREFLY* follows an iterative best-fitting procedure controlled by the Bayesian Information Criterion. The code does not apply any prior but rather it assigns a weight to all the solutions. This procedure allows studying the effects of intrinsic degeneracies in the SED, such as age, metallicity, and dust reddening on the stellar population properties. The estimated stellar population properties (age, metallicity, $\mathrm{E\,(B-V)}$) provided by the code are light- and mass-weighted.

iv) *CIGALE*[5] (Code Investigating GALaxy Emission Boquien et al., 2019; Burgarella et al., 2005; Noll et al., 2009; Yang et al., 2020; Yang et al., 2022): model the FUV to radio spectrum of galaxies estimating their physical properties (e.g., SFR, attenuation, dust luminosity, $M_{\star}$, and etc. Boquien et al., 2019). The code combines the SSP models with highly flexible SFHs, quantifies the emission from ionized gas by massive stars, and attenuates both stellar and gas components with a flexible attenuation curve. CIGALE is based on energy balance, i.e., the

---

[3] `https://ascl.net/1108.010`

[4] `http://www.icg.port.ac.uk/firefly/`

[5] `https://cigale.lam.fr/`

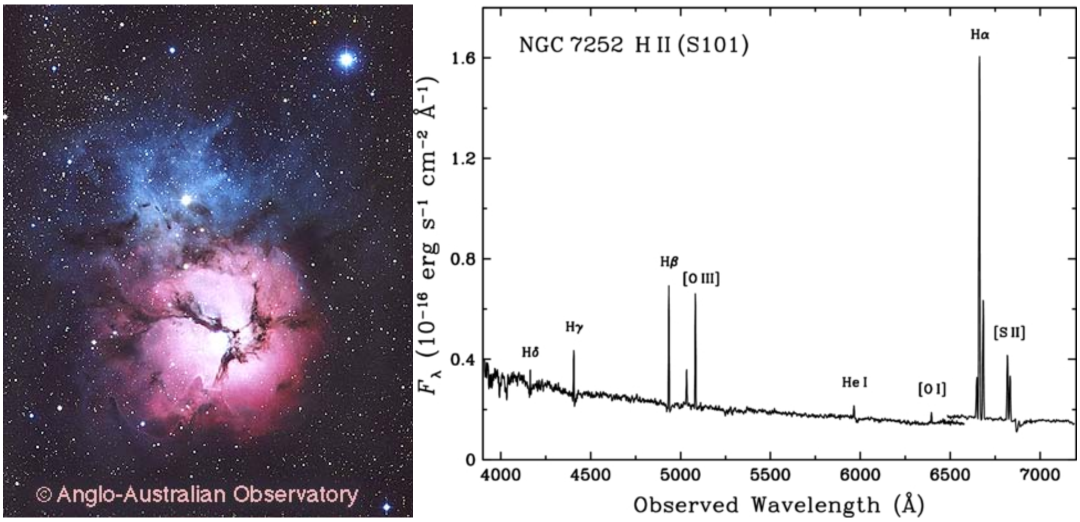

Figure 2.4: Left panel: the optical image of the Trifid nebula M20 (HII region). Right panel: Spectrum of the HII region NGC 7252. Credits: C. Mihos (`http://burro.case.edu/Academics/Astr222/Galaxy/Structure/gas.html`).

absorbed energy in the UV and optical part of the SED is then re-emitted by the dust in the MIR and FIR. The code produces a large grid of model templates used to fit the observed data and to compute the physical properties. CIGALE is able to build grids of millions of models.

2.4 Measure the star formation rate

Young newborn stars strongly emit in the UV part of the spectrum. The UV radiation ionizes completely the hydrogen around them. The young population of stars is then surrounded by a cloud of ionized hydrogen, the so-called HII region (see the left panel in Fig. 2.4). The recombination of electrons and protons happens generally at high energy levels (large n). The electrons fall in lower levels emitting the Balmer lines. The Balmer lines are bright emission lines visible in the spectra of HII regions (see the right panel in Fig. 2.4).

In galaxies, the nebular lines are responsible for emitting light absorbed by stellar luminosity at shorter wavelengths, below the Lyman limit. The nebular lines serve as a direct indicator of the presence of a young, massive stellar population. By measuring the Hα line, it is possible to obtain an accurate measurement of the SFR (Kennicutt, 1998). Other helpful lines for this purpose include the Hβ, Pα, Pβ, Brα, and Brγ.

In order to calculate the SFR, it is necessary to use an evolutionary synthesis model to calibrate the emission lines. The main contribution comes from stars with masses $> 10\ M_\odot$ and lifetimes < 20 Myr. The SFR obtained from the calibrated lines provides an instantaneous measure that is independent of the previous SFH. However, this method has limitations, such as its sensitivity to uncertainties in extinction and the IMF, and the assumption that all of the star formation is traced by the ionized gas (Kennicutt, 1998).

Beyond a redshift of approximately 0.5, the Hα emission line cannot be detected in optical spectra. To accurately measure the SFR beyond this threshold, it is necessary to use bluer emission lines as quantitative SFR tracers. However, the integrated fluxes of Hβ and the higher order Balmer emission lines are not reliable SFR diagnostics due to their smaller intrinsic fluxes and susceptibility to stellar absorption.

The strongest emission in the blue part of the spectra is from the forbidden [O II] λ3727 doublet. The luminosities of forbidden lines depend on gas abundance, the ionization state, and are not directly related to ionizing luminosity. However, the [O II] λ3727 line can be used as a quantitive SFR tracer by calibrating it empirically through Hα (Kennicutt, 1998). This calibration is particularly useful for studying distant galaxies, as the [O II] λ3727 line can be observed in optical spectra up to $z \sim 1.6$ (Cowie et al., 1996, 1997; Ellis, 1997; Figueira et al., 2022; Lamareille et al., 2009; Pérez-Montero et al., 2009; Pistis et al., 2022, 2023a,b; Vietri et al., 2022).

2.5 Measure the metallicity

The gas phase metallicity can be measured mainly in three ways (Maiolino et al., 2019; Peimbert et al., 2017):

i) direct method based on electron temperature;

ii) abundances from metal recombination lines;

iii) photoionization models.

In astrophysical conditions, the ionized gas spectra contain a variety of collisionally excited emission lines (CEL). The emissivity of each metal line is determined by the abundance of its elements. By measuring the emissivity, the abundances can be calculated (Aller, 1984).

The emissivity of metal lines is affected by both the electron temperature T_e and electron density n_e. When dealing with a two-level ion, the rate of collisional de-excitation (per unit volume) for the transition from energy level 2 to energy level 1 can be calculated using the formula $n_2 n_0 C_{21}$. Here, n_2 refers to the density of ions with the second energy level populated, n_0 is the density of colliding particles (usually electrons), and C_{21} is the collisional de-excitation coefficient given by

$$C_{21} = \left(\frac{2\pi}{kT_2}\right)^{0.5} \frac{\hbar^2}{m^{3/2}} \frac{\Omega\left(1,2\right)}{\omega_2}, \tag{2.1}$$

where $\Omega\left(1,2\right)$ is the collisional strenght of the transition and ω_2 is the statistical weight of the second energy level. The rate of collisional excitation has a similar form, $n_1 n_0 C_{12}$, where

$$C_{12} = \frac{\omega_2}{\omega_1} e^{E_{21}/kT_e} C_{21}. \tag{2.2}$$

The coefficients C_{21} and C_{12} have a different dependency on the T_e. The former depends on T_e as $\sqrt{T_e}$, while the latter depends exponentially on T_e.

A CEL is emitted by the collisional excitation of the upper level followed by a radiative de-excitation. With the hypothesis that stimulated emission and absorption can be neglected in diffuse nebulae, the population n_2 is given by

$$\frac{dn_2}{dt} = -n_2\left(A_{21} + n_e C_{21}\right) + n_1 n_e C_{12}, \tag{2.3}$$

where A_{21} is the Einstein coefficient. At equilibrium we have $dn_2/dt = 0$, then:

$$\frac{n_2}{n_1} \frac{n_e C_{12}}{A_{21} + n_e C_{21}}. \tag{2.4}$$

A critical density n_c can be defined as $n_c = A_{21}/C_{21}$, allowing us to rewrite the density ratio as:

$$\frac{n_2}{n_1} = \frac{n_e/n_c e^{E/kTe}}{1 + n_e/n_c}. \tag{2.5}$$

In case the density of the medium is much lower than the critical density of the transition (i.e., $n_e \ll n_c$), n_2 depends exponentially on T_e and $n_1 \sim n_x$, where n_x is the density of the species x. The volumetric emissivity J_{21} of the metal line is given by

$$J_{21} = h\nu_{21} \frac{n_2 A_{21}}{4\pi} \sim n_e n_x e^{-E_{21}/kT_e}. \tag{2.6}$$

Once we measure n_e and T_e, the ionic abundance is derived by the comparison of the CEL flux with the hydrogen recombination line. The total metal abundance is computed by adding up the abundances of the observed ions and assuming an ionization correction for the ions not observed (Aller, 1954; Bresolin et al., 2009; Dinerstein, 1990; Pérez et al., 2016; Perez-Martinez, 2014; Pérez-Montero, 2014; Pilyugin et al., 2009, 2010; Pilyugin et al., 2005, 2006).

To determine the concentration of ions, specifically those with a similar concentration to the critical density, density-sensitive doublets are utilized. Emission ratios of ions, such as [O II] λ3726, 3729 and [S II] λ6717, 6731, depend on the density in this specific range. To calculate the temperature of the ions, "auroral lines" emitted from high quantum levels are compared to brighter lines emitted from a different energy level of the same species. Common auroral lines used include [O III] λ1661, 1666, [O III] λ4363, [O II] λ7320, 7330, [S II] λ4069, [N II] λ5755, and [S III] λ6312 (Castellanos et al., 2002; Pérez-Montero, 2017). Reliable results require multiple lines as they trace different parts of the emitting region. However, the use of auroral lines is limited by their intrinsic luminosity, typically 10–100 times fainter than the corresponding Balmer lines. Auroral lines are commonly observed in local or low redshift, metal-poor, SF galaxies (Amorín et al., 2015; Haurberg et al., 2015; Izotov et al., 2006a,b, 2012, 2018; Izotov et al., 2007, 2011; Kennicutt et al., 2003; Kreckel et al., 2015; Lagos et al., 2016b; Ly et al., 2016; Pilyugin et al., 2015; Sánchez Almeida et al., 2016), while at higher redshift ($z > 1$) the observation is much more difficult.

A more direct way to estimate the metallicity is via the permitted recombination lines (RL) of metal ions. The volumetric emissivity of a permitted line of ion x, in the standard condition of HII regions (with no stimulated emission), due to the transition between the levels i and j is

$$J_{ij} = \frac{h\nu_{ij}}{4\pi} n_{x^{+i+1}} n_e \alpha_{ij}^{\mathrm{eff}} \left(x^{+i}, T_e \right), \tag{2.7}$$

where $\alpha_{ij}^{\mathrm{eff}}$ has only a weak dependence on T_e. The ionic abundance is then computed by comparing it with the hydrogen RL which has the same dependency on density. The estimated density is, in this case, insensitive to the gas density. The main RL used to measure metallicity are O I λ8446, 8447, O II λ4639, 4642, 4649, O III λ3265, O IV λ4631, N II λ4237, 4242, N III λ4379, C II λ4267, C III λ4647, and C IV λ4657.

As an alternative to the direct method, photoionization models can be used to predict or interpret the relative strength of the main nebular lines (Maiolino et al., 2019). Although this method has limitations in exploring only a small number of parameters in the models, it is not limited to exploring the possible properties of SF regions such as the metallicity range and properties of the ionizing spectrum. For this reason, this method is used in high-redshift sources, including those with extremely metal-poor environments or extreme ionizing spectra that do not have local replicas (Jaskot et al., 2016; Kewley et al., 2013c; Schaerer, 2003; Xiao et al., 2018). Other properties (e.g., the ionization parameter) can be constrained by the photoionization models. Additionally, these models can be used to empirically calibrate strong-line diagnostics related to lines that are not possible to calibrate with direct methods. Photoionization models overestimate the gas metallicity from ~ 0.2 to ~ 0.6 dex and the deviation is stronger at high metallicities (Maiolino et al., 2019).

The emission lines necessary to compute the metallicity are very faint and difficult to observe. For this reason, the direct methods are usually limited to local galaxies and HII regions or by stacking a large number of spectra (Andrews et al., 2013; Curti et al., 2017). For this reason, it was necessary to calibrate (the so-called "strong line method") relatively strong emission lines which can be detected easily even in low S/N spectra. The calibrations of the strong lines have been achieved via direct methods (Curti et al., 2017; Pettini et al., 2004; Pilyugin et al., 2010, 2016; Pilyugin et al., 2005), photoionization models (Dopita et al., 2016; Kewley et al., 2002; Kobulnicky et al., 2004; McGaugh, 1991; Nagao et al., 2011; Tremonti et al., 2004; Zaritsky et al., 1994), or a combination of both (Denicoló et al., 2002; Maiolino et al., 2008; Nagao et al., 2006).

CHAPTER 3

Data selection

This chapter describes the data used in this work with a focus on the data surveys used (Sect. 3.1), the data selection (Sect. 3.2), and the measurements of the main properties, such as $M_\star$ (Sect. 3.3), SFR (Sect. 3.4), metallicity (Sect.3.5), and the fit of the MS (Sect. 3.7). This chapter also describes how we build different control samples (Sect. 3.8) that will be used in the following analysis (Chapter 5). The original work is presented in the papers with titles: F. Pistis et al. (July 2022). The fundamental metallicity relation from SDSS (z $\sim$ 0) to VIPERS (z $\sim$ 0.7). Data selection or evolution. A&A 663, A162, A162. DOI: `10.1051/0004-6361/202142430`. arXiv: `2206.02458 [astro-ph.GA]`; F. Pistis et al. (2023a). A comparative study of the fundamental metallicity relation. The impact of methodology on its observed evolution. A&A submitted; F. Pistis et al. (2023b). Galaxy evolution footprint on the fundamental metallicity relation. A machine learning approach. in prep.

3.1 Surveys

We use spectroscopic data from two surveys: SDSS ($0 < z < 0.3$) and VIPERS ($0.5 < z < 1.2$). We also make use of the VIMOS VLT Deep Survey (VVDS, Le Fèvre et al., 2013) to validate the spectroscopic measurements performed on the VIPERS sample and to validate the shape of the MZR obtained with VIPERS. Table 3.1 summarizes the data selection at each step.

3.1.1 SDSS

The best choice of the low-z comparison sample is the SDSS sample. This sample was already used in many studies about MZR and FMR (e.g., Curti et al., 2020; Mannucci et al., 2010; Salim et al., 2014; Tremonti et al., 2004). This survey observed a large portion of the sky (93 80 deg^2) for the spectroscopic sample with a resolution $R \sim 1\,800$–$2\,200$ and wavelength coverage of 3 800–9 200 Å making it the most extended spectroscopic survey at low redshift.

We constructed the sample at median $z \sim 0.09$ by cross-matching two catalogs: the MPA/JHU catalog[1] based on SDSS DR7, composed of 927 552 galaxies with spectroscopic redshift and line fluxes (Brinchmann et al., 2004; Kauffmann et al., 2003a; Tremonti et al., 2004) and the A2.1 version of the GALEX-SDSS-WISE Legacy

---

[1] `https://wwwmpa.mpa-garching.mpg.de/SDSS/DR7/`

Table 3.1: Steps of data selection and size of VIPERS and SDSS samples after each selection step. Selection on S/N on Hα was applied only for the SDSS as this line is not visible in the VIPERS spectra. The redshift range of the VIPERS sample ($0.48 < z < 0.8$) is a natural consequence of the requirement of having the lines Hβ, [O II] λ3727, [O III] λ4959, and [O III] λ5007 in the spectral range. In the SDSS, we do not use the redshift nor line flags, but the spectral quality is assured by the high S/N of Hα and we limit the redshift at $z \geq 0.027$ to include [O II] doublet in the spectra.

Selection	VIPERS	SDSS
Spectroscopic sample	88 340	927 552
Sample with properties	39 204	601 082
Hα (S/N > 15)	–	299 070
Hβ (S/N > 3)	20 545	296 027
Redshift	–	279 851
Redshift flag	20 545	–
E (B – V) < 0.8	20 545	267 922
Line flags	9 290	–
BPT diagram	6 251	158 416
Upper branch	6 221	157 144
Metallicity calibration (Z > 8.4)	6 220	157 144
Error on metallicity ($\sigma_Z < 0.3$)	6 203	155 931

Catalog[2] (GSWLC-2, Salim et al., 2016, 2018) with 640 659 galaxies at $z < 0.3$ based on SDSS DR10 (Ahn et al., 2014), and containing physical properties ($M_\star$, SFR, and absolute magnitudes) obtained through SED fitting with CIGALE. The cross-matched sample contains 601 082 galaxies.

3.1.2 VVDS

The VIMOS VLT Deep Survey (VVDS[3] Le Fèvre et al., 2013) is a deep galaxy spectroscopic redshift survey conducted by the VIMOS collaboration with the VIMOS multi-slit spectrograph at the ESO-VLT. The VVDS is a combination of 3 purely magnitude selected surveys: Wide ($17.5 \leq i_{\rm AB} \leq 22.5$; 8.7deg^2), Deep ($17.5 \leq i_{\rm AB} \leq 24$; 0.74deg^2), Ultra-Deep ($23 \leq i_{\rm AB} \leq 25.75$; 512arcmin^2), with a total of 25 805, 11 486, 938 galaxies with a total redshifts coverage in the range $0 < z < 6.7$.

3.1.3 VIPERS

In this work, we use a sample of galaxies from the VIMOS Public Extragalactic Redshift Survey (VIPERS, Garilli et al., 2014; Guzzo et al., 2013; Scodeggio et al., 2018), which is a spectroscopic survey made with the VIMOS spectrograph (Le Fèvre et al., 2003a) whose main purpose was to measure the redshift of 10^5 galaxies in the range $0.5 < z < 1.2$. The area covered by VIPERS is about 25.5 deg^2 on the sky and only galaxies brighter than $i_{AB} = 22.5$ were observed — a pre-selection in the $(u - g)$ and $(r - i)$ color-color plane was used to remove galaxies at lower redshifts; see Guzzo et al. (2014) for a more detailed description of this survey. The Canada-France-Hawaii Telescope Legacy Survey Wide (CFHTLS-Wide: Mellier et al., 2008) W1 and W4 equatorial fields compose our galaxy sample, at R.A $\simeq$ 2 and

---

[2] `https://salims.pages.iu.edu/gswlc/`

[3] `https://cesam.lam.fr/vvds/`

$\simeq$ 22 hours, respectively. The VIPERS spectral resolution ($R \sim 250$) allows for the study of individual spectroscopic properties of galaxies with an observed wavelength coverage of 5 500–9 500 Å. The data reduction pipeline and redshift quality system are described in Garilli et al. (2014). The final data release provides reliable spectroscopic measurements and photometric properties for 86 775 galaxies (Scodeggio et al., 2018).

This catalog was then cross-matched with the one used in Turner et al. (2021), then analyzed with the SED fitting with CIGALE fitting core (Boquien et al., 2019; Burgarella et al., 2005; Noll et al., 2009; Yang et al., 2020; Yang et al., 2022). This catalog is based on the photometric catalog built by Moutard et al. (2016a,b), which is not complete[4] in the W4 field, and it contains physical properties ($M_\star$, SFR, and magnitudes).

Measurement of spectroscopic lines

This catalog is then supplemented with the spectroscopic measurements of fluxes and equivalent widths (EWs) of the emission lines of interest in this work: Hβ, [O II] λ3727, [O III] λ4959, and [O III] λ5007. The VIPERS spectra are analyzed with the penalized pixel fitting code (*pPXF,* Cappellari, 2017, 2022; Cappellari et al., 2004), which allows fitting both the stellar and gas components via full spectrum fitting. After shifting the observed spectra to the rest frame and masking out the emission lines, the stellar component of the spectra is fitted via a linear combination of stellar templates from the *MILES* library (Vazdekis et al., 2010) after being convolved to the same spectral resolution as the observations. The gas component is then fitted with a single Gaussian for each emission line, giving the integrated fluxes and their errors as a result. In order to have a better estimation of the error, the error given by *pPXF* is then multiplied by the χ^2_{red} of the fit under the emission line.

In order to estimate the EWs from the *pPXF* results, it is useful to normalize the spectrum with the continuum normalized to one. We build the normalized spectrum by dividing the best fit by the stellar component of the fit. The spectra are then analyzed with *specutils*, an astropy package for spectroscopy (Astropy Collaboration et al., 2013, 2018; Price-Whelan et al., 2018) in a range of ±1.06 full-width half maximum (FWHM), which is equivalent to 5 standard deviation of the Gaussian fit (Vietri et al., 2022), around the centroid of the emission line to estimate the EW and its uncertainty.

For this new catalog of spectroscopic measurements, we adopt the same flag system used in the VIPERS catalogs (Figueira et al., 2022; Garilli et al., 2010; Pistis et al., 2022) in the form of a 4 digits number $xyzt$. The x-value is equal to 1 if the difference between the centroid of the fit and the observed data is less or equal to 7 Å (equivalent to 1 pixel of the spectrograph), else its value is 0. The y-value is equal to 1 if the FWHM is in the range 7–22 Å equivalent to 1–3 pixels of the spectrograph, else its value is 0. The z-value is equal to 1 if the difference between the peak of the data and the fit is less than 30%, else its value is 0. Finally, the t-value is equal to 2 if the signal-to-noise ratio (S/N) for the EW is at least 3.5 or the S/N for the flux is at least 8, its value is 1 if the S/N for the EW is at least 3 or the S/N for the flux is at least 7, else its value is 0.

The catalog of line measurements obtained by this procedure is cross-matched with the physical properties (in particular $M_\star$) catalog for VIPERS galaxies (Turner et al., 2021) measured via the spectral energy distribution (SED) fitting with the Code Investigating GALaxy Emission (*CIGALE*, Boquien et al., 2019; Burgarella et al., 2005;

---

[4] The catalog with the CIGALE results contains only galaxies with $3.0 \leq z_{\mathrm{flag}} \leq 4.5$.

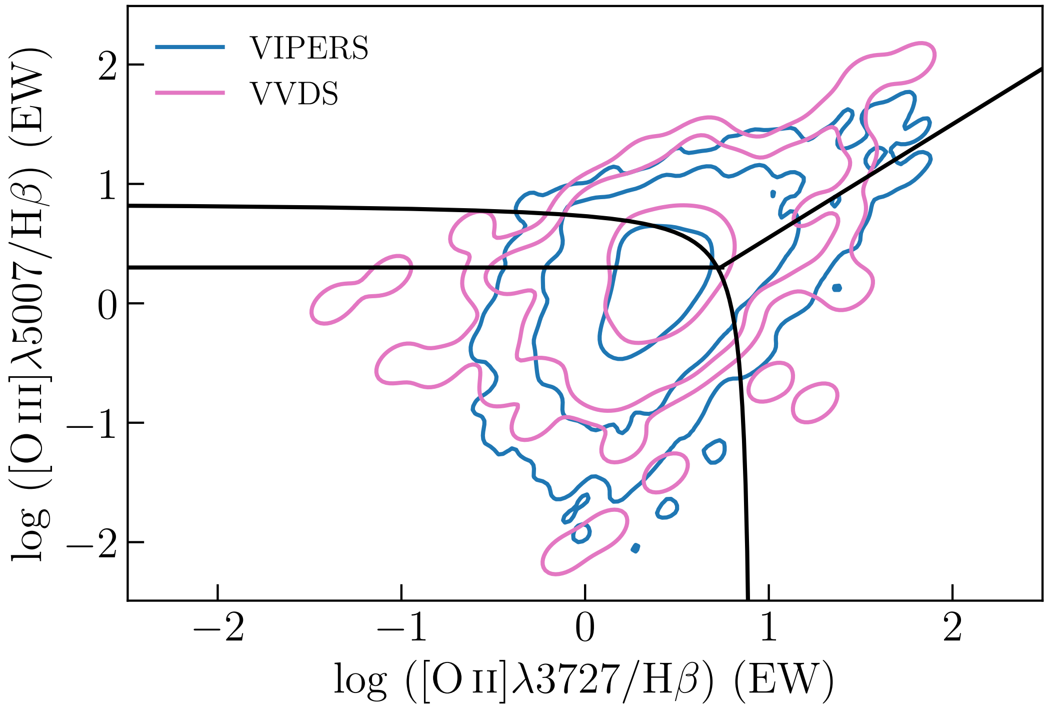

Figure 3.1: "Blue" BPT diagram (Lamareille, 2010) for VIPERS (blue) and VVDS (pink) samples. Contours present 1, 2, and 3 standard deviation levels of the distributions.

Noll et al., 2009). The construction of the catalog reduces the sample to 39 204 galaxies because the physical properties catalog is not complete in the W4 field.

Validation of the new VIPERS spectroscopic catalog

As a check for the quality of the measurements, we compare our results with a catalog from the VVDS (Lamareille et al., 2009), as both VIPERS and VVDS used the same instrumental configuration of VIMOS spectrograph (Le Fèvre et al., 2003b). We select all galaxies from the VVDS sample covering the same z and $z_{\rm flag}$ ranges as the VIPERS sample. We also limited the VVDS sample to the same magnitude as VIPERS, $i_{\rm AB} < 22.5$, removing deep observations included in VVDS. The resulting catalog has similar characteristics as VIPERS, both from an instrumental and continuum treatment point of view. For the comparison, we select galaxies from the VIPERS sample with a minimum flag of 1110.

The VVDS sample has been analyzed with the *platefit_vimos* pipeline (Lamareille et al., 2009), which is the adapted version of *platefit* used to analyze high-resolution SDSS spectra (Brinchmann et al., 2004; Tremonti et al., 2004). To make the comparison between VIPERS and VVDS consistent, the same treatment of the continuum and stellar part adopted by *platefit_vimos* was used in pPXF.

Figure 3.1 shows the 1, 2, and 3 standard deviation levels of the distributions in the BPT diagram (Baldwin et al., 1981) for VIPERS and VVDS samples. Both samples show very compatible distributions.

We compare here directly the distributions of the fluxes and EWs for all the lines used in this work between VIPERS and VVDS samples. Figure 3.2 and Fig. 3.3 show the comparison of the distributions of fluxes and EWs, respectively, for both VIPERS and VVDS samples.

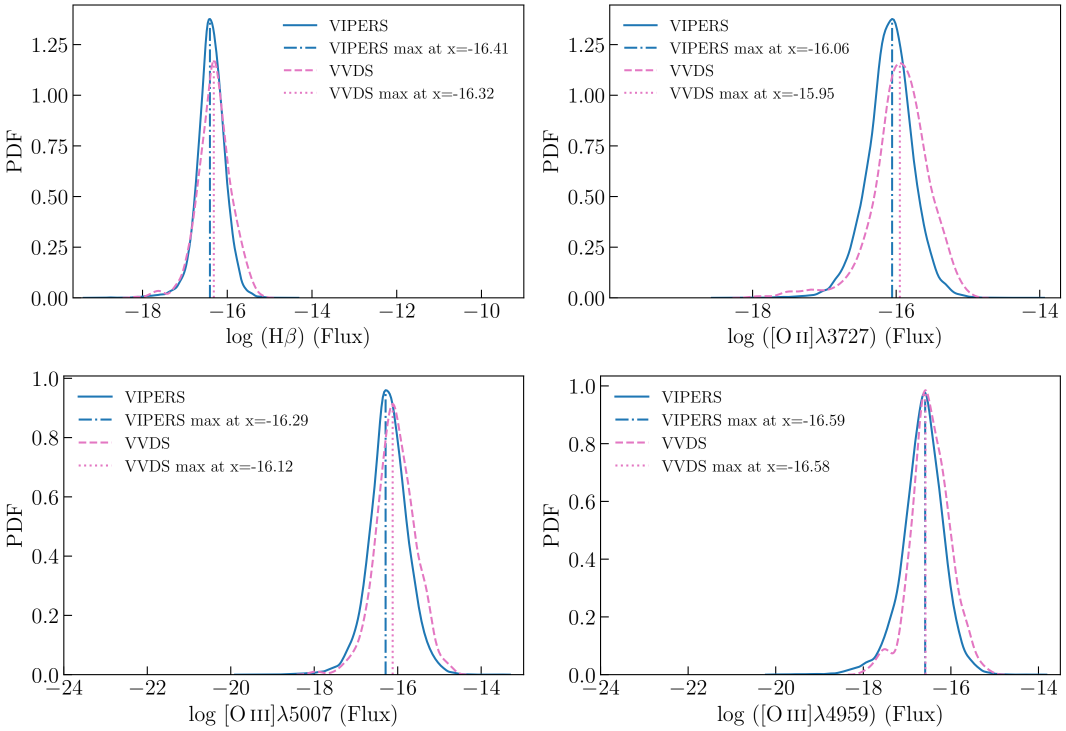

Figure 3.2: Comparison of flux distributions for Hβ (upper left), [O II] λ3727 (upper right), [O III] λ5007 (bottom left), and [O III] λ4959 (bottom right) lines between VIPERS (blue solid line) and VVDS (pink dashed line) samples. In the same plot is highlighted the position of the maximum of each distribution.

Table 3.2: Statistic of the comparison between the distributions.

Emission line	Median flux		MAD flux	
	VIPERS	VVDS	VIPERS	VVDS
Hβ	5.56	4.95	1.78	2.44
[O II] λ3727	8.35	12.04	3.57	5.68
[O III] λ5007	6.04	8.52	3.52	5.13
[O III] λ4959	2.39	3.21	1.42	1.80

Notes. The fluxes and MADs are expressed in units of 10^{-17}erg s^{-1}cm^{-2}.

Table 3.2 summarize the comparison between the distribution of the fluxes. Table 3.3 summarize the comparison between the distribution of the EWs. We find a good agreement between the flux and EW distributions for all the lines in exam according to their median, MAD, and position of the peaks. We also perform a KS-test for the null hypothesis that two samples were drawn from the same distribution. We choose a confidence level of 95%; that is, we will reject the null hypothesis in favor of the alternative if the p-value is less than 0.05 which we report in Table 3.4. According to the p-value of the KS-test only the distributions for Hβ EW is consistent with the null hypothesis, in the other cases the null hypothesis must be rejected.

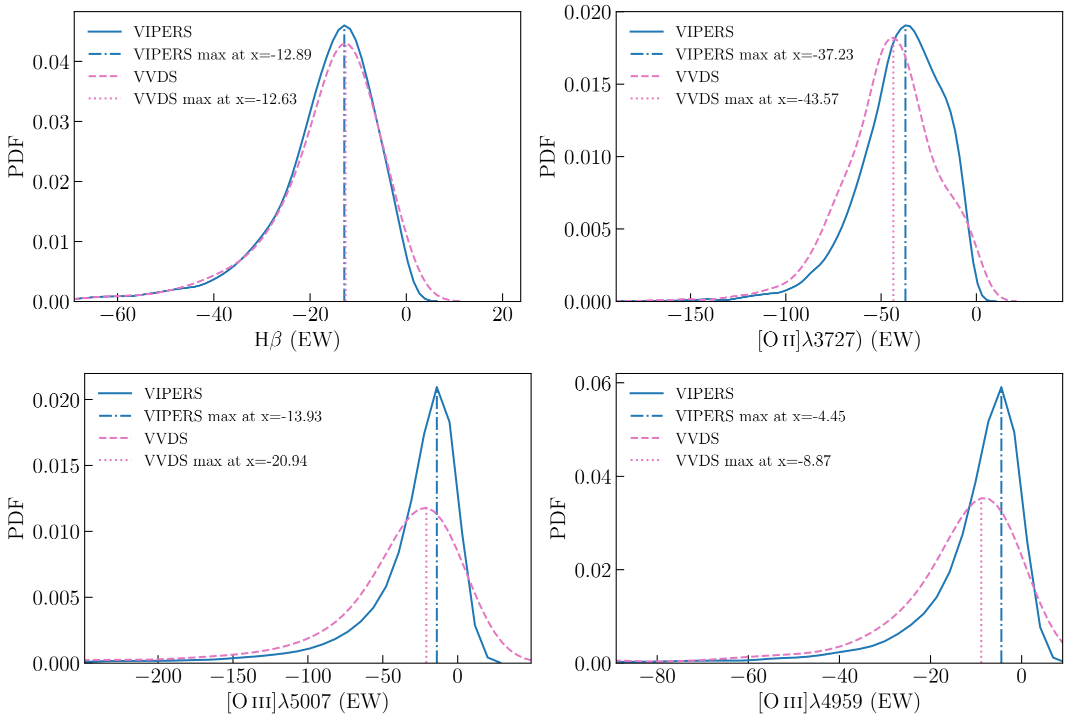

Figure 3.3: Comparison of EW distributions for Hβ (upper left), [O II] λ3727 (upper right), [O III] λ5007 (bottom left), and [O III] λ4959 (bottom right) lines between VIPERS (blue solid line) and VVDS (pink dashed line) samples. In the same plot is highlighted the position of the maximum of each distribution.

Table 3.3: Statistic of the comparison between the distributions.

Emission line	Median EW		MAD EW	
	VIPERS	VVDS	VIPERS	VVDS
Hβ	-14.97	-14.33	5.98	5.80
[O II] λ3727	-37.29	-44.66	14.13	14.38
[O III] λ5007	-19.45	-26.85	12.41	17.11
[O III] λ4959	-7.03	-10.57	4.57	6.04

Notes. The EWs and MADs are expressed in units of Å.

Table 3.4: Statistic of the comparison between the distributions.

Emission line	KS-test p-value	
	Flux	EW
Hβ	8.57×10^{-8}	0.30
[O II] λ3727	9.71×10^{-31}	1.57×10^{-13}
[O III] λ5007	7.55×10^{-17}	5.16×10^{-12}
[O III] λ4959	1.65×10^{-17}	6.12×10^{-17}

3.2 Data selection

To obtain the sample we will use in our analysis, we followed the data selection introduced by Curti et al. (2020). We apply an S/N limit of 15 and 3 for Hα and

Hβ spectral lines, respectively, in the SDSS sample. The SDSS sample is reduced to 296 027 galaxies. In the VIPERS sample, we applied only the selection on the S/N of Hβ, reducing the sample to 20 545 galaxies. We limited the SDSS sample to $z \geq 0.027$ to include the [O II] line in the observed spectra, reducing the sample to 279 851 galaxies. The selection on redshift is not directly made on the VIPERS sample. We also select only galaxies with an excess color $\mathrm{E}\left(\mathrm{B}-\mathrm{V}\right) < 0.8$ in both samples. This selection reduces only the SDSS sample to 267 922 galaxies.

The flux of emission lines in the SDSS sample is corrected for attenuation using the Balmer decrement, assuming the case B recombination (Hα/Hβ = 2.87, Baker et al., 1938) and adopting the Cardelli et al. (1989) law with $R_V = 3.1$. In the VIPERS sample, the flux of emission lines is corrected for attenuation using the attenuation in the V-band (A_V) provided by the fit of the SED via the *Hyperz* code (Bolzonella et al., 2000b, 2010; Davidzon et al., 2016), the color excess $\mathrm{E}\left(\mathrm{B}-\mathrm{V}\right)$ derived from Schlegel et al. (1998) maps, and a Cardelli et al. (1989) attenuation law with $R_V = 3.1$.

To select SF galaxies and exclude LINERS and Seyfert galaxies from the sample, we use the lines ratio classification BPT diagram. The original BPT diagram to select different types of active galaxies uses [O III] λ5007, [N II] λ6584, [S II] λ6717, 6731, Hα, and Hβ. Because of the redshift range of VIPERS and its wavelength coverage (5 500 – 9 500 Å), the emission lines [N II] λ6584 and Hα are not detected ([N II] λ6584 and [S II] λ6717, 6731) or detected only for few galaxies (Hα). For this sample, it is necessary to use the so-called "blue" BPT diagram (Lamareille, 2010). This version of the BPT diagram works at a higher redshift range and uses the [O II] λ3727, [O III] λ4959, 5007, and Hβ spectral lines.

In particular, to distinguish between different sub-samples we use the equivalent widths (EWs) of the oxygen lines ([O II] λ3727 and [O III] λ5007) relative to Hβ line. We used:

$$\log\left(\left[\mathrm{O\,III}\right]/\mathrm{H}\beta\right) = \frac{0.11}{\log\left(\left[\mathrm{O\,II}\right]/\mathrm{H}\beta\right) - 0.92} + 0.85 \tag{3.1}$$

as a boundary line between AGN and SF galaxies, and

$$\log\left(\left[\mathrm{O\,III}\right]/\mathrm{H}\beta\right) = 0.95 \times \log\left(\left[\mathrm{O\,II}\right]/\mathrm{H}\beta\right) - 0.4 \tag{3.2}$$

to separate LINERs from Seyfert 2-type AGNs. Our classification method is reliable for all galaxies with $z < 1$ because the change in ISM conditions in SF galaxies with redshift is not as strong as for galaxies at $z > 1$ (Kewley et al., 2013a,c).

Lamareille, 2010 found a non-negligible number of Seyfert 2 galaxies falling into the SF region of the BPT diagram. They define the boundary of this "mix" region, located within SF galaxies, by the condition:

$$\log\left(\left[\mathrm{O\,III}\right]/\mathrm{H}\beta\right) > 0.3. \tag{3.3}$$

We exclude these galaxies from our study. They also define a composite region by the condition:

$$\begin{cases} \log\left(\left[\mathrm{O\,III}\right]/\mathrm{H}\beta\right) \leq -\left(\log\left(\left[\mathrm{O\,II}\right]/\mathrm{H}\beta\right) - 1.0\right)^2 + \\ \qquad\qquad - 0.1\log\left(\left[\mathrm{O\,II}\right]/\mathrm{H}\beta\right) + 0.25 \\ \log\left(\left[\mathrm{O\,III}\right]/\mathrm{H}\beta\right) \geq \left(\log\left(\left[\mathrm{O\,II}\right]/\mathrm{H}\beta\right) - 0.2\right)^2 - 0.6 \end{cases}, \tag{3.4}$$

where $\sim 85\%$ of galaxies are classified as SF and $\sim 15\%$ as LINERs (Lamareille, 2010). This contamination is the same for both samples (low redshift SDSS and intermediate redshift VIPERS) and it would just add a systematic to the metallicity.

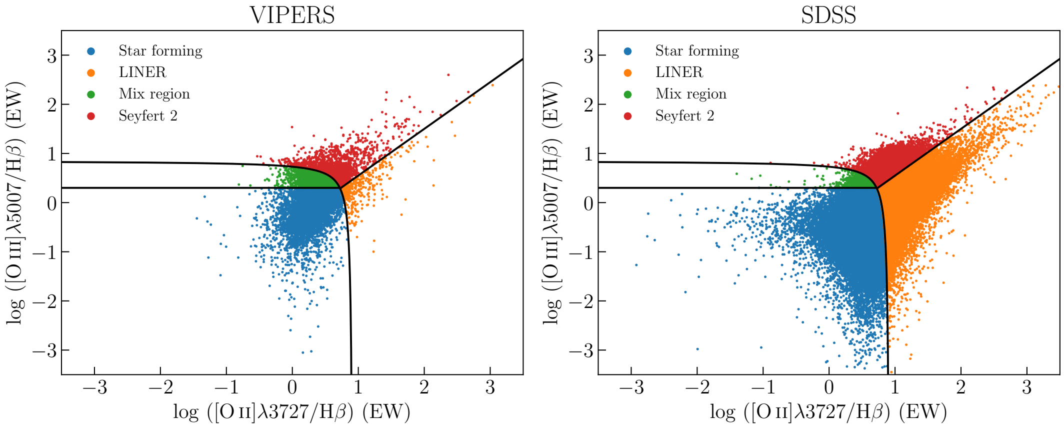

Figure 3.4: Diagnostic diagram using two line ratios: log ([O III] $\lambda 5007/\mathrm{H}\beta$) vs log ([O II] $\lambda 3727/\mathrm{H}\beta$) for VIPERS (left panel) and SDSS (right panel) samples. Solid lines show classification boundaries proposed by Lamareille (2010), blue points are the SF galaxies, orange points are the LINERs, green points are galaxies in the mix region, and red points are the Seyfert 2.

Table 3.5: Number of galaxies (and the fraction of the total sample) for each galaxy type sub-sample defined according to the BPT diagram for both VIPERS and SDSS samples.

	VIPERS		SDSS	
Type	Number of galaxies	Fraction (%)	Number of galaxies	Fraction (%)
SF	9 666	65.2	158 416	61.2
Mix	3 360	22.7	1578	0.6
Seyfert	1 455	9.8	9261	3.6
LINER	352	2.3	89 766	34.7
Total	14 833	100	259 021	100

Figure 3.4 shows the distributions of both samples in the blue BPT diagram. The selection of SF galaxies based on the Lamareille (2010) recipe reduces the sample the VIPERS sample to 6 251 SF galaxies and the SDSS sample to 158 416 SF galaxies. Table 3.5 reports the number of galaxies for each galaxy type sub-sample defined according to the BPT diagram.

3.3 Stellar mass measurement

Since VIPERS and SDSS cover different wavelength ranges, we decided to use the estimation of the $\mathrm{M}_{\star}$ made with the same tool with comparable parameters. The measurement for SDSS data is based on the integrated photometry to have the total $\mathrm{M}_{\star}$ not suffering from the fiber effects.

The Bayesian analysis of the SEDs of both samples (Turner et al., 2021) is based on simulated spectra generated with the SSP by Bruzual et al. (2003) based on a Chabrier (2003) IMF. This SSP is then attenuated by dust assuming a specific dust attenuation law, the choice of which can strongly alter the derivation of $\mathrm{M}_{\star}$es (e.g., as shown in Buat et al., 2019; Hamed et al., 2021; Lo Faro et al., 2017; Małek et al., 2018). The attenuation law used is a generalization of the Calzetti et al. (2000) attenuation curve, modified to let its slope vary and to add a UV bump (Noll et al., 2009).

The templates are then combined with SFHs described by double exponentially declining events of star-formation, which produce an old and a young stellar population, for both samples and the second exponential models the burst. The difference between both samples is the length of the burst. For VIPERS short bursts (10–1000 Myr) are allowed, while in the SDSS the bursts are longer (100–5000 Myr). The old component in VIPERS has an additional, short e-folding time τ included in the models to allow us to reach a quiescent sSFR at $z \sim 1$.

3.4 SFR measurement

The SFR estimation of the SED fitting technique is more sensitive to the wavelength range covered by photometric data with a big influence from the infrared data compared to the estimation of $\mathrm{M}_\star$ (Baes, 2020). Since the VIPERS sample is missing observations at long wavelengths, we decided to measure the SFR from [O II] luminosity ($\mathrm{L}_{[\mathrm{O\,II}]}$, Kennicutt, 1998) to obtain a comparable SFR between both samples and use all information inside the spectra. Among different SFR estimators for SF galaxies, Figueira et al. (2022) found good agreement (scatter but no bias) between [O II]-based and SED-based SFR. The [O II]-based SFR is defined by:

$$\mathrm{SFR}\left(M_\odot\ \mathrm{yr}^{-1}\right) = (1.4 \pm 0.4) \times 10^{-41} \mathrm{L}_{[\mathrm{O\,II}]}\left(\mathrm{erg\ s}^{-1}\right), \tag{3.5}$$

where $\mathrm{L}_{[\mathrm{O\,II}]} = 4\pi \mathrm{f}_{[\mathrm{O\,II}]} \mathrm{d}_\mathrm{L}^2$, $\mathrm{f}_{[\mathrm{O\,II}]}$ is the flux of the emission line, and d_L is the luminosity distance.

Because of the fiber system of the SDSS survey which measures the light with different spatial coverage, the SFR needs a correction to take into account the fiber aperture (Hopkins et al., 2003):

$$\mathrm{SFR}_\mathrm{tot}\left(M_\odot\ \mathrm{yr}^{-1}\right) = \mathrm{SFR}\left(M_\odot\ \mathrm{yr}^{-1}\right) \times 10^{-0.4(u_\mathrm{Petro} - u_\mathrm{fiber})}, \tag{3.6}$$

where u_Petro and u_fiber are the modified form of the Petrosian magnitude (Petrosian, 1976) and the magnitude measured within the aperture of the spectroscopic fiber, respectively. The VIPERS sample does not need a spectroscopic fiber correction because the finite width of the slit is chosen to not overlap for different sources and it is expected to fully cover the galaxies on the CCD (Bottini et al., 2005; Mohammad et al., 2018; Pezzotta et al., 2017). These values are then multiplied by the constant 0.63 to pass from the IMF of Salpeter (1955) to the one of Chabrier (2003) (Madau et al., 2014).

3.5 Metallicity measurement

Because direct comparisons are possible only between studies that used the same methods (Kewley et al., 2008), we decided to estimate the metallicity, for SDSS and VIPERS samples, based on the R_{23} estimator (Kewley et al., 2002; McGaugh, 1991; Pagel et al., 1979) defined as:

$$R_{23} = \frac{[\mathrm{O\,II}]\,\lambda 3727 + [\mathrm{O\,III}]\,\lambda 4959,5007}{\mathrm{H}\beta}. \tag{3.7}$$

Thanks to that we can make a comparative analysis at low and intermediate redshift ranges.

The R_{23} is widely used and it is based on the emission lines of both the main ionization stages of oxygen, O^{+} and O^{2+}. For this reason, it is not strongly affected by the ionization stage of the HII regions (Maiolino et al., 2019). A strong effect is due to the dependence on the ionization parameter. Another problem of this estimator is its double-branched behavior (i.e., a single value of R_{23} can be associated with a double value of metallicity). Also, since the [O II] λ3727 line is distant in wavelength from Hβ and [O III] λ4959, 5007, R_{23} is quite sensitive to the dust reddening.

Regarding the calibration, we use the definition by Tremonti et al. (2004). This calibration is valid for the upper branch of the double-valued R_{23}-abundance relation. Following Nagao et al. (2006) we divided the upper-branch ([O III] λ5007/ [O II] $\lambda 3727 < 2$) from the lower-branch. In this passage, we removed $\sim 0.5\%$ (~ 30) of galaxies in the VIPERS sample and $\sim 0.8\%$ (~ 1272) in the SDSS sample.

The T04 calibration estimates the metallicity from the theoretical model fits of strong emission lines. The model fits are calculated by combining single stellar population (SSP) synthesis models from Bruzual et al. (2003) and *CLOUDY* photoionization models (Ferland et al., 1998). The relation between metallicity and R_{23} is given by:

$$12 + \log\left(\mathrm{O/H}\right) = 9.185 - 0.313x - 0.264x^2 - 0.321x^3, \tag{3.8}$$

where $x \equiv \log R_{23}$. The precision of this calibration is around 0.09 dex and is valid for $12 + \log\left(\mathrm{O/H}\right) \geq 8.4$. The metallicity errors are estimated via the bootstrap procedure. We remove all galaxies with a metallicity error $\sigma_{\mathrm{Z}} > 0.3$. The final samples are composed of 6 203 SF galaxies for the VIPERS sample and 155 931 SF galaxies for the SDSS sample.

3.6 Overdensity measurement

The galaxies underwent a merging event result more scattered with respect to the FMR defined in the local Universe (Bustamante et al., 2018, 2020). As shown in Chapter 5, the difference in metal dilution due to the processes above and below the MS between intermediate and low redshift can be interpreted by a different merging rate.

In order to look for a correlation with the environment (Chapter 6), we use the measure of the local density as a probe of the probability to have a merging event. The local density is defined by Cucciati et al. (2014, 2017) as:

$$\delta = \frac{\rho\left(\mathrm{ra}, \mathrm{dec}, \mathrm{z}\right) - \langle\rho\left(z\right)\rangle}{\langle\rho\left(z\right)\rangle} - 1 \tag{3.9}$$

where $\langle\rho\left(z\right)\rangle$ is the average density a redshift z, ra and dec are the equatorial coordinates (right ascension and declination). It is calculated in a cylinder with a half-length of $1000/\mathrm{c} \times \left(1 + c\right)$ km/s and a radius corresponding to the distance to the 5th nearest neighbor (NN).

3.7 Homogeneous main sequence

In Chapter 5, we make use of the distance of galaxies from the MS. For this purpose, we need a homogeneous definition of the MS at low and intermediate redshift. In order to take into account the MS evolution in the wide redshift range of the VIPERS

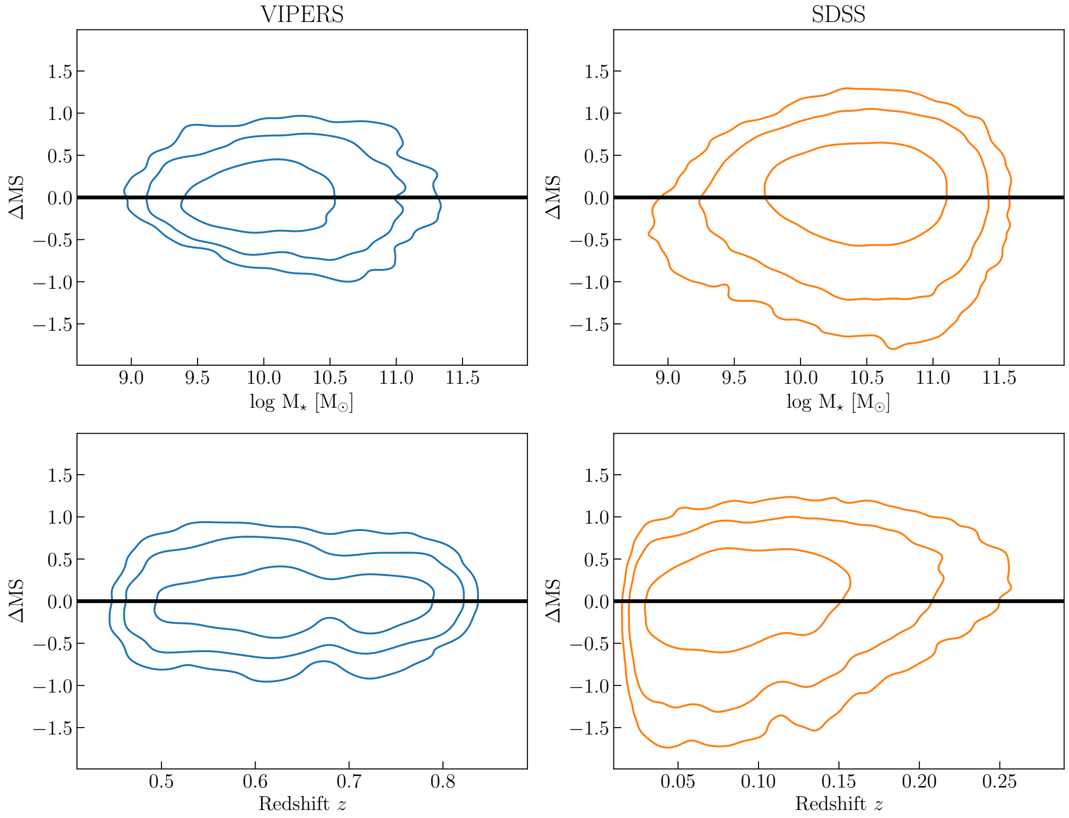

Figure 3.5: Scatter around the MS as a function of $M_\star$ (upper panels) and redshift (bottom panels) for VIPERS (blue) and SDSS (orange) samples. Contours show the 1σ, 2σ, and 3σ levels of the distributions.

sample ($0.5 \leq z \leq 0.8$), we divide this sample into three redshift bins: $0.5 \leq z < 0.6$, $0.6 \leq z \leq 0.7$, and $0.7 < z \leq 0.8$. We perform a linear fit of the SFR-$M_\star$ distribution separately in all three redshift bins. In the next step, we perform another linear fit to the redshift dependence of the MS parameters (slopes and intercepts) based on these three fits. In this way, we obtain a redshift-dependent MS relation:

$$\log \mathrm{SFR}_{\mathrm{MS}}^{\mathrm{VIPERS}}\left(z, M_\star\right) = \alpha\left(z\right) \log M_\star + \beta\left(z\right), \tag{3.10}$$

with $\alpha\left(z\right) = -0.80\, z + 0.66$ and $\beta\left(z\right) = 9.19\, z - 7.06$, valid in the redshift range 0.5–0.8. For a detailed analysis of the VIPERS MS check Pearson et al. (2023).

The redshift range explored by SDSS is small enough so that a single linear fit of the SFR-$M_\star$ relation is sufficient for our analysis. The SDSS MS relation is given by:

$$\log \mathrm{SFR}_{\mathrm{MS}}^{\mathrm{SDSS}}\left(M_\star\right) = 0.63 \log M_\star - 6.10. \tag{3.11}$$

Figure 3.5 shows the scatter around the MS as a function of $M_\star$ and redshift for VIPERS and SDSS samples, demonstrating a lack of any statistically significant trend with either $M_\star$ and redshift for both samples. Both samples show a similar 1 standard deviation level of the distributions. The low-z (SDSS) sample has a bigger scatter around the MS compared to the intermediate redshift (VIPERS) sample, especially at high-$M_\star$ and low-z. It can be caused by contamination with galaxies moving between active and passive stages that are not removed by the blue BPT diagram used to select SF galaxies. Checking the NUVrK diagram (see Fig. 3.6, Davidzon et al., 2016), we

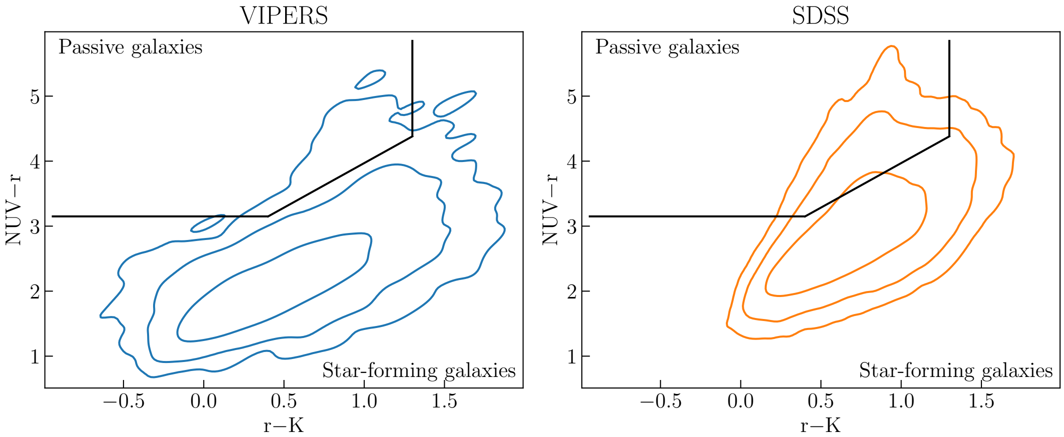

Figure 3.6: Distribution in the NUVrK diagram for VIPERS (blue) and SDSS (orange) samples. Contours show the 1σ, 2σ, and 3σ levels of the distributions.

find 25 ($\sim$ 0.4% of the sample) remaining passive galaxies in the VIPERS sample and 3 643 ($\sim$ 2.3% of the sample) remaining passive galaxies in the SDSS sample.

3.8 Control samples

In order to study FMR evolution and the robustness of the result against different observational biases, three control samples have been built from our main sample of SDSS galaxies (see Sect. 3.1.1). These are:

- the property-control sample (hereafter p-control) having similar $M_\star$ and SFR as VIPERS galaxies,
- the mass-control sample (hereafter m-control) having the same galaxy mass function,
- the distance-control sample (hereafter d-control) having the same relative distance from the MS as VIPERS.

If the FMR is fundamental — the metallicity depends only on the given $M_\star$ and SFR and not from the galaxy evolution — and does not evolve with redshift, the differences in metallicity in the FMR and its projections between the VIPERS sample and the four SDSS samples (all selected SF galaxies, p-control, m-control, and d-control samples) should be independent of each other. If the metallicity differences in the FMR and its projections are independent of the methodology of cross-matching, the differences depend only on the physical properties ($M_\star$ and SFR) of galaxies.

To build the p-control sample, we select for each VIPERS galaxy the three closest SDSS galaxies on the $M_\star$-SFR plane, up to 0.1 dex. In this way, we avoid unbalancing the galaxy distribution towards the region of the MS where SDSS is much denser compared to the VIPERS sample. This selection reduces the p-control SDSS sample to 15 604 galaxies ($\sim$ 10% of the sample).

Since the VIPERS sample is not mass complete (Davidzon et al., 2016), we build a second control sample starting from the p-control sample that follows the same galaxy mass function as the VIPERS sample. In this way, we force the SDSS sample to have the same mass in-completeness as the VIPERS sample. In order to arrive at the same mass in-completeness, we sampled the p-control sample to get the same

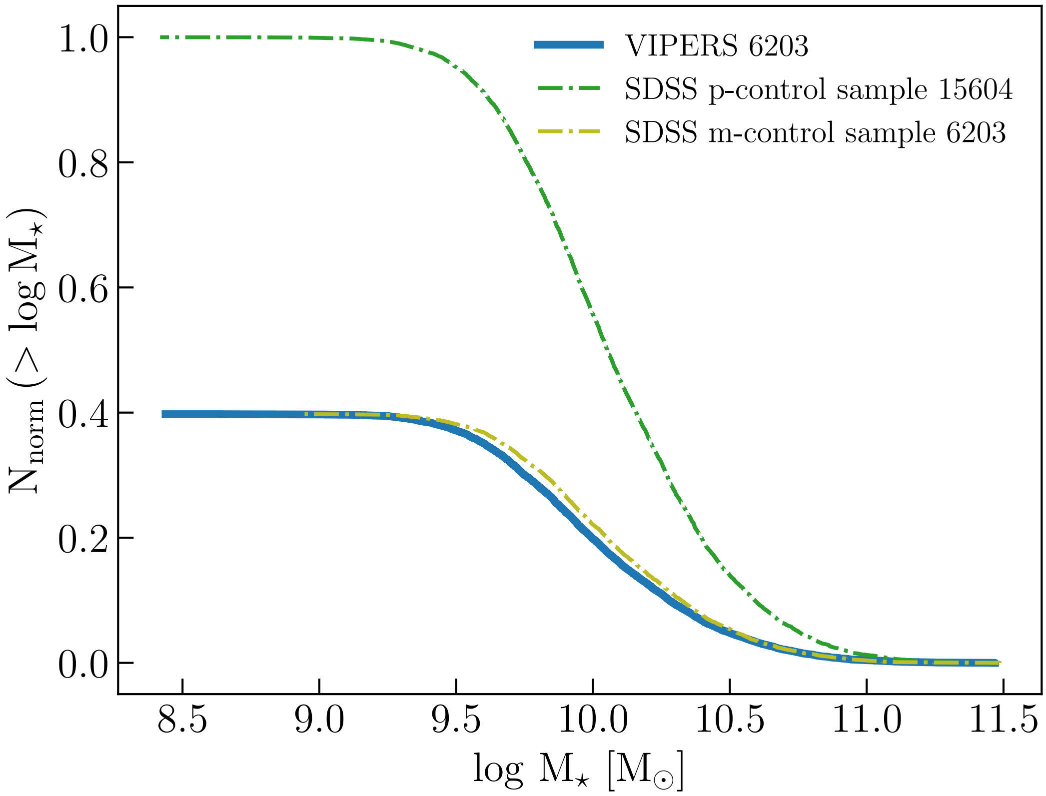

Figure 3.7: Galaxy mass function of VIPERS (blue solid line), SDSS p-control sample (green dash-dotted line), and SDSS m-control sample (olive dash-dotted line) normalized to the total number of galaxies in the p-control sample.

number of galaxies in $M_\star$ bins of the cumulative distribution. Figure 3.7 shows the galaxy mass function of the VIPERS, p-control, and m-control samples normalized to the total number of galaxies in the p-control sample. Then, the m-control sample has the same number of galaxies as the VIPERS sample in each mass bin.

The MS relations for both SDSS and VIPERS were defined in the same homogeneous way, so it can be used to build the d-control sample. To create this sample, we search for SDSS counterparts to each VIPERS galaxy with the same $M_\star$ and SFR corresponding to the MS at low-z. We then simulate the scatter around the local MS for the d-control sample adding a random number with Gaussian distribution centered at $\mu = 0$ and width σ (standard deviation of SFR in a 0.1 dex width bin around $M_\star$ of VIPERS sample):

$$\log \mathrm{SFR}_{\text{d-control}}\left(M_\star\right) = \log \mathrm{SFR}_{\mathrm{MS}}^{\mathrm{SDSS}}\left(M_\star\right) + N\left(\mu, \sigma\right). \tag{3.12}$$

We then proceed to select a maximum of three closest SDSS galaxies in a radius of 0.1 dex in the $M_\star$-SFR plane. The d-control sample constructed in this way is composed of 7 939 SDSS galaxies ($\sim$ 5% of the sample) with the same distance from MS as galaxies in the VIPERS sample.

To summarize, we have five samples: i) the VIPERS sample at intermediate redshift and ii) the SDSS sample at low redshift, both built using similar selection criteria and consisting of SF galaxies, and three control samples based on the SDSS: iii) the p-control, iv) the m-control, and v) d-control samples. In the parametric method, we use both main and control samples. In the non-parametric method, instead, we

Table 3.6: Binning scheme for VIPERS and SDSS (main, p-control, m-control, and d-control) samples according to the property to bin.

	VIPERS sample and SDSS-based control samples		SDSS full sample	
Property (to bin)	Range	Method	Range	Method
$\log M_\star\ [M_\odot]$	$[8.4, 11.5]$	0.15 dex width	< 9.0	Quantile based
			$[9.0, 11.5]$	0.15 dex width
			> 11.5	Quantile based
$\log \mathrm{SFR}\ \left[M_\odot\ \mathrm{yr}^{-1}\right]$	$[-0.9, -1.5]$	0.15 dex width	< -1.0	Quantile based
			< -1.0	0.15 dex width
$\log \mathrm{sSFR}\ \left[\mathrm{yr}^{-1}\right]$	$[-11.8, -7.8]$	0.15 dex width	$[-12.0, -7.5]$	0.15 dex width

Notes. Quantile based: the same number of galaxies in each bin.

use only the main samples.

3.9 Binning of the samples

To show the FMR, we present the median 2D projection of the samples. Table 3.6 reports the binning method of the main samples used in this work. We proceed into dividing each sample according to the binning method according to the x-axis. We defined two errors based on: i) the distribution of the population inside the bin σ_{dist} from the 84th and 16th percentile (equivalent to 68% of the population inside each bin), and ii) the error on the median $\sigma_{\mathrm{med}} = \sigma_{\mathrm{dist}}/\sqrt{N}$ (N is the number of galaxies in the bin). In the following analysis, we use σ_{med} to draw conclusions about the possible evolution of the considered relations, while σ_{dist} provides us with information about their scatter.

3.9.1 General properties of VIPERS and SDSS main samples and three control samples

Figure 3.8 presents the kernel density estimation (KDE) of the distributions for the main physical features of the two main samples (VIPERS and SDSS) and the three control samples (p-control, m-control, and d-control samples). This figure shows the distribution of $M_\star$, SFR, metallicity, redshift, sSFR, and the distance from the MS.

All p-control, m-control, and d-control samples, being built from the SDSS sample by construction to match the $M_\star$ and SFR distribution of VIPERS galaxies, recover with high precision the distribution of $M_\star$ and SFR of VIPERS galaxies. The p-control sample shows a small shift towards lower values in the distribution of sSFR compared to the VIPERS sample, while the d-control sample has a peak of the sSFR distribution shifted towards even lower values. The m-control sample is a smaller but otherwise almost identical counterpart of the p-sample, in terms of all considered properties. Table 3.7 summarizes the differences of the median values of $M_\star$, SFR, and sSFR for all control samples with respect to VIPERS. The distributions of the shift from the MS (defined as the SFR-difference between the measured value and the MS value, shown in the bottom right panel of Fig. 3.8) also differ with the d-control sample having a much narrower distribution than the other samples.

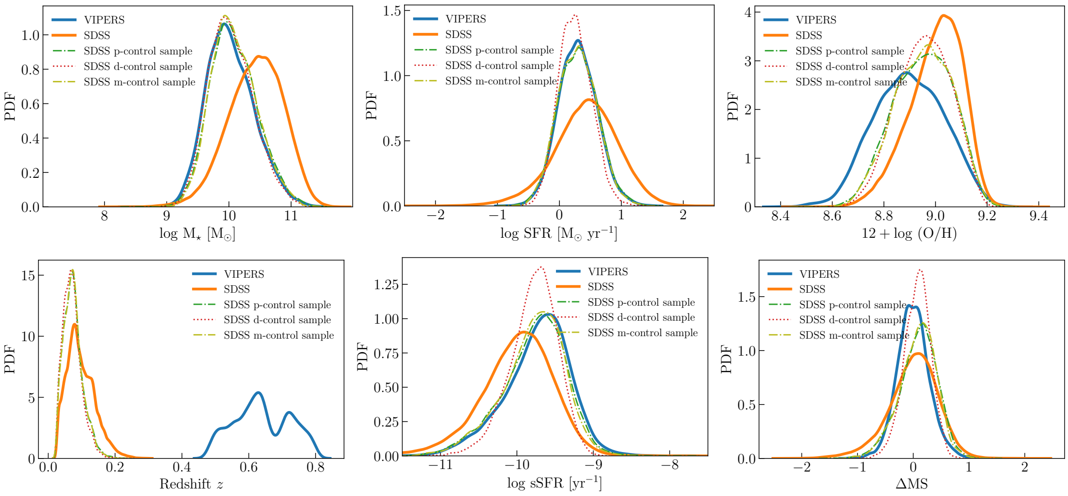

Figure 3.8: Kernel density estimations (KDEs) of $M_\star$ (upper left panel), SFR (upper mid panel), metallicity (upper right panel), redshift (bottom left panel), sSFR (bottom mid panel), and difference with respect to the corresponding MS (bottom right panel) for the VIPERS (blue solid line), SDSS (orange solid line), SDSS p-control (green dash-dotted line), SDSS m-control (olive dash-dotted line), and SDSS d-control (red dotted line) samples.

Table 3.7: Differences of the median values of $M_\star$, SFR, and sSFR between VIPERS and control samples.

Difference	p-control	m-control	d-control
$\Delta \log M_\star$	-0.1 ± 0.5	$+0.1 \pm 0.5$	-0.0 ± 0.5
$\Delta \log \mathrm{SFR}$	-0.0 ± 0.5	-0.0 ± 0.5	$+0.1 \pm 0.5$
$\Delta \log \mathrm{sSFR}$	$+0.1 \pm 0.5$	$+0.1 \pm 0.5$	$+0.1 \pm 0.5$

The metallicity distribution of all SDSS control samples is shifted towards lower values compared to the SDSS sample. However, for all SDSS-based samples, it remains higher than the VIPERS metallicity distribution. From Fig. 3.8 we also notice that the redshift distribution of both SDSS control samples is narrower than in the original SDSS catalog, and p-control and d-control selections removed the high-z end of the SDSS distribution.

CHAPTER 4

Biases introduced by data selection and observations

This chapter describes how different biases (Sect. 4.1) introduced by data selection and observation can affect the conclusion about the studies of the FMR and its projections. In particular, we studied the effects due to the choice of the BPT diagram (Sect. 4.1.1), the S/N selection (Sect. 4.1.2), selection on the quality of spectra (Sect. 4.1.3), the intrinsic luminosity evolution of galaxies (Sect. 4.1.4), and the fraction of blue galaxies observed (Sect. 4.1.5). We then compare the VIPERS and SDSS samples (Sect. 4.2). Finally, wee report the final discussion (Sect. 4.3), and the conclusions (Sect. 4.4). The original work is presented in F. Pistis et al. (July 2022). The fundamental metallicity relation from SDSS ($z \sim 0$) to VIPERS ($z \sim 0.7$). Data selection or evolution. A&A 663, A162, A162. DOI: `10.1051/0004-6361/202142430`. arXiv: `2206.02458 [astro-ph.GA]`.

4.1 Study of biases

To do a fair comparison, we need to make SDSS as close as possible to the VIPERS SF selection and we need to check how different selections can affect the projections of the FMR. The characterization of a spectroscopic sample depends mostly on all the intrinsic characteristics of the spectrograph, of the sources at different redshift, for instance, the need to reliably detect different emission lines that have different intrinsic luminosity, as well as on the spectra analysis. For these reasons, when different samples are compared (especially between significantly different redshift ranges), the sample selection criteria are generally different.

Observations at high redshift are usually more limited than local observations in the number of sources, at lower $M_\star$, due to the rest-frame cut-off in magnitude. Therefore, a meaningful comparison between local and high redshift samples can be properly made only after taking into account the limitations that characterize both samples. By analyzing these constraints on the local data, we can say if the differences observed between different samples are physical or due to some selection effects. In the following subsections, we analyze different selection criteria individually: the S/N cut of emission lines used to compute the metallicity, the quality of the spectra (the only bias studied on both samples), the selection on the blue rest-frame absolute magnitude, and the fraction of blue galaxies.

In the following analysis, the samples are divided into bins of 0.15 dex width in $M_\star$, SFR, and sSFR. We keep only bins with as many galaxies inside as higher than

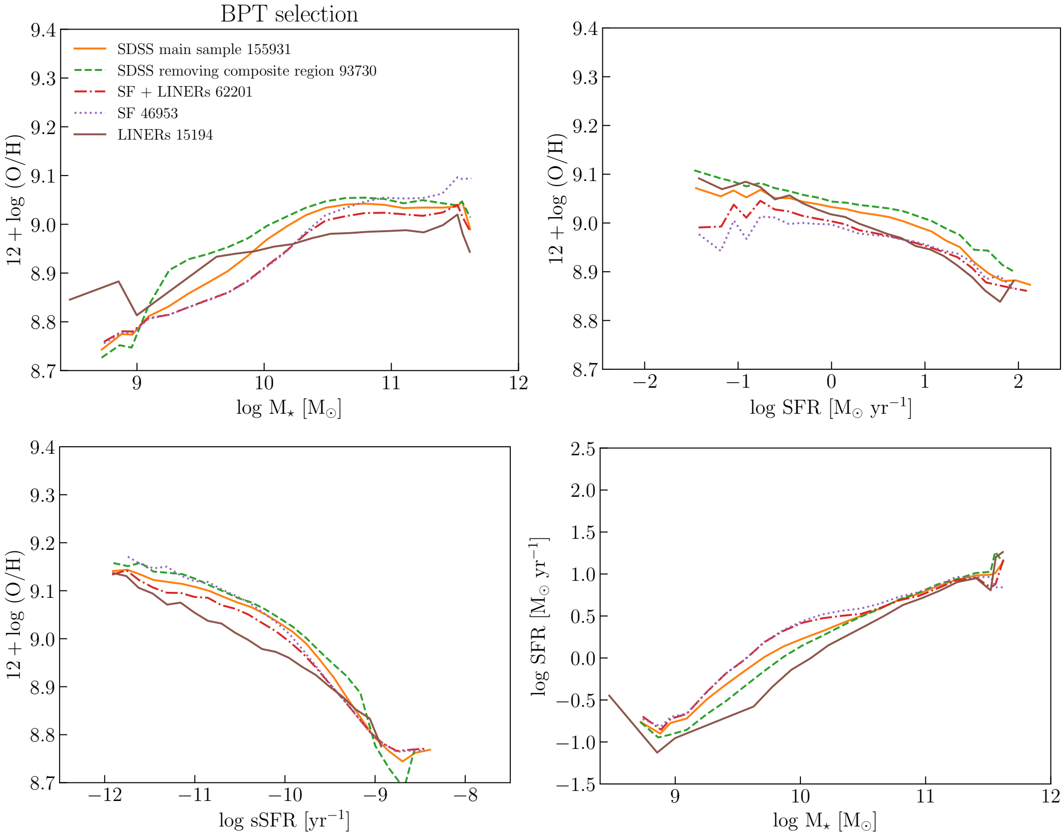

Figure 4.1: Effects of BPT diagram choice on the projections of the FMR (main sample: orange solid line); SDSS removing completely the composite region (green dashed line); composite region defined by Eq. 3.4 (Lamareille, 2010) (SF + LINERs, red dash-dotted line); SF of the composite region (purple dotted line); and LINERs of the composite region (brown solid line).

25 (Curti et al., 2020). The binning scheme is presented in Table 3.6 (Chapter 3). We used a different method of binning the properties of SDSS in the range explored in this sample but not in VIPERS. Finally, we estimate the median value inside each bin for both samples and their 1*s* uncertainties are estimated from the 16th and 84th percentiles of the distributions inside the bin.

4.1.1 Choise of the BPT diagram

The SDSS sample allows us to check if the use of the version of the BPT diagram described by Lamareille, 2010 instead of the original diagram can introduce a bias in the metallicity. First, we selected all sources in the composite region defined by Eq. 3.4 (Lamareille, 2010). Then, we separate SF galaxies and LINERs following Kauffmann et al., 2003b, according to which a galaxy is defined as non-SF when

$$\log\left([\mathrm{O\,III}]\,/\mathrm{H}\beta\right) > \frac{0.61}{\log\left([\mathrm{N\,II}]\,/\mathrm{H}\alpha\right) - 0.05} + 1.3. \qquad (4.1)$$

Figure 4.1 shows the effects of the choice of the BPT diagram on the FMR projections. In these plots, we show in particular the effects of removing completely the composite region defined by Lamareille, 2010 and removing only the LINERs inside the same region. Removing the composite region completely (62 228 SF plus LINERs galaxies, $\sim 40\%$ of the main sample) affects mainly the MZR at low $M_\star$, changing the overall shape of the MZR itself. This selection does not have a statistically significant effect on the other projections.

Regarding the effect of the LINERs contamination inside the composite region, 15 196 LINERs galaxies ($\sim$ 25% of the composite region and $\sim$ 10% of the main sample), we checked the FMR projections for: i) the full composite region, ii) the SF galaxies, and iii) only LINERs. Figure 4.1 shows statistically negligible effects on the projections between the full composite region and only the SF galaxies inside this region. Since removing completely this region affects the results the most significantly, we decide to keep the LINERs contaminated area in our sample.

4.1.2 S/N selection

The second bias analyzed is related to different S/N cutoffs. We simultaneously applied an S/N cut on all emission lines used to compute the metallicities for different best percentages (10%, 25%, 50%; namely, the X% best-percentage means we keep the X% of the full SDSS sample with the highest S/N) and cut in the same range of S/N as the VIPERS sample.

Figure 4.2 shows the projection of the FMR after the application of the S/N selections. Decreasing the best percentage of the S/N (i.e. increasing the cutoff on the lines) increases the flattening of the MZR and shifts it towards lower metallicities. A selection of higher S/N sources removes mainly metal-rich galaxies at higher $M_\star$es with a median $\Delta \log(\mathrm{O/H}) = 0.09$ dex and a maximum $\Delta \log(\mathrm{O/H}) = 0.11$ dex — $\Delta \log(\mathrm{O/H})$ is defined as the difference in metallicity between the SDSS and VIPERS samples in each bin. This means that metal-poor galaxies at a given $M_\star$es have intrinsically higher S/N of emission lines, an effect that is in agreement with the one described by Curti et al., 2020. This type of galaxies also has a higher SFR, with a younger stellar population that can emphasize the emission lines increasing the photo-ionization state of the gas-phase metals. It is important to note that the sample with S/N in the same range of the VIPERS data has higher metallicity in the range $9.0 \leq \log M_\star\,[M_\odot] \leq 10.25$ than the main sample.

In the SFR-metallicity plane, the cut is mainly at low SFR for sources with higher metallicities and flattens the curve. In this plane, the median $\Delta \log(\mathrm{O/H}) = 0.17$ dex and a maximum $\Delta \log(\mathrm{O/H}) = 0.22$ dex, showing a much more important dependence on this selection than the MZR. The curves at low $M_\star$es and high SFRs are almost invariant with these cuts. It is interesting to note that the metallicity versus the sSFR plane, is almost insensitive to the cut on S/N. This means that the effects of the cut as a function of the $M_\star$ and SFR cancel each other out.

Increasing the S/N cut removes the galaxies from the bottom part of the main sequence from the analysis. The same part with galaxies containing a higher abundance of metals. This bias moves the distribution of the main sequence toward the top part of the diagram.

4.1.3 Quality of spectra: flag selection

The next step is to check which kind of bias can be introduced by a selection of the quality flag of the emission lines described in Sect. 3.1.3 (Chapter 3). The flag definition is more complicated than the simple S/N selection. In particular, the first three values need a specific analysis of the spectra. In this part, we checked the effects of the flag selection on all the lines at the same time for the VIPERS sample; while on the SDSS sample, we checked the effects on the selection to fulfill the loose

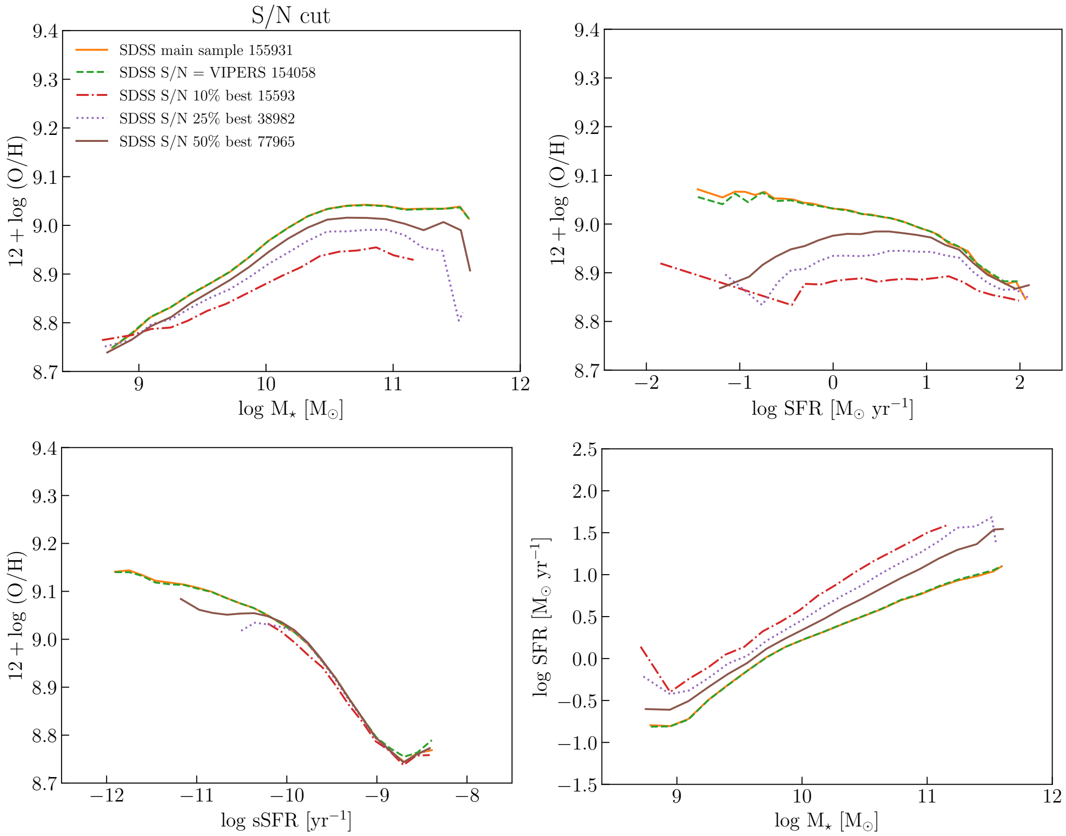

Figure 4.2: Effects of S/N cuts of the emission lines on the projections of the FMR (main sample: orange solid line; S/N interval equal to VIPERS: green dashed line; 10% best: red dash-dotted line; 25% best, purple dotted line; 50% best: brown solid line).

condition (EW $\geq 3\sigma$ or flux $\geq 7\sigma$) of the flag t-value of VIPERS for each emission line separately.

Figure 4.3 shows the effects on the FMR projections of the selections of the quality flag for the VIPERS sample. Each selection removes galaxies at high $M_\star$ and low SFR reducing the range explored in the corresponding projection. Another effect is to remove the metal-rich galaxies. This cut leads to flattening the MZR and the relation in the metallicity-SFR plane; while the relation in the metallicity-sSFR is not sensitive to these selections (it is only sensitive to the reduction of data at high $M_\star$ and low SFR). The main sequence (bottom right panel of Fig. 4.3) shows instead a shift towards the top of the diagram. The same shift is found in the case of the S/N selection (Fig. 4.2). Although the flattening of the relations is negligible compared to the error on metallicity ($\sim$ 0.1 dex), the selection of the quality flag remains a possible source of bias.

Figure 4.4 shows the projections of the FMR for the SDSS sample. The selection flattens the relations as already seen for the VIPERS sample. Thanks to the larger statistics of the SDSS sample and a wider interval in the SFR, it is possible to see that the selection on the oxygen line flag leads to an inversion of the relation with the metallicity increasing at high SFR. The relation in the metallicity-sSFR seems also to be much more sensitive to this selection compared to the VIPERS sample.

The MZR is shifted toward lower metallicity when the selection is applied on [O II] λ3727 and [O III] λ5007, namely, we mainly cut the metal-rich galaxies at high

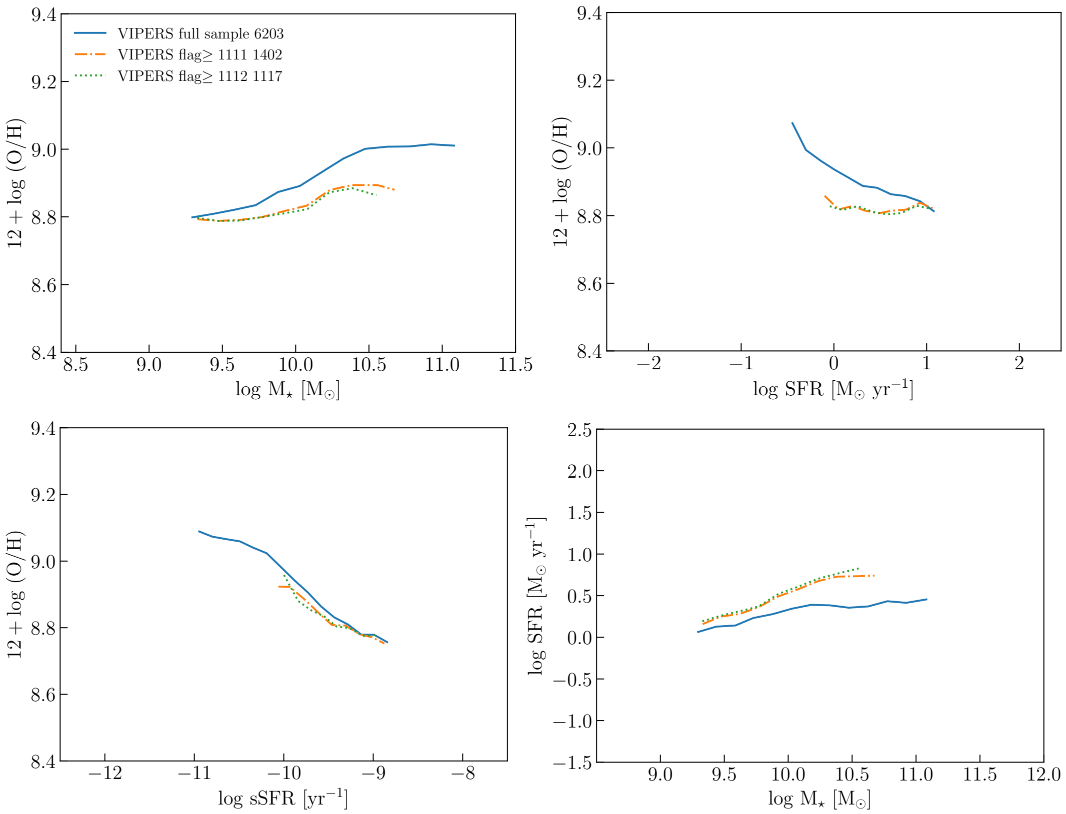

Figure 4.3: Effects of the flag selections on the projections of the FMR effects of flag selection (main sample: blue solid line; minimum flag equal to 1111: orange dash-dotted line; minimum flag equal to 1112: green dotted line) for the VIPERS sample.

$M_\star$es. The selection performed solely on [O III] λ4959 gives a further shift towards lower metallicities and a further flattening. This is the selection with the strongest effect. The selection on Hβ only does not produce any difference. In this plane the median $\Delta \log\left(\mathrm{O/H}\right) = 0.06$ dex and a maximum $\Delta \log\left(\mathrm{O/H}\right) = 0.12$ dex in the case of the selection on all the emission lines together.

In the plane metallicity versus SFR, the bias affects the relation with a minimum around $\log \mathrm{SFR}\left[M_\odot\ \mathrm{yr}^{-1}\right] \sim -1$ and then remains flat with the selection on [O II] λ3727 and [O III] λ5007, that is, we cut mainly metal-rich galaxies at lower SFRs. The selection on [O III] λ4959 shifts further the relation towards lower metallicity. Again, the selection on Hβ only does not produce any difference. In this plane the median $\Delta \log\left(\mathrm{O/H}\right) = 0.14$ dex and a maximum $\Delta \log\left(\mathrm{O/H}\right) = 0.30$ dex in the case of the selection on all the emission lines together. Again, this plane is more sensitive to the selection than the MZR.

In this case, the metallicity versus the sSFR plane is not anymore insensitive but all the selections move in the same way as other projections with the selection on [O II] λ3727 and [O III] λ5007 that cuts mainly metal-rich galaxies at lower sSFR and the selection on [O III] λ4959 line is the strongest bias. The main sequence is shifted toward the top left part of the diagram when the selection on all lines is applied.

To understand the reason why the effect is mainly due to the line [O III] λ4959, we studied the relation between the ratio of the [O III] doublet, [O III] λ5007/ [O III] λ4959, and the S/N of the line [O III] λ4959. The results are shown in Fig. 4.5. This plot shows that following the data selection used by Curti et al., 2020 it is not possible to remove galaxies with very low S/N ($\log \mathrm{S/N} < -1$) of [O III] λ4959.

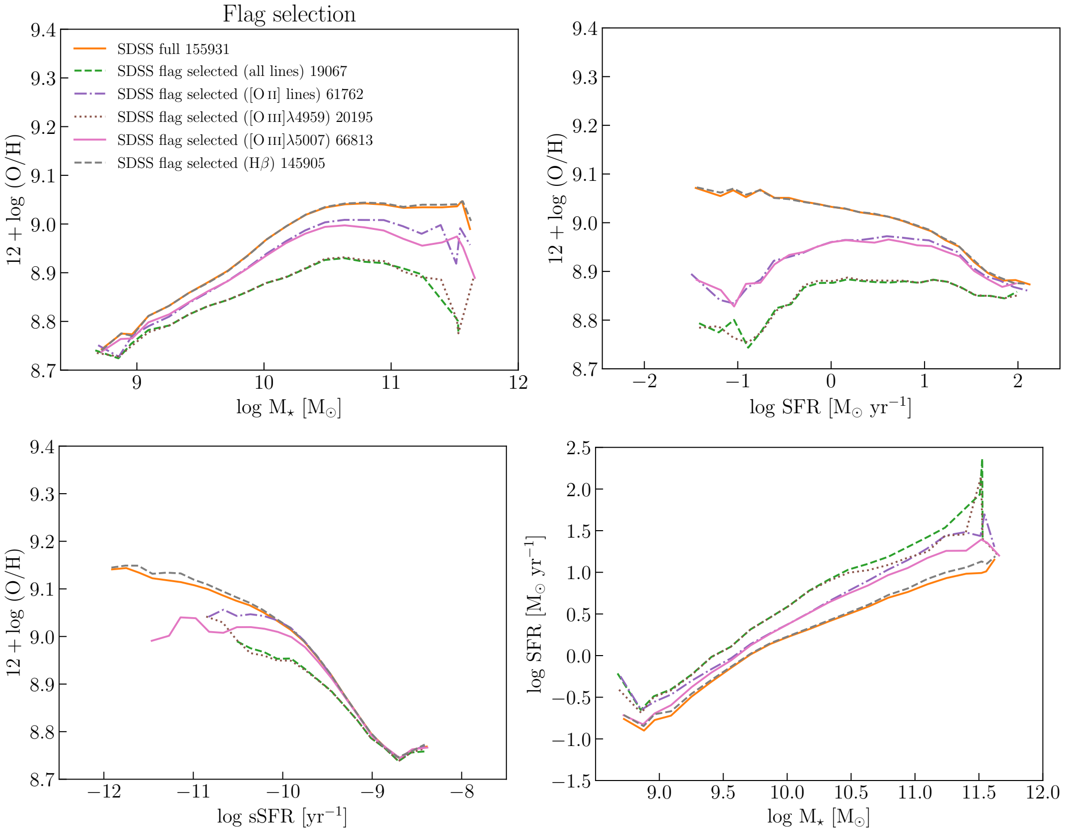

Figure 4.4: Effects of the selection on the t-value flag for the emission lines (orange solid line: main sample; green dashed line: all lines; purple dash-dotted line: [O II]; brown dotted line: [O III] λ4959; pink solid line: [O III] λ5007; grey dashed line: Hβ) on the projections for SDSS sample.

4.1.4 $B - B^*$ volume

The fourth bias analyzed here involves the range in absolute blue magnitude $B - B^*$, where B^* is the characteristic magnitude at which the luminosity function changes dependence (from power law to exponential). In this way, we take into account the evolution of the luminosity function itself ($B^* = -20.95$ for VIPERS and $B^* = -19.11$ for SDSS, these values are used for the whole redshift range, Ilbert et al., 2005, 2006b). Then, we can observe the same luminosity interval of the distribution after considering its shift due to the redshift.

Figure 4.6 shows the distributions of both samples in $B - B^*$ with the cutoffs at $-1.5 \leq B - B^* \leq 2$ mag. B^* is defined as the magnitude at which the luminosity function changes dependence (from power law to exponential) and it is redshift-dependent. In this way, we can analyze the same interval of the luminosity function for both samples.

Figure 4.7 shows the comparison of projections of the FMR between the main sample of SDSS data and after the cut. The MZR and the metallicity versus sSFR are insensitive to the selection on luminosity; while in the metallicity versus the SFR plane, the bias mainly cut the metal-rich galaxies at high SFR. In this plane the median $\Delta \log(O/H) = 0.01$ dex and a maximum $\Delta \log(O/H) = 0.03$ dex. The main sequence is moved toward the bottom left part of the diagram.

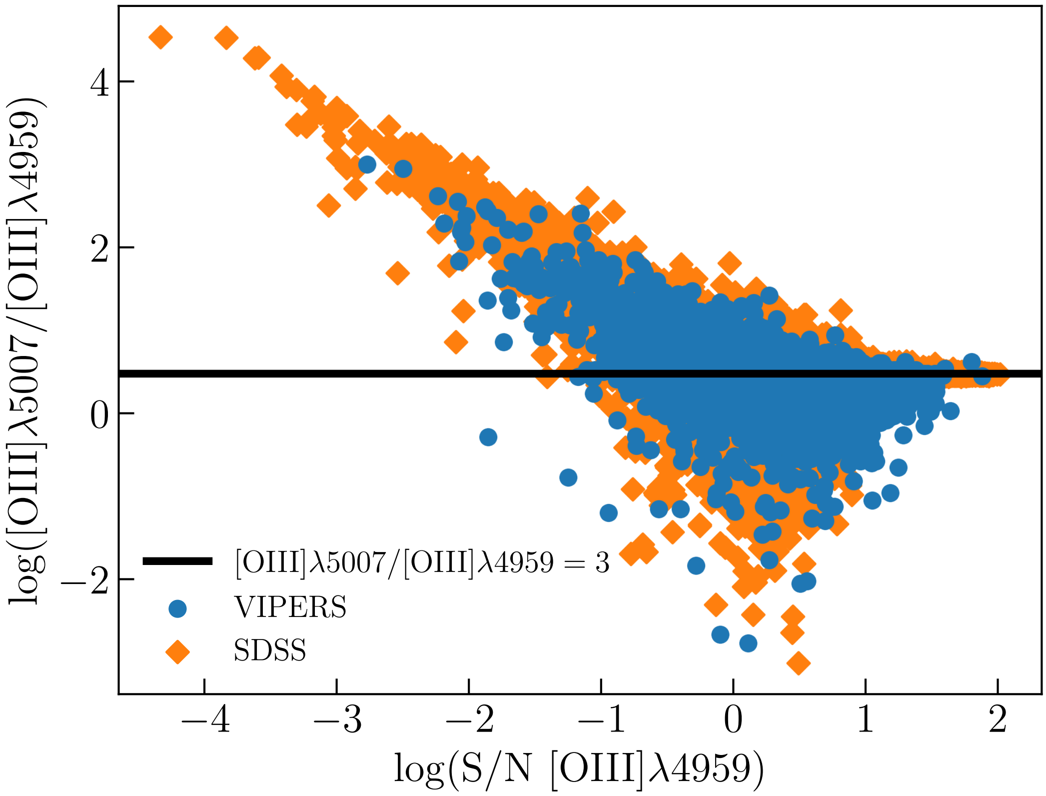

Figure 4.5: Line ratio [O III] λ5007/ [O III] λ4959 vs S/N of the line [O III] λ4959 for VIPERS (blue dot) and SDSS (orange diamonds) samples. The solid black line shows the intrinsic value of the line ratio.

4.1.5 Fraction of blue galaxies

The last bias we analyze here is the fraction of blue galaxies selected on the distributions of the sSFR. There are two effects at work here: i) the observation of blue galaxies is reduced with the redshift since this type is mainly low-mass and is cut at high redshift because of the limited magnitude of the observations; ii) blue galaxies can be over-selected at high redshift — namely, the VIPERS i-band selection translates to a B-band selection at high-z and for galaxies with bright emission lines is easier to estimate their metallicity. We wanted to check if the second point can introduce an observational bias in the studies on the FMR. We may also have introduced a bias with the redshift confidence level. This is because blue galaxies have brighter strong emission lines which are used to measure the spectroscopic redshift. We selected the blue galaxies via the sSFR distributions (VIPERS: $-12 \leq \log \mathrm{sSFR}\left[\mathrm{yr}^{-1}\right] \leq -8$; SDSS: $-15 \leq \log \mathrm{sSFR}\left[\mathrm{yr}^{-1}\right] \leq -8$).

We defined the fraction of blue galaxies as the ratio between the number of sources inside the sub-sample and the number of sources inside the full catalog:

$$f_B = \frac{\mathrm{N}_{\text{sub-sample}}\left(M_\star, \mathrm{SFR}\right)}{\mathrm{N}_{\text{full catalog}}\left(M_\star, \mathrm{SFR}\right)}. \tag{4.2}$$

We estimate the error on the fraction of blue galaxies as the propagation of the Poissonian errors of the counts.

We used the full catalog without doing any kind of selection (no selection on

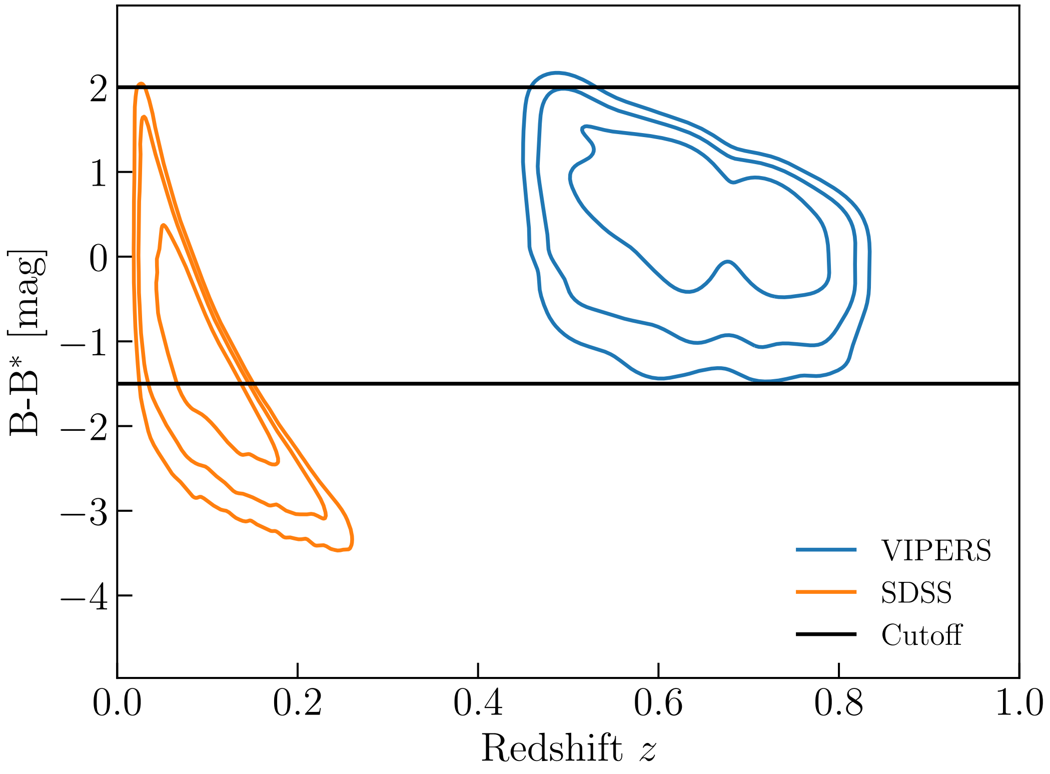

Figure 4.6: $\mathrm{B} - \mathrm{B}^*$ vs redshift diagram and cutoff (black solid line) for the VIPERS (blue) and the SDSS (orange) samples.

S/N of lines or selection based on BPT diagram) for VIPERS (75 369 sources with a corresponding average confidence level between 50% and 99% for the redshift) and the full SDSS sample (536 140 sources). We also cut the SDSS sample to have the same fraction of blue galaxies (in the mass bin of the VIPERS sample). We are aware that we might introduce a bias on the possible evolution with redshift. However, we want to check if the ease of observing galaxies with the brightest emission lines can produce an over selection of these kinds of sources.

Figure 4.8 shows the fraction of blue galaxies in function of $M_\star$ and SFR. For VIPERS the fraction decreases with $M_\star$ while there is a maximum around $\log M_\star\,[M_\odot] \sim 10.25$ for the SDSS sample. With the respect to the SFR, the two samples also showed different behavior: the fraction increases with SFR for VIPERS while it shows a maximum around $\log \mathrm{SFR}\,\left[M_\odot\ \mathrm{yr}^{-1}\right] = 0.5$ for SDSS. Since the completeness of the VIPERS sample is always higher than the completeness of the SDSS sample, from the latter it is not possible to reproduce the first.

4.2 Comparison between VIPERS and SDSS

Finally, we selected a sub-sample of the SDSS sample with the same characteristics as the VIPERS sample in terms of S/N and $\mathrm{B} - \mathrm{B}^*$. We did not apply any selection on the quality of the spectra because it would completely change the shape of the relations, especially of the projections. The SDSS sub-sample equivalent to the VIPERS sample is composed of 91 170 SF galaxies ($\sim$ 58% of the full sample).

Figure 4.9 shows the comparisons of the FMR projections: MZR, metallicity versus SFR, metallicity versus sSFR, and the main sequence for the VIPERS, the full SDSS,

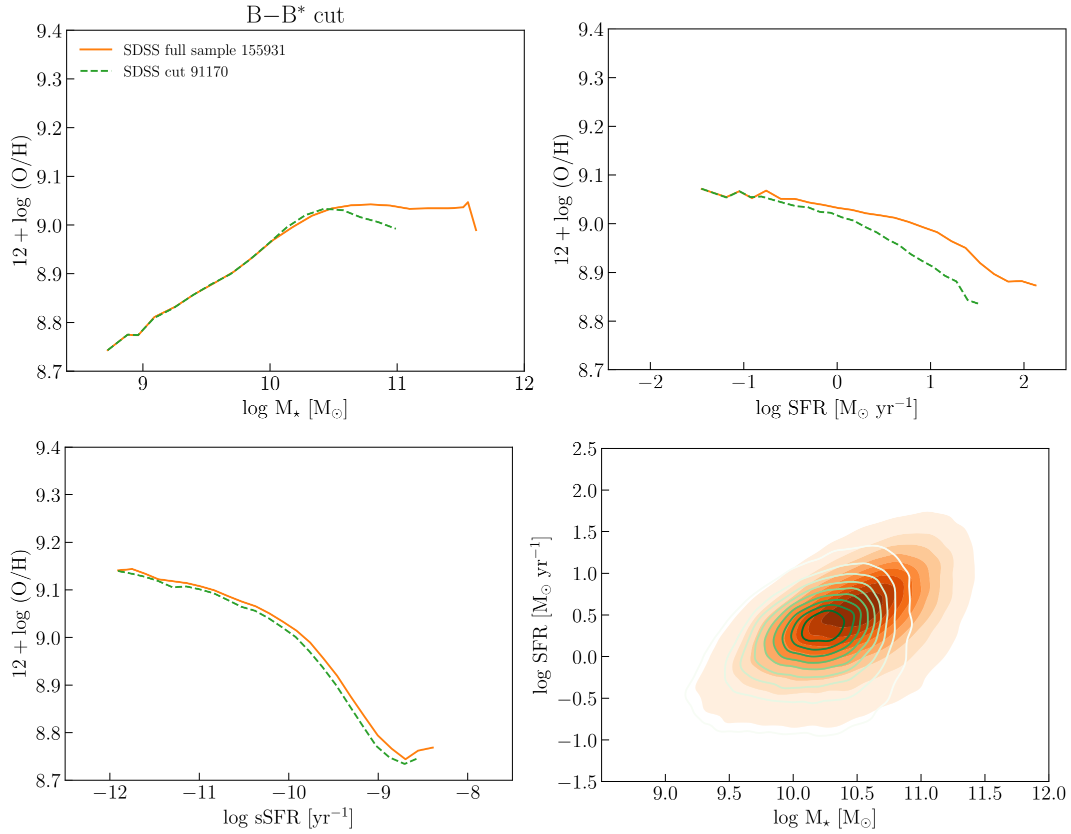

Figure 4.7: Effects of the selection on $B - B^*$ on the projections of the FMR (main sample: orange solid line; same luminosity volume than VIPERS: green dashed line).

and SDSS after all the cuts to reproduce the characteristics of the VIPERS sample. The MZR of the VIPERS sample does not show the characteristic flattening at high $M_\star$, while it shows this behavior at low $M_\star$. In this projection, the biases, once taken into account, do not have any effects. In the metallicity versus SFR plane, the VIPERS sample has lower metallicity than SDSS at the same SFR. Once the biases are taken into account, the relation for SDSS gets close to the one of VIPERS in the medium-high range covered from the latter. Finally, in the metallicity versus the sSFR plane, the two samples are in the closest agreement and the biases do not have any significant effect.

Figure 4.10 represents the metallicity difference, color-coded according to the difference between SDSS and VIPERS sample, on the MS relation. This is the most direct comparison between the two samples. The difference between them increases towards higher $M_\star$ and SFR. The median difference is $\sim 0.4 \langle\sigma_{\rm dist}\rangle_{\rm VIPERS}$ and $\sim 0.3 \langle\sigma_{\rm dist}\rangle_{\rm VIPERS}$ with and without accounting biases, respectively. As it can be seen from Fig. 4.10, biases decrease the difference mainly at high $M_\star$ and SFR.

4.3 Discussion

We analyzed the effects of four different biases introduced by observations (range in $B - B^*$ and the fraction of blue galaxies) and data selection (S/N ratio and quality flags) on the SDSS sample to understand how they could affect the comparison between different samples. We find that the biggest bias is the data selection on quality flags of the spectra. The main result of this analysis is that the metallicity

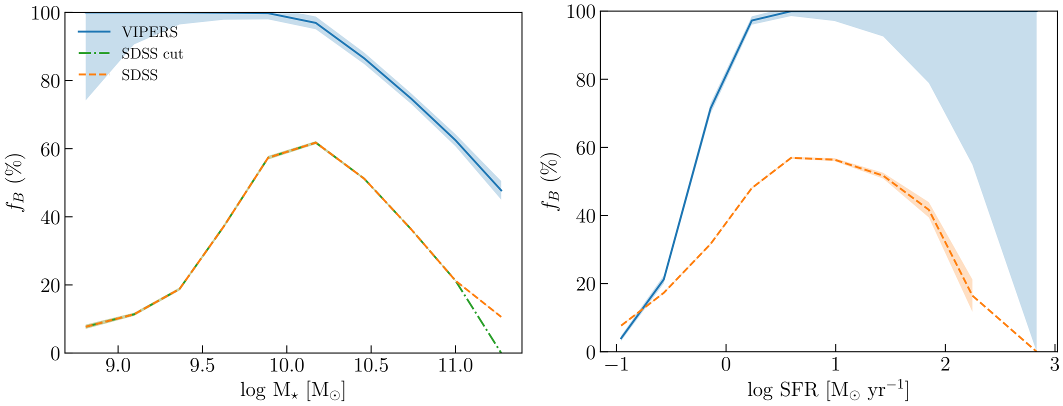

Figure 4.8: Comparison of the fraction of blue galaxies of VIPERS (blue solid line) and SDSS (orange dashed line) samples in function of the $M_\star$ (left) and SFR (right). In green dash-dotted line is reported the fraction of blue galaxies of the SDSS sample after cutting it to have the same fraction in function of the $M_\star$ than the VIPERS sample.

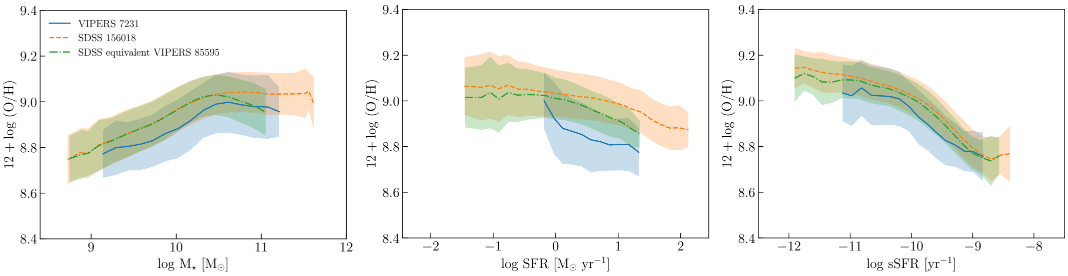

Figure 4.9: Three projections of the FMR: MZR (left), metallicity vs SFR (mid right), metallicity vs sSFR (right) for VIPERS (blue solid line), SDSS (orange dashed line), and SDSS equivalent to VIPERS (green dash-dotted line) samples.

versus the sSFR relation is the least sensitive to the biases analyzed here (completely independent of the selection on the range in $\mathrm{B} - \mathrm{B}^*$ and the fraction of blue galaxies; dependent on the selection criteria on oxygen lines.) This adds value to the non-parametric framework described by Salim et al., 2014, 2015, which allows for a generalization of the study neglecting the effects of these biases.

The biases occurring due to data selection (S/N selection and quality flag on the spectra of galaxy samples at different redshifts) can mimic an evolution mainly of the MZR and in the plane metallicity versus SFR. Restrictive sample cleaning, which requires galaxies with high S/N line detection, can lead to a non-physical MZR. It can result in a non-monotonic relation with a fall at high $M_\star$ or a complete cancellation of the anti-correlation between metallicity and SFR. This nonphysical behavior is stronger when the cutoff is “safer” on oxygen lines, especially if applied to [O III] λ4959. This line is weaker than [O III] λ5007 and not always well measured. For this reason, it will be particularly sensitive to the S/N level leading to the selection of the most SF galaxies, in the case of VIPERS. This results in a distortion of the FMR projections, especially in the case of the MZR and metallicity versus the SFR plane.

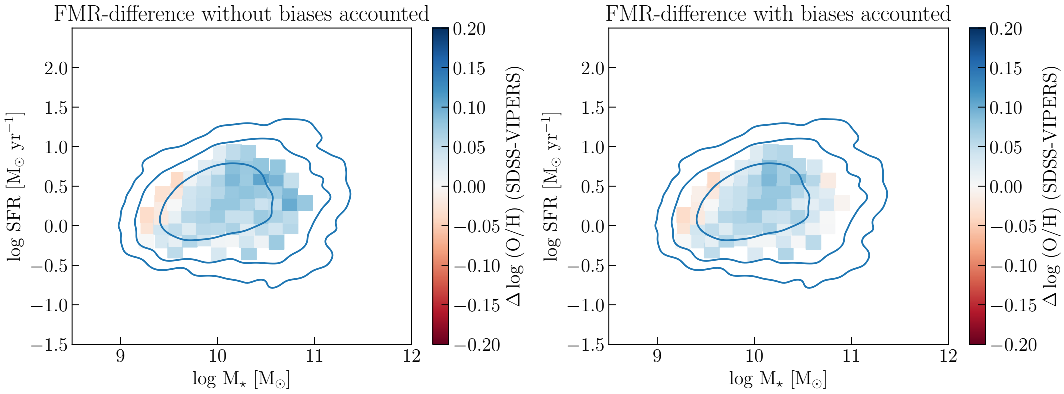

Figure 4.10: Difference in metallicity between SDSS without (left) and with (right) biases accounted and VIPERS projected on the main sequence of VIPERS sample (KDE contour plot).

4.4 Conclusions

Since many studies of FMR are based on comparisons of differently selected samples, we have analyzed the effects of different biases that can be introduced during the sample selection on the relations between metallicity, $M_\star$, and SFR to assess how comparable in reality so constructed samples are. We studied biases introduced by physical constraints (evolution of the luminosity function and differences in the fraction of blue galaxies) or data selection (S/N and quality of the spectra).

The study of FMR projections is not the same comparison as for the full FMR. For example, the evolution of the MZR does not affect the FMR (Mannucci et al., 2010). For this reason, the study of a more direct comparison from non-parametric analysis (being, indeed, a more reliable study of FMR) will be the subject of a subsequent separate paper.

The main conclusions reached in this work can be summarised as follows.

i) The VIPERS sample is in good agreement with the SDSS sample with "standard" data selection, with an average metallicity difference of $\sim 0.4\,\langle\sigma_{\mathrm{dist}}\rangle_{\mathrm{VIPERS}}$. The biases taken into account can reduce the metallicity difference between these samples to $\sim 0.3\,\langle\sigma_{\mathrm{dist}}\rangle_{\mathrm{VIPERS}}$. The reader should note that this does not yet provide a conclusion of evolution - or lack of evolution - of the FMR itself; this will be closely examined in the chapter 5.

ii) Data selection based on S/N cutoff and flag quality of the lines affects the MZR and the metallicity versus the SFR plane. It leads to nonphysical relations (fall of the MZR at large $M_\star$ and hiding of the anti-correlation between the galactic properties in the plane metallicity versus the SFR), which can be misunderstood as evidence of evolution. These kinds of selections can introduce biases if applied, for instance, to the oxygen lines — especially if applied to [O III] λ4959.

iii) The plane metallicity versus $\log M_\star - 0.32\log \mathrm{SFR}$ reduces the metallicity difference between the two samples. In this plane and in the MZR, the VIPERS sample is in good agreement with the zCOSMOS data (Cresci et al., 2012).

iv) VIPERS sample is in agreement with the relation found by Savaglio et al., 2005 in the whole range of $M_\star$ ($9.25 \leq \log M_\star\,[M_\odot] \leq 11.0$) and with the relations found by Lee et al., 2006, Huang et al., 2019, and Bellstedt et al., 2021 at high $M_\star$

(log $M_\star$ $[M_\odot] > 10.0$). This comparison suggests that an over-selection of metal-rich galaxies or an overestimation of the metallicity at low $M_\star$ is still present in the VIPERS sample.

v) The main bias is the selection of the flags of spectra quality which is not easily simulated by the selection of the S/N ratios of the emission lines. It shows that metal-poor SF galaxies have spectra with intrinsically better quality.

vi) S/N cutoffs affect the MZR and metallicity versus the SFR selectively cut the high metallicity at higher $M_\star$ and lower SFR flattening the curves. In the plane metallicity versus the sSFR, this cut has negligible effects within uncertainties.

vii) The plane metallicity versus $\log M_\star - 0.32 \log \mathrm{SFR}$ and metallicity versus sSFR are the least sensitive to observational biases among the 2D relations.

viii) When analyzing metallicity versus $M_\star$ or SFR, we have to be careful when carrying out the sample selection as this may introduce biases.

As demonstrated, a sample-selection-based comparison can be complicated to do even if often used in the literature (e.g. Calabrò et al., 2017; Huang et al., 2019; Savaglio et al., 2005). In addition, the FMR projections do not fully describe the FMR itself. A more direct comparison of the FMR at different redshifts can be provided by a non-parametric framework (e.g. Salim et al., 2014, 2015).

CHAPTER 5

The impact of methodology on the observed evolution of FMR

In order to investigate if the FMR is really fundamental, or depends on (redshift variant) methods of comparing the samples, we make use of the unprecedented statistics of VIPERS to study and compare, for the first time with a high statistical significance, the MZR and FMR at $z \sim 0.8$ and at median $z \sim 0.09$. In this Chapter, we use a variety of methods of comparison (Sect. 5.1) in order to determine how strong the conclusions are against the method used.
We apply the following methods: i) a family of parametric methods, based on the direct comparison of different projections of the FMR and using control samples (Sect. 3.8), ii) a non-parametric method based on Salim et al. (2014, 2015). The non-parametric method is based on the comparison between the metallicity and the normalized sSFR in different $M_\star$ bins. The choice of normalization for the sSFR in the non-parametric method allows us to choose the properties that will be compared between the samples.
We then describe the comparison of the FMR at different redshifts (Sect. 5.2) via these methods, the evolution of the MZR and metallicity-SFR relation (Sect. 5.3), the final discussion (Sect. 5.4), and the conclusions (Sect. 5.5). The original work is presented in F. Pistis et al. (2023a). A comparative study of the fundamental metallicity relation. The impact of methodology on its observed evolution. A&A submitted.

5.1 Methods of comparison

In order to compare samples at different redshifts (from $z \sim 0.8$, VIPERS, to $z \sim 0$, SDSS), we apply two families of methods to study the FMR: i) parametric: the study of the projections of the FMR; ii) non-parametric: the study of the normalized metallicity-sSFR relation in different mass bins. The idea for the parametric method is to infer information about the FMR via the median projections on different planes. Here, we study: i) the MZR (Curti et al., 2020; Mannucci et al., 2010; Savaglio et al., 2005; Tremonti et al., 2004); ii) the metallicity-SFR relation; iii) the metallicity-sSFR relation; iv) the projection of minimum scatter (Mannucci et al., 2010); v) the metallicity difference in $M_\star$-SFR bins. The study of the projections of the FMR has the problem to be affected by biases introduced by the observations and by the data selection (Pistis et al., 2022), especially the MZR and the metallicity-SFR relation. In this method, it is necessary to cross-match the samples in order to compare galaxies with specific properties. This, in turn, tends to introduce additional selection effects to the samples.

The non-parametric method (Salim et al., 2014, 2015) studies the relation between the normalized sSFR and the metallicity. Because of the use of the sSFR, this method is independent of the simple shift of $M_\star$ and/or SFR resulting from different techniques of estimation of those physical values, e.g., if different samples have physical properties derived using different IMF, the sSFR takes into account automatically the shift. This method has the advantage to use the projection of the FMR that is less affected by biases (Pistis et al., 2022). The original method (Salim et al., 2014, 2015) defines the normalized sSFR as

$$\Delta \log \mathrm{sSFR} = \log \mathrm{sSFR} - \langle \log \mathrm{sSFR} \rangle \,, \tag{5.1}$$

where $\langle \log \mathrm{sSFR} \rangle$ is the average or median sSFR in the mass bin of the sample at low redshift, for both samples. We also divide the sample into four $M_\star$ bins centered at $\log M_\star\,[M_\odot] = 9.5$, 10.0, 10.5, and 11.0 with bin width equal to 0.5 dex. This normalization allows comparing galaxies with the same $M_\star$ and SFR.

In this work, we decide to use also a second normalization defined as

$$\delta \log \mathrm{sSFR} = \log \mathrm{sSFR} - \log \mathrm{sSFR}_{\mathrm{MS}}, \tag{5.2}$$

where $\log \mathrm{sSFR}_{\mathrm{MS}}$ is the "local" MS at the redshift of each sample. This normalization allows comparing galaxies with the same relative distance from the MS, giving information about the processes that generate the scatter of the MS itself.

The anti-correlation between metallicity and sSFR has been interpreted in terms of gas accretion from the IGM and circumgalactic medium (CGM, Curti et al., 2020; Kumari et al., 2021; Mannucci et al., 2010). The accreted gas dilutes the gas metallicity and enhances the star formation. However, the large scatter of sSFR per fixed metallicity means that galaxies with the most significant offsets from the MS are not always those with fewer metals with respect to their MS counterparts. This implies the complexity of physical mechanisms in galaxy evolution, e.g., environmental effects (shock heated gas in overdensities cannot cool down efficiently and galaxies become metal-rich rapidly due to the suppression of pristine gas inflow, Lilly et al., 2013; Peng et al., 2014a).

Galaxies with negative scatter ($\delta \log \mathrm{sSFR} < 0$) with respect to the MS were most probably undergo a quenching process in the recent history (e.g., via depletion or outflows of gas; Ciesla et al., 2016, 2018), while galaxies with a positive scatter ($\delta \log \mathrm{sSFR} > 0$) with respect to the MS experienced a recent SFR enhancement (burst, e.g., via merging event or inflows of gas; Elbaz et al., 2018).

In order to account for these processes, we divide the samples into the sub-samples of galaxies above the MS ($\delta \log \mathrm{sSFR} > 0$) and below the MS ($\delta \log \mathrm{sSFR} < 0$). By studying the slope of the normalized (according to the MS) metallicity-sSFR relation as a function of the mass, we can infer the impact of processes that enhance or quench the SFR on the metallicity during galaxy evolution.

5.2 FMR comparison of samples at different redshift

In this section, we present the results of the comparison of the FMR of the main samples at median $z \sim 0.09$ (SDSS), median $z \sim 0.63$ (VIPERS), and the control samples. In Sect. 5.2.1 we report the results using the parametric method. In Sect. 5.2.3 we report the results using the non-parametric method.

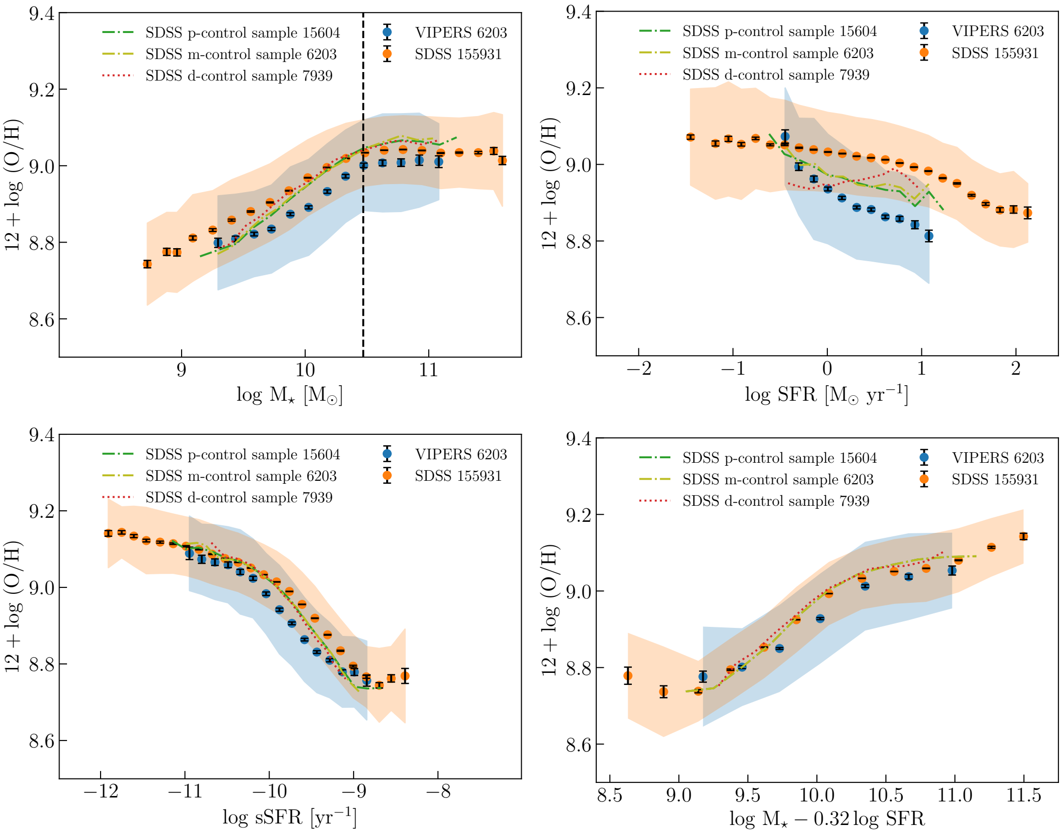

Figure 5.1: Four projections of the FMR: MZR (top left),metallicity-SFR relation (top right), metallicity versus. sSFR (bottom left), and metallicity versus. $\log M_\star - 0.32 \log \mathrm{SFR}$ (bottom right) for VIPERS (blue dots), SDSS (orange dots), SDSS p-control (green dash-dotted line), SDSS m-control (olive dash-dotted line), and SDSS d-control (red dotted line). The shaded areas show the $1\sigma_{\mathrm{dist}}$ while the black errorbars show the $1\sigma_{\mathrm{med}}$ for the metallicity. We report the number of galaxies in each sample in the legend. The vertical black dashed line in the MZR plane shows the most conservative mass limit for completeness ($\log M_\star\,[M_\odot] = 10.47$ for $0.65 < z <= 0.8$) in the redshift range observed by VIPERS (Davidzon et al., 2016). For each sample, we report the number of galaxies in the legend.

5.2.1 Parametric method: FMR projections with control samples

We proceed with the comparison of the samples at median $z \sim 0.09$ (SDSS), median $z \sim 0.63$ (VIPERS), and the SDSS-based control samples via the parametric method. Figure 5.1 shows the projections of the FMR on the $M_\star$, SFR, sSFR, and $M_\star - 0.32 \log \mathrm{SFR}$ (the plane of minimum scatter, Mannucci et al., 2010) planes.

MZR

The MZR (Fig. 5.1, upper left panel) of galaxies at intermediate redshift shows lower metallicities at a given $M_\star$ with respect to galaxies at low redshift. This shift is statistically significant with respect to σ_{med} showing an evolution of the MZR with the redshift.

However, a large scatter of both populations should be noted. As seen from the upper left panel of Fig. 5.1, the separation between them is below $1\sigma_{\mathrm{dist}}$ of both samples. The samples at both low and intermediate redshifts show a similar scatter, given by σ_{dist}, suggesting a lack of evolution of the scatter itself. Artificially reducing the percentile range to estimate the uncertainty due to the galaxy distributions inside each bin we find that this separation is $0.3\sigma_{\text{dist}}$ for both samples. This implies that the detection or non-detection of the evolution of MZR may be sensitive to source selection in small samples.

All control samples follow the same MZR. The control samples have a small deviation (again within uncertainties) from the main SDSS sample at lower $M_\star$, getting closer to the VIPERS sample at low $M_\star$, hence containing lower-metallicity galaxies at fixed $M_\star$.

Metallicity-SFR relation

The metallicity-SFR relation (Fig. 5.1, upper right panel) of galaxies at intermediate redshift shows lower metallicities at a given SFR with respect to galaxies at low redshift. Like the case of the MZR, also the metallicity-SFR relation shows a shift statistically significant with respect to σ_{med}, showing an evolution of the relation with the redshift.

Again, a large scatter of both populations should be noted. As seen from the upper right panel of Fig. 5.1, the separation between them is below $1\sigma_{\text{dist}}$ of both samples. The samples at both low and intermediate redshifts show a similar scatter, given by σ_{dist}, suggesting a lack of evolution of the scatter itself.

The p-control and m-control samples show a closer metallicity-SFR relation closer to the VIPERS sample. The process of cross-matching removes metal-rich galaxies in the SFR interval of the VIPERS sample when the control samples are built. The VIPERS sample still shows a stronger anti-correlation between metallicity and SFR than p-control and m-control samples. At the same time, the d-control sample does not show any or even a positive correlation between metallicity and SFR.

Metallicity-sSFR relation

The metallicity-sSFR relation (Fig. 5.1, bottom left panel) shows smaller differences between low and intermediate redshifts. Again, this difference is significant with respect to σ_{med}, showing an evolution of the metallicity-sSFR relation. However, the difference between low and intermediate redshifts is reduced at the edges of the sSFR range explored by the VIPERS sample.

Again, a large scatter of both populations should be noted. As seen from the bottom left panel of Fig. 5.1, the separation between them is below $1\sigma_{\text{dist}}$ of both samples. The samples at both low and intermediate redshifts show a similar scatter, given by σ_{dist}, suggesting a lack of evolution of the scatter itself.

All control samples follow the same metallicity-sSFR relation. The differences between the SDSS and all control samples are negligible in the metallicity-sSFR relation with respect to σ_{dist}. The difference between the SDSS and all control samples increases with the sSFR, with the control samples getting close to the VIPERS sample. The m-control sample follows a consistent relation within uncertainties as the p-control sample.

Projection of minimum scatter

The projection of minimum scatter (defined in Mannucci et al., 2010), $\log M_\star - 0.32 \log \text{SFR}$-metallicity plane (Fig. 5.1, bottom right panel), among all the projections of the FMR here, shows the smallest difference between SDSS-based samples. Also,

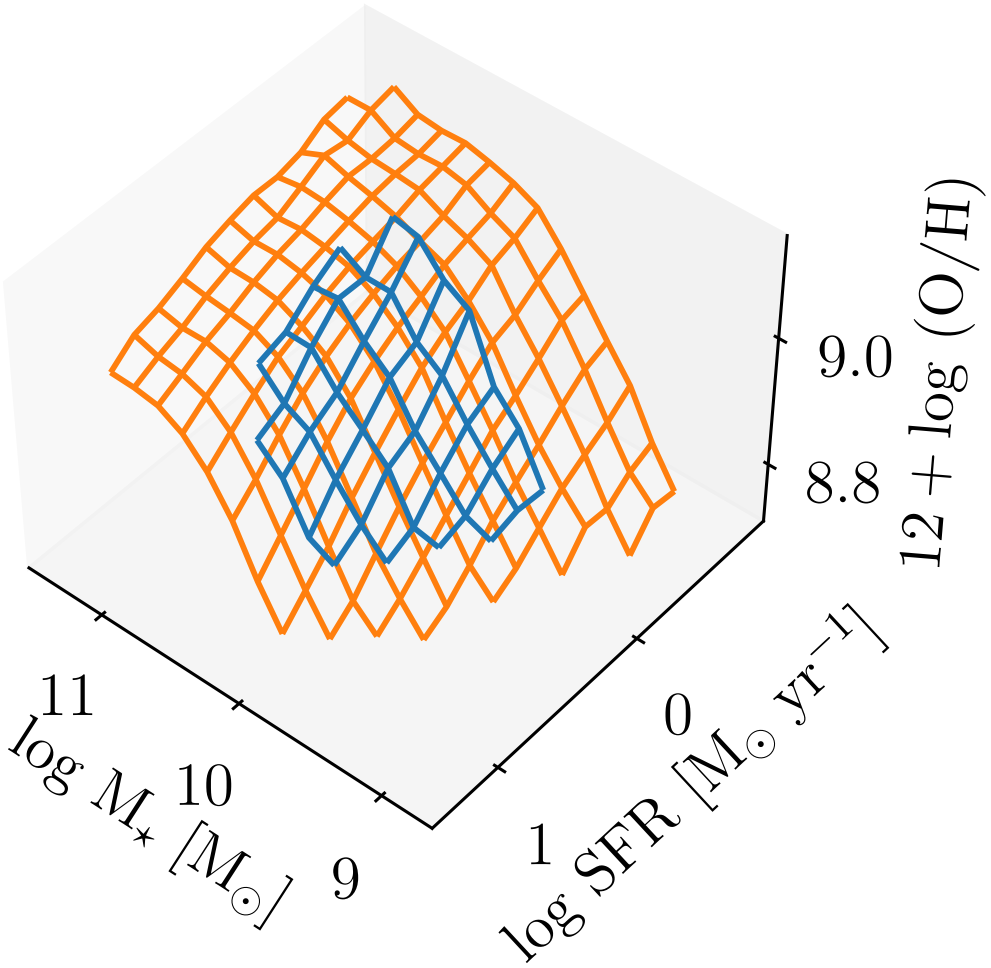

Figure 5.2: Surfaces of the FMR for SDSS (orange) and VIPERS (blue) samples.

the difference between low and intermediate redshifts is reduced with respect to other projections.

The projection of minimum scatter shows smaller differences between low and intermediate redshifts. Again, this difference is significant with respect to σ_{med}, showing an evolution of the metallicity-sSFR relation. However, the difference between low and intermediate redshifts is reduced at the bottom edge of the $\log M_\star - 0.32 \log \mathrm{SFR}$ range explored by the VIPERS sample where the two samples cross each other.

Again, a large scatter of both populations should be noted. As seen from the upper right panel of Fig. 5.1, the separation between them is below $1\sigma_{\mathrm{dist}}$ of both samples. The samples at both low and intermediate redshifts show a similar scatter, given by σ_{dist}, suggesting a lack of evolution of the scatter itself.

5.2.2 Surface of the fundamental metallicity relation

Figure 5.2 shows the surfaces of the FMR for both SDSS and VIPERS samples. The shapes of the two surfaces agree with each other at high $M_\star$. Both surfaces show a flattening at high $M_\star$.

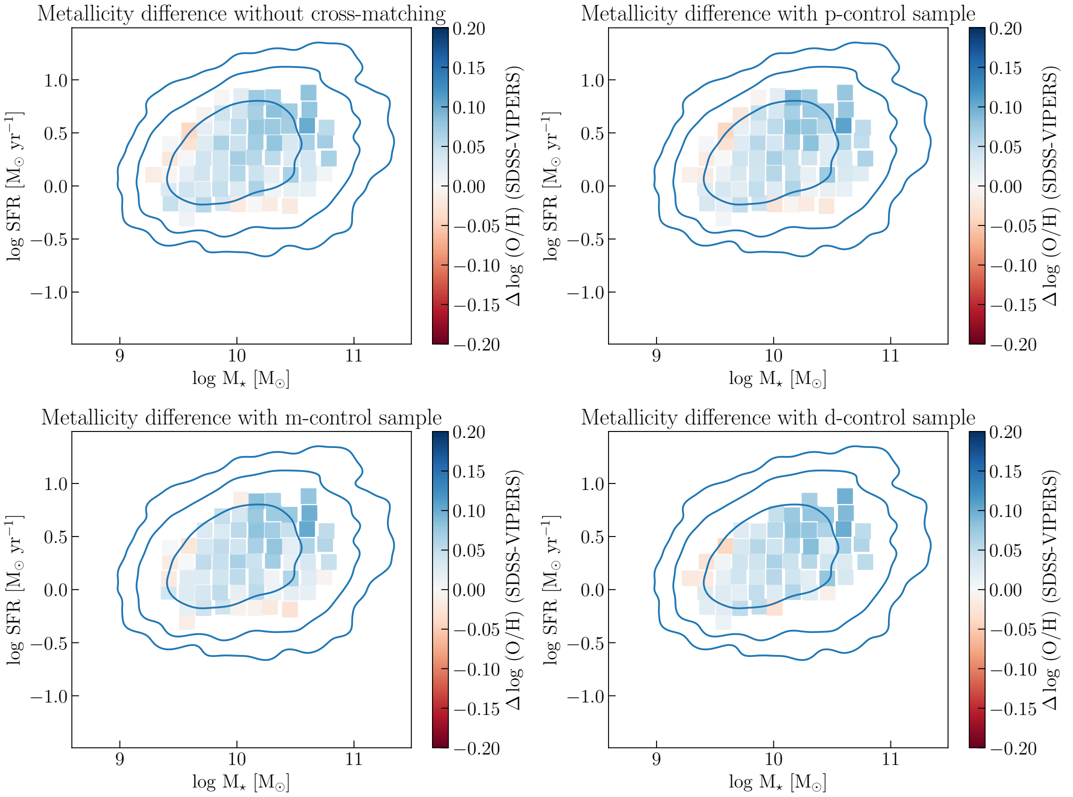
Metallicity difference without cross-matching

Metallicity difference with p-control sample

Metallicity difference with m-control sample

Metallicity difference with d-control sample

Figure 5.3: Metallicity differences between SDSS (upper left), SDSS p-control (upper right), SDSS m-control (bottom left), and SDSS d-control (bottom right) samples and VIPERS. Contours show the 1σ, 2σ, and 3σ levels of the MS distributions for the VIPERS sample.

Table 5.1: Average (over bins) differences in metallicity between all SDSS-based and VIPERS samples (as in Fig. 5.3) in $M_\star$-SFR bins. The differences are expressed in absolute units, in units of $\langle\sigma_{\rm dist}\rangle_{\rm VIPERS}$, and in units of $\langle\sigma_{\rm med}\rangle_{\rm VIPERS}$.

Sample	$\Delta\log\mathrm{(O/H)}$ $(\langle\sigma_{\rm dist}\rangle_{\rm VIPERS})$	$\Delta\log\mathrm{(O/H)}$ $(\langle\sigma_{\rm med}\rangle_{\rm VIPERS})$	$\Delta\log\mathrm{(O/H)}$ (dex)
SDSS main sample	0.379	3.145	0.040
SDSS p-control sample	0.333	2.760	0.035
SDSS m-control sample	0.378	3.132	0.039
SDSS d-control sample	0.395	3.274	0.042

Metallicity difference in $M_\star$-SFR bins

Figure 5.3 presents the metallicity difference between SDSS-based and VIPERS samples for each $M_\star$-SFR bin. This is the most direct comparison of the FMR between samples. The average difference in metallicity between all SDSS-based and VIPERS samples is listed in Table 5.1 where $\langle\sigma\rangle_{\rm VIPERS}$ is the average standard deviation in metallicity inside the $M_\star$-SFR bin of VIPERS sample. The small changes in the $\Delta\log\mathrm{(O/H)}$ values for the control samples are mainly due to the limited area in the MS observed in these sub-samples with respect to the main sample. In all cases, the difference increases systematically with $M_\star$.

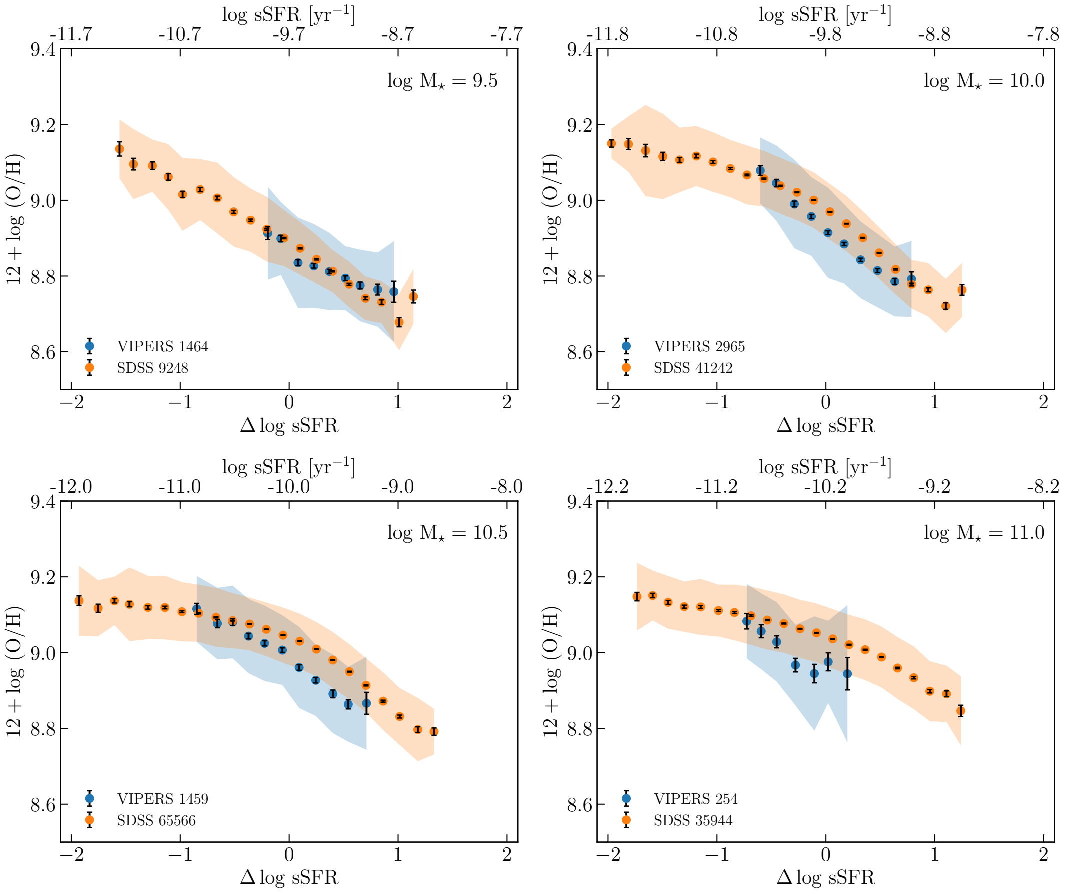

Figure 5.4: Comparison in the non-parametric method (Salim et al., 2014, 2015) between VIPERS (blue dots) and SDSS (orange dots) samples. The shaded areas show the $1\sigma_{\text{dist}}$ while the black errorbars show the $1\sigma_{\text{med}}$ for the metallicity. Mass bins are centered on the values indicated in each panel and are 0.5 dex wide. We also report the number of galaxies for both samples in each mass bin.

5.2.3 Non-parametric method

In this subsection, we proceed to compare the main samples at median $z \sim 0.09$ (SDSS) and median $z \sim 0.63$ (VIPERS) via the non-parametric method. First, we normalize the sSFR of both samples by the median sSFR of the low redshift sample, to assure that we compare galaxies with both the same $M_\star$ and SFR.

Inside each mass bin, we divided the sample in 0.15 dex-wide bins in $\Delta \log \text{sSFR}$. Then, we estimated the median in each bin and we estimate the errors according to σ_{dist} and σ_{med} Figure 5.4 shows the relations for the main samples. Even in this case, the difference between the two samples increases with the $M_\star$.

Then, we normalize the sSFR of each sample by the value of their "local" MS. In this way, we compare galaxies with the same relative distance to the MS. We proceeded in the same way as the non-parametric method with the division in the same $M_\star$ bins. In each mass bin, we divided the sample in 0.15 dex-wide bin in $\delta \log \text{sSFR}$. Then, we estimated the median in each bin and we estimate the errors according to σ_{dist} and σ_{med}. Figure 5.5 shows bigger differences between the samples compared to the normalization with respect to the median value.

To analyze the processes that lead the galaxies to move around the MS, we study the slope of the normalized metallicity-sSFR relation as a function of the $M_\star$ for

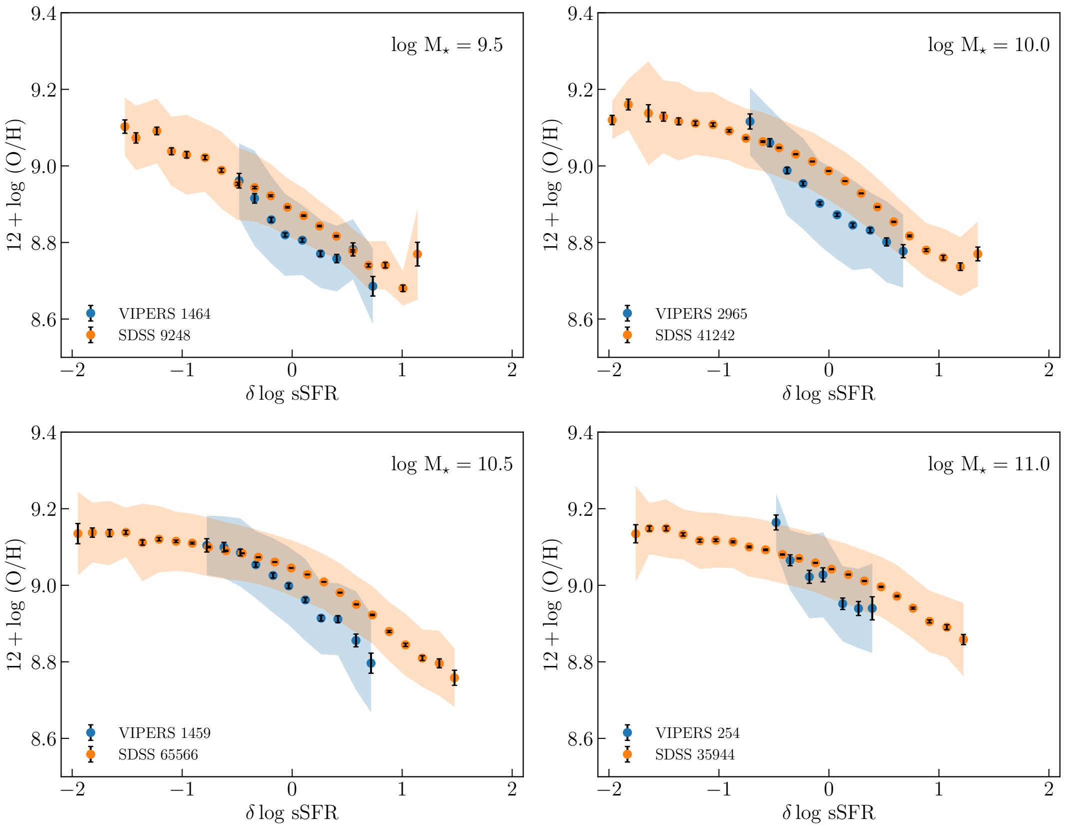

Figure 5.5: Comparison in the non-parametric method (Salim et al., 2014, 2015) normalized according to the MS between VIPERS (blue dots) and SDSS (orange dots) samples. The shaded areas show the $1\sigma_{\text{dist}}$ while the black errorbars show the $1\sigma_{\text{med}}$ for the metallicity. Mass bins are centered on the values indicated in each panel and are 0.5 dex wide. We also report the number of galaxies for both samples in each mass bin.

galaxies above ($\delta \log \text{sSFR} > 0$) and below ($\delta \log \text{sSFR} < 0$) the MS. Table 5.2 reports the values of the slope. Figure 5.6 shows the slope of the normalized metallicity-sSFR relation as a function of the $M_\star$. For both samples and both positions with respect to the MS, a negative slope indicates processes that are diluting the metals in the ISM while quenching or enhancing the SFR of the galaxies.

Above the MS ($\delta \log \text{sSFR} > 0$) we find stronger dilution effects from processes enhancing the SFR at low redshift for smaller $M_\star$. The difference between low and intermediate redshifts decreases with $M_\star$. Below the MS ($\delta \log \text{sSFR} < 0$) we find a consistent relation within uncertainties between low and intermediate redshifts with less dilution of the metals increasing the $M_\star$. Again the differences between samples reduce increasing the $M_\star$. Below MS, the dilution of metals remains much stronger at intermediate redshift in comparison to the low redshift for the whole range of $M_\star$.

5.3 Evolution of the MZR and metallicity-SFR relation

Being particularly careful to homogenize the property estimations of both samples, we want to statistically quantify the evolution (within the uncertainties) of the MZR, metallicity-SFR relation up to $z \sim 0.8$ (Fig. 5.1 upper panels), and FMR. The systematic trend of the VIPERS sample having lower metallicities than the SDSS at almost all the

Table 5.2: Slope of the $\delta \log \mathrm{sSFR}$-metallicity relation for $\delta \log \mathrm{sSFR} < 0$ and $\delta \log \mathrm{sSFR} > 0$.

	$\delta \log \mathrm{sSFR} < 0$		$\delta \log \mathrm{sSFR} > 0$	
$\log M_\star$ [$M_\odot$]	VIPERS	SDSS	VIPERS	SDSS
9.5	-0.39 ± 0.03	-0.15 ± 0.01	-0.13 ± 0.03	-0.20 ± 0.01
10.0	-0.32 ± 0.03	-0.09 ± 0.01	-0.16 ± 0.01	-0.21 ± 0.01
10.5	-0.16 ± 0.00	-0.05 ± 0.00	-0.22 ± 0.03	-0.20 ± 0.01
11.0	-0.20 ± 0.04	-0.05 ± 0.00	-0.15 ± 0.03	-0.14 ± 0.01

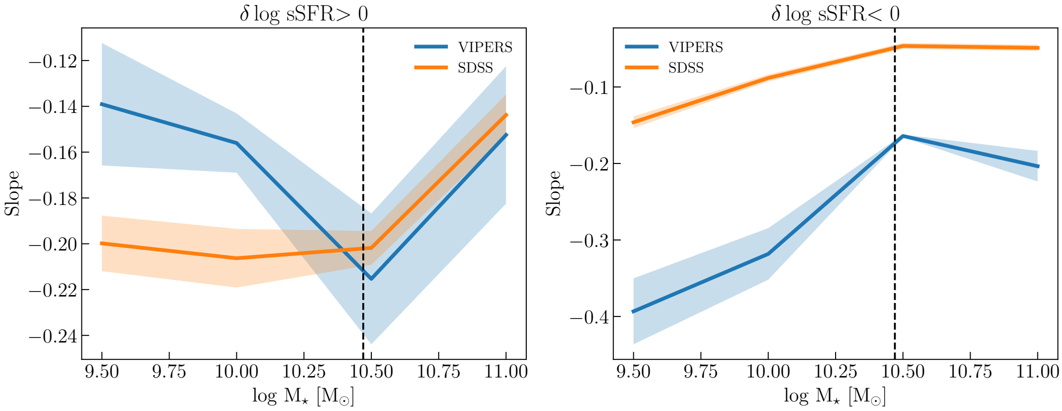

Figure 5.6: Slope of the relation between metallicity and $\delta \log \mathrm{sSFR}$ as a function of the $M_\star$ above (left) and below (right) the MS for VIPERS (blue solid line) and SDSS (orange solid line) samples. The vertical black dashed line shows the most conservative mass limit for completeness ($\log M_\star\,[M_\odot] = 10.47$ for $0.65 < z <= 0.8$) in the redshift range observed by VIPERS (Davidzon et al., 2016).

examined mass ranges is visible but given the scatter of both samples, it is significant only at the level of σ_{med}. On the other hand, we observe bigger differences with redshift in the metallicity-SFR relation (Fig. 5.1 upper right panel).

A possible reason for this apparent weak evolution of the scatter in the MZR and metallicity-SFR relation could be observational biases in the VIPERS sample, in particular, the fact that the sample is not mass complete, i.e. with increasing z we lose less bright, and consequently less massive galaxies. To check if this small evolution between SDSS and VIPERS samples results from the VIPERS lower redshift galaxies dominating the MZR and metallicity-SFR relation of the whole sample, we conducted a series of tests, described below. To check the impact of the mixture of galaxies at different redshifts, we split the VIPERS sample into two redshift bins (with a threshold at the central redshift $z = 0.65$).

To test for the mass incompleteness effect, following Davidzon et al. (2016), we adopt the mass threshold as $\log M_\star\,[M_\odot] = 10.18$ for $0.51 < z \leq 0.65$, $\log M_\star\,[M_\odot] = 10.47$ for $0.65 < z \leq 0.8$, and $\log M_\star\,[M_\odot] = 10.66$ for $0.8 < z \leq 0.9$. We apply these thresholds to the VIPERS sample and check how both the MZR and the metallicity-SFR relation change. Figure 5.7 shows the MZR and the metallicity-SFR relation for different VIPERS-based sub-samples.

Any difference in the MZR (left panel in Fig 5.7) between the sub-samples is

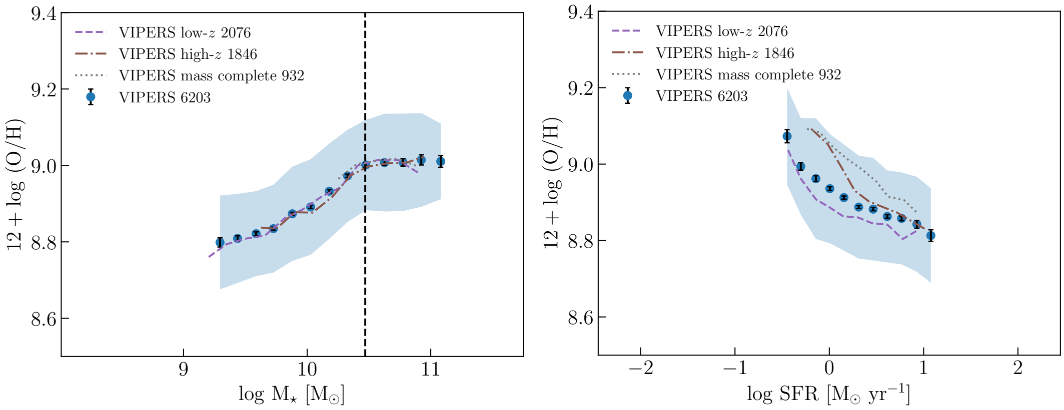

Figure 5.7: MZR (left) and the metallicity-SFR relation (right) for full VIPERS (blue dots), VIPERS low redshift (purple dashed line), VIPERS high-z (brown dash-dotted line), and VIPERS mass complete (gray dotted line). The vertical black dashed line shows the most constrictive mass limit for completeness ($\log M_\star\,[M_\odot] = 10.47$ for $0.65 < z <= 0.8$) in the redshift range observed by VIPERS (Davidzon et al., 2016). The shaded areas show the $1\sigma_{\rm dist}$ while the black errorbars show the $1\sigma_{\rm med}$ for the metallicity. For each sample, we report the number of galaxies in the legend.

negligible, well below the statistical $\sigma_{\rm dist}$ of the measurements. The metallicity-SFR relation (right panel in Fig 5.7) of the two redshift sub-samples shows bigger differences than the MZR, with the high-z sub-sample having higher metallicity (likely because of being dominated by more massive galaxies) and showing a stronger anti-correlation. Also, the mass complete sub-sample shifts towards higher metallicity (also likely because it is dominated by higher mass galaxies) but it keeps an almost parallel relation to the main sample. However, all these differences are not statistically significant compared to the $\sigma_{\rm dist}$ of the metallicity.

In order to quantify SDSS and VIPERS are statistically different, we perform a Kolmogorov-Smirnov test (KS-test). We divide both samples in the same $M_\star$ or SFR bins and we perform the KS-test between the distributions of the samples within each bin. Figure 5.8 shows the resulting p-value as a function of the $M_\star$ and SFR. Only the five highest $M_\star$ bins have a p-value ≥ 0.05, meaning the probability that the two samples are drawn by the same distribution is statistically significant ($\geq 95\%$). The two samples are, instead, statistically different for all the SFR bins. Figure 5.8 also shows the probability of having the samples drawn from the same distribution in $M_\star$ and SFR ranges. Here, only for $\log M_\star\,[M_\odot] \geq 10.75$ the samples are statistically equivalent. For $\log M_\star\,[M_\odot] < 10.75$ and for the whole range of SFR, the two samples are drawn from different distributions. From the point of view of the evolution of the MZR and metallicity-SFR relation, only the high $M_\star$ end of the MZR is comparable between low and intermediate redshifts. The evolution between SDSS and VIPERS samples for the MZR at low $\log M_\star\,[M_\odot] < 10.75$ and for the metallicity-SFR relation for the whole SFR range is statistically significant.

We also compare the metallicity distributions in $M_\star$-SFR bins in order to compare the FMR at low and intermediate redshifts by KS-test. Figure 5.9 shows the scatter in the $M_\star$-SFR plane color-coded according to the p-value resulting from the KS-test. Only three bins at the bottom-right edge of the surface explored by the VIPERS sample show a p-value $\geq$ 0.05. For the majority of the bins, the two samples are drawn from different distributions. Also, the evolution of the FMR is statistically significant between low and intermediate redshifts.

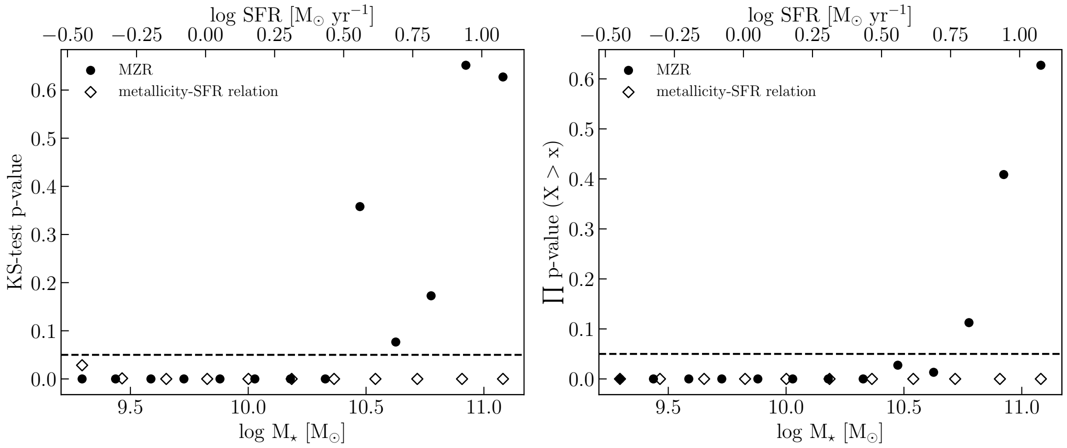

Figure 5.8: Results of the KS-test between VIPERS and SDSS samples in order to check the evolution of the MZR and the metallicity-SFR relation. The left panel shows the p-value of the KS-test performed in $M_\star$ bins for the MZR (dots) and SFR bins for the metallicity-SFR relation (diamonds). The right panel is like the top panel but we report the product of the sequence for X $>$ x where X is the $M_\star$ or the SFR and x is the value on the x-axis. The dashed horizontal line ($y = 0.05$) shows the threshold for the 95% confidence level of the KS-test.

Figure 5.10 shows the comparison between the MZR for the VIPERS and the SDSS samples with different fit reported in the literature (Curti et al., 2020; Huang et al., 2019; Mannucci et al., 2010; Savaglio et al., 2005; Tremonti et al., 2004). We also report the fits of the MZR of studies claiming to measure the evolution of the MZR (Huang et al., 2019; Savaglio et al., 2005). The shape of the MZR for both samples agrees with the literature at high-$M_\star$ but the tail at low-$M_\star$ seems to be too much flatter in the VIPERS sample.

In the same plot, the MZR of the VVDS wide ($i_{\mathrm{AB}} < 22.5$) and deep ($i_{\mathrm{AB}} < 24.0$) fields are also reported. These VVDS samples are cross-matched by the catalogs used by Lamareille et al., 2009 and Le Fèvre et al., 2013. Since we use here the VVDS sample only to validate the shape of the MZR, we do not recompute the physical properties using the values found in the catalog (Lamareille et al., 2009). The MZR of the VIPERS sample follows the same shape as the VVDS samples showing a flattening at the low-$M_\star$ tail. This behavior happens for $\log M_\star\ [M_\odot] < 10.0$ where the VIPERS survey is not mass complete while the completeness of the VVDS sample is ensured in the whole magnitude range of the spectroscopic survey (Le Fèvre et al., 2013; McCracken et al., 2003).

5.4 Discussion

In this work, we studied the FMR at low redshift (SDSS data, median $z \sim 0.09$) and intermediate redshift (VIPERS data, median $z \sim 0.63$) using two different methods:

i) the study of the FMR projections using also direct cross-matching between samples at different redshift;

ii) the non-parametric which compares the metallicity versus the normalized sSFR at different $M_\star$ bins cross-matching galaxies accordingly to the normalization of the sSFR.

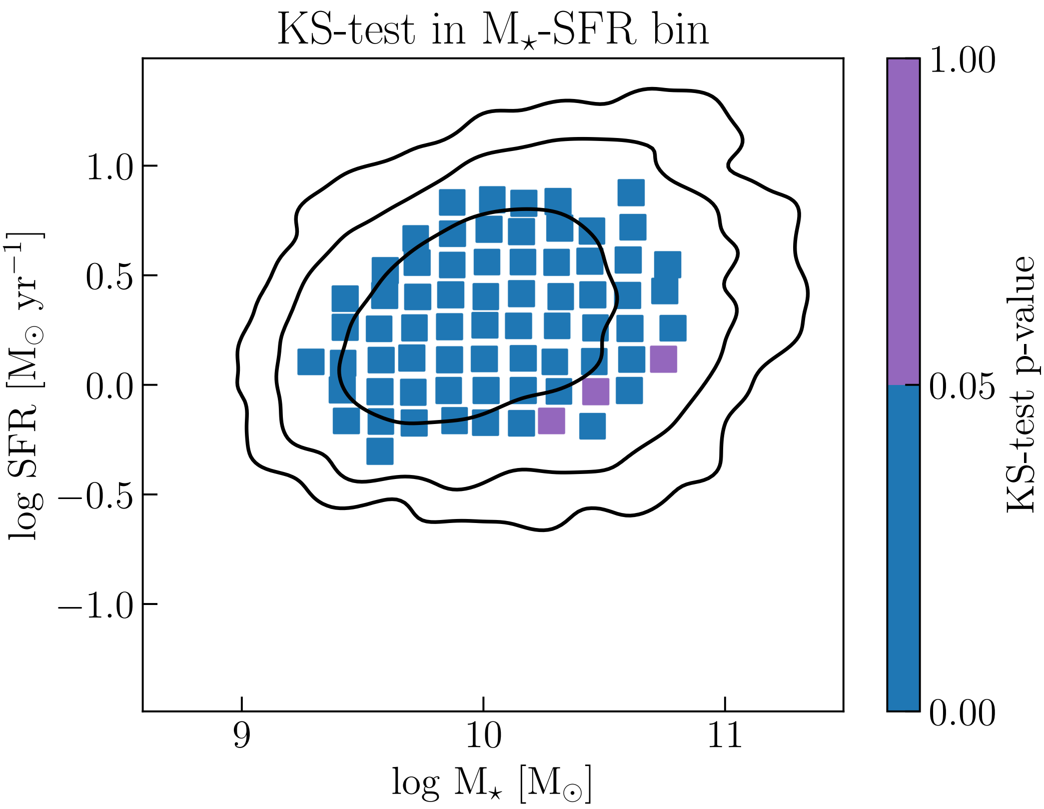

Figure 5.9: Results of the KS-test between VIPERS and SDSS samples in order to check the evolution of the FMR. The scatter plot is color-coded according to the p-value resulting from the KS-test in $M_\star$-SFR bins. The color bar shows the two colors chosen above and below the threshold for the 95% confidence level of the KS-test.

We aimed to study the influence of the methods on the conclusion about the evolution of the FMR. At the same time, we decided to check for the presence of observational biases that were not taken into account by cross-matching the catalogs at low and intermediate redshifts (Pistis et al., 2022). In this section, we discuss the results of the methods used for the comparison of the FMR between different redshift ranges (Sect. 5.4.1), the comparison of the samples (Sect. 5.4.2), and the evolution of the MZR and the metallicity-SFR relation (Sect. 5.4.3).

5.4.1 Methods of comparison

In the study using the parametric method, we built three control samples with the following characteristics:

i) cross-matching physical properties ($M_\star$ and SFR, p-control sample);

ii) reproducing the galaxy mass distribution of VIPERS sample (m-control sample);

iii) reproducing the relative distance from the MS of the VIPERS sample (d-control sample).

We used two different normalizations in the non-parametric method:

i) with respect to the median sSFR of the sample at low redshift allowing us to compare galaxies with the same physical properties ($M_\star$ and SFR);

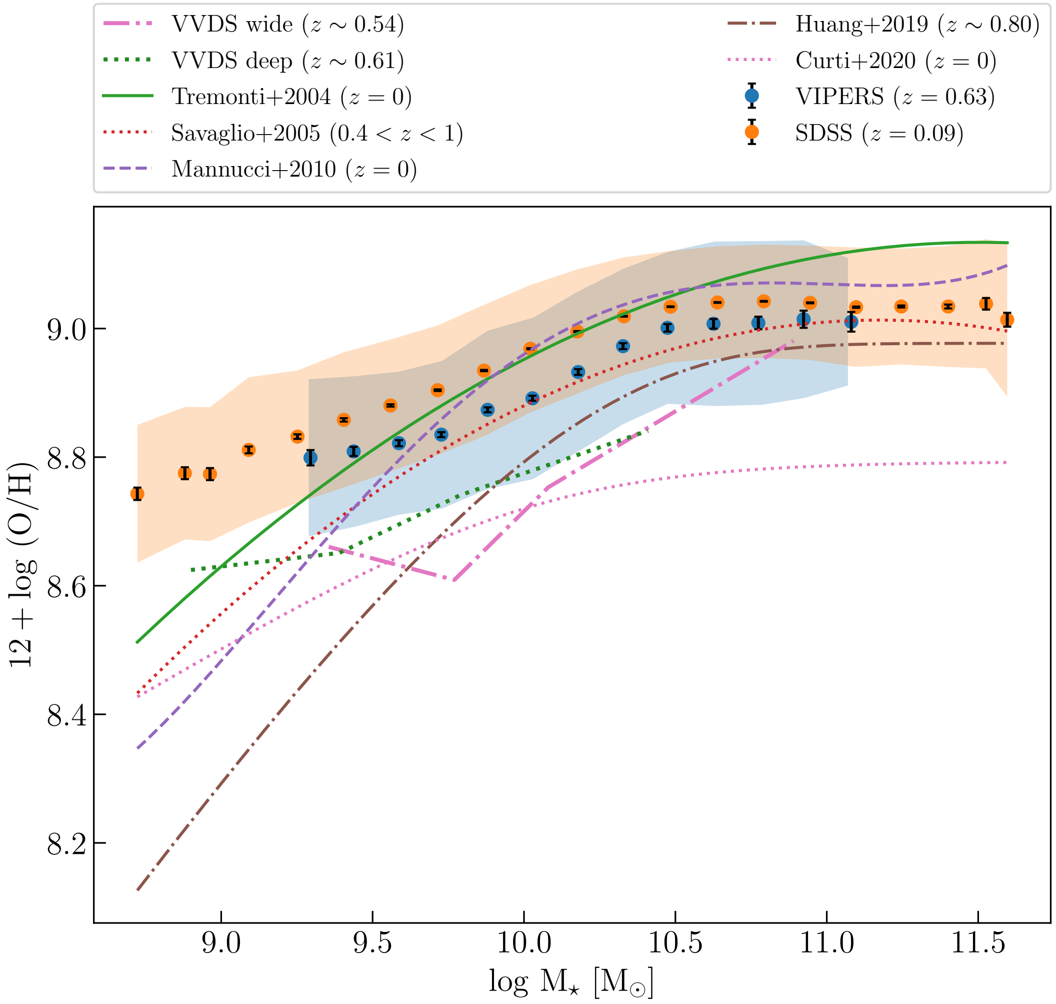

Figure 5.10: Comparison of the MZR for the VIPERS (blue dots), the SDSS (orange dots), VVDS wide (dash-dotted pink line), and VVDS deep (dotted forest-green line) samples together with the fit functions in the literature. The shaded areas show the $1\sigma_{\text{dist}}$ while the black errorbars show the $1\sigma_{\text{med}}$ for the metallicity. The median redshifts are reported for the samples.

ii) with respect to the sSFR value from the fit of the MS allowing us to compare galaxies with the same relative distance from the MS at different redshift.

This last method allows us to study the processes that move galaxies around the MS producing the intrinsic scatter of the MS itself via enhancement of the SFR or starvation of the galaxy. We find that:

i) parametric method has the problem of inferring information about the FMR surface from the study of its median projections. In fact, these are expected to evolve compared to the whole surface. Moreover, in other to compare samples with specific properties, it is necessary to cross-match the specific properties.

ii) non-parametric method has the advantage to be mostly independent of bias. Changing the normalization, this method allows us to compare galaxies with the same physical properties ($M_{\star}$ and SFR) or galaxies with the same relative distance from the MS between low and intermediate redshift.

Advantages: The non-parametric method is simpler to use than the various projections having the advantage of straightly comparing galaxies with similar physical properties or relative distance from the MS without the necessity to cross-match the catalogs. They are also independent of the biases that could be introduced by observation and data selection. The non-parametric method, using the normalization from the MS, gives also information about the processes which lead to a drop or an enhancement of the SFR.

Disadvantages: The parametric method needs to be taken with high caution as it can be affected by biases introduced by observation and data selection as the FMR projections are sensitive to these kinds of biases, (combining the $M_\star$ and SFR reduces the effects due to biases). Since the FMR projections are expected to evolve compared to the FMR itself, it can be difficult to deduce information on the whole FMR starting from its projections. To compare specific properties between different samples, it is necessary to cross-match these properties.

5.4.2 Comparison of FMR between different redshifts ranges

Being particularly careful to homogenize the samples at different redshifts, the expected evolution of the MZR (Fig. 5.1, upper left panel) is statistically significant compared with the σ_{med} on metallicity. This evolution is confirmed by the KS-test (Sect. 5.3, Fig. 5.8). The m-control sample follows the same MZR as the p-control sample (Fig. 5.1, upper left panel), from which is derived. This lack of difference between the m-control and p-control samples leads to the conclusion that not having a mass complete sample at small $M_\star$ is a negligible bias in the MZR.

The metallicity difference between SDSS-based and VIPERS samples (Fig. 5.3 and Table 5.1) in $M_\star$-SFR bins does not show any particular variation for different SDSS-based samples but shows a systematic increase with $M_\star$. Since the metallicity difference remains the same for all SDSS-based samples, it proves that the physical properties shape completely the FMR. However, the systematic increase of the metallicity difference with $M_\star$ shows an evolution with redshift.

The study of the slopes in the normalized (by the value expected by the MS) metallicity-sSFR relation (Fig. 5.5) shows an increasing difference between samples at intermediate and low redshift with $M_\star$. The same shift in $M_\star$ was also found by Salim et al., 2015 at $z \sim 2.3$ based on Steidel et al., 2014 from the Keck Baryonic Structure Survey (KBSS).

The study of the slopes in the normalized (by the value expected from the MS) metallicity-sSFR relation (Fig. 5.5) allows us to study the processes that move the galaxies around the MS. Galaxies above the MS ($\delta \log \text{sSFR} > 0$, Fig. 5.6 upper panel) undergo processes enhancing the SFR. From the point of view of gas-inflow, the small dilution (shallower slope) at intermediate redshift suggests an advanced stage of evolution of the infalling gas, with metallicity closer to the ISM. The small metallicity difference between ISM and infalling gas can be explained by assuming a less processed ISM or a more processed infalling gas. The first scenario does not seem to be accurate since the metallicity of galaxies at intermediate redshift is not (statistically significant) different from those at median $z \sim 0.09$. According to the hierarchical model of galaxy formation, the merging rate increases with redshift assuming closer galaxies inside the clusters. This already "metal-rich" gas can be previously expelled into the intracluster medium (ICM), suggesting environmental effects. This also suggests that the assumption of the pristine nature of the infalling gas is not always true.

The difference in metal dilution between the VIPERS and SDSS samples is more prominent at low-$M_\star$, but such an effect is less prominent towards higher $M_\star$. It has been shown that metallicity dilution can be increasingly significant in the case of gaseous mergers (both major and minor, e.g., Ellison et al., 2013). Bustamante et al., 2020 show that mergers cause a large scatter of FMR and the trends continue to the post-merger stage. Similar conclusions were obtained by theoretical studies that utilize idealized hydro simulations (e.g., Bustamante et al., 2018). Although a detailed analysis of galaxy merger impact on estimated FMR is out of the scope of the present paper, the fact that galaxy merging rate rises with redshift (e.g., Ventou et al., 2017) may partly explain the difference between the slopes inferred from VIPERS and SDSS data.

Below the main sequence ($\delta \log \mathrm{sSFR} < 0$, Fig. 5.6 bottom panel), the intermediate redshift sample shows, compared to the low redshift sample, ongoing processes that are diluting more significantly the metals in the whole $M_\star$ range. Again the difference at different redshifts decreases with increasing $M_\star$. In this case, the situation is inverted at low-$M_\star$ with the low redshift sample having weaker dilution of the metals.

On the one hand, it can reflect the dilution-starvation scenario proposed in recent studies (e.g., more recent star formation dilutes metals more efficiently, while suppression of fresh gas leads to enhanced metallicity and lower SFR, Kumari et al., 2021). On the other hand, among the processes that can happen to quench galaxy SFR ($\delta \log \mathrm{sSFR} < 0$) there are the so-called dry merger (Bell et al., 2006; Khochfar et al., 2009). These dry merging events are characterized by a low amount of gas, suggesting the participation of older galaxies already in an advanced stage of evolution, and they occur for massive galaxies ($\log M_\star\,[M_\odot] \geq 10.4$). The reduction in dilution, corresponding to a shallower slope, can be explained by dry merging events. From the point of view of outflows instead, a more negative slope at small $M_\star$ suggests a higher efficiency in removing the metals from the ISM with the main production of metals in the bulge of the galaxy or a bigger amount of gas expelled from the galaxy itself (starvation).

Our study does not aim at quantifying dust masses of the different samples used, mainly due to the lack of infrared detections for the majority of these galaxies. However, dust content in galaxies plays a major role in the evolution of the ISM, and a driver of the SFR. Higher redshift galaxies tend to have larger dust reservoirs (e.g., Takeuchi et al., 2005; Whitaker et al., 2017). Additionally, galaxies with higher $M_\star$ have larger dust masses (Beeston et al., 2018). Metals can be converted into dust during the complex evolution of the ISM. Therefore, Fig. 5.6 can be seen as a metal depletion process by the current content of dust. In fact, for actively SF galaxies ($\delta \log \mathrm{sSFR} > 0$), the similar depletion efficiency of metals at higher $M_\star$ at different redshifts, can potentially be explained by the supposed larger dust content towards the higher $M_\star$. For lower $M_\star$, metal depletion of VIPERS galaxies is weaker than that of SDSS.

For the less SF galaxies ($\delta \log \mathrm{sSFR} < 0$), the metal depletion efficiency at low redshift is weaker than at higher redshift for the whole range of $M_\star$. The difference is likely to be driven by more efficient dust-to-metal ratio and higher fraction of available cold gas (De Vis et al., 2019). Indeed, very recent studies of dust to metal coevolution in galaxies at intermediate redshifts ($z < 0.7$) found that the conversion of metals to dust can be efficient even in evolved systems with old stellar ages (Donevski et al., 2023). Our finding displayed in Fig. 5.6 qualitatively agrees with this scenario.

All the aforementioned physical aspects of galaxies are responsible for metal depletion at different redshift ranges. Even though dark matter and galaxy environment are responsible for shaping the evolution of galaxies, dust is crucial in the interaction between the ISM components. The metallicity plays an important role in dust content and consequently dust attenuation (Casasola et al., 2022; Hamed et al., 2023b; Pantoni et al., 2021; Shivaei et al., 2020), along with the dependence on the environment (Hamed et al., 2023a, in prep.).

The reduced change between different redshifts at higher $M_\star$ can be explained by the dark matter halo bias. This bias leads to a faster evolution of massive galaxies. For the same reason, the MZR and FMR flatten at high $M_\star$.

5.4.3 Evolution of the MZR and metallicity-SFR relation

Looking for the most comparable and homogeneous measurements of the galaxy properties, we observe a small shift between the low redshift and intermediate redshift samples. This evolution is statistically significant with respect to the $\sigma_{\rm med}$ on metallicity. However, we do not observe any evolution of the scatter around the relation with respect to the $\sigma_{\rm dist}$ from intermediate and low redshift. Once the intermediate sample is divided into two redshift bins, $0.48 < z < 0.65$ and $0.65 < z < 0.80$, the MZR within the redshift bins overlaps entirely with the MZR using the whole sample (Fig. 5.7 upper panel). Once taken into account the mass completeness, the VIPERS mass-complete sub-sample follows the same MZR as the main VIPERS sample. Then, mass completeness is not a relevant bias in the MZR. Instead, the metallicity-SFR relation is slightly more sensitive to both redshift and mass completeness. The differences remain within the $\sigma_{\rm dist}$ in metallicity but not within the $\sigma_{\rm med}$. Also, the KS-tests performed on the distribution of the samples at low and intermediate redshift within $M_\star$, SFR, and $M_\star$-SFR bins confirm the evolution of the MZR and FMR (Sect. 5.3, Fig. 5.8, and Fig. 5.9).

5.5 Conclusion

We check if the so-called unified or fundamental relations, in particular the FMR, stand at different redshifts or under various sample selections and methods of comparison. Our analysis focused on the FMR and its behavior at low (SDSS data, median $z \sim 0.09$) and intermediate redshifts (VIPERS data, median $z \sim 0.63$). We found as main results:

i) the metallicity at median $z \sim 0.63$ is lower at given $M_\star$ and SFR;

ii) the evolution of both the FMR and MZR up to $z \sim 0.8$ is statistically significant;

iii) the KS-test confirms the evolution of both MZR and FMR between low and intermediate redshift;

iv) no evolution of the scatter around the MZR and FMR is observed up to $z \sim 0.8$;

v) the difference in metallicity increases systematically with $M_\star$ when comparing $M_\star$-SFR bins;

vi) reduction of metal dilution of galaxies below the MS ($\delta \log \mathrm{sSFR} < 0$) at high $M_\star$ suggests a non-negligible fraction of dry merging events;

vii) the reduction of metal dilution of galaxies above the MS ($\delta \log \mathrm{sSFR} > 0$) suggests an inflow of metal-rich gas with metallicity close to the ISM at intermediate redshift;

viii) the difference in metal dilution between different redshift decreases with $M_\star$;

ix) the non-parametric method allows for a better comparison of samples at different redshifts to study the evolution (normalizing both samples with respect to the median sSFR value at $z \sim 0$) and specific processes occurring in galaxies along the MS (normalizing each sample with respect to the sSFR predicted by the MS describing each sample).

This study results in the first proof of an evolution of the FMR up to $z \sim 0.63$ with a significance of $\sim 3 \, \langle \sigma_{\mathrm{med}} \rangle_{\mathrm{VIPERS}}$.

CHAPTER 6

Galaxy evolution footprint on the fundamental metallicity relation

To search for footprints left on the FMR (and MZR) by processes that shape them and to search for outliers, we apply machine learning (ML) algorithms independently to the data from the SDSS and the VIMOS Public Extragalactic Redshift Survey (VIPERS). Applying the ML (Sect. 6.1) algorithms independently to both samples, we check if the hypothesis that the FMR is independent of the galaxy's history during its evolution is correct. We perform initially the principal component analysis (PCA) to reduce the dimensionality of the problem, then we look for clusters of galaxies in the space defined by the first two principal components (PC) via the K-means clustering algorithm. In the same space, we look for outliers. Finally, we study the physical properties of the cluster and outliers from the point of view of the FMR itself (Sect. 6.2), different selection diagrams (spectroscopic as BPT, and photometric as color diagrams), and different population properties (D4000n break and overdensity). The original work is presented in F. Pistis et al. (2023b). Galaxy evolution footprint on the fundamental metallicity relation. A machine learning approach. in prep.

6.1 Machine learning approach

ML algorithms are useful to find hidden structures in the data. Especially unsupervised algorithms, which take a set of data only as input, are used to group or cluster the data. Since no labels or corrections are given in unsupervised algorithms, these identify common properties (or the lack of them) in the data. Figure 6.1 summarizes out the ML approach used in this work.

ML algorithms can be sensitive to the order of magnitude of the properties used as input. The pre-processing of the data is commonly used for many ML algorithms. Typically this is done by removing the mean and scaling to unit variance. However, one of the goals of the paper is to look for outliers. The outliers can often influence the sample mean/variance in a negative way. In such cases, the median and the interquartile range (IQR; range between the 1st quartile and the 3rd quartile) often give better results. Scaling all the properties to a similar range, we avoid giving higher significance to properties only because of their wider range. We remove the median and scale the data according to the IQR to reduce the significance of the outliers. We center and scale independently each feature by computing the relevant statistics on the samples

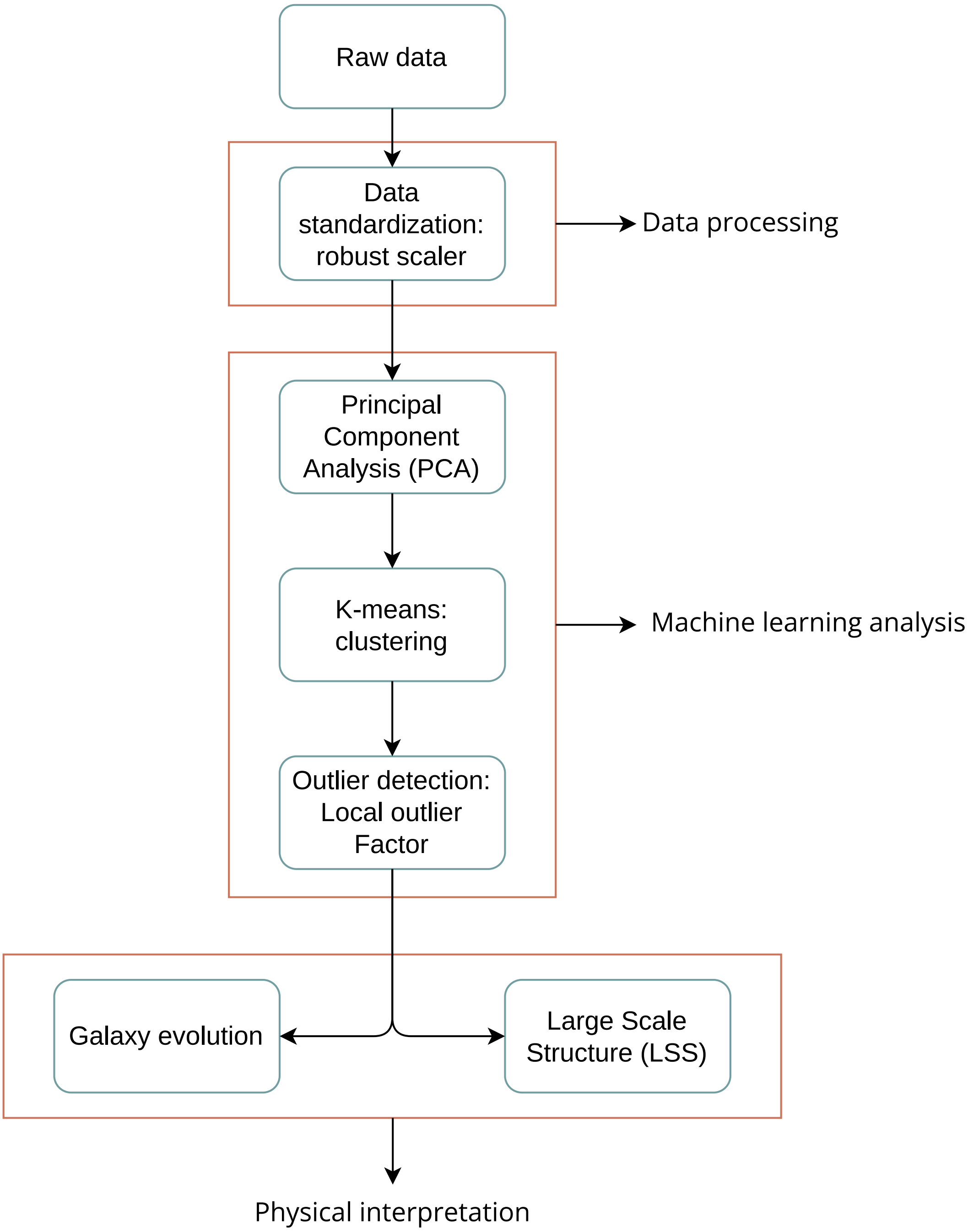

Figure 6.1: Concept map diagram of the analysis steps done via the machine learning approach.

In this work, our ML approach can be divided into three steps. First step: we apply the principal component analysis (PCA) to reduce the dimensionality of the data keeping only the properties with higher variance. Once the data are projected in the PC space, closer data have closer features with respect to data at the same distance in the input space. Second step: in the PC space, we apply the clustering algorithm. In this work, we use k-means clustering to divide the data into k clusters minimizing the distance of data within the clusters. Third step: in the PC space, we apply the algorithm for searching the outliers. In this work, we use the Local Outlier Factor (LOF). The LOF finds odd data points by measuring the local deviation of a

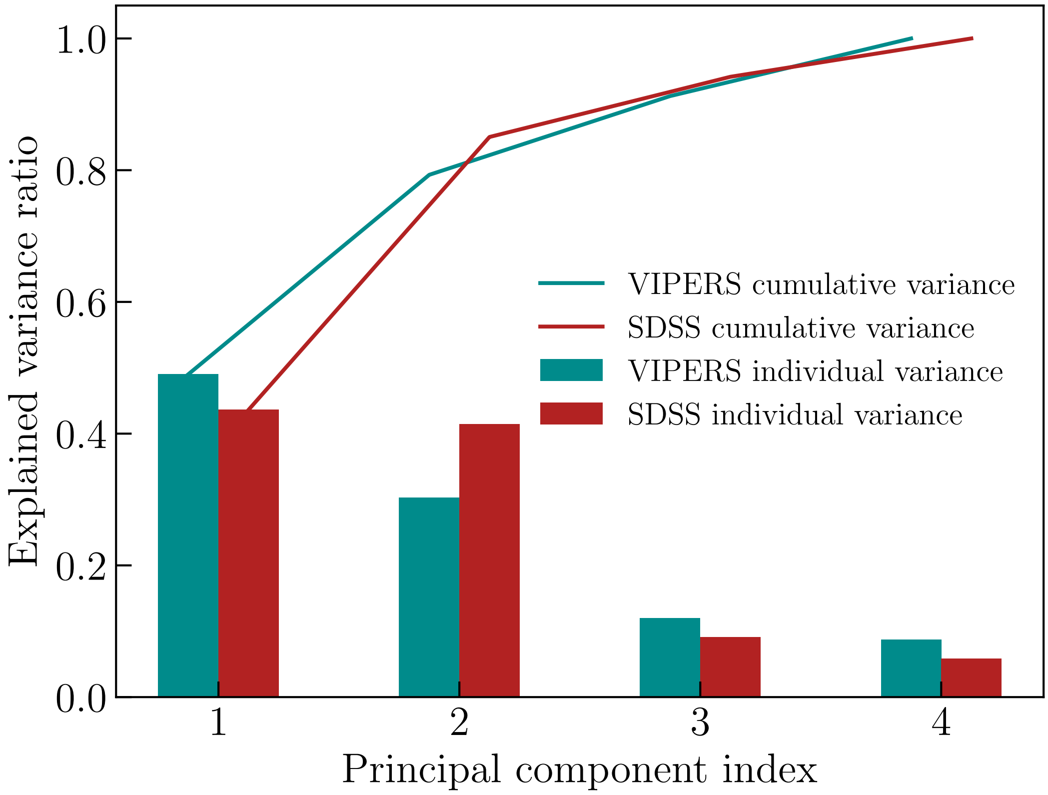

Figure 6.2: Histogram of the explained variance for each PC and cumulative variance (solid lines) for SDSS (red) and VIPERS (blue) samples.

given data point with respect to its neighbors.

6.1.1 Principal component analysis

The PCA let us reduce the dimensionality of the problem by finding the axes with the highest value of variance and projecting the data on these new axes. The method consists of the diagonalization of the covariance matrix. The eigenvalues give the explained variance of each component, while the eigenvectors give the direction of the new axes. By projecting the data on the new axes defined by the PCs, it is possible to reduce the dimensionality of the problem without losing the variance of the data. We perform the PCA on the data composed by the following features: $M_\star$, redshift, the flux of the emission lines (Hβ, [O III] λ5007, [O III] λ4959, and [O II] λ3727), SFR, sSFR, and metallicity.

Figure 6.2 shows the histogram of the explained variance for each PC and the cumulative variance for both samples. Four PCs are enough to reach a threshold of variance $> 95\%$ of the data. Table 6.1 reports in detail the fraction of variance in each PC. Figure 6.3 reports the direction between each feature and the PCs. From the correlation between features and PCs, the flux of the emission lines turn out to be redundant. Figure 6.4 shows the data projected onto the first and second PCs.

6.1.2 K-means clustering

The second step is to look for clusters of galaxies with similar properties. We perform a K-means clustering algorithm. This is an interactive algorithm where a certain

Table 6.1: Fraction of variance in each PC for SDSS and VIPERS samples.

PCA index	SDSS (%)	VIPERS (%)
1	43.6	49.0
2	41.4	30.2
3	9.14	12.0
4	5.81	8.75
Total	99.95	99.95

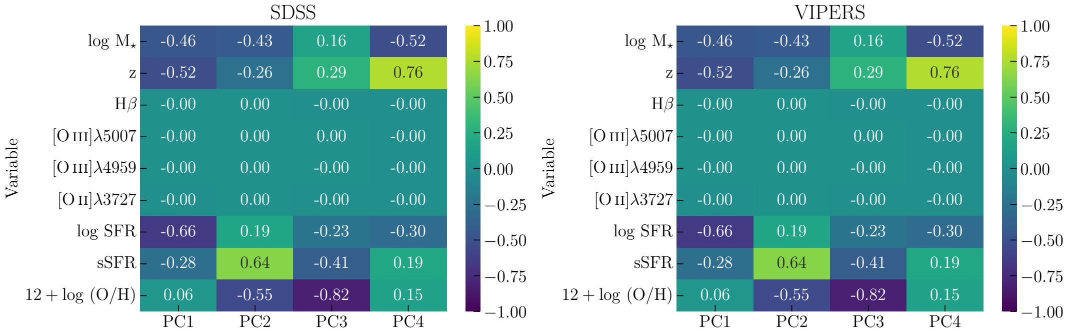

SDSS

Variable	PC1	PC2	PC3	PC4
log $M_\star$	-0.46	-0.43	0.16	-0.52
z	-0.52	-0.26	0.29	0.76
Hβ	-0.00	0.00	-0.00	-0.00
[O III]λ5007	-0.00	0.00	0.00	-0.00
[O III]λ4959	-0.00	0.00	-0.00	-0.00
[O II]λ3727	-0.00	0.00	-0.00	-0.00
log SFR	-0.66	0.19	-0.23	-0.30
sSFR	-0.28	0.64	-0.41	0.19
$12 + \log$ (O/H)	0.06	-0.55	-0.82	0.15

VIPERS

Variable	PC1	PC2	PC3	PC4
log $M_\star$	-0.46	-0.43	0.16	-0.52
z	-0.52	-0.26	0.29	0.76
Hβ	-0.00	0.00	-0.00	-0.00
[O III]λ5007	-0.00	0.00	0.00	-0.00
[O III]λ4959	-0.00	0.00	-0.00	-0.00
[O II]λ3727	-0.00	0.00	-0.00	-0.00
log SFR	-0.66	0.19	-0.23	-0.30
sSFR	-0.28	0.64	-0.41	0.19
$12 + \log$ (O/H)	0.06	-0.55	-0.82	0.15

Figure 6.3: Direction between each feature and the PCs for SDSS (left) and VIPERS (right) samples. The directions are color-coded according to the correlation between the feature and PC.

number of centers are initially chosen randomly. Then, each point is labeled according to its distance to the centers. Once all points are labeled, the new centers are estimated at each step until convergence is reached.

To choose the number of clusters K, we calculate the WCSS (Within-Cluster Sum of Square) as a function of the number of clusters. The WCSS is the sum of squared distances between each point and the center of the cluster. For $k = 1$ the WCSS has its maximum value, then it starts to decrease rapidly. At a certain value of k, the WCSS starts to be more or less constant, reaching the zero value when k is equal to the number of points. The plot of the WCSS in the function of the cluster number has an elbow shape. The k where the WCSS starts to flatten is the maximum number of clusters that minimize the distance of points in each group. Figure 6.5 shows the elbow plot for both samples when the K-means algorithm is performed on the data projected on the first two PCs. We choose to look for five clusters in both cases. Figure 6.4 shows the five clusters in the PC space. Table 6.2 summarize the number of galaxies (and fraction with respect to the whole sample) in each cluster. We choose the number of clusters in order to reduce the value of the WCSS without introducing sub-classes with minimal differences.

6.1.3 Local Outlier Factor

To look for outliers, we applied the LOF algorithm. The algorithm consists into give a score (LOF) that measures the local density deviation of a given data point with respect to its neighbors. The idea of the algorithm is to detect the points with a substantially lower density than their neighbors.

The LOF score of a data point is equal to the ratio of the average local density of his n-nearest neighbors, and its own local density. A normal sample has a local

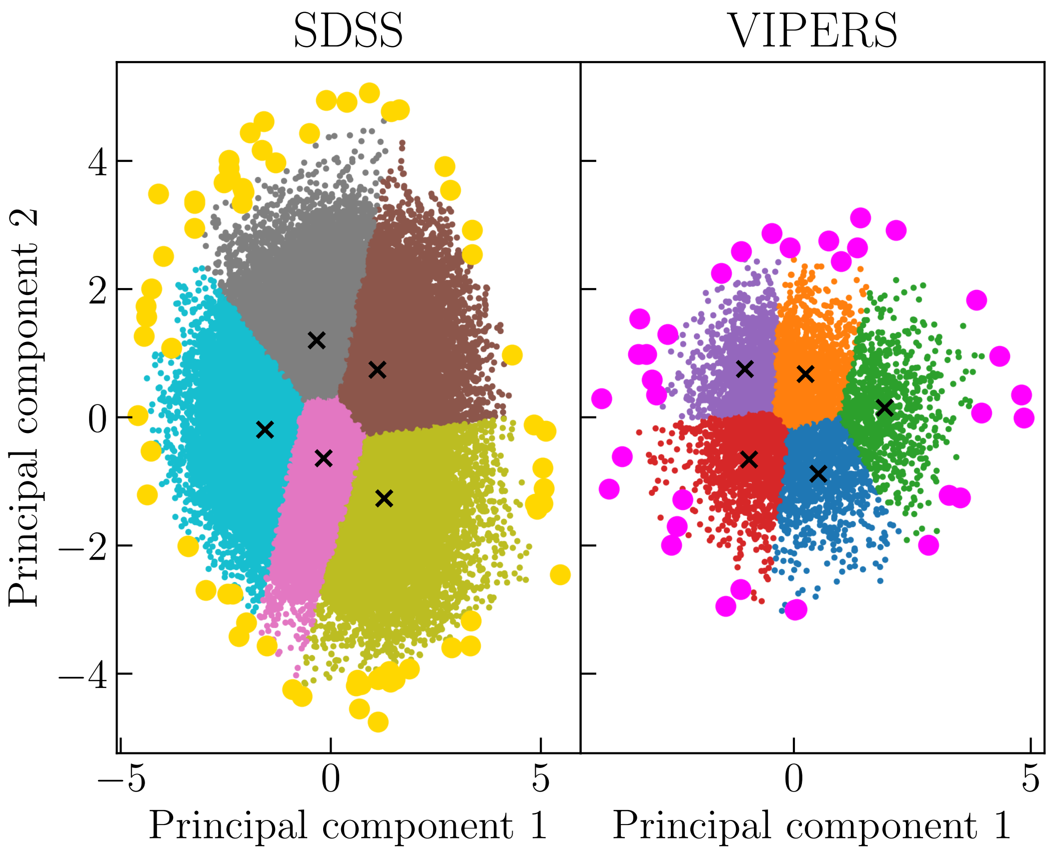

Figure 6.4: Clusters and outliers in the space defined by first and second PCs for SDSS (left panel) and VIPERS (sample). Different clusters correspond to different colors. The black crosses show the center of each cluster. The outliers are plotted in green for the SDSS sample and in magenta for the VIPERS sample.

density similar to that of its neighbors, while outliers have a much smaller local density. The LOF algorithm takes into account both the local and global properties of samples.

Using a number of neighbors $n = 20$ and performing the algorithm on the whole sample in the space of first and second PCs, we find 41 outliers in the VIPERS sample (8.6‰ of the full sample) and 62 in SDSS sample (0.4‰). Figure 6.4 shows the outliers for both SDSS and VIPERS samples in the PC space. All the outliers are distributed in a circle around the normal samples. We then proceed to understand the physical meaning of these clusters and outliers.

6.1.4 Representation of the clusters and fundamental metallicity relation

For better visualization, while studying the physical meaning of the cluster (Sect.6.2), we represent each cluster centered at its median values of the properties reported on each axis, the error bars correspond to the IQR, and by an ellipse whose semi-axes correspond to the normalized median absolute deviation (NMAD, Hoaglin et al., 1983) defined as:

$$\mathrm{NMAD} = 1.4826 \cdot \mathrm{median}\left(\left|P - \mathrm{median}\left(P\right)\right|\right) \tag{6.1}$$

where P corresponds to the properties reported on each axis.

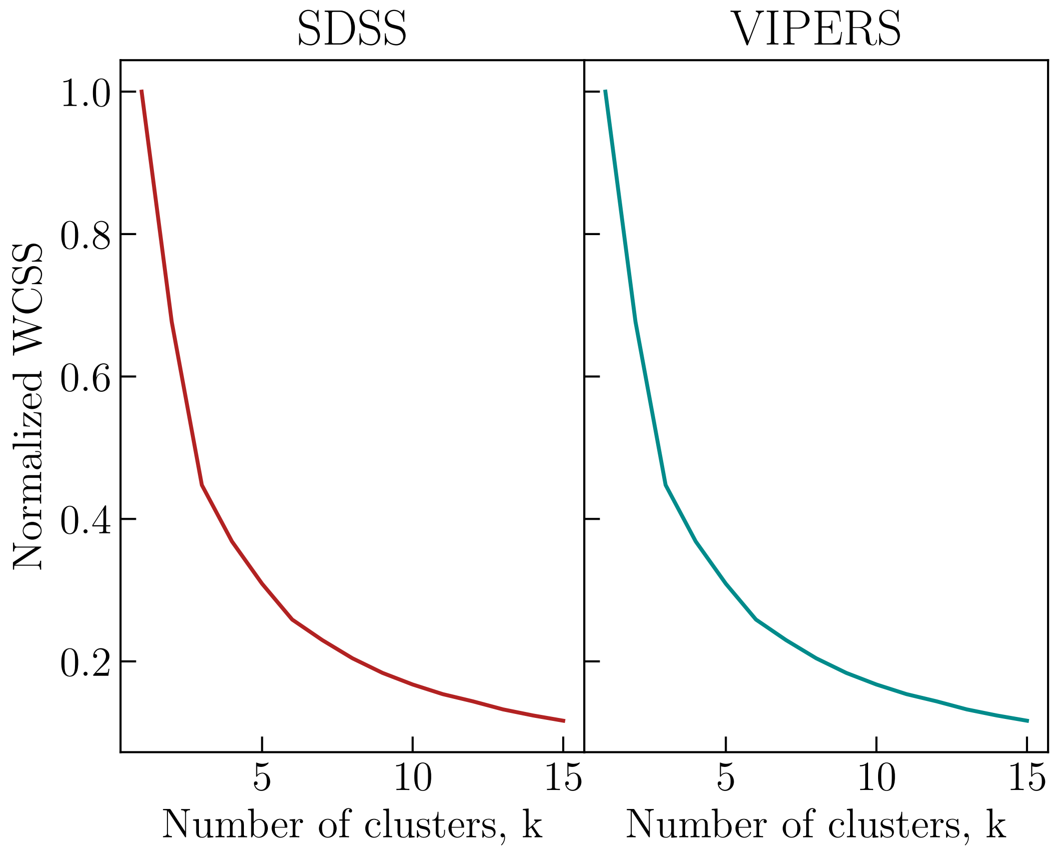

Figure 6.5: Normalized WCSS as a function of the number of clusters k, for SDSS (left in red) and VIPERS (right in blue).

Table 6.2: Number of galaxies in each cluster.

	VIPERS		SDSS	
Label	Color	# galaxies	Color	# galaxies
0	Blue	1 197 (19%)	Brown	46 082 (30%)
1	Orange	1 455 (23%)	Pink	31 232 (20%)
2	Green	868 (14%)	Gray	31 034 (20%)
3	Red	1 470 (24%)	Olive	27 473 (18%)
4	Purple	1 213 (20%)	Cyan	20 195 (13%)
Outliers	Magenta	33 (5.3‰)	Gold	62 (0.4‰)

We study the FMR (Sect. 6.2.2) by its projection in the non-parametric framework defined by Salim et al., 2014, 2015 and used on the same data by Pistis et al., 2022. This method allows us to study the relation between the normalized sSFR and the metallicity. The original method (Salim et al., 2014, 2015) defines the normalized sSFR as

$$\Delta \log \mathrm{sSFR} = \log \mathrm{sSFR} - \langle \log \mathrm{sSFR} \rangle \,, \tag{6.2}$$

where $\langle \log \mathrm{sSFR} \rangle$ is the average or median sSFR in the mass bin of the sample at low-z, for both samples. We also divide the sample into four $M_\star$ bins centered at $\log M_\star\,[M_\odot] = 9.5$, 10.0, 10.5, and 11.0 with bin width equal to 0.5 dex. We also check different projections of the FMR, such as star-forming main sequence, MZR, and metallicity-SFR relation.

6.2 Physical interpretation of the clusters and outliers

To understand the physical meaning of the clusters, we check their distribution in various feature spaces. The first step is to check if the algorithm is simply clustering galaxies in luminosity/redshift samples (Sect. 6.2.1). The second step is to check if the clusters are meaningful from the point of view of the FMR (Sect. 6.2.2). Then we check if the clusters are meaningful in the BPT diagram (different excitation states of the ISM, Sect. 6.2.3), in color diagrams (NUVrK and UVJ, different populations with different star-formation activity, Sect. 6.2.4), and their relationship with the D4000n break (Sect. 6.2.5) and overdensity (Sect. 6.2.6).

6.2.1 Redshift and luminosity dependence

To check if the clusters depend on luminosity we look, first, for a correlation between $M_\star$, SFR, sSFR, and the cluster label exists at the same time. We use $M_\star$ and SFR as probes for luminosity. This choice has the advantage to use properties that are not independent but are linked to each other by the MS relation. For this reason, if a correlation between clusters and luminosity exists, it has to be present for all the properties at the same time.

Figure 6.6 shows the median $M_\star$, SFR, and sSFR as a function of the cluster labels for both SDSS and VIPERS samples. The possible correlation between the physical properties and cluster label depends extremely on the order of the labels. If the correlation is truly physical, the correlation has to exist simultaneously between both the $M_\star$ and the SFR/sSFR with the cluster labels because of the non-independence of the physical properties. From this plot, if we force the correlation between a physical property ($M_\star$ or SFR/sSFR) and the cluster labels, we break the correlation on the other property (SFR/sSFR or $M_\star$) at the same time. The behavior of the correlation is valid for both samples.

Figure 6.7 shows the $M_\star$, SFR, sSFR, and i-mag as a function of the redshift. However, the clusters do not split in the same way for the four physical properties of both samples. Since these four properties depend on each other, these plots (Fig. 6.6 and Fig. 6.7) prove that the clusters do not represent different classes of luminosity/redshift.

6.2.2 Fundamental metallicity relation

We now check the meaning of the clusters from the point of view of the FMR. Looking at the MS (Fig. 6.8 we find that the clusters are quite separated in this plane, with the outliers lying mainly around the bulk of the galaxies, beyond the 3σ level of the whole distribution of the data samples in the plane. The clusters are mainly distributed inside the 1σ level of the distribution. Also, the MZR and metallicity-SFR relation (Fig. 6.9) show quite well-separated clusters. Here some of the outliers are mixed with the bulk of galaxies.

From the point of view of the MS, the outliers can be divided into smaller groups (Fig. 6.10). The first selection is according to their EW ratios ([O III] $\lambda5007/\mathrm{H}\beta$) dividing the outliers in broad (EW ratio > 1) and narrow (EW ratio ≤ 1). Figure 6.10 shows the distribution of broad and narrow line outliers in the three FMR projections. In all of the projections, the two populations are well separated in two separated areas of the plane.

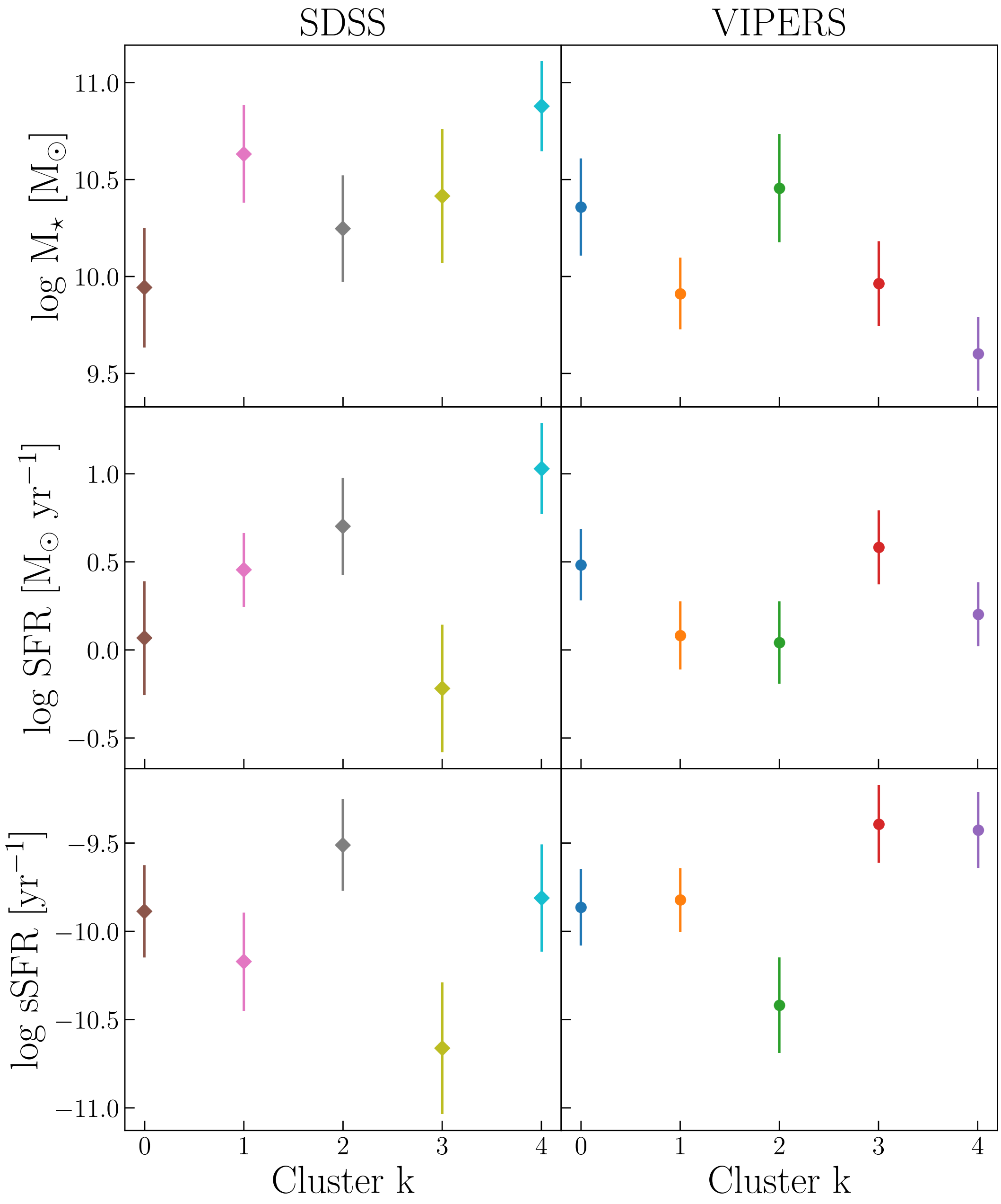

Figure 6.6: Median $M_\star$ (upper row), SFR (mid row), and sSFR (bottom row) as a function of the cluster label for SDSS (left column) and VIPERS (right column) samples. The error bars correspond to the difference between the 84th and 16th percentile. The points are color-coded according to the cluster label.

We then proceed to divide visually the outliers into smaller groups according to their position in the MS. The same groups remain separated also in the MZR and in the metallicity-SFR relation. Figure 6.11 shows the distribution in sSFR for VIPERS samples, outliers, and the different sub-groups of outliers. Assuming a value of $\log \mathrm{sSFR}\left[\mathrm{yr}^{-1}\right] = -10.5$ to divide passive (lower values) and SF galaxies (higher values), the outliers group can be classified as: i) two groups of passive galaxies with narrow lines, ii) two groups of star-burst galaxies with broad lines, and iii) two groups of normal SF galaxies (one group of galaxies with broad and one with narrow lines).

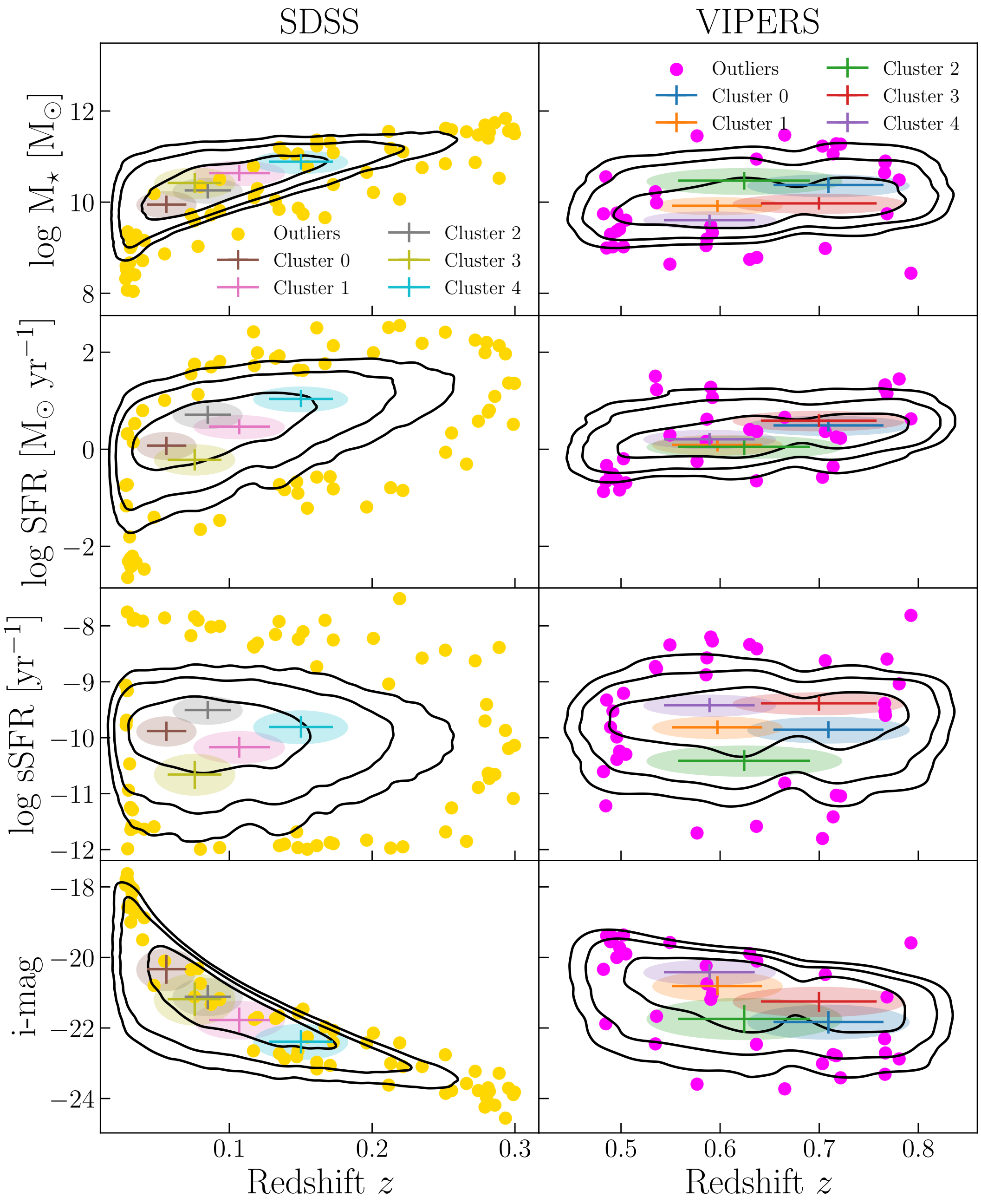

Figure 6.7: M$_\star$ (upper row), SFR (mid row), and i-mag (bottom row) as a function of the redshift for SDSS (left column) and VIPERS (right column) samples. The points are color-coded according to the cluster label. The outliers are plotted in green for the SDSS sample and in magenta for the VIPERS sample. The black contours show the 1, 2, and 3 σ levels of the distributions.

Figure 6.12 shows the stacked spectra by groups of the outliers defined in the VIPERS sample. As expected, groups 3 and 4, resulting in the groups with lower sSFR, have a higher value of the average D4000n break. At the same time, the groups 1, 6, and 7, resulting in the groups with higher sSFR, shows the strongest emission lines.

Looking at the whole FMR (Fig. 6.13), the clusters lie in well-defined places of the relation. In the FMR, some clusters lie beyond the 1σ level of the distribution

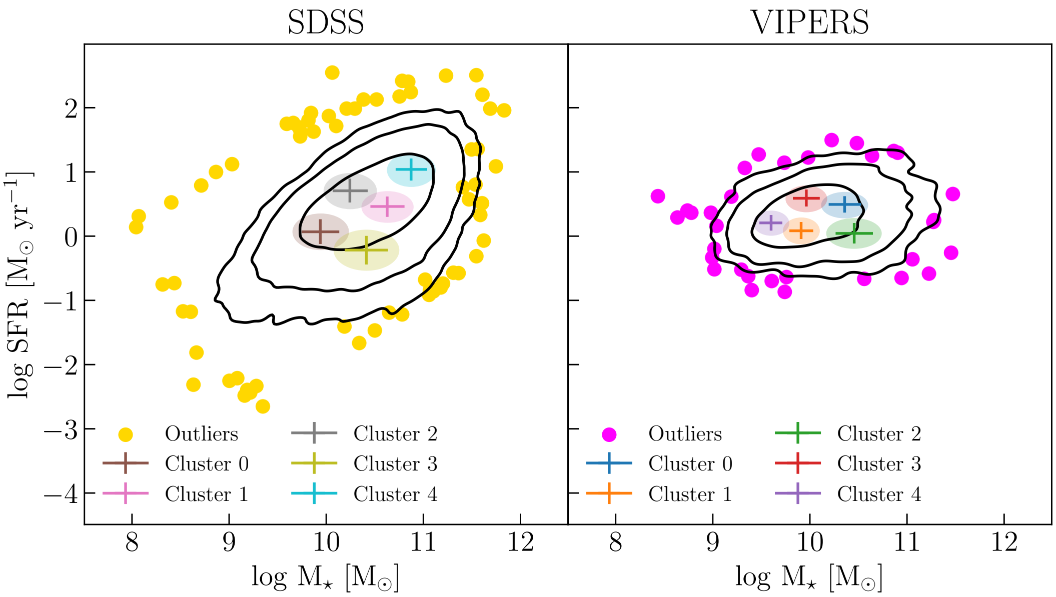

Figure 6.8: Main sequence of SDSS (left) and VIPERS (right) samples. The points are color-coded according to the cluster label. The error bars correspond to the IQR and the two semiaxes of the ellipses correspond to the NMAD. The outliers are plotted in gold for the SDSS sample and in magenta for the VIPERS sample. The black contours show the 1, 2, and 3 σ levels of the distributions.

of the whole data sample. The outliers are mainly high-metallicity–low-ΔsSFR or low-metallicity–high-ΔsSFR for the mass bins studied.

From the FMR point of view, the outliers can be visually divided into two groups. We divide outliers according to their $\Delta \log \mathrm{sSFR}$ (threshold at $\Delta \log \mathrm{sSFR} = 0$). Then, we check the typical spectra of these two groups in each $M_\star$-bin. Figure 6.14 shows the stacked spectra in each $M_\star$-bin for both groups. Outliers at $\Delta \log \mathrm{sSFR} > 0$ have much stronger emission lines (with respect to outliers at $\Delta \log \mathrm{sSFR} < 0$) because of the highest excitation due to the higher SFR.

6.2.3 Ionization state

The BPT diagrams aim to separate SF galaxies from other types of sources via the ionization state of the ISM within galaxies measured from spectral features. Figure 6.15 shows the distributions of the clusters. The clusters lay in different areas between SDSS and VIPERS samples. For the SDSS sample, the clusters lay at $\log([\mathrm{O\,II}]\,\lambda3727/\mathrm{H}\beta) \geq 0.5$ and $\log([\mathrm{O\,III}]\,\lambda5007/\mathrm{H}\beta) \sim -0.5$, while for the VIPERS sample, the clusters lay at $0.0 \leq \log([\mathrm{O\,II}]\,\lambda3727/\mathrm{H}\beta) \leq 0.5$ and $\log([\mathrm{O\,III}]\,\lambda5007/\mathrm{H}\beta) \geq -0.5$ showing a bigger area of the spread between each other. SDSS clusters are also concentrated in the 1σ level of the distribution of the whole data sample.

6.2.4 Stellar population

Color diagrams aim to separate red galaxies, assumed as quiescent and containing old stellar population, from blue galaxies, assumed as SF and containing young stellar population. The population boundaries are usually determined visually by occupying the color diagram space and observing the red and blue galaxy clusters.

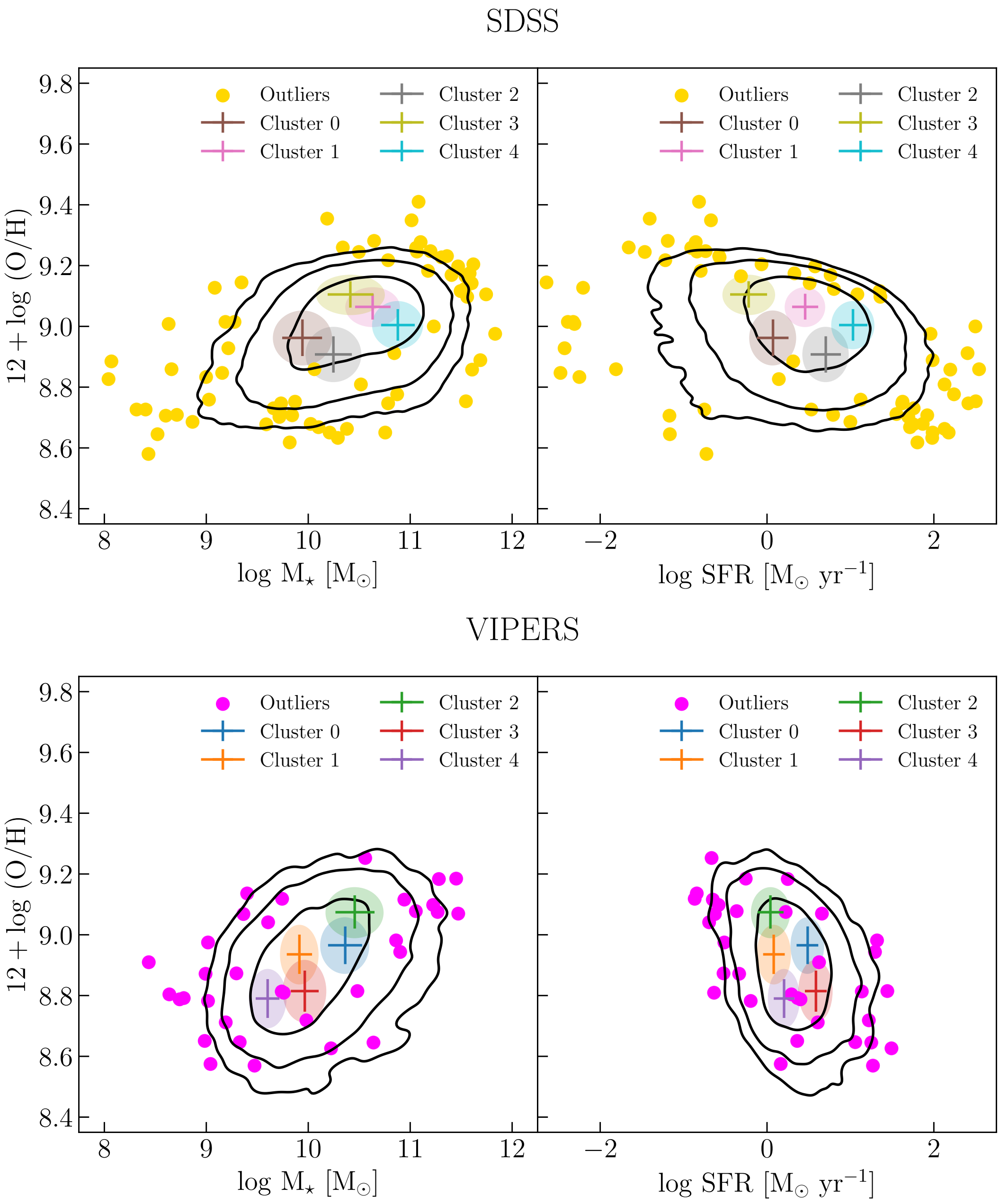

Figure 6.9: MZR (left) and metallicity versus SFR (right) for SDSS (upper) and VIPERS (bottom) samples. The points are color-coded according to the cluster label. The error bars correspond to the IQR and the two semiaxes of the ellipses correspond to the NMAD. The outliers are plotted in gold for the SDSS sample and in magenta for the VIPERS sample. The black contours show the 1, 2, and 3 σ levels of the distributions.

The separation line is drawn to split the two populations of galaxies. Different diagrams are all based on this same logic.

The first color diagram analyzed exploits the NUV, r, and K photometric bands

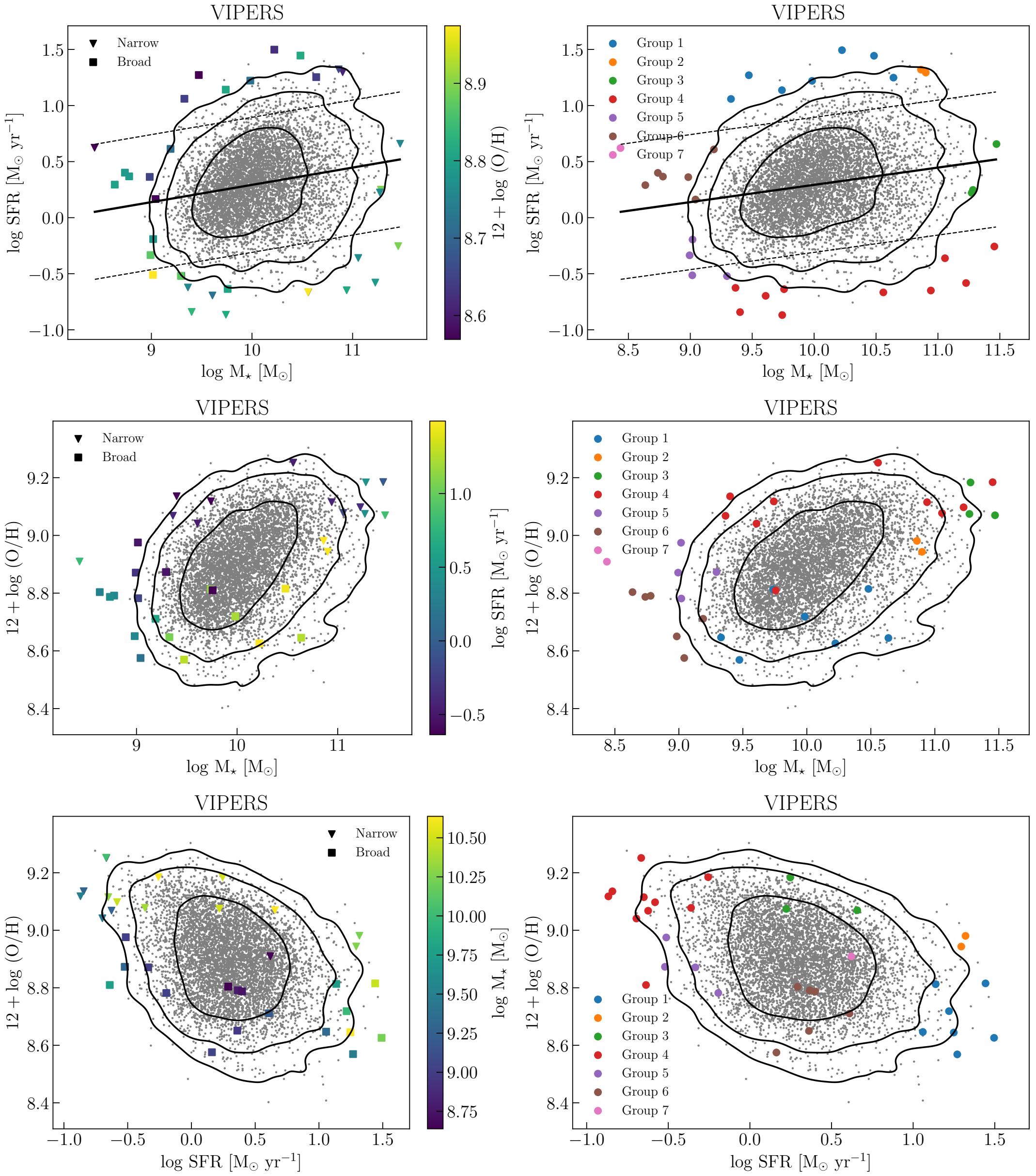

Figure 6.10: Scatter of VIPERS sample (grey dots) in the different projections of the FMR (top: MS, mid: MZR, bottom: metallicity-SFR relation). The outliers are divided into broad (square) or narrow (triangle) lines and color-coded according to the third property of the FMR (left column) or according to visual groups (right column). In the MS, we report the MS (solid line) fit from Pistis et al., 2022 and the range ±4 × MS (dashed line).

(NUVrK, Fig. 6.16; Davidzon et al., 2016) to separate the red-old galaxies from blue-young galaxies. The selection criteria are defined as

$$\begin{aligned} (\mathrm{NUV}-\mathrm{r}) &< 1.37\,(\mathrm{r}-\mathrm{K}) + 2.6 \text{ or,} \\ (\mathrm{NUV}-\mathrm{r}) &< 3.15 \text{ or,} \\ (\mathrm{r}-\mathrm{K}) &> 1.3. \end{aligned} \tag{6.3}$$

Regarding the SDSS sample, the clusters are more concentrated, not showing a defined separation, compared to the VIPERS sample. For the VIPERS, the clusters are

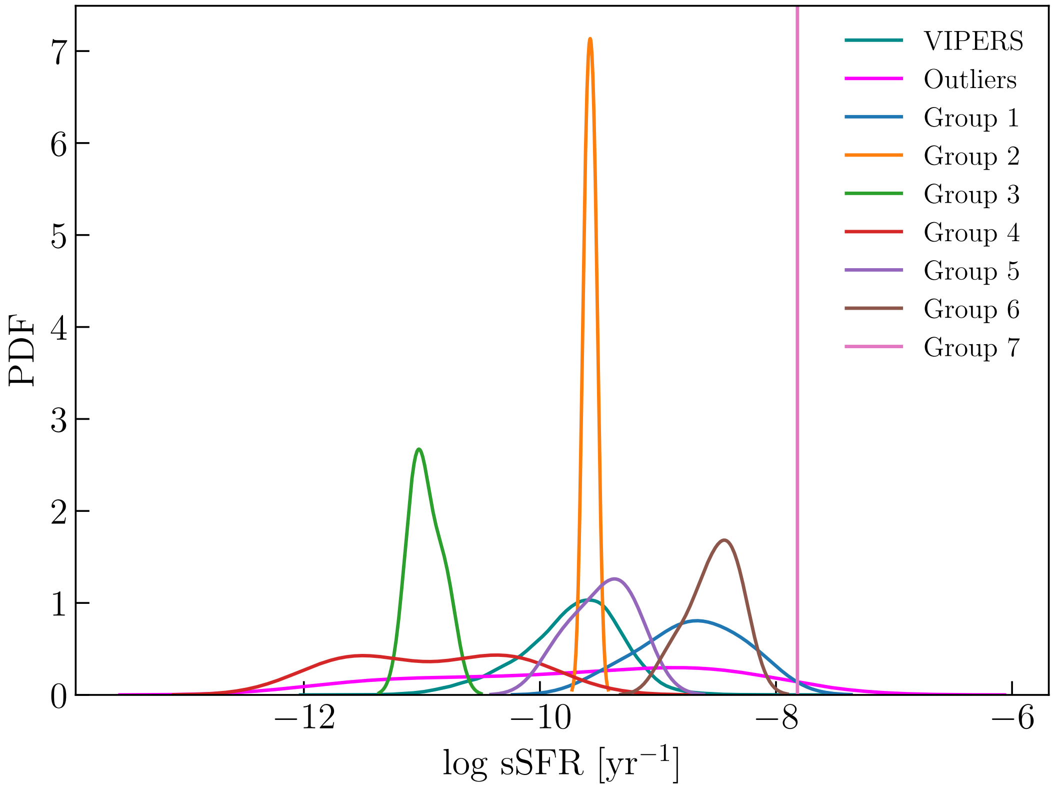

Figure 6.11: Kernel density estimation (KDE) of the sSFR distribution of the VIPERS sample (blue), the outliers (magenta), and the sub-groups of outliers.

distributed along a line, more or less following the classes 5–9 defined in Siudek et al., 2018. The outliers are mainly distributed along the whole distribution of the clusters.

The second color diagram analyzed exploits the U, V, and J photometric bands (UVJ, Fig. 6.17; Whitaker et al., 2011) to separate again red-old galaxies from blue-young galaxies. The selection criteria are defined as

$$\begin{aligned} (U - V) &< 0.88 \times (V - J) + 0.59 \text{ or}, \\ (U - V) &< 1.30 \text{ or}, \\ (V - J) &> 1.60. \end{aligned} \tag{6.4}$$

Also in this diagram (Fig. 6.17), like the NUVrK diagram, the clusters are more separated for the VIPERS sample laying along a line, corresponding to the classes 6–9 defined by Siudek et al., 2018, while for the SDSS sample, the clusters are concentrated in a smaller area. Again, the outliers are distributed along the whole distribution of the clusters for both samples.

6.2.5 Age of the stellar population

Another way to divide galaxies according to the age of their stellar population is the use of the D4000n break, with the young stellar population having D4000n $<$ 1.5 and old stellar population having D4000n $>$ 1.5 (Haines et al., 2017; Kauffmann et al., 2003a; Vergani et al., 2008). Figure 6.18 shows how the different clusters are

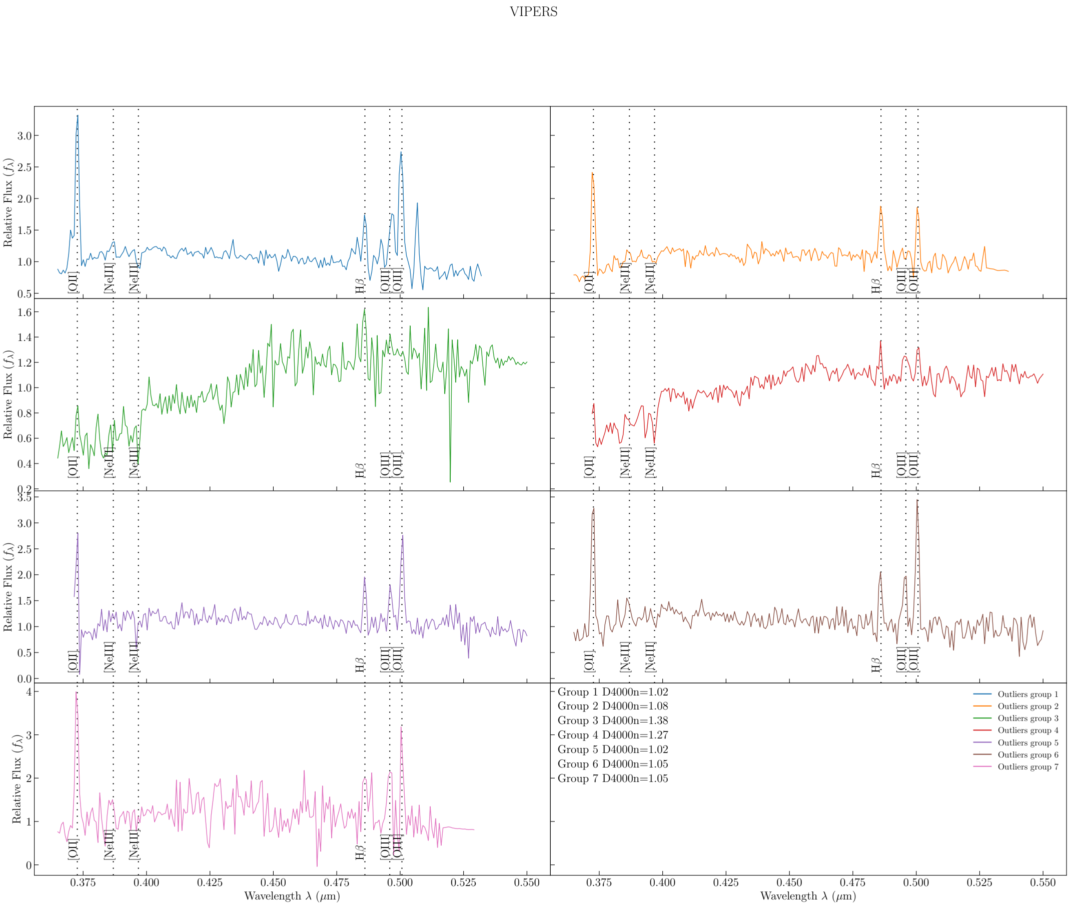

Figure 6.12: Average spectra of the outliers in VIPERS spectra divided into groups. In the last panel is reported the average D400n break value.

distributed in the FMR. In the same figure, we report the hexbin histogram color-coded according to the median D4000n break value. Here, we found a correlation between the clusters and D4000n break.

6.2.6 Large scale structure and environment

Peng et al. (2014b) observed a strong dependency between the metallicity and the local density for SF satellite galaxies, while no correlation is observed for SF central galaxies. In the same study, the strong correlation for Sf satellites is related to a progressive metal-enriched inflow in over-dense regions. Peng et al. (2014b) also observed that the SFR distribution at a given stellar mass does not depend either on the local density or the division between central/satellite galaxies. These two aspects together lead the authors to the hypothesis that the FMR of SF central galaxies would be independent of the environment, while the dependence on the environment of the FMR of satellite galaxies would be driven by the dependence of the metallicity on the environment.

Figure 6.19 shows how the different clusters are distributed in the FMR for the VIPERS sample. In the same figure, we report the hexbin histogram color-coded according to the median overdensity value. In this case, contrary to the case of the D4000n break (Fig. 6.18), there is no strong correlation between the clusters and the overdensity on average.

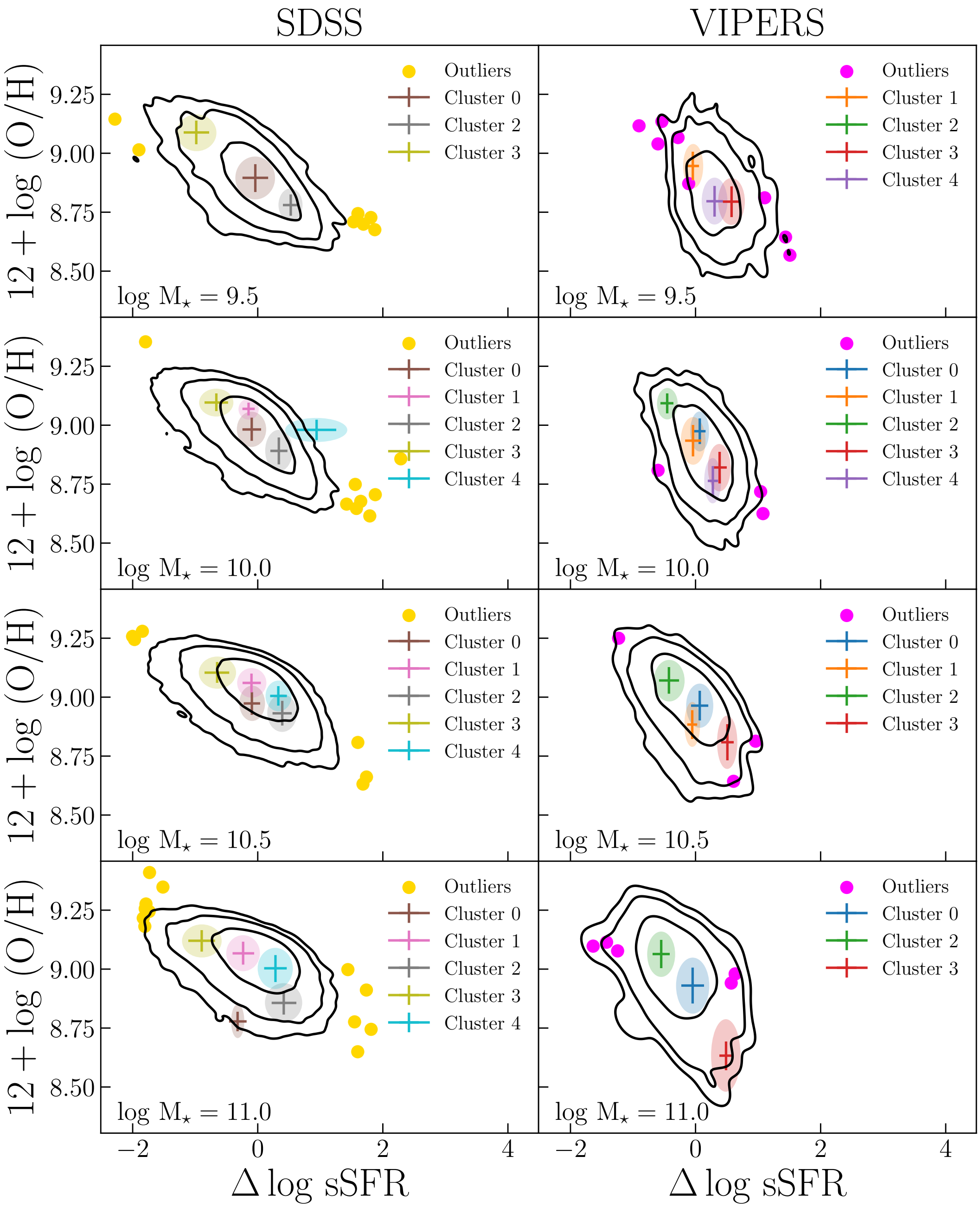

Figure 6.13: FMR in the non-parametric framework (Salim et al., 2014, 2015) for SDSS (left) and VIPERS (right) samples. The points are color-coded according to the cluster label. The error bars correspond to the IQR and the two semiaxes of the ellipses correspond to the NMAD. The outliers are plotted in gold for the SDSS sample and in magenta for the VIPERS sample. The black contours show the 1, 2, and 3 σ levels of the distributions.

In order to avoid effects due to the overdensity dependence on the $M_\star$, we define, for each outlier,

$$\overline{\rho} = \log\left(\frac{\rho - \langle\rho\left(\mathrm{M}_*\right)\rangle}{\langle\rho\left(\mathrm{M}_*\right)\rangle}\right) \tag{6.5}$$

where $\langle\rho\left(\mathrm{M}_*\right)\rangle$ is the average overdensity in a $M_\star$ bin of width 0.15 dex of the SF galaxies subsample. Figure 6.20 shows the $\overline{\rho}$ as a function of the mass. The majority

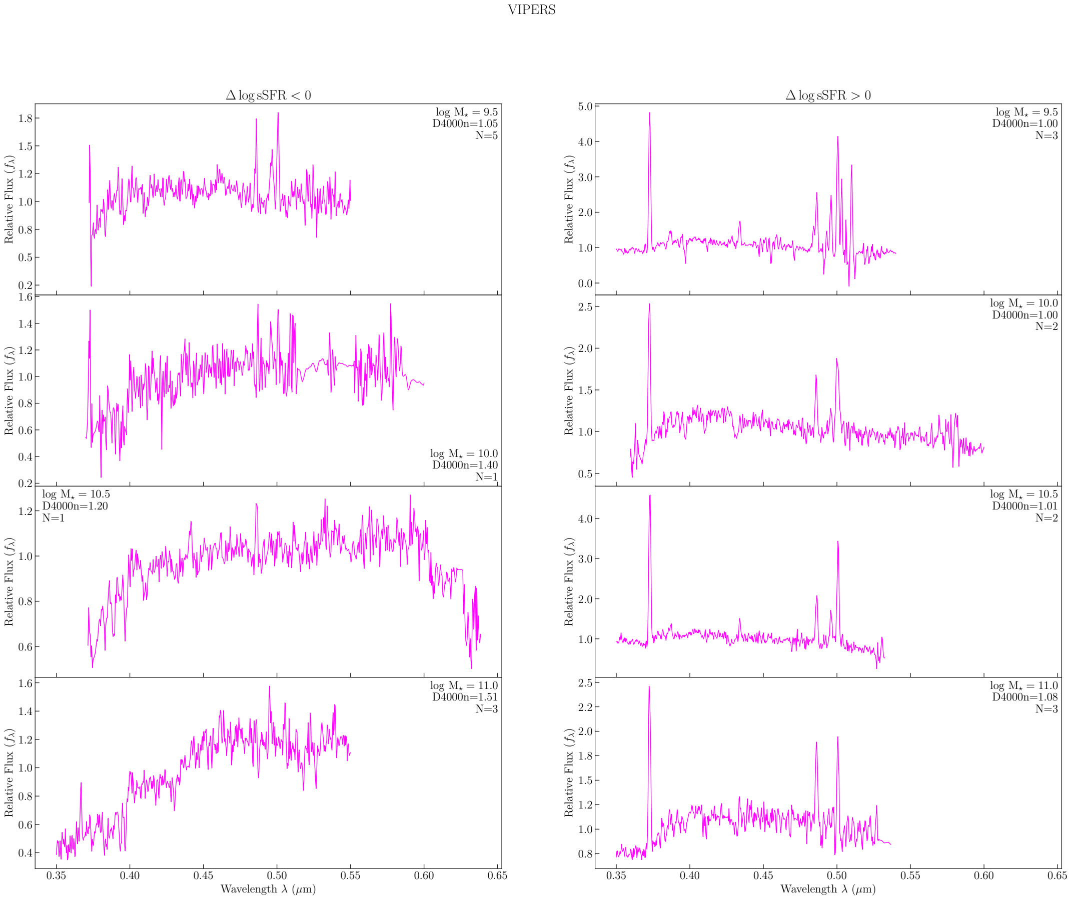

Figure 6.14: Average spectra of the outliers in VIPERS spectra divided into $\Delta \log \mathrm{sSFR} < 0$ and $\Delta \log \mathrm{sSFR} > 0$ for each mass bin. In each panel is reported the number of spectra (N) that are stacked and the average D400n break value.

of outliers, with the exception of two, result to be in an underdense environment with respect to the average in the same $M_\star$ bin. Figure 6.20 also shows the best-fit spectrum of the galaxy with the most underdense environment. The spectrum shows an SF galaxy with strong emission lines having a young stellar population D4000n < 1.5.

6.3 Discussion

Via ML algorithms, we defined 5 clusters for both SDSS and VIPERS samples. At the same time, we found 33 and 62 outliers for VIPERS and SDSS, respectively. The 5 clusters do not show a dependency on the luminosity (Fig. 6.6 and Fig. 6.7) but remain quite well-separated in the FMR (Fig. 6.13) and its projections (Fig. 6.8 and Fig. 6.9). The analysis of the correlation with the ionization state (Sect. 6.2.3), stellar population (Sect. 6.2.4), and environment (Sect. 6.2.6) do not show any strong correlation with the clusters. Only the analysis of the correlation with the age of the stellar population (Sect. 6.2.5) shows a correlation between different areas of the FMR with the average D4000n break value.

The VIPERS outliers can be divided into three populations according to their distributions in sSFR and the EW ratios of [O III] $\lambda 5007/\mathrm{H}\beta$. The resulting populations gather i) two groups of passive galaxies with narrow lines, ii) two groups of star-burst

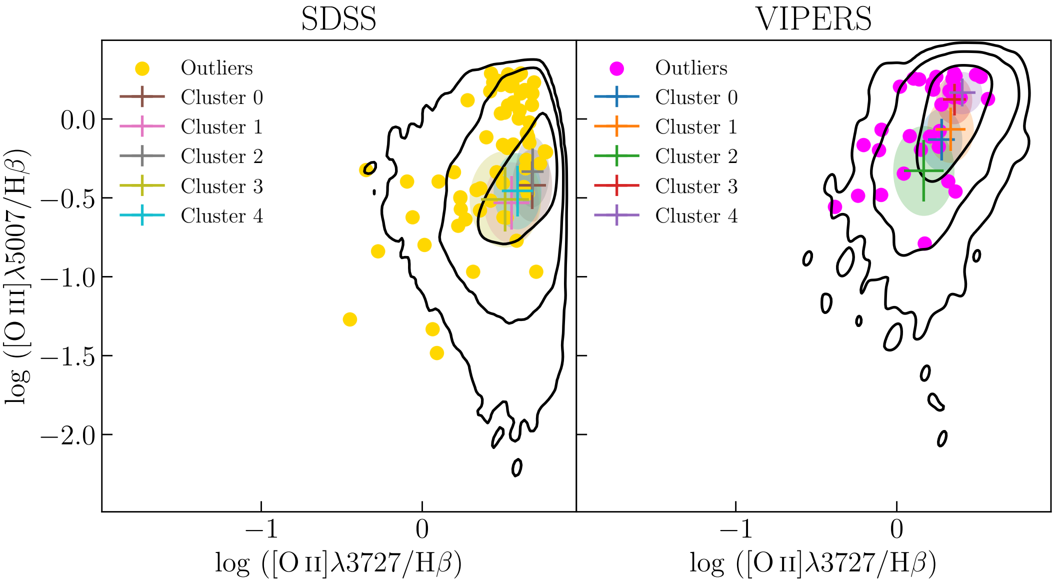

Figure 6.15: Clusters' distribution in the BPT diagram for SDSS (left) and VIPERS (right) samples. The points are color-coded according to the cluster label. The error bars correspond to the IQR and the two semiaxes of the ellipses correspond to the NMAD. The outliers are plotted in gold for the SDSS sample and in magenta for the VIPERS sample. The black contours show the 1, 2, and 3 σ levels of the distributions.

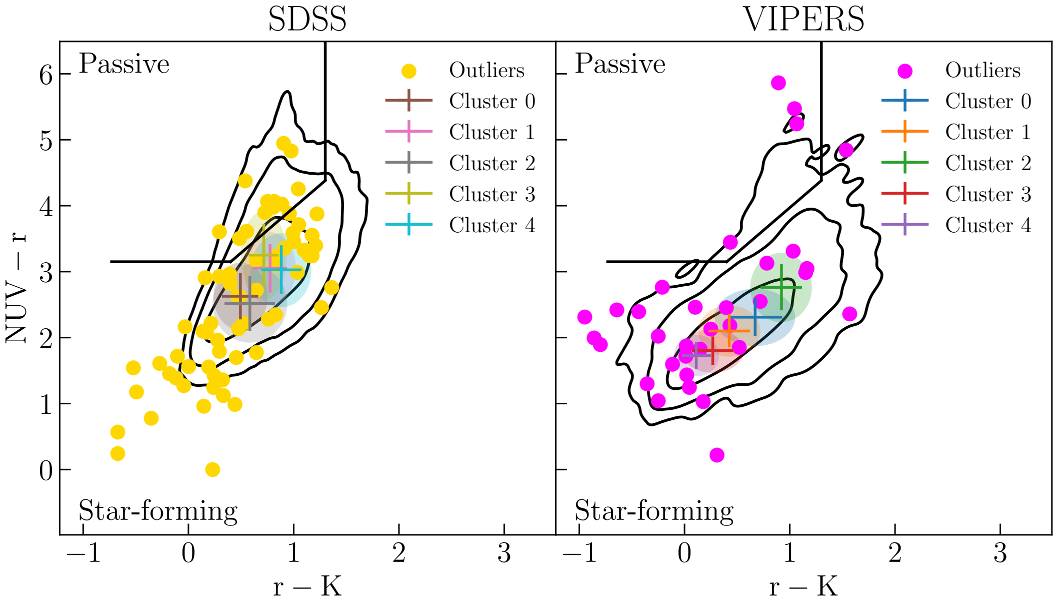

Figure 6.16: Clusters' distribution in the NUVrK diagram for SDSS (left) and VIPERS (right) samples. The points are color-coded according to the cluster label. The error bars correspond to the IQR and the two semiaxes of the ellipses correspond to the NMAD. The outliers are plotted in gold for the SDSS sample and in magenta for the VIPERS sample. The black contours show the 1, 2, and 3 σ levels of the distributions.

galaxies with broad lines, and iii) two groups of normal SF galaxies (one group of galaxies with broad and one with narrow lines).

The stacked VIPERS spectra (Fig. 6.14) show strong emission lines for outliers

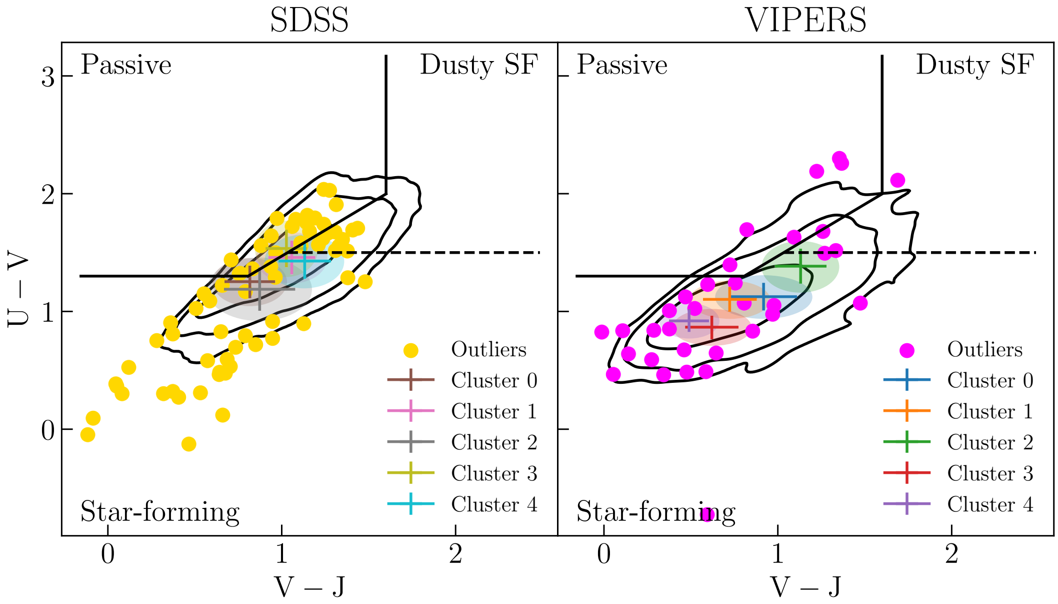

Figure 6.17: Clusters' distribution in the UVJ diagram for SDSS (left) and VIPERS (right) samples. The points are color-coded according to the cluster label. The error bars correspond to the IQR and the two semiaxes of the ellipses correspond to the NMAD. The outliers are plotted in gold for the SDSS sample and in magenta for the VIPERS sample. The black contours show the 1, 2, and 3 σ levels of the distributions.

at $\Delta \log \mathrm{sSFR} > 0$ and weak emission lines for outliers at $\Delta \log \mathrm{sSFR} < 0$. Only the stacked spectrum of outliers at $\Delta \log \mathrm{sSFR} < 0$ and $\log M_\star = 9.5$ show strong emission lines. Since the sSFR is normalized with respect to the average sSFR of the SDSS sample, galaxies with $\Delta \log \mathrm{sSFR} < 0$ in the VIPERS sample are extremely passive. Also using the D4000n break as a probe to divide passive and active galaxies, only the stacked spectrum of outliers at $\Delta \log \mathrm{sSFR} < 0$ and $\log M_\star = 11.0$ shows a value > 1.5.

Siudek et al., 2018 divided the VIPERS sample into eleven classes using the unsupervised ML algorithm Fisher Expectation-Maximization (FEM, Bouveyron et al., 2011). They classified the galaxies according to their rest-frame magnitudes and spectroscopic redshift. In total, they found eleven classes of VIPERS galaxies and an additional class of broad-line active galactic nuclei (AGNs). The eleven classes are grouped into three broader classes: i) red (three FEM classes), ii) green (three FEM classes), and iii) blue (five FEM classes) categories. The galaxies in each class share joint physical and spectroscopic properties that were not considered during the classification. The blue category hosts the disk-shaped galaxies with active SF and is populated by young stellar populations. This blue category may consist of low-metallicity galaxies, or AGNs according to its localization on the BPT diagram. The green category hosts galaxies having more concentrated light profiles and lower gas contents than SF galaxies. The red category hosts the reddest spheroidal-shape galaxies with no sign of star formation activity and is dominated by old stellar populations.

Here, we check any shared properties between the two classifications between this work and the classifications by Siudek et al., 2018. Figure 6.21 shows the common fraction between the cluster defined by k-means clustering algorithms and the FEM classes. The blue category dominates all the k-means clusters and outliers (FEM

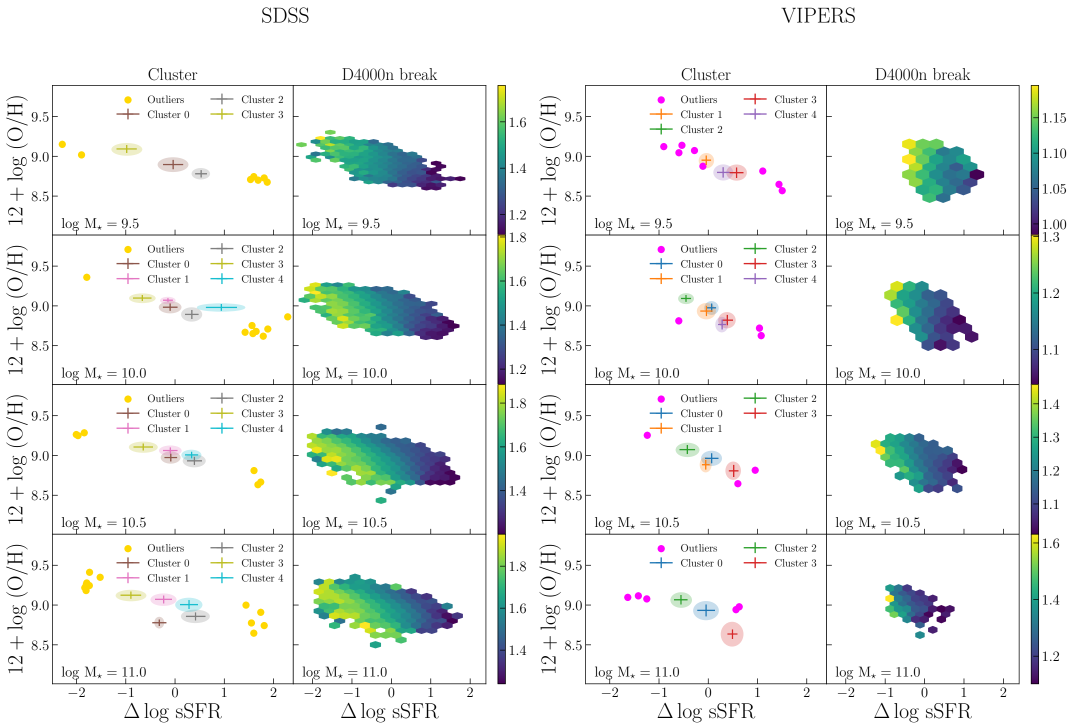

Figure 6.18: Scatter plot of the FMR for SDSS (left panel) and VIPERS (right panel) samples. The points are color-coded according to the cluster label. The error bars correspond to the IQR and the two semiaxes of the ellipses correspond to the NMAD. The outliers are plotted in gold for the SDSS sample and in magenta for the VIPERS sample. The hexbins are color-coded according to the average D4000n break value within the bin.

classes from 7 to 11). The majority of galaxies are then active SF (as expected) and populated by a young stellar population. Clusters 0, 1, 2, and outliers have also a non-negligible population from the green category (FEM classes from 4 to 6). A good fraction of galaxies in these clusters are compact galaxies and lower amount of gas. The outliers are the only group with an important fraction from the red category (FEM classes from 1 to 3). Part of the outliers is composed of passive galaxies with an old stellar population (as shown in Fig. 6.16 and 6.17) that passed the BPT selection.

6.4 Conclusion

We check if the so-called unified or fundamental relations show footprints left by the galaxy evolution on the environment via ML algorithms. Our analysis focused on the FMR and its behavior at low (SDSS data, median $z \sim 0.09$) and intermediate redshifts (VIPERS data, median $z \sim 0.63$). We found as main results:

- the ML algorithms divide both samples into sub-classes that are meaningful from the point of view of the FMR (Fig. 6.13), being quite well separated in this projections;
- the clusters do not depend on luminosity or redshift (Fig. 6.6 and Fig. 6.9);
- the outliers are meaningful from the point of view of the FMR (Fig. 6.13) and its projections (Fig. 6.9), being at the extreme of the distributions;

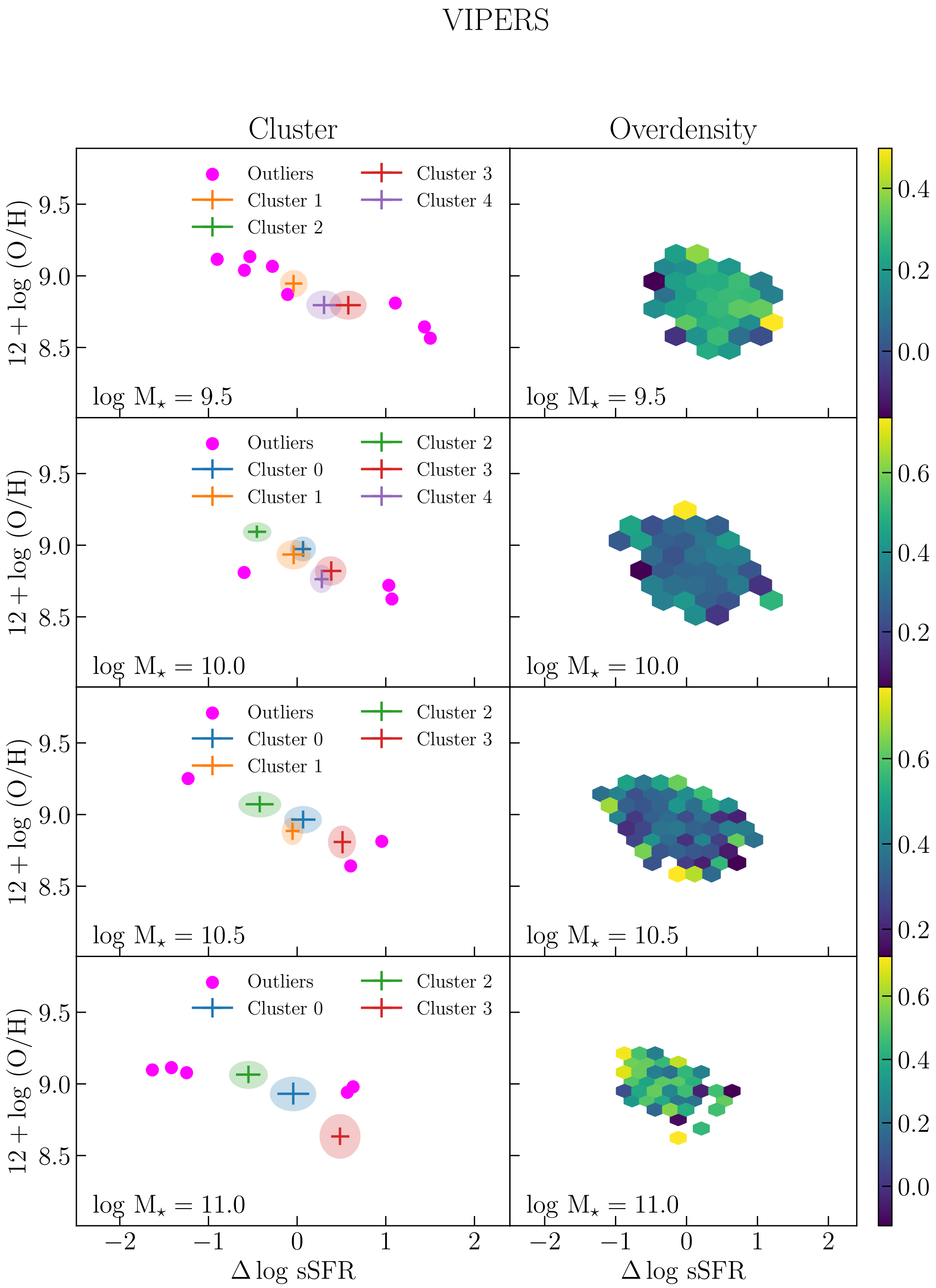

Figure 6.19: Scatter plot of the FMR for SDSS (left panel) and VIPERS (right panel) samples. The points are color-coded according to the cluster label. The error bars correspond to the IQR and the two semiaxes of the ellipses correspond to the NMAD. The outliers are plotted in gold for the SDSS sample and in magenta for the VIPERS sample. The hexbins are color-coded according to the average overdensity value within the bin.

- the VIPERS outliers can be divided into three populations according to their distributions in sSFR and the EW ratios of [O III] $\lambda5007/\mathrm{H}\beta$;

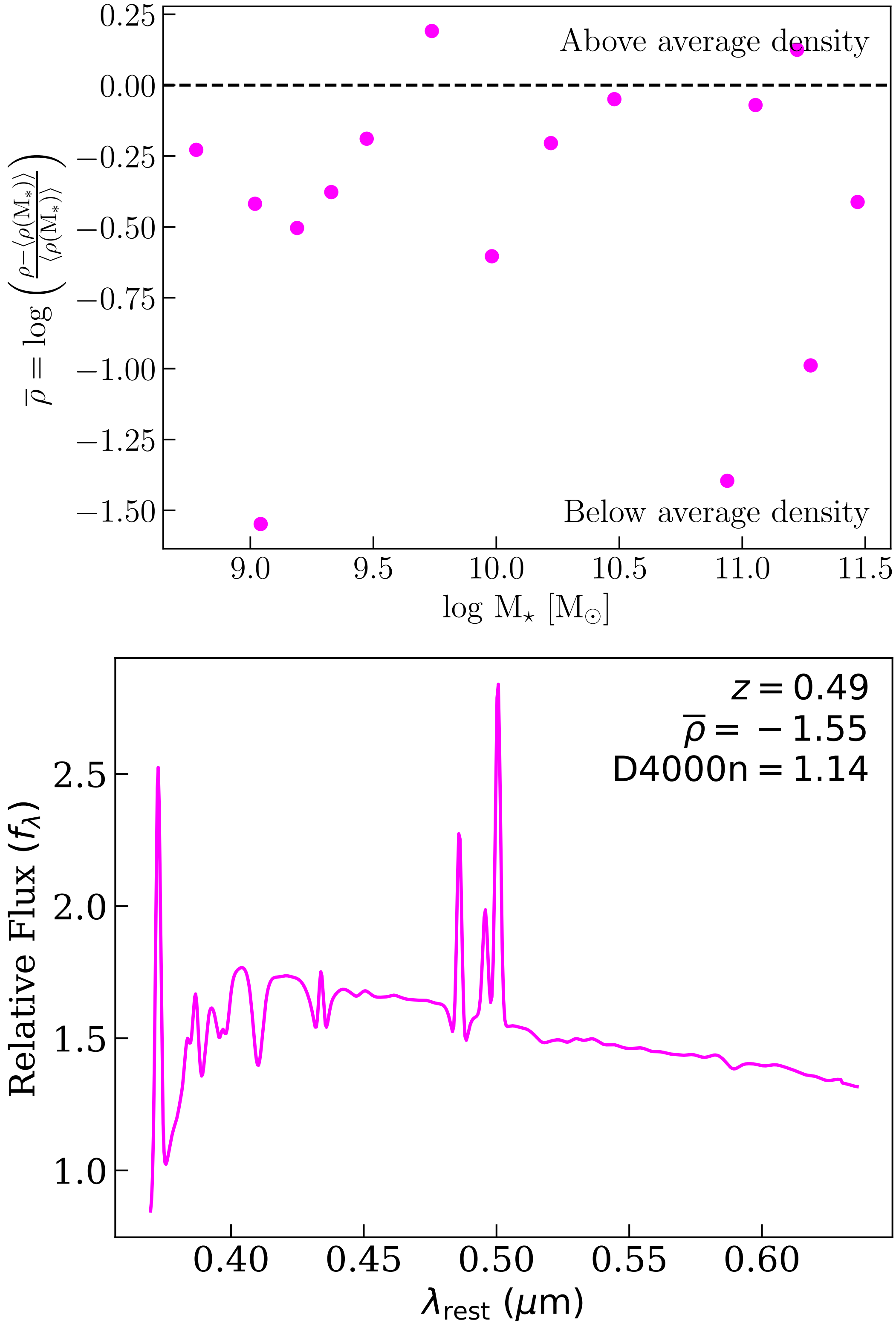

Figure 6.20: Upper panel: scatter of the outliers in the $\overline{\rho}$-$M_\star$ plane. Bottom panel: best-fit spectrum of the outliers having the most underdense environment ($\overline{\rho} = -1.55$).

- the three outliers populations regroup passive galaxies with narrow lines, starburst galaxies with broad lines, and normal SF galaxies;

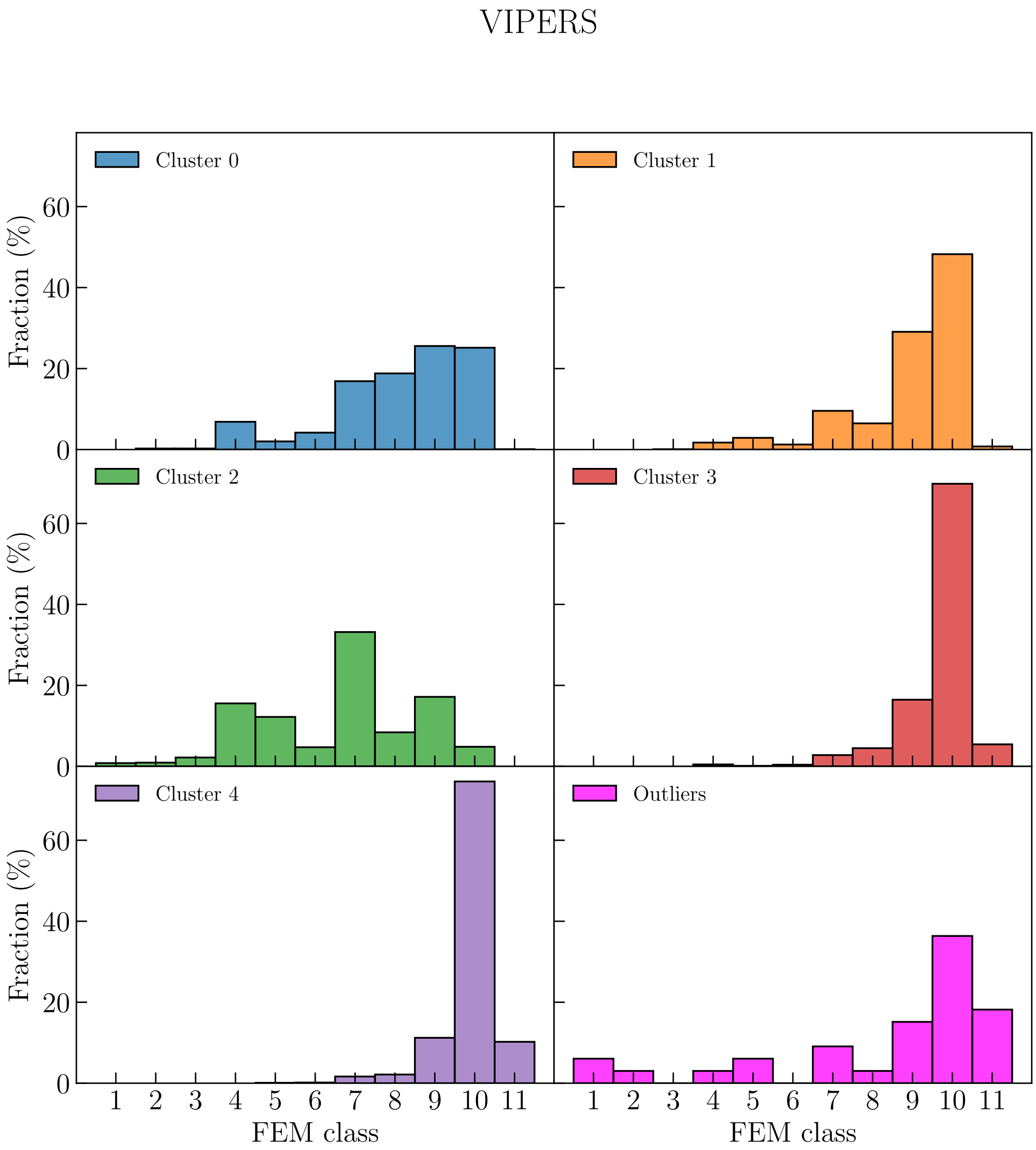

Figure 6.21: Fraction in each FEM class (Siudek et al., 2018) for each cluster defined in this work.

- the clusters in the BPT diagram (Fig. 6.15) are more concentrated for the SDDS sample compared to the VIPERS sample for which the clusters lay over a line and in a bigger range of the emission line ratios;
- the same behavior of the clusters is observed in the color-color diagrams (Fig. 6.16 and Fig. 6.17) with the SDSS sample more concentrated compared to the VIPERS sample;
- the D4000n break increases with increasing metallicity and reducing the relative sSFR (Fig. 6.18);
- the correlation between D4000n break and cluster can be dominated by the degeneracy between metallicity and D4000n break;
- the shape of the FMR does not seem to be related to the environment and the overdensity

- the outliers lie in underdense regions with respect to the average of galaxies with similar $M_\star$ (Fig. 6.20);
- the outliers are the main group polluted by passive galaxies according to the FEM classes (Siudek et al., 2018), FEM classes 1–3.

CHAPTER 7

Summary

The focus of this Ph.D. work is to compare the FMR at different redshifts using SDSS and VIPERS data, using a consistent methodology for both data samples, and profiting from unprecedented statistics of the VIPERS catalog at $z > 0.5$. The aim was to obtain the best measurement of the evolution — or non-evolution — of FMR and its projections up to date, as well as developing a new methodological framework for future analyses. For the purpose of this work, the author re-measured the line properties of the VIPERS galaxies, using the Penalized PiXel-Fitting (pPXF) code.

To have a reliable comparison, different details were taken into account, such as biases introduced by the data selection and observations (Chapter 4) and the different methods used to study the FMR itself (Chapter 5). Additionally, once the data at different redshifts were homogenized, we used simple ML algorithms to divide the samples into sub-classes to determine if different evolutionary paths left any footprints over the FMR surface (Chapter 6).

While the MZR is widely observed to evolve (e.g., Bellstedt et al., 2021; Lian et al., 2018a; Lilly et al., 2013; Mannucci et al., 2010; Pérez-Montero et al., 2009; Savaglio et al., 2005; Zahid et al., 2011a), the FMR so far was observed to evolve only above redshift $2 \sim 2.5$ (Curti et al., 2023; Mannucci et al., 2010; Topping et al., 2021), In this work, we measured the evolution of the MZR and metallicity-SFR up to $z = 0.8$ (upper panels in Fig. 5.1, andFig. 5.8, Chapter 5), but for the first time a statistically significant evolution of the FMR up to $z = 0.8$ (Fig. 5.9, Chapter 5).

We analyzed the effects of the biases on the FMR and its projections (Chapter 4). In particular, we analyzed biases introduced by data selection (choice of the BPT diagram, S/N selection, selection on the spectra quality) and observation (intrinsic luminosity evolution of galaxies, fraction of blue galaxies). Regarding the study of the biases, the main results can be summarized as follows:

i) the VIPERS sample is in good agreement with the SDSS sample, with an average metallicity difference of $\sim 0.4\ \langle\sigma_{\rm dist}\rangle_{\rm VIPERS}$;

ii) the metallicity difference can be reduced to $\sim 0.3\ \langle\sigma_{\rm dist}\rangle_{\rm VIPERS}$ taking into account the biases;

iii) the FMR projections most affected by the biases are the MZR and the metallicity-SFR, especially when an S/N cutoff is applied to [O III] λ4959;

iv) the least affected projections by the biases are those with a combination of $M_\star$ and SFR.

We then analyzed different methods of comparison of samples at different redshifts (Chapter 5). We analyzed a parametric method, a study of the FMR projections, and a non-parametric method, a study of the metallicity-relative sSFR. The relative sSFR can be computed by normalizing the SFR by different choices, allowing us to compare different properties between the samples at different redshifts. Regarding the study of methods of comparison, the main results can be summarized as follows:

i) to compare specific properties of galaxies via the FMR projections, parametric method, it is necessary to create control samples with specific criteria according to the property to compare;

ii) the parametric method has the problem of inferring information about the whole FMR surface by looking at the median projections;

iii) the non-parametric method allows the choice of the normalization in order to choose which galaxy property to compare;

iv) the non-parametric method has the advantage of being mostly independent of biases.

Finally, we look for any footprint left by galaxy evolution and environmental effects on the FMR by applying machine learning algorithms to both samples. At the same time, we look for outliers. We applied the PCA algorithm in order to define a 2D space with the highest variance due to all the properties from which the FMR depends. In this space, we applied the K-means algorithm in order to group the samples into smaller classes with similar characteristics. In the same space, we applied the LOF algorithm in order to define the outliers. Regarding the search for footprints left over the FMR surface, the main results can be summarized as follows:

i) the simple ML algorithms used are able to divide the samples into clusters quite well separated by the point of view of the FMR;

ii) the clusters do not show any correlation in the BPT and color-color diagrams;

iii) the clusters are correlated only with the D4000n break value (age-metallicity degeneracy);

iv) the outliers are found in an underdense environment with comparison to the average SF galaxies with the same $M_\star$;

v) the VIPERS outliers can be divided into three populations according to their distributions in sSFR and the EW ratios of [O III] $\lambda 5007/\mathrm{H}\beta$;

vi) the three outliers populations regroup passive galaxies with narrow lines, starburst galaxies with broad lines, and normal SF galaxies.

The main result of this work is the first evidence of the evolution of the FMR between $z \sim 0$ and the intermediate redshift ($0.48 < z < 0.80$). This work also outlines a set of methods and tests which can lead to less biased and more statistically proper comparisons between samples at different redshifts and can be used in future studies.

The attempt to select sub-populations (in preparation) based on the FMR still misses a full understanding of the sub-populations found. However, at the same time, we separated a sample of the VIPERS outliers that can be divided into at least three well-distinguished populations according to their distribution in sSFR and EW ratios of [O III] $\lambda 5007/\mathrm{H}\beta$. These outliers will be the subject of future analyses.

CHAPTER 8

Future prospectives

Several questions remain open on the FMR. The origin of the FMR itself and its evolution are widely discussed. Some studies (Baker et al., 2023; Bothwell et al., 2016a,b; Davé et al., 2017; Finlator et al., 2008; Lilly et al., 2013; Ma et al., 2016; Torrey et al., 2019) claim that a more fundamental relation is defined by $M_\star$, metallicity, and gas mass, and the FMR results from the connection between gas mass and SFR (Kennicutt, 1998). The existence of the FMR at high redshift implies that the chemical evolution is driven by the gas content, and therefore the SFR. The lack of evolution of the FMR suggests that galaxies at different cosmic times are governed by the same scaling of metal-enriched outflows and gas fraction as a function of $M_\star$ and SFR (Sanders et al., 2021). Different models have been proposed for the evolution of the mass-metallicity relation (MZR) going from a time-dependent star formation efficiency (SFR Lilly et al., 2013) to a time-dependent metal outflow or time-dependent initial mass function (IMF Lian et al., 2018a,b). Once the SFR dependency is added to the MZR, no evolution is observed up to the "cosmic noon" ($z \sim 2.5$ Mannucci et al., 2010) disconnecting completely the 3D relation from one of its projections. The studies about the evolution of the FMR above $z \sim 1$ are particularly limited by the low amount of good spectroscopic data at high redshift.

Recently, the FMR has been expanded for galaxies identified as non-SF according to the BPT diagram (BPT-non-SF, i.e., classified as LI(N)ERs/AGNs Kumari et al., 2019, 2021). Galaxies above the MS result being more metal-poor than their counterparts on the MS. This shift in metallicity can be interpreted in terms of gas accretion enhancing star formation and diluting the metallicity (Kumari et al., 2021). Quiescent galaxies (i.e., low-$M_\star$ galaxies below the MS) have higher metallicities than their MS counterparts. This shift in metallicity can be interpreted in terms of starvation (i.e. suppression of fresh gas supply) inhibiting star formation and decreasing the dilution effect, consequently resulting in a higher level of chemical enrichment (Kumari et al., 2021). High-$M_\star$ galaxies below the MS have a much closer gas metallicity to their MS counterparts and much lower than expected from their stellar metallicities. These galaxies can be explained assuming a scenario where massive nearly quiescent galaxies with LI(N)ER-like nebular emission have recently accreted gas from the CGM/IGM (Kumari et al., 2021). Overall, the local BPT-non-SF galaxies follow the same FMR defined by SF galaxies at low redshift. It remains to answer some questions: does the FMR for BPT-non-SF galaxies lack evolution in the same way as BPT-SF galaxies? Is it completely independent of the AGN feedback mechanisms?

Galaxy pairs show lower gas-phase metallicities and a higher SFR compared to isolated galaxies with comparable stellar masses (Cortijo-Ferrero et al., 2017; Ellison et al., 2008b; Scudder et al., 2012). The metallicity deficiency can be caused by inflows of metal-poor gas due to the tidal forces and gravitational torques associated with galaxy mergers. The inflows dilute the metal content of the central region. Such metallicity dilution occurs in state-of-the-art cosmological simulations of galaxy formation (Bustamante et al., 2018). In major mergers, the metal dilution is usually around 0.1 dex and becomes noticeable at projected separations of less than 40 kpc. Minor mergers also experience metallicity dilution but to a lesser magnitude (Bustamante et al., 2018). This behavior is also observed directly in galaxy pairs, having stronger dilution in the gas-phase metallicity and enhanced star formation activity with decreasing projected separation. Despite the qualitative consistency with FMR studies, the observed metal dilution in SDSS galaxy pairs is more significant than what was predicted by the FMR itself. This is likely due to the FMR not accounting for the different evolutionary phases of galaxies interacting with companions, making mergers an identifiable outlier population. Only galaxy pairs separated by more than 110 kpc are consistent with the FMR (Bustamante et al., 2020). The number of FMR outliers due to merging events increases with redshift because of the increase of the merging rate (O'Leary et al., 2021; Pearson et al., 2019). At which redshift the outliers became a statistically significant population? Can the merging rate explain the evolution of the FMR?

Bibliography

Abazajian, Kevork N. et al. (June 2009). The Seventh Data Release of the Sloan Digital Sky Survey. ApJS 182.2, pp. 543–558. DOI: `10.1088/0067-0049/182/2/543`. arXiv: `0812.0649 [astro-ph]`.

Abramson, Louis E. et al. (Apr. 2014). The Mass-independence of Specific Star Formation Rates in Galactic Disks. ApJ 785.2, L36, p. L36. DOI: `10.1088/2041-8205/785/2/L36`. arXiv: `1402.7076 [astro-ph.GA]`.

Ahn, Christopher P. et al. (Apr. 2014). The Tenth Data Release of the Sloan Digital Sky Survey: First Spectroscopic Data from the SDSS-III Apache Point Observatory Galactic Evolution Experiment. ApJS 211.2, 17, p. 17. DOI: `10.1088/0067-0049/211/2/17`. arXiv: `1307.7735 [astro-ph.IM]`.

Aller, L. H. (1984). *Physics of thermal gaseous nebulae*. DOI: `10.1007/978-94-010-9639-3`.

Aller, Lawrence H. (Nov. 1954). The Composition of the Planetary Nebula NGC 7027. ApJ 120, p. 401. DOI: `10.1086/145931`.

Amorín, R. et al. (June 2015). Extreme emission-line galaxies out to z ~1 in zCOSMOS. I. Sample and characterization of global properties. A&A 578, A105, A105. DOI: `10.1051/0004-6361/201322786`. arXiv: `1403.3441 [astro-ph.GA]`.

Andrews, Brett H. et al. (Mar. 2013). The Mass-Metallicity Relation with the Direct Method on Stacked Spectra of SDSS Galaxies. ApJ 765.2, 140, p. 140. DOI: `10.1088/0004-637X/765/2/140`. arXiv: `1211.3418 [astro-ph.CO]`.

Arnouts, S. et al. (Dec. 1999). Measuring and modelling the redshift evolution of clustering: the Hubble Deep Field North. MNRAS 310.2, pp. 540–556. DOI: `10.1046/j.1365-8711.1999.02978.x`. arXiv: `astro-ph/9902290 [astro-ph]`.

Astropy Collaboration et al. (Oct. 2013). Astropy: A community Python package for astronomy. A&A 558, A33, A33. DOI: `10.1051/0004-6361/201322068`. arXiv: `1307.6212 [astro-ph.IM]`.

Astropy Collaboration et al. (Sept. 2018). The Astropy Project: Building an Open-science Project and Status of the v2.0 Core Package. AJ 156.3, 123, p. 123. DOI: `10.3847/1538-3881/aabc4f`. arXiv: `1801.02634 [astro-ph.IM]`.

Baes, Maarten (Jan. 2020). Panchromatic SED fitting codes and modelling techniques. *Panchromatic Modelling with Next Generation Facilities*. Ed. by Médéric Boquien et al. Vol. 341, pp. 26–34. DOI: `10.1017/S1743921319003016`. arXiv: `1910.04065 [astro-ph.GA]`.

Baker, James G. et al. (July 1938). Physical Processes in Gaseous Nebulae. III. The Balmer Decrement. ApJ 88, p. 52. DOI: `10.1086/143959`.

Baker, William M. et al. (Jan. 2023). The molecular gas main sequence and Schmidt-Kennicutt relation are fundamental, the star-forming main sequence is a (useful) byproduct. MNRAS 518.3, pp. 4767–4781. DOI: `10.1093/mnras/stac3413`. arXiv: `2211.10449 [astro-ph.GA]`.

Baldry, I. K. et al. (Aug. 2008). On the galaxy stellar mass function, the mass-metallicity relation and the implied baryonic mass function. MNRAS 388.3, pp. 945–959. DOI: `10.1111/j.1365-2966.2008.13348.x`. arXiv: `0804.2892 [astro-ph]`.

Baldry, Ivan K. et al. (Aug. 2003). Constraints on a Universal Stellar Initial Mass Function from Ultraviolet to Near-Infrared Galaxy Luminosity Densities. ApJ 593.1, pp. 258–271. DOI: `10.1086/376502`. arXiv: `astro-ph/0304423 [astro-ph]`.

Baldwin, J. A. et al. (Feb. 1981). Classification parameters for the emission-line spectra of extragalactic objects. PASP 93, pp. 5–19. DOI: `10.1086/130766`.

Beeston, R. A. et al. (June 2018). GAMA/H-ATLAS: the local dust mass function and cosmic density as a function of galaxy type - a benchmark for models of galaxy evolution. MNRAS 479.1, pp. 1077–1099. DOI: `10.1093/mnras/sty1460`. arXiv: `1712.07261 [astro-ph.GA]`.

Bell, Eric F. et al. (Aug. 2003). The properties of spiral galaxies: confronting hierarchical galaxy formation models with observations. MNRAS 343.2, pp. 367–384. DOI: `10.1046/j.1365-8711.2003.06673.x`. arXiv: `astro-ph/0303531 [astro-ph]`.

Bell, Eric F. et al. (Mar. 2006). Dry Mergers in GEMS: The Dynamical Evolution of Massive Early-Type Galaxies. ApJ 640.1, pp. 241–251. DOI: `10.1086/499931`. arXiv: `astro-ph/0506425 [astro-ph]`.

Belli, Sirio et al. (Aug. 2013). Testing the Universality of the Fundamental Metallicity Relation at High Redshift Using Low-mass Gravitationally Lensed Galaxies. ApJ 772.2, 141, p. 141. DOI: `10.1088/0004-637X/772/2/141`. arXiv: `1302.3614 [astro-ph.CO]`.

Bellstedt, Sabine et al. (Feb. 2021). Galaxy And Mass Assembly (GAMA): The inferred mass–metallicity relation from $z = 0$ to 3.5 via forensic SED fitting. *arXiv e-prints*, arXiv:2102.11514, arXiv:2102.11514. arXiv: `2102.11514 [astro-ph.GA]`.

Bennett, C. L. et al. (Oct. 2013). Nine-year Wilkinson Microwave Anisotropy Probe (WMAP) Observations: Final Maps and Results. ApJS 208.2, 20, p. 20. DOI: `10.1088/0067-0049/208/2/20`. arXiv: `1212.5225 [astro-ph.CO]`.

Bian, Fuyan et al. (Jan. 2017). Mass-Metallicity Relation for Local Analogs of High-redshift galaxies: Implications for the Evolution of the Mass-Metallicity Relations. ApJ 834.1, 51, p. 51. DOI: `10.3847/1538-4357/834/1/51`. arXiv: `1611.08595 [astro-ph.GA]`.

Bolzonella, M. et al. (Nov. 2000a). Photometric redshifts based on standard SED fitting procedures. A&A 363, pp. 476–492. DOI: `10.48550/arXiv.astro-ph/0003380`. arXiv: `astro-ph/0003380 [astro-ph]`.

Bolzonella, M. et al. (Nov. 2000b). Photometric redshifts based on standard SED fitting procedures. A&A 363, pp. 476–492. arXiv: `astro-ph/0003380 [astro-ph]`.

Bolzonella, M. et al. (Dec. 2010). Tracking the impact of environment on the galaxy stellar mass function up to $z \sim 1$ in the 10 k zCOSMOS sample. A&A 524, A76, A76. DOI: `10.1051/0004-6361/200912801`. arXiv: `0907.0013 [astro-ph.CO]`.

Boquien, M. et al. (Feb. 2019). CIGALE: a python Code Investigating GALaxy Emission. A&A 622, A103, A103. DOI: `10.1051/0004-6361/201834156`. arXiv: `1811.03094 [astro-ph.GA]`.

Bothwell, M. S. et al. (Oct. 2016a). Galaxy metallicities depend primarily on stellar mass and molecular gas mass. A&A 595, A48, A48. DOI: `10.1051/0004-6361/201527918`. arXiv: `1606.04102 [astro-ph.GA]`.

Bothwell, M. S. et al. (Jan. 2016b). Molecular gas as the driver of fundamental galactic relations. MNRAS 455.2, pp. 1156–1170. DOI: `10.1093/mnras/stv2121`. arXiv: `1507.01004 [astro-ph.GA]`.

Bottini, D. et al. (Sept. 2005). The Very Large Telescope Visible Multi-Object Spectrograph Mask Preparation Software. PASP 117.835, pp. 996–1103. DOI: `10.1086/432150`.

Bouveyron, Charles et al. (2011). Simultaneous model-based clustering and visualization in the Fisher discriminative subspace. *arXiv preprint arXiv:1101.2374*.

Bresolin, Fabio et al. (July 2009). Extragalactic Chemical Abundances: Do H II Regions and Young Stars Tell the Same Story? The Case of the Spiral Galaxy NGC 300. ApJ 700.1, pp. 309–330. DOI: `10.1088/0004-637X/700/1/309`. arXiv: `0905.2791 [astro-ph.CO]`.

Brinchmann, J. et al. (July 2004). The physical properties of star-forming galaxies in the low-redshift Universe. MNRAS 351.4, pp. 1151–1179. DOI: `10.1111/j.1365-2966.2004.07881.x`. arXiv: `astro-ph/0311060 [astro-ph]`.

Brisbin, Drew et al. (May 2012). Galaxy Mass, Metallicity, Radius, and Star Formation Rates. ApJ 750.2, 142, p. 142. DOI: `10.1088/0004-637X/750/2/142`. arXiv: `1110.5862 [astro-ph.CO]`.

Brook, C. B. et al. (Oct. 2014). MaGICC baryon cycle: the enrichment history of simulated disc galaxies. MNRAS 443.4, pp. 3809–3818. DOI: `10.1093/mnras/stu1406`. arXiv: `1306.5766 [astro-ph.CO]`.

Brooks, A. M. et al. (Jan. 2007). The Origin and Evolution of the Mass-Metallicity Relationship for Galaxies: Results from Cosmological N-Body Simulations. ApJ 655.1, pp. L17–L20. DOI: `10.1086/511765`. arXiv: `astro-ph/0609620 [astro-ph]`.

Brown, Jonathan S. et al. (May 2016). A recalibration of strong-line oxygen abundance diagnostics via the direct method and implications for the high-redshift universe. MNRAS 458.2, pp. 1529–1547. DOI: `10.1093/mnras/stw392`. arXiv: `1602.01087 [astro-ph.GA]`.

Bruzual, G. et al. (Oct. 2003). Stellar population synthesis at the resolution of 2003. MNRAS 344.4, pp. 1000–1028. DOI: `10.1046/j.1365-8711.2003.06897.x`. arXiv: `astro-ph/0309134 [astro-ph]`.

Buat, V. et al. (Dec. 2019). Cold dust and stellar emissions in dust-rich galaxies observed with ALMA: a challenge for SED-fitting techniques. A&A 632, A79, A79. DOI: `10.1051/0004-6361/201936643`.

Burgarella, D. et al. (July 2005). Star formation and dust attenuation properties in galaxies from a statistical ultraviolet-to-far-infrared analysis. MNRAS 360.4, pp. 1413–1425. DOI: `10.1111/j.1365-2966.2005.09131.x`. arXiv: `astro-ph/0504434 [astro-ph]`.

Bustamante, Sebastián et al. (Sept. 2018). Merger-induced metallicity dilution in cosmological galaxy formation simulations. MNRAS 479.3, pp. 3381–3392. DOI: `10.1093/mnras/sty1692`. arXiv: `1712.03250 [astro-ph.GA]`.

Bustamante, Sebastián et al. (May 2020). Galaxy pairs in the Sloan Digital Sky Survey - XIV. Galaxy mergers do not lie on the fundamental metallicity relation. MNRAS 494.3, pp. 3469–3480. DOI: `10.1093/mnras/staa1025`. arXiv: `2004.06121 [astro-ph.GA]`.

Calabrò, A. et al. (May 2017). Characterization of star-forming dwarf galaxies at $0.1 \lesssim z \lesssim 0.9$ in VUDS: probing the low-mass end of the mass-metallicity relation. A&A 601, A95, A95. DOI: `10.1051/0004-6361/201629762`. arXiv: `1701.04418 [astro-ph.GA]`.

Calzetti, Daniela et al. (Apr. 2000). The Dust Content and Opacity of Actively Star-forming Galaxies. ApJ 533.2, pp. 682–695. DOI: `10.1086/308692`. arXiv: `astro-ph/9911459 [astro-ph]`.

Cappellari, Michele (Apr. 2017). Improving the full spectrum fitting method: accurate convolution with Gauss-Hermite functions. MNRAS 466.1, pp. 798–811. DOI: `10.1093/mnras/stw3020`. arXiv: `1607.08538 [astro-ph.GA]`.

— (Aug. 2022). Full spectrum fitting with photometry in ppxf: non-parametric star formation history, metallicity and the quenching boundary from 3200 LEGA-C galaxies at redshift z∼0.8. *arXiv e-prints*, arXiv:2208.14974, arXiv:2208.14974. arXiv: `2208.14974 [astro-ph.GA]`.

Cappellari, Michele et al. (Feb. 2004). Parametric Recovery of Line-of-Sight Velocity Distributions from Absorption-Line Spectra of Galaxies via Penalized Likelihood. PASP 116.816, pp. 138–147. DOI: `10.1086/381875`. arXiv: `astro-ph/0312201 [astro-ph]`.

Cardelli, Jason A. et al. (Oct. 1989). The Relationship between Infrared, Optical, and Ultraviolet Extinction. ApJ 345, p. 245. DOI: `10.1086/167900`.

Casasola, Viviana et al. (Dec. 2022). The resolved scaling relations in DustPedia: Zooming in on the local Universe. A&A 668, A130, A130. DOI: `10.1051/0004-6361/202245043`. arXiv: `2210.15993 [astro-ph.GA]`.

Castellanos, Marcelo et al. (Jan. 2002). A comprehensive study of reported high-metallicity giant H II regions - I. Detailed abundance analysis. MNRAS 329.2, pp. 315–335. DOI: `10.1046/j.1365-8711.2002.04987.x`. arXiv: `astro-ph/0109115 [astro-ph]`.

Cautun, Marius et al. (July 2014). Evolution of the cosmic web. MNRAS 441.4, pp. 2923–2973. DOI: `10.1093/mnras/stu768`. arXiv: `1401.7866 [astro-ph.CO]`.

Chabrier, Gilles (July 2003). Galactic Stellar and Substellar Initial Mass Function. PASP 115.809, pp. 763–795. DOI: `10.1086/376392`. arXiv: `astro-ph/0304382 [astro-ph]`.

Chisholm, J. et al. (Dec. 2018). Metal-enriched galactic outflows shape the mass-metallicity relationship. MNRAS 481.2, pp. 1690–1706. DOI: `10.1093/mnras/sty2380`. arXiv: `1808.10453 [astro-ph.GA]`.

Cicone, C. et al. (Feb. 2014). Massive molecular outflows and evidence for AGN feedback from CO observations. A&A 562, A21, A21. DOI: `10.1051/0004-6361/201322464`. arXiv: `1311.2595 [astro-ph.CO]`.

Ciesla, L. et al. (Jan. 2016). The imprint of rapid star formation quenching on the spectral energy distributions of galaxies. A&A 585, A43, A43. DOI: `10.1051/0004-6361/201527107`. arXiv: `1510.07657 [astro-ph.GA]`.

Ciesla, L. et al. (July 2018). Identification of galaxies that experienced a recent major drop of star formation. A&A 615, A61, A61. DOI: `10.1051/0004-6361/201832715`. arXiv: `1803.10239 [astro-ph.GA]`.

Conroy, Charlie et al. (July 2009). The Propagation of Uncertainties in Stellar Population Synthesis Modeling. I. The Relevance of Uncertain Aspects of Stellar Evolution and the Initial Mass Function to the Derived Physical Properties of Galaxies. ApJ 699.1, pp. 486–506. DOI: `10.1088/0004-637X/699/1/486`. arXiv: `0809.4261 [astro-ph]`.

Contini, Thierry et al. (Feb. 2002). Chemical abundances in a UV-selected sample of galaxies. MNRAS 330.1, pp. 75–91. DOI: `10.1046/j.1365-8711.2002.05042.x`. arXiv: `astro-ph/0109395 [astro-ph]`.

Cortijo-Ferrero, C. et al. (June 2017). Star formation histories in mergers: the spatially resolved properties of the early-stage merger luminous infrared galaxies IC 1623 and NGC 6090. MNRAS 467.4, pp. 3898–3919. DOI: `10.1093/mnras/stx383`. arXiv: `1702.06544 [astro-ph.GA]`.

Cowie, L. L. et al. (Oct. 2008). An Integrated Picture of Star Formation, Metallicity Evolution, and Galactic Stellar Mass Assembly. ApJ 686.1, pp. 72–116. DOI: `10.1086/591176`. arXiv: `0806.3457 [astro-ph]`.

Cowie, Lennox L. et al. (Sept. 1996). New Insight on Galaxy Formation and Evolution From Keck Spectroscopy of the Hawaii Deep Fields. AJ 112, p. 839. DOI: `10.1086/118058`. arXiv: `astro-ph/9606079 [astro-ph]`.

Cowie, Lennox L. et al. (May 1997). The Evolution of the Distribution of Star Formation Rates in Galaxies. ApJ 481.1, pp. L9–L13. DOI: `10.1086/310648`. arXiv: `astro-ph/9702235 [astro-ph]`.

Cresci, G. et al. (Mar. 2012). The metallicity properties of zCOSMOS galaxies at $0.2 < z < 0.8$. MNRAS 421.1, pp. 262–269. DOI: `10.1111/j.1365-2966.2011.20299.x`. arXiv: `1110.4408 [astro-ph.CO]`.

Cresci, G. et al. (July 2019). Fundamental metallicity relation in CALIFA, SDSS-IV MaNGA, and high-z galaxies. A&A 627, A42, A42. DOI: `10.1051/0004-6361/201834637`. arXiv: `1811.06015 [astro-ph.GA]`.

Cucciati, O. et al. (May 2014). The VIMOS Public Extragalactic Redshift Survey (VIPERS). Never mind the gaps: comparing techniques to restore homogeneous sky coverage. A&A 565, A67, A67. DOI: `10.1051/0004-6361/201423409`. arXiv: `1401.3745 [astro-ph.CO]`.

Cucciati, O. et al. (June 2017). The VIMOS Public Extragalactic Redshift Survey (VIPERS). The decline of cosmic star formation: quenching, mass, and environment connections. A&A 602, A15, A15. DOI: `10.1051/0004-6361/201630113`. arXiv: `1611.07049 [astro-ph.GA]`.

Cullen, F. et al. (Jan. 2014a). Mass-metallicity relation and fundamental metallicity relation at $z \gtrsim 2$. Mem. Soc. Astron. Italiana 85, p. 413.

— (May 2014b). The mass-metallicity-star formation rate relation at z $\gtrsim$ 2 with 3D Hubble Space Telescope. MNRAS 440.3, pp. 2300–2312. DOI: `10.1093/mnras/stu443`. arXiv: `1310.0816 [astro-ph.CO]`.

Curti, M. et al. (Feb. 2017). New fully empirical calibrations of strong-line metallicity indicators in star-forming galaxies. MNRAS 465.2, pp. 1384–1400. DOI: `10.1093/mnras/stw2766`. arXiv: `1610.06939 [astro-ph.GA]`.

Curti, Mirko et al. (Jan. 2020). The mass-metallicity and the fundamental metallicity relation revisited on a fully T_e-based abundance scale for galaxies. MNRAS 491.1, pp. 944–964. DOI: `10.1093/mnras/stz2910`. arXiv: `1910.00597 [astro-ph.GA]`.

Curti, Mirko et al. (Jan. 2023). The chemical enrichment in the early Universe as probed by JWST via direct metallicity measurements at z $\sim$ 8. MNRAS 518.1, pp. 425–438. DOI: `10.1093/mnras/stac2737`. arXiv: `2207.12375 [astro-ph.GA]`.

Daddi, E. et al. (Nov. 2007). Multiwavelength Study of Massive Galaxies at z$\sim$2. I. Star Formation and Galaxy Growth. ApJ 670.1, pp. 156–172. DOI: `10.1086/521818`. arXiv: `0705.2831 [astro-ph]`.

Davé, Romeel et al. (May 2017). MUFASA: Galaxy star formation, gas, and metal properties across cosmic time. MNRAS 467.1, pp. 115–132. DOI: `10.1093/mnras/stx108`. arXiv: `1610.01626 [astro-ph.GA]`.

Davidzon, I. et al. (Feb. 2016). The VIMOS Public Extragalactic Redshift Survey (VIPERS). Environmental effects shaping the galaxy stellar mass function. A&A 586, A23, A23. DOI: `10.1051/0004-6361/201527129`. arXiv: `1511.01145 [astro-ph.GA]`.

Davè, Romeel et al. (Sept. 2011). Galaxy evolution in cosmological simulations with outflows - II. Metallicities and gas fractions. MNRAS 416.2, pp. 1354–1376. DOI: `10.1111/j.1365-2966.2011.19132.x`. arXiv: `1104.3156 [astro-ph.CO]`.

Dayal, Pratika et al. (Dec. 2018). Early galaxy formation and its large-scale effects. Phys. Rep. 780, pp. 1–64. DOI: `10.1016/j.physrep.2018.10.002`. arXiv: `1809.09136 [astro-ph.GA]`.

De Rossi, M. E. et al. (Aug. 2018). Evolution of the stellar metallicities of galaxies in the EAGLE simulation. *Boletin de la Asociacion Argentina de Astronomia La Plata Argentina* 60, pp. 121–123. DOI: `10.48550/arXiv.1805.06119`. arXiv: `1805.06119 [astro-ph.GA]`.

De Rossi, María Emilia et al. (Dec. 2017). Galaxy metallicity scaling relations in the EAGLE simulations. MNRAS 472.3, pp. 3354–3377. DOI: `10.1093/mnras/stx2158`. arXiv: `1704.00006 [astro-ph.GA]`.

De Vis, P. et al. (Mar. 2019). A systematic metallicity study of DustPedia galaxies reveals evolution in the dust-to-metal ratios. A&A 623, A5, A5. DOI: `10.1051/0004-6361/201834444`. arXiv: `1901.09040 [astro-ph.GA]`.

Denicoló, Glenda et al. (Feb. 2002). New light on the search for low-metallicity galaxies - I. The N2 calibrator. MNRAS 330.1, pp. 69–74. DOI: `10.1046/j.1365-8711.2002.05041.x`. arXiv: `astro-ph/0110356 [astro-ph]`.

Dinerstein, Harriet L. (Jan. 1990). Abundances in extragalactic H II regions. *The Interstellar Medium in Galaxies*. Ed. by Jr. Thronson Harley A. et al. Vol. 161. Astrophysics and Space Science Library, pp. 257–285. DOI: `10.1007/978-94-009-0595-5_10`.

Donevski, Darko et al. (Apr. 2023). In pursuit of giants: II. Evolution of dusty quiescent galaxies over the last six billion years from the hCOSMOS survey. *arXiv e-prints*, arXiv:2304.05842, arXiv:2304.05842. DOI: `10.48550/arXiv.2304.05842`. arXiv: `2304.05842 [astro-ph.GA]`.

Dopita, Michael A. et al. (Feb. 2016). Chemical abundances in high-redshift galaxies: a powerful new emission line diagnostic. Ap&SS 361, 61, p. 61. DOI: `10.1007/s10509-016-2657-8`. arXiv: `1601.01337 [astro-ph.GA]`.

Dunne, L. et al. (Oct. 2011). Herschel-ATLAS: rapid evolution of dust in galaxies over the last 5 billion years. MNRAS 417.2, pp. 1510–1533. DOI: `10.1111/j.1365-2966.2011.19363.x`. arXiv: `1012.5186 [astro-ph.CO]`.

Eggen, O. J. et al. (Nov. 1962). Evidence from the motions of old stars that the Galaxy collapsed. ApJ 136, p. 748. DOI: `10.1086/147433`.

Elbaz, D. et al. (June 2007). The reversal of the star formation-density relation in the distant universe. A&A 468.1, pp. 33–48. DOI: `10.1051/0004-6361:20077525`. arXiv: `astro-ph/0703653 [astro-ph]`.

Elbaz, D. et al. (Aug. 2018). Starbursts in and out of the star-formation main sequence. A&A 616, A110, A110. DOI: `10.1051/0004-6361/201732370`. arXiv: `1711.10047 [astro-ph.GA]`.

Elbers, Willem et al. (Apr. 2023). Persistent topology of the reionization bubble network - II. Evolution and classification. MNRAS 520.2, pp. 2709–2726. DOI: `10.1093/mnras/stad120`. arXiv: `2209.03948 [astro-ph.CO]`.

Ellis, Richard S. (Jan. 1997). Faint Blue Galaxies. ARA&A 35, pp. 389–443. DOI: `10.1146/annurev.astro.35.1.389`. arXiv: `astro-ph/9704019 [astro-ph]`.

Ellison, Sara L. et al. (Jan. 2008a). Clues to the Origin of the Mass-Metallicity Relation: Dependence on Star Formation Rate and Galaxy Size. ApJ 672.2, p. L107. DOI: `10.1086/527296`. arXiv: `0711.4833 [astro-ph]`.

— (May 2008b). Galaxy Pairs in the Sloan Digital Sky Survey. I. Star Formation, Active Galactic Nucleus Fraction, and the Mass-Metallicity Relation. AJ 135.5, pp. 1877–1899. DOI: `10.1088/0004-6256/135/5/1877`. arXiv: `0803.0161 [astro-ph]`.

Ellison, Sara L. et al. (Nov. 2013). Galaxy pairs in the Sloan Digital Sky Survey - VIII. The observational properties of post-merger galaxies. MNRAS 435.4, pp. 3627–3638. DOI: `10.1093/mnras/stt1562`. arXiv: `1308.3707 [astro-ph.CO]`.

Epinat, B. et al. (Sept. 2009). Integral field spectroscopy with SINFONI of VVDS galaxies. I. Galaxy dynamics and mass assembly at 1.2 < z < 1.6. A&A 504.3, pp. 789–805. DOI: `10.1051/0004-6361/200911995`. arXiv: `0903.1216 [astro-ph.CO]`.

Erb, Dawn K. et al. (June 2006a). The Mass-Metallicity Relation at $z \gtrsim 2$. ApJ 644.2, pp. 813–828. DOI: `10.1086/503623`. arXiv: `astro-ph/0602473 [astro-ph]`.

Erb, Dawn K. et al. (July 2006b). The Stellar, Gas, and Dynamical Masses of Star-forming Galaxies at z ~2. ApJ 646.1, pp. 107–132. DOI: `10.1086/504891`. arXiv: `astro-ph/0604041 [astro-ph]`.

Erb, Dawn K. et al. (Aug. 2010). Physical Conditions in a Young, Unreddened, Low-metallicity Galaxy at High Redshift. ApJ 719.2, pp. 1168–1190. DOI: `10.1088/0004-637X/719/2/1168`. arXiv: `1006.5456 [astro-ph.CO]`.

Ferland, G. J. et al. (July 1998). CLOUDY 90: Numerical Simulation of Plasmas and Their Spectra. PASP 110.749, pp. 761–778. DOI: `10.1086/316190`.

Figueira, M. et al. (Nov. 2022). SFR estimations from z = 0 to z = 0.9. A comparison of SFR calibrators for star-forming galaxies. A&A 667, A29, A29. DOI: `10.1051/0004-6361/202141701`. arXiv: `2209.04390 [astro-ph.GA]`.

Finkelstein, Steven L. et al. (Mar. 2011). The HETDEX Pilot Survey. III. The Low Metallicities of High-redshift Lyα Galaxies. ApJ 729.2, 140, p. 140. DOI: `10.1088/0004-637X/729/2/140`. arXiv: `1011.0431 [astro-ph.CO]`.

Finlator, Kristian et al. (Apr. 2008). The origin of the galaxy mass-metallicity relation and implications for galactic outflows. MNRAS 385.4, pp. 2181–2204. DOI: `10.1111/j.1365-2966.2008.12991.x`. arXiv: `0704.3100 [astro-ph]`.

Fioc, M. et al. (Oct. 1997). PEGASE: a UV to NIR spectral evolution model of galaxies. Application to the calibration of bright galaxy counts. A&A 326, pp. 950–962. DOI: `10.48550/arXiv.astro-ph/9707017`. arXiv: `astro-ph/9707017 [astro-ph]`.

Fioc, Michel et al. (Dec. 1999). PEGASE.2, a metallicity-consistent spectral evolution model of galaxies: the documentation and the code. *arXiv e-prints*, astro-ph/9912179, astro–ph/9912179. DOI: `10.48550/arXiv.astro-ph/9912179`. arXiv: `astro-ph/9912179 [astro-ph]`.

— (Mar. 2019). PÉGASE.3: A code for modeling the UV-to-IR/submm spectral and chemical evolution of galaxies with dust. A&A 623, A143, A143. DOI: `10.1051/0004-6361/201833556`. arXiv: `1902.07929 [astro-ph.GA]`.

Fluetsch, A. et al. (Mar. 2019). Cold molecular outflows in the local Universe and their feedback effect on galaxies. MNRAS 483.4, pp. 4586–4614. DOI: `10.1093/mnras/sty3449`. arXiv: `1805.05352 [astro-ph.GA]`.

Förster Schreiber, N. M. et al. (Dec. 2009). The SINS Survey: SINFONI Integral Field Spectroscopy of z ~2 Star-forming Galaxies. ApJ 706.2, pp. 1364–1428. DOI: `10.1088/0004-637X/706/2/1364`. arXiv: `0903.1872 [astro-ph.CO]`.

Gao, YuLong et al. (Dec. 2018). Mass-Metallicity Relation and Fundamental Metallicity Relation of Metal-poor Star-forming Galaxies at $0.6 < Z < 0.9$ from the eBOSS Survey. ApJ 869.1, 15, p. 15. DOI: `10.3847/1538-4357/aae9ef`. arXiv: `1810.08928 [astro-ph.GA]`.

Garilli, B. et al. (July 2010). EZ: A Tool For Automatic Redshift Measurement. PASP 122.893, p. 827. DOI: `10.1086/654903`. arXiv: `1005.2825 [astro-ph.IM]`.

Garilli, B. et al. (Feb. 2014). The VIMOS Public Extragalactic Survey (VIPERS). First Data Release of 57 204 spectroscopic measurements. A&A 562, A23, A23. DOI: `10.1051/0004-6361/201322790`. arXiv: `1310.1008 [astro-ph.CO]`.

Garnett, Donald R. (Dec. 2002). The Luminosity-Metallicity Relation, Effective Yields, and Metal Loss in Spiral and Irregular Galaxies. ApJ 581.2, pp. 1019–1031. DOI: `10.1086/344301`. arXiv: `astro-ph/0209012 [astro-ph]`.

Genzel, R. et al. (Feb. 2015). Combined CO and Dust Scaling Relations of Depletion Time and Molecular Gas Fractions with Cosmic Time, Specific Star-formation Rate, and Stellar Mass. ApJ 800.1, 20, p. 20. DOI: `10.1088/0004-637X/800/1/20`. arXiv: `1409.1171 [astro-ph.GA]`.

Grasshorn Gebhardt, Henry S. et al. (Jan. 2016). Young, Star-forming Galaxies and Their Local Counterparts: The Evolving Relationship of Mass-SFR-Metallicity Since z $\sim$ 2.1. ApJ 817.1, 10, p. 10. DOI: `10.3847/0004-637X/817/1/10`. arXiv: `1511.08243 [astro-ph.GA]`.

Guo, Yicheng et al. (May 2016). Stellar Mass-Gas-phase Metallicity Relation at 0.5 $\leq$ z $\leq$ 0.7: A Power Law with Increasing Scatter toward the Low-mass Regime. ApJ 822.2, 103, p. 103. DOI: `10.3847/0004-637X/822/2/103`. arXiv: `1603.04863 [astro-ph.GA]`.

Guzzo, L. et al. (Mar. 2013). VIPERS: An Unprecedented View of Galaxies and Large-scale Structure Halfway Back in the Life of the Universe. *The Messenger* 151, pp. 41–46. arXiv: `1303.3930 [astro-ph.CO]`.

Guzzo, L. et al. (June 2014). The VIMOS Public Extragalactic Redshift Survey (VIPERS). An unprecedented view of galaxies and large-scale structure at $0.5 < z < 1.2$. A&A 566, A108, A108. DOI: `10.1051/0004-6361/201321489`. arXiv: `1303.2623 [astro-ph.CO]`.

Haines, C. P. et al. (Aug. 2017). The VIMOS Public Extragalactic Redshift Survey (VIPERS). Downsizing of the blue cloud and the influence of galaxy size on mass quenching over the last eight billion years. A&A 605, A4, A4. DOI: `10.1051/0004-6361/201630118`. arXiv: `1611.07050 [astro-ph.GA]`.

Hamed, M. et al. (Feb. 2021). Multiwavelength dissection of a massive heavily dust-obscured galaxy and its blue companion at $z \sim 2$. A&A 646, A127, A127. DOI: `10.1051/0004-6361/202039577`. arXiv: `2101.07724 [astro-ph.GA]`.

Hamed, M. et al. (2023a). Decoding the IRX-β dust attenuation relation in star-forming galaxies at intermediate redshift. A&A submitted.

Hamed, M. et al. (Apr. 2023b). The slippery slope of dust attenuation curves: Correlation of dust attenuation laws with star-to-dust compactness up to z = 4. *arXiv e-prints*, arXiv:2304.13713, arXiv:2304.13713. DOI: `10.48550/arXiv.2304.13713`. arXiv: `2304.13713 [astro-ph.GA]`.

Haurberg, Nathalie C. et al. (Mar. 2013). Metal Abundances of 12 Dwarf Irregulars from the ADBS Survey. ApJ 765.1, 66, p. 66. DOI: `10.1088/0004-637X/765/1/66`. arXiv: `1301.7513 [astro-ph.CO]`.

Haurberg, Nathalie C. et al. (Feb. 2015). Oxygen Abundance Measurements of SHIELD Galaxies. ApJ 800.2, 121, p. 121. DOI: `10.1088/0004-637X/800/2/121`. arXiv: `1501.05159 [astro-ph.GA]`.

Heckman, T. M. (Jan. 2002). Galactic Superwinds Circa 2001. *Extragalactic Gas at Low Redshift*. Ed. by John S. Mulchaey et al. Vol. 254. Astronomical Society of the Pacific Conference Series, p. 292. DOI: `10.48550/arXiv.astro-ph/0107438`. arXiv: `astro-ph/0107438 [astro-ph]`.

Heckman, Timothy M. et al. (Aug. 2015). The Systematic Properties of the Warm Phase of Starburst-Driven Galactic Winds. ApJ 809.2, 147, p. 147. DOI: `10.1088/0004-637X/809/2/147`. arXiv: `1507.05622 [astro-ph.GA]`.

Heckman, Timothy M. et al. (Jan. 2017). Galactic Winds and the Role Played by Massive Stars. *arXiv e-prints*, arXiv:1701.09062, arXiv:1701.09062. DOI: `10.48550/arXiv.1701.09062`. arXiv: `1701.09062 [astro-ph.GA]`.

Henry, Alaina et al. (Oct. 2013a). Low Masses and High Redshifts: The Evolution of the Mass-Metallicity Relation. ApJ 776.2, L27, p. L27. DOI: 10.1088/2041-8205/776/2/L27. arXiv: 1309.4458 [astro-ph.CO].

Henry, Alaina et al. (June 2013b). The Metallicity Evolution of Low-mass Galaxies: New Constraints at Intermediate Redshift. ApJ 769.2, 148, p. 148. DOI: 10.1088/0004-637X/769/2/148. arXiv: 1304.4239 [astro-ph.CO].

Hirschauer, Alec S. et al. (Feb. 2018). Metal Abundances of KISS Galaxies. VI. New Metallicity Relations for the KISS Sample of Star-forming Galaxies. AJ 155.2, 82, p. 82. DOI: 10.3847/1538-3881/aaa4ba. arXiv: 1801.01133 [astro-ph.GA].

Hoaglin, David C. et al. (1983). *Understanding robust and exploratory data anlysis*.

Hoopes, Charles G. et al. (Dec. 2007). The Diverse Properties of the Most Ultraviolet-Luminous Galaxies Discovered by GALEX. ApJS 173.2, pp. 441–456. DOI: 10.1086/516644. arXiv: astro-ph/0609415 [astro-ph].

Hopkins, A. M. et al. (Dec. 2003). Star Formation Rate Indicators in the Sloan Digital Sky Survey. ApJ 599.2, pp. 971–991. DOI: 10.1086/379608. arXiv: astro-ph/0306621 [astro-ph].

Hoyos, C. et al. (Dec. 2005). The DEEP2 Galaxy Redshift Survey: Discovery of Luminous, Metal-poor Star-forming Galaxies at Redshifts z ∼0.7. ApJ 635.1, pp. L21–L24. DOI: 10.1086/499232. arXiv: astro-ph/0510843 [astro-ph].

Huang, Chi et al. (Nov. 2019). The Mass-Metallicity Relation at $z \sim 0.8$: Redshift Evolution and Parameter Dependency. ApJ 886.1, 31, p. 31. DOI: 10.3847/1538-4357/ab4902. arXiv: 1910.08689 [astro-ph.GA].

Hunt, Leslie et al. (Dec. 2012). Scaling relations of metallicity, stellar mass and star formation rate in metal-poor starbursts - I. A Fundamental Plane. MNRAS 427.2, pp. 906–918. DOI: 10.1111/j.1365-2966.2012.21761.x. arXiv: 1209.1100 [astro-ph.CO].

Ilbert, O. et al. (Sept. 2005). The VIMOS-VLT deep survey. Evolution of the galaxy luminosity function up to $z = 2$ in first epoch data. A&A 439.3, pp. 863–876. DOI: 10.1051/0004-6361:20041961. arXiv: astro-ph/0409134 [astro-ph].

Ilbert, O. et al. (Oct. 2006a). Accurate photometric redshifts for the CFHT legacy survey calibrated using the VIMOS VLT deep survey. A&A 457.3, pp. 841–856. DOI: 10.1051/0004-6361:20065138. arXiv: astro-ph/0603217 [astro-ph].

Ilbert, O. et al. (July 2006b). The VIMOS-VLT Deep Survey. Galaxy luminosity function per morphological type up to $z = 1.2$. A&A 453.3, pp. 809–815. DOI: 10.1051/0004-6361:20053632. arXiv: astro-ph/0604010 [astro-ph].

Ilbert, O. et al. (Feb. 2010). Galaxy Stellar Mass Assembly Between 0.2 < z < 2 from the S-COSMOS Survey. ApJ 709.2, pp. 644–663. DOI: 10.1088/0004-637X/709/2/644. arXiv: 0903.0102 [astro-ph.CO].

Izotov, Y. I. et al. (Mar. 2006a). The chemical composition of metal-poor emission-line galaxies in the Data Release 3 of the Sloan Digital Sky Survey. A&A 448.3, pp. 955–970. DOI: 10.1051/0004-6361:20053763. arXiv: astro-ph/0511644 [astro-ph].

Izotov, Y. I. et al. (Nov. 2006b). VLT/GIRAFFE spectroscopic observations of the metal-poor blue compact dwarf galaxy SBS 0335-052E. A&A 459.1, pp. 71–84. DOI: 10.1051/0004-6361:20065622. arXiv: astro-ph/0608203 [astro-ph].

Izotov, Y. I. et al. (Oct. 2012). Hunting for extremely metal-poor emission-line galaxies in the Sloan Digital Sky Survey: MMT and 3.5 m APO observations. A&A 546, A122, A122. DOI: 10.1051/0004-6361/201219733. arXiv: 1207.5971 [astro-ph.CO].

Izotov, Y. I. et al. (Aug. 2015). On the universality of luminosity-metallicity and mass-metallicity relations for compact star-forming galaxies at redshifts $0 < z < 3$. MNRAS 451.3, pp. 2251–2262. DOI: 10.1093/mnras/stv1115. arXiv: 1505.05853 [astro-ph.GA].

Izotov, Y. I. et al. (Jan. 2018). J0811+4730: the most metal-poor star-forming dwarf galaxy known. MNRAS 473.2, pp. 1956–1966. DOI: 10.1093/mnras/stx2478. arXiv: 1709.00202 [astro-ph.GA].

Izotov, Yuri I. et al. (Aug. 2007). MMT Observations of New Extremely Metal-poor Emission-Line Galaxies in the Sloan Digital Sky Survey. ApJ 665.2, pp. 1115–1128. DOI: 10.1086/519922. arXiv: 0704.3842 [astro-ph].

Izotov, Yuri I. et al. (Feb. 2011). Green Pea Galaxies and Cohorts: Luminous Compact Emission-line Galaxies in the Sloan Digital Sky Survey. ApJ 728.2, 161, p. 161. DOI: 10.1088/0004-637X/728/2/161. arXiv: 1012.5639 [astro-ph.CO].

Jaskot, A. E. et al. (Dec. 2016). Photoionization Models for the Semi-forbidden C III] 1909 Emission in Star-forming Galaxies. ApJ 833.2, 136, p. 136. DOI: 10.3847/1538-4357/833/2/136. arXiv: 1610.03778 [astro-ph.GA].

Johnston, Russell et al. (Nov. 2015). The evolving relation between star formation rate and stellar mass in the VIDEO survey since z = 3. MNRAS 453.3, pp. 2540–2557. DOI: 10.1093/mnras/stv1715. arXiv: 1507.07503 [astro-ph.GA].

Kacprzak, Glenn G. et al. (July 2016). Cold-mode Accretion: Driving the Fundamental Mass-Metallicity Relation at z ~2. ApJ 826.1, L11, p. L11. DOI: 10.3847/2041-8205/826/1/L11. arXiv: 1607.00014 [astro-ph.GA].

Kashino, D. et al. (Jan. 2017). The FMOS-COSMOS Survey of Star-forming Galaxies at $z \approx 1.6$. IV. Excitation State and Chemical Enrichment of the Interstellar Medium. ApJ 835.1, 88, p. 88. DOI: 10.3847/1538-4357/835/1/88. arXiv: 1604.06802 [astro-ph.GA].

Kauffmann, Guinevere et al. (May 2003a). Stellar masses and star formation histories for 10^5 galaxies from the Sloan Digital Sky Survey. MNRAS 341.1, pp. 33–53. DOI: 10.1046/j.1365-8711.2003.06291.x. arXiv: astro-ph/0204055 [astro-ph].

Kauffmann, Guinevere et al. (Dec. 2003b). The host galaxies of active galactic nuclei. MNRAS 346.4, pp. 1055–1077. DOI: 10.1111/j.1365-2966.2003.07154.x. arXiv: astro-ph/0304239 [astro-ph].

Kennicutt Robert C., Jr. (Jan. 1998). Star Formation in Galaxies Along the Hubble Sequence. ARA&A 36, pp. 189–232. DOI: 10.1146/annurev.astro.36.1.189. arXiv: astro-ph/9807187 [astro-ph].

Kennicutt Robert C., Jr. et al. (July 2003). The Composition Gradient in M101 Revisited. II. Electron Temperatures and Implications for the Nebular Abundance Scale. ApJ 591.2, pp. 801–820. DOI: 10.1086/375398. arXiv: astro-ph/0303452 [astro-ph].

Kennicutt, Robert C. et al. (Sept. 2012). Star Formation in the Milky Way and Nearby Galaxies. ARA&A 50, pp. 531–608. DOI: 10.1146/annurev-astro-081811-125610. arXiv: 1204.3552 [astro-ph.GA].

Kewley, L. J. et al. (Sept. 2002). Using Strong Lines to Estimate Abundances in Extragalactic H II Regions and Starburst Galaxies. ApJS 142.1, pp. 35–52. DOI: 10.1086/341326. arXiv: astro-ph/0206495 [astro-ph].

Kewley, Lisa J. et al. (July 2008). Metallicity Calibrations and the Mass-Metallicity Relation for Star-forming Galaxies. ApJ 681.2, pp. 1183–1204. DOI: 10.1086/587500. arXiv: 0801.1849 [astro-ph].

Kewley, Lisa J. et al. (Sept. 2013a). The Cosmic BPT Diagram: Confronting Theory with Observations. ApJ 774.1, L10, p. L10. DOI: 10.1088/2041-8205/774/1/L10. arXiv: 1307.0514 [astro-ph.CO].

Kewley, Lisa J. et al. (Sept. 2013b). Theoretical Evolution of Optical Strong Lines across Cosmic Time. ApJ 774.2, 100, p. 100. DOI: 10.1088/0004-637X/774/2/100. arXiv: 1307.0508 [astro-ph.CO].

Kewley, Lisa J. et al. (Sept. 2013c). Theoretical Evolution of Optical Strong Lines across Cosmic Time. ApJ 774.2, 100, p. 100. DOI: `10.1088/0004-637X/774/2/100`. arXiv: `1307.0508 [astro-ph.CO]`.

Kewley, Lisa J. et al. (Oct. 2015). A Rise in the Ionizing Photons in Star-forming Galaxies over the Past 8 Billion Years. ApJ 812.2, L20, p. L20. DOI: `10.1088/2041-8205/812/2/L20`. arXiv: `1507.07932 [astro-ph.GA]`.

Khochfar, S. et al. (July 2009). Dry mergers: a crucial test for galaxy formation. MNRAS 397.1, pp. 506–510. DOI: `10.1111/j.1365-2966.2009.14958.x`. arXiv: `0809.1734 [astro-ph]`.

Kinman, T. D. et al. (Jan. 1981). Spectroscopic observations of 10 emission-line dwarf galaxies. ApJ 243, pp. 127–139. DOI: `10.1086/158575`.

Kobulnicky, Henry A. et al. (Dec. 2003). The DEEP Groth Strip Survey. VII. The Metallicity of Field Galaxies at 0.26 < z < 0.82 and the Evolution of the Luminosity-Metallicity Relation. ApJ 599.2, pp. 1006–1030. DOI: `10.1086/379360`. arXiv: `astro-ph/0310346 [astro-ph]`.

Kobulnicky, Henry A. et al. (Dec. 2004). Metallicities of $0.3 < z < 1.0$ Galaxies in the GOODS-North Field. ApJ 617.1, pp. 240–261. DOI: `10.1086/425299`. arXiv: `astro-ph/0408128 [astro-ph]`.

Kokorev, Vasily I. et al. (Nov. 2021). The Evolving Interstellar Medium of Star-forming Galaxies, as Traced by Stardust. ApJ 921.1, 40, p. 40. DOI: `10.3847/1538-4357/ac18ce`. arXiv: `2109.06209 [astro-ph.GA]`.

Köppen, J. et al. (Feb. 2007). A possible origin of the mass-metallicity relation of galaxies. MNRAS 375.2, pp. 673–684. DOI: `10.1111/j.1365-2966.2006.11328.x`. arXiv: `astro-ph/0611723 [astro-ph]`.

Kreckel, K. et al. (Jan. 2015). The Metallicity of Void Dwarf Galaxies. ApJ 798.1, L15, p. L15. DOI: `10.1088/2041-8205/798/1/L15`. arXiv: `1410.5821 [astro-ph.GA]`.

Kroupa, Pavel (Apr. 2001). On the variation of the initial mass function. MNRAS 322.2, pp. 231–246. DOI: `10.1046/j.1365-8711.2001.04022.x`. arXiv: `astro-ph/0009005 [astro-ph]`.

Kumari, Nimisha et al. (May 2019). Metallicity calibrations for diffuse ionized gas and low-ionization emission regions. MNRAS 485.1, pp. 367–381. DOI: `10.1093/mnras/stz366`. arXiv: `1902.01408 [astro-ph.GA]`.

Kumari, Nimisha et al. (Aug. 2021). The extension of the Fundamental Metallicity Relation beyond the BPT star-forming sequence: evidence for both gas accretion and starvation. *arXiv e-prints*, arXiv:2108.12437, arXiv:2108.12437. arXiv: `2108.12437 [astro-ph.GA]`.

Kurczynski, Peter et al. (Mar. 2016). Evolution of Intrinsic Scatter in the SFR-Stellar Mass Correlation at 0.5 < z < 3. ApJ 820.1, L1, p. L1. DOI: `10.3847/2041-8205/820/1/L1`. arXiv: `1602.03909 [astro-ph.GA]`.

Lagos, Claudia del P. et al. (July 2016a). The Fundamental Plane of star formation in galaxies revealed by the EAGLE hydrodynamical simulations. MNRAS 459.3, pp. 2632–2650. DOI: `10.1093/mnras/stw717`. arXiv: `1510.08067 [astro-ph.GA]`.

Lagos, P. et al. (Feb. 2016b). On the properties of the interstellar medium in extremely metal-poor blue compact dwarf galaxies. A VIMOS-IFU study of the cometary galaxy and Ly α absorber Tol 65. MNRAS 456.2, pp. 1549–1564. DOI: `10.1093/mnras/stv2702`. arXiv: `1511.06707 [astro-ph.GA]`.

Lamareille, F. (Jan. 2010). Spectral classification of emission-line galaxies from the Sloan Digital Sky Survey. I. An improved classification for high-redshift galaxies. A&A 509, A53, A53. DOI: `10.1051/0004-6361/200913168`. arXiv: `0910.4814 [astro-ph.CO]`.

Lamareille, F. et al. (Feb. 2009). Physical properties of galaxies and their evolution in the VIMOS VLT Deep Survey. I. The evolution of the mass-metallicity relation up to z
sim0.9. A&A 495.1, pp. 53–72. DOI: 10.1051/0004-6361:200810397. arXiv: 0811.2053 [astro-ph].

Lara-López, M. A. et al. (Oct. 2010). A fundamental plane for field star-forming galaxies. A&A 521, L53, p. L53. DOI: 10.1051/0004-6361/201014803. arXiv: 1005.0509 [astro-ph.CO].

Law, David R. et al. (Feb. 2007). The Physical Nature of Rest-UV Galaxy Morphology during the Peak Epoch of Galaxy Formation. ApJ 656.1, pp. 1–26. DOI: 10.1086/510357. arXiv: astro-ph/0610693 [astro-ph].

Law, David R. et al. (Jan. 2009). Kinematics and Formation Mechanisms of High-Redshift Galaxies. *astro2010: The Astronomy and Astrophysics Decadal Survey*. Vol. 2010, p. 172. DOI: 10.48550/arXiv.0902.2567. arXiv: 0902.2567 [astro-ph.GA].

Le Fèvre, O. et al. (Nov. 2013). The VIMOS VLT Deep Survey final data release: a spectroscopic sample of 35 016 galaxies and AGN out to z ~6.7 selected with 17.5 $\leq$ i_{AB} $\leq$ 24.75. A&A 559, A14, A14. DOI: 10.1051/0004-6361/201322179. arXiv: 1307.0545 [astro-ph.CO].

Le Fèvre, Oliver et al. (Mar. 2003a). Commissioning and performances of the VLT-VIMOS instrument. *Instrument Design and Performance for Optical/Infrared Ground-based Telescopes*. Ed. by Masanori Iye et al. Vol. 4841. Society of Photo-Optical Instrumentation Engineers (SPIE) Conference Series, pp. 1670–1681. DOI: 10.1117/12.460959.

— (Mar. 2003b). Commissioning and performances of the VLT-VIMOS instrument. *Instrument Design and Performance for Optical/Infrared Ground-based Telescopes*. Ed. by Masanori Iye et al. Vol. 4841. Society of Photo-Optical Instrumentation Engineers (SPIE) Conference Series, pp. 1670–1681. DOI: 10.1117/12.460959.

Lee, Henry et al. (Aug. 2006). On Extending the Mass-Metallicity Relation of Galaxies by 2.5 Decades in Stellar Mass. ApJ 647.2, pp. 970–983. DOI: 10.1086/505573. arXiv: astro-ph/0605036 [astro-ph].

Lee, Nicholas et al. (Mar. 2015). A Turnover in the Galaxy Main Sequence of Star Formation at M_* ~10^{10} $M_\odot$ for Redshifts z < 1.3. ApJ 801.2, 80, p. 80. DOI: 10.1088/0004-637X/801/2/80. arXiv: 1501.01080 [astro-ph.GA].

Lehnert, M. D. et al. (July 2009). Physical Conditions in the Interstellar Medium of Intensely Star-Forming Galaxies at Redshift~2. ApJ 699.2, pp. 1660–1678. DOI: 10.1088/0004-637X/699/2/1660. arXiv: 0902.2784 [astro-ph.CO].

Lequeux, J. et al. (Dec. 1979). Reprint of 1979A&A....80..155L. Chemical composition and evolution of irregular and blue compact galaxies. A&A 500, pp. 145–156.

Lian, J. H. et al. (Jan. 2015). The mass-metallicity relation of Lyman-break analogues and its dependence on galaxy properties. MNRAS 446.2, pp. 1449–1457. DOI: 10.1093/mnras/stu2184. arXiv: 1411.6331 [astro-ph.GA].

Lian, Jianhui et al. (Dec. 2018a). Modelling the MZR of galaxies from $z \sim 3.5$ to 0. MNRAS 481.3, pp. 4000–4008. DOI: 10.1093/mnras/sty2506. arXiv: 1809.04079 [astro-ph.GA].

Lian, Jianhui et al. (Feb. 2018b). The mass-metallicity relations for gas and stars in star-forming galaxies: strong outflow versus variable IMF. MNRAS 474.1, pp. 1143–1164. DOI: 10.1093/mnras/stx2829. arXiv: 1710.11135 [astro-ph.GA].

Lilly, Simon J. et al. (Aug. 2013). Gas Regulation of Galaxies: The Evolution of the Cosmic Specific Star Formation Rate, the Metallicity-Mass-Star-formation Rate Relation, and the Stellar Content of Halos. ApJ 772.2, 119, p. 119. DOI: 10.1088/0004-637X/772/2/119. arXiv: 1303.5059 [astro-ph.CO].

Liu, Xin et al. (May 2008). Metallicities and Physical Conditions in Star-forming Galaxies at z ~1.0-1.5. ApJ 678.2, pp. 758–779. DOI: 10.1086/529030. arXiv: 0801.1670 [astro-ph].

Lo Faro, B. et al. (Dec. 2017). Characterizing the UV-to-NIR shape of the dust attenuation curve of IR luminous galaxies up to $z \sim 2$. MNRAS 472.2, pp. 1372–1391. DOI: 10.1093/mnras/stx1901. arXiv: 1707.09805 [astro-ph.GA].

Ly, Chun et al. (Sept. 2016). The Metal Abundances across Cosmic Time (MACT) Survey. II. Evolution of the Mass-metallicity Relation over 8 Billion Years, Using [OIII]4363AA-based Metallicities. ApJ 828.2, 67, p. 67. DOI: 10.3847/0004-637X/828/2/67. arXiv: 1602.01098 [astro-ph.GA].

Ma, Xiangcheng et al. (Feb. 2016). The origin and evolution of the galaxy mass-metallicity relation. MNRAS 456.2, pp. 2140–2156. DOI: 10.1093/mnras/stv2659. arXiv: 1504.02097 [astro-ph.GA].

Madau, Piero et al. (Aug. 2014). Cosmic Star-Formation History. ARA&A 52, pp. 415–486. DOI: 10.1146/annurev-astro-081811-125615. arXiv: 1403.0007 [astro-ph.CO].

Maier, C. et al. (May 2004). The metallicity-luminosity relation at medium redshift based on faint CADIS emission line galaxies. A&A 418, pp. 475–485. DOI: 10.1051/0004-6361:20035795. arXiv: astro-ph/0402048 [astro-ph].

Maier, C. et al. (Dec. 2005). Near-Infrared Spectroscopy of 0.4 < z < 1.0 CFRS Galaxies: Oxygen Abundances, SFRs, and Dust. ApJ 634.2, pp. 849–860. DOI: 10.1086/497091. arXiv: astro-ph/0508239 [astro-ph].

Maier, C. et al. (Mar. 2006). Oxygen Gas Abundances at z~1.4: Implications for the Chemical Evolution History of Galaxies. ApJ 639.2, pp. 858–867. DOI: 10.1086/499518. arXiv: astro-ph/0511255 [astro-ph].

Maier, C. et al. (Sept. 2014). The Mass-Metallicity and Fundamental Metallicity Relations at z > 2 Using Very Large Telescope and Subaru Near-infrared Spectroscopy of zCOSMOS Galaxies. ApJ 792.1, 3, p. 3. DOI: 10.1088/0004-637X/792/1/3. arXiv: 1406.6069 [astro-ph.GA].

Maier, C. et al. (May 2015a). Mass-metallicity relation of zCOSMOS galaxies at z $\approx$ 0.7, its dependence on star formation rate, and the existence of massive low-metallicity galaxies. A&A 577, A14, A14. DOI: 10.1051/0004-6361/201425224. arXiv: 1410.7389 [astro-ph.GA].

Maier, Christian et al. (Feb. 2015b). Oxygen abundances of zCOSMOS galaxies at z ~1.4 based on five lines and implications for the fundamental metallicity relation. *Galaxies in 3D across the Universe*. Ed. by Bodo L. Ziegler et al. Vol. 309, pp. 281–282. DOI: 10.1017/S1743921314009867. arXiv: 1408.5896 [astro-ph.GA].

Maiolino, R. et al. (Sept. 2008). AMAZE. I. The evolution of the mass-metallicity relation at $z > 3$. A&A 488.2, pp. 463–479. DOI: 10.1051/0004-6361:200809678. arXiv: 0806.2410 [astro-ph].

Maiolino, R. et al. (Feb. 2019). De re metallica: the cosmic chemical evolution of galaxies. A&A Rev. 27.1, 3, p. 3. DOI: 10.1007/s00159-018-0112-2. arXiv: 1811.09642 [astro-ph.GA].

Małek, K. et al. (Nov. 2018). HELP: modelling the spectral energy distributions of Herschel detected galaxies in the ELAIS N1 field. A&A 620, A50, A50. DOI: 10.1051/0004-6361/201833131. arXiv: 1809.00529 [astro-ph.GA].

Mannucci, F. et al. (Oct. 2009). LSD: Lyman-break galaxies Stellar populations and Dynamics - I. Mass, metallicity and gas at $z \sim 3.1$. MNRAS 398.4, pp. 1915–1931. DOI: 10.1111/j.1365-2966.2009.15185.x. arXiv: 0902.2398 [astro-ph.CO].

Mannucci, F. et al. (Nov. 2010). A fundamental relation between mass, star formation rate and metallicity in local and high-redshift galaxies. MNRAS 408.4, pp. 2115–2127. DOI: 10.1111/j.1365-2966.2010.17291.x. arXiv: 1005.0006 [astro-ph.CO].

Maraston, C. et al. (Dec. 2011). Stellar population models at high spectral resolution. MNRAS 418.4, pp. 2785–2811. DOI: 10.1111/j.1365-2966.2011.19738.x. arXiv: 1109.0543 [astro-ph.CO].

Maraston, Claudia (Sept. 2005). Evolutionary population synthesis: models, analysis of the ingredients and application to high-z galaxies. MNRAS 362.3, pp. 799–825. DOI: 10.1111/j.1365-2966.2005.09270.x. arXiv: astro-ph/0410207 [astro-ph].

Marchesini, Danilo et al. (Aug. 2009). The Evolution of the Stellar Mass Function of Galaxies from z = 4.0 and the First Comprehensive Analysis of its Uncertainties: Evidence for Mass-Dependent Evolution. ApJ 701.2, pp. 1765–1796. DOI: 10.1088/0004-637X/701/2/1765. arXiv: 0811.1773 [astro-ph].

Martin, Crystal L. et al. (Dec. 2012). Demographics and Physical Properties of Gas Outflows/Inflows at 0.4 < z < 1.4. ApJ 760.2, 127, p. 127. DOI: 10.1088/0004-637X/760/2/127. arXiv: 1206.5552 [astro-ph.CO].

Matteucci, Francesca (2012). *Chemical Evolution of Galaxies*. DOI: 10.1007/978-3-642-22491-1.

Matthee, Jorryt et al. (Mar. 2019). The origin of scatter in the star formation rate-stellar mass relation. MNRAS 484.1, pp. 915–932. DOI: 10.1093/mnras/stz030. arXiv: 1805.05956 [astro-ph.GA].

McCracken, H. J. et al. (Oct. 2003). The VIRMOS deep imaging survey. II: CFH12K BVRI optical data for the 0226-04 deep field. A&A 410, pp. 17–32. DOI: 10.1051/0004-6361:20031081. arXiv: astro-ph/0306254 [astro-ph].

McGaugh, Stacy S. (Oct. 1991). H II Region Abundances: Model Oxygen Line Ratios. ApJ 380, p. 140. DOI: 10.1086/170569.

Mellier, Y et al. (2008). The CFHTLS T0005 Release.

Menci, N. et al. (Aug. 2006). The Abundance of Distant and Extremely Red Galaxies: The Role of AGN Feedback in Hierarchical Models. ApJ 647.2, pp. 753–762. DOI: 10.1086/505528. arXiv: astro-ph/0605123 [astro-ph].

Michałowski, M. J. et al. (May 2012). The stellar masses and specific star-formation rates of submillimetre galaxies. A&A 541, A85, A85. DOI: 10.1051/0004-6361/201016308. arXiv: 1108.6058 [astro-ph.CO].

Mitra, Sourav et al. (Jan. 2017). Equilibrium model prediction for the scatter in the star-forming main sequence. MNRAS 464.3, pp. 2766–2776. DOI: 10.1093/mnras/stw2527. arXiv: 1606.07436 [astro-ph.GA].

Mohammad, F. G. et al. (Nov. 2018). The VIMOS Public Extragalactic Redshift Survey (VIPERS). Unbiased clustering estimate with VIPERS slit assignment. A&A 619, A17, A17. DOI: 10.1051/0004-6361/201833853. arXiv: 1807.05999 [astro-ph.CO].

Mollá, Mercedes et al. (Aug. 2015). Galactic chemical evolution: stellar yields and the initial mass function. MNRAS 451.4, pp. 3693–3708. DOI: 10.1093/mnras/stv1102. arXiv: 1505.03341 [astro-ph.GA].

Moustakas, John et al. (Dec. 2011). Evolution of the Stellar Mass-Metallicity Relation Since z=0.75. *arXiv e-prints*, arXiv:1112.3300, arXiv:1112.3300. DOI: 10.48550/arXiv.1112.3300. arXiv: 1112.3300 [astro-ph.CO].

Moustakas, John et al. (Apr. 2013). PRIMUS: Constraints on Star Formation Quenching and Galaxy Merging, and the Evolution of the Stellar Mass Function from z = 0-1. ApJ 767.1, 50, p. 50. DOI: 10.1088/0004-637X/767/1/50. arXiv: 1301.1688 [astro-ph.CO].

Moutard, T. et al. (May 2016a). The VIPERS Multi-Lambda Survey. I. UV and near-IR observations, multi-colour catalogues, and photometric redshifts. A&A 590, A102, A102. DOI: `10.1051/0004-6361/201527945`. arXiv: `1602.05915 [astro-ph.GA]`.

Moutard, T. et al. (May 2016b). The VIPERS Multi-Lambda Survey. II. Diving with massive galaxies in 22 square degrees since $z = 1.5$. A&A 590, A103, A103. DOI: `10.1051/0004-6361/201527294`. arXiv: `1602.05917 [astro-ph.GA]`.

Naab, Thorsten et al. (Aug. 2017). Theoretical Challenges in Galaxy Formation. ARA&A 55.1, pp. 59–109. DOI: `10.1146/annurev-astro-081913-040019`. arXiv: `1612.06891 [astro-ph.GA]`.

Nagao, T. et al. (Nov. 2006). Gas metallicity diagnostics in star-forming galaxies. A&A 459.1, pp. 85–101. DOI: `10.1051/0004-6361:20065216`. arXiv: `astro-ph/0603580 [astro-ph]`.

Nagao, T. et al. (Feb. 2011). Metallicity diagnostics with infrared fine-structure lines. A&A 526, A149, A149. DOI: `10.1051/0004-6361/201015471`. arXiv: `1012.2471 [astro-ph.CO]`.

Nakajima, Kimihiko et al. (Jan. 2012). Average Metallicity and Star Formation Rate of Lyα Emitters Probed by a Triple Narrowband Survey. ApJ 745.1, 12, p. 12. DOI: `10.1088/0004-637X/745/1/12`. arXiv: `1105.2824 [astro-ph.CO]`.

Nakajima, Kimihiko et al. (May 2013). First Spectroscopic Evidence for High Ionization State and Low Oxygen Abundance in Lyα Emitters. ApJ 769.1, 3, p. 3. DOI: `10.1088/0004-637X/769/1/3`. arXiv: `1208.3260 [astro-ph.CO]`.

Nakajima, Kimihiko et al. (July 2014). Ionization state of inter-stellar medium in galaxies: evolution, SFR-M_*-Z dependence, and ionizing photon escape. MNRAS 442.1, pp. 900–916. DOI: `10.1093/mnras/stu902`. arXiv: `1309.0207 [astro-ph.CO]`.

Neyrinck, Mark C. et al. (Apr. 2018). The cosmic spiderweb: equivalence of cosmic, architectural and origami tessellations. *Royal Society Open Science* 5.4, 171582, p. 171582. DOI: `10.1098/rsos.171582`. arXiv: `1710.04509 [astro-ph.CO]`.

Niino, Yuu (Dec. 2012). The Redshift Evolution of the Relation between Stellar Mass, Star Formation Rate, and Gas Metallicity of Galaxies. ApJ 761.2, 126, p. 126. DOI: `10.1088/0004-637X/761/2/126`. arXiv: `1205.1897 [astro-ph.CO]`.

Noeske, K. G. et al. (May 2007). Star Formation in AEGIS Field Galaxies since z=1.1: The Dominance of Gradually Declining Star Formation, and the Main Sequence of Star-forming Galaxies. ApJ 660.1, pp. L43–L46. DOI: `10.1086/517926`. arXiv: `astro-ph/0701924 [astro-ph]`.

Noll, S. et al. (Dec. 2009). Analysis of galaxy spectral energy distributions from far-UV to far-IR with CIGALE: studying a SINGS test sample. A&A 507.3, pp. 1793–1813. DOI: `10.1051/0004-6361/200912497`. arXiv: `0909.5439 [astro-ph.CO]`.

O'Leary, Joseph A. et al. (Mar. 2021). EMERGE: empirical predictions of galaxy merger rates since $z \sim 6$. MNRAS 501.3, pp. 3215–3237. DOI: `10.1093/mnras/staa3746`. arXiv: `2001.02687 [astro-ph.GA]`.

Onodera, M. et al. (Aug. 2015). The Ages, Metallicities, and Element Abundance Ratios of Massive Quenched Galaxies at $z \approx 1.6$. ApJ 808.2, 161, p. 161. DOI: `10.1088/0004-637X/808/2/161`. arXiv: `1411.5023 [astro-ph.GA]`.

Onodera, M. et al. (May 2016). ISM Excitation and Metallicity of Star-forming Galaxies at $z \simeq 3.3$ from Near-IR Spectroscopy. ApJ 822.1, 42, p. 42. DOI: `10.3847/0004-637X/822/1/42`. arXiv: `1602.02779 [astro-ph.GA]`.

Pagel, B. E. J. et al. (Oct. 1979). On the composition of H II regions in southern galaxies - I. NGC 300 and 1365. MNRAS 189, pp. 95–113. DOI: `10.1093/mnras/189.1.95`.

Pagel, B. E. J. et al. (Jan. 1981). Abundances in stellar populations and the interstellar medium in galaxies. ARA&A 19, pp. 77–113. DOI: `10.1146/annurev.aa.19.090181.000453`.

Pantoni, L. et al. (Nov. 2021). An ALMA view of 11 dusty star-forming galaxies at the peak of cosmic star formation history. MNRAS 507.3, pp. 3998–4015. DOI: `10.1093/mnras/stab2346`. arXiv: `2108.05596 [astro-ph.GA]`.

Papastergis, Emmanouil et al. (Nov. 2012). A Direct Measurement of the Baryonic Mass Function of Galaxies and Implications for the Galactic Baryon Fraction. ApJ 759.2, 138, p. 138. DOI: `10.1088/0004-637X/759/2/138`. arXiv: `1208.5229 [astro-ph.CO]`.

Papovich, Casey et al. (Oct. 2001). The Stellar Populations and Evolution of Lyman Break Galaxies. ApJ 559.2, pp. 620–653. DOI: `10.1086/322412`. arXiv: `astro-ph/0105087 [astro-ph]`.

Pearson, W. J. et al. (July 2018). Main sequence of star forming galaxies beyond the Herschel confusion limit. A&A 615, A146, A146. DOI: `10.1051/0004-6361/201832821`. arXiv: `1804.03482 [astro-ph.GA]`.

Pearson, W. J. et al. (Nov. 2019). Effect of galaxy mergers on star-formation rates. A&A 631, A51, A51. DOI: `10.1051/0004-6361/201936337`. arXiv: `1908.10115 [astro-ph.GA]`.

Pearson, W. J. et al. (2023). Influence of star-forming galaxy selection on the galaxy main sequence. A&A submitted.

Peeples, Molly S. et al. (May 2014). A Budget and Accounting of Metals at z ~0: Results from the COS-Halos Survey. ApJ 786.1, 54, p. 54. DOI: `10.1088/0004-637X/786/1/54`. arXiv: `1310.2253 [astro-ph.CO]`.

Peimbert, M. et al. (Aug. 1970). On the Chemical Abundance of NGC 6822. A&A 7, p. 311.

Peimbert, Manuel et al. (Aug. 2017). Nebular Spectroscopy: A Guide on Hii Regions and Planetary Nebulae. PASP 129.978, p. 082001. DOI: `10.1088/1538-3873/aa72c3`. arXiv: `1705.06323 [astro-ph.GA]`.

Peng, Ying-jie et al. (Oct. 2014a). From haloes to Galaxies - I. The dynamics of the gas regulator model and the implied cosmic sSFR history. MNRAS 443.4, pp. 3643–3664. DOI: `10.1093/mnras/stu1288`. arXiv: `1402.5964 [astro-ph.CO]`.

— (Feb. 2014b). The dependence of the galaxy mass-metallicity relation on environment and the implied metallicity of the IGM. MNRAS 438.1, pp. 262–270. DOI: `10.1093/mnras/stt2175`. arXiv: `1311.1816 [astro-ph.CO]`.

Penzias, A. A. et al. (July 1965). A Measurement of Excess Antenna Temperature at 4080 Mc/s. ApJ 142, pp. 419–421. DOI: `10.1086/148307`.

Pérez, José M. et al. (Jan. 2016). Direct determination of oxygen abundances in line-emitting star-forming galaxies at intermediate redshift. MNRAS 455.3, pp. 3359–3366. DOI: `10.1093/mnras/stv1949`. arXiv: `1508.05222 [astro-ph.GA]`.

Perez-Martinez, J. M. (Dec. 2014). Derivation of chemical abundances in star-forming galaxies at intermediate redshift. *arXiv e-prints*, arXiv:1412.3853, arXiv:1412.3853. DOI: `10.48550/arXiv.1412.3853`. arXiv: `1412.3853 [astro-ph.GA]`.

Pérez-Montero, E. (July 2014). Deriving model-based T_e-consistent chemical abundances in ionized gaseous nebulae. MNRAS 441.3, pp. 2663–2675. DOI: `10.1093/mnras/stu753`. arXiv: `1404.3936 [astro-ph.GA]`.

Pérez-Montero, E. et al. (Feb. 2009). Physical properties of galaxies and their evolution in the VIMOS VLT Deep Survey. II. Extending the mass-metallicity relation to the range $z \approx 0.89$-1.24. A&A 495.1, pp. 73–81. DOI: `10.1051/0004-6361:200810558`. arXiv: `0811.2085 [astro-ph]`.

Pérez-Montero, E. et al. (Jan. 2013). The cosmic evolution of oxygen and nitrogen abundances in star-forming galaxies over the past 10 Gyr. A&A 549, A25, A25. DOI: `10.1051/0004-6361/201220070`. arXiv: `1210.0334 [astro-ph.CO]`.

Pérez-Montero, Enrique (Apr. 2017). Ionized Gaseous Nebulae Abundance Determination from the Direct Method. PASP 129.974, p. 043001. DOI: `10.1088/1538-3873/aa5abb`. arXiv: `1702.04255 [astro-ph.GA]`.

Petrosian, V. (Dec. 1976). Surface Brightness and Evolution of Galaxies. ApJ 210, p. L53. DOI: `10.1086/182301`.

Pettini, Max et al. (Mar. 2004). [OIII]/[NII] as an abundance indicator at high redshift. MNRAS 348.3, pp. L59–L63. DOI: `10.1111/j.1365-2966.2004.07591.x`. arXiv: `astro-ph/0401128 [astro-ph]`.

Pezzotta, A. et al. (July 2017). The VIMOS Public Extragalactic Redshift Survey (VIPERS). The growth of structure at $0.5 < z < 1.2$ from redshift-space distortions in the clustering of the PDR-2 final sample. A&A 604, A33, A33. DOI: `10.1051/0004-6361/201630295`. arXiv: `1612.05645 [astro-ph.CO]`.

Pilyugin, L. S. et al. (Sept. 2009). On the electron temperatures in high-metallicity HII regions. MNRAS 398.1, pp. 485–496. DOI: `10.1111/j.1365-2966.2009.15182.x`. arXiv: `0907.0084 [astro-ph.CO]`.

Pilyugin, L. S. et al. (Apr. 2010). The electron temperatures of SDSS high-metallicity giant extragalactic H ii regions. MNRAS 403.2, pp. 896–905. DOI: `10.1111/j.1365-2966.2009.16166.x`. arXiv: `0912.2596 [astro-ph.CO]`.

Pilyugin, L. S. et al. (June 2013). The metallicity-redshift relations for emission-line SDSS galaxies: examination of the dependence on the star formation rate. MNRAS 432.2, pp. 1217–1230. DOI: `10.1093/mnras/stt539`. arXiv: `1304.0191 [astro-ph.CO]`.

Pilyugin, L. S. et al. (July 2015). On the radial abundance gradients in discs of irregular galaxies. MNRAS 450.3, pp. 3254–3263. DOI: `10.1093/mnras/stv932`.

Pilyugin, L. S. et al. (Apr. 2016). New calibrations for abundance determinations in H II regions. MNRAS 457.4, pp. 3678–3692. DOI: `10.1093/mnras/stw238`. arXiv: `1601.08217 [astro-ph.GA]`.

Pilyugin, Leonid S. et al. (Sept. 2005). Oxygen Abundance Determination in H II Regions: The Strong Line Intensities-Abundance Calibration Revisited. ApJ 631.1, pp. 231–243. DOI: `10.1086/432408`.

Pilyugin, Leonid S. et al. (Aug. 2006). On the relation between electron temperatures in the O^{+} and O^{++} zones in high-metallicity HII regions. MNRAS 370.4, pp. 1928–1934. DOI: `10.1111/j.1365-2966.2006.10618.x`. arXiv: `astro-ph/0605695 [astro-ph]`.

Pistis, F. et al. (July 2022). The fundamental metallicity relation from SDSS ($z \sim 0$) to VIPERS ($z \sim 0.7$). Data selection or evolution. A&A 663, A162, A162. DOI: `10.1051/0004-6361/202142430`. arXiv: `2206.02458 [astro-ph.GA]`.

Pistis, F. et al. (2023a). A comparative study of the fundamental metallicity relation. The impact of methodology on its observed evolution. A&A submitted.

Pistis, F. et al. (2023b). Galaxy evolution footprint on the fundamental metallicity relation. A machine learning approach. in prep.

Planck Collaboration et al. (Nov. 2014). Planck 2013 results. I. Overview of products and scientific results. A&A 571, A1, A1. DOI: `10.1051/0004-6361/201321529`. arXiv: `1303.5062 [astro-ph.CO]`.

Popesso, P. et al. (Mar. 2019). The main sequence of star-forming galaxies - I. The local relation and its bending. MNRAS 483.3, pp. 3213–3226. DOI: `10.1093/mnras/sty3210`. arXiv: `1812.07057 [astro-ph.GA]`.

Popesso, P. et al. (Feb. 2023). The main sequence of star-forming galaxies across cosmic times. MNRAS 519.1, pp. 1526–1544. DOI: `10.1093/mnras/stac3214`. arXiv: `2203.10487 [astro-ph.GA]`.

Price-Whelan, Adrian M et al. (2018). The Astropy project: Building an open-science project and status of the v2.0 core package. *The Astronomical Journal* 156.3, p. 123.

Qu, Yan et al. (Jan. 2017). A chronicle of galaxy mass assembly in the EAGLE simulation. MNRAS 464.2, pp. 1659–1675. DOI: `10.1093/mnras/stw2437`. arXiv: `1609.07243 [astro-ph.GA]`.

Randriamampandry, S. M. et al. (Nov. 2020). Effect of the environment on star formation activity and stellar mass for star-forming galaxies in the COSMOS field. MNRAS 499.1, pp. 948–956. DOI: `10.1093/mnras/staa2669`. arXiv: `2008.13131 [astro-ph.GA]`.

Renzini, Alvio et al. (Mar. 2015). An Objective Definition for the Main Sequence of Star-forming Galaxies. ApJ 801.2, L29, p. L29. DOI: `10.1088/2041-8205/801/2/L29`. arXiv: `1502.01027 [astro-ph.GA]`.

Riccio, G. et al. (2023). X-ray luminosity - star formation rate scaling relation: constraints from the eROSITA Final Equatorial Depth Survey (eFEDS). A&A submitted.

Rodrigues, M. et al. (Apr. 2012). A decrease of the gas exchanges between galaxies and the intergalactic medium, from 12 to 6 billion years ago. MNRAS 421.4, pp. 2888–2903. DOI: `10.1111/j.1365-2966.2012.20518.x`. arXiv: `1203.6248 [astro-ph.CO]`.

Salim, Samir et al. (Dec. 2014). A Critical Look at the Mass-Metallicity-Star Formation Rate Relation in the Local Universe. I. An Improved Analysis Framework and Confounding Systematics. ApJ 797.2, 126, p. 126. DOI: `10.1088/0004-637X/797/2/126`. arXiv: `1411.7391 [astro-ph.GA]`.

Salim, Samir et al. (July 2015). On the Mass-Metallicity-Star Formation Rate Relation for Galaxies at $z \sim 2$. ApJ 808.1, 25, p. 25. DOI: `10.1088/0004-637X/808/1/25`. arXiv: `1506.03080 [astro-ph.GA]`.

Salim, Samir et al. (Nov. 2016). GALEX-SDSS-WISE Legacy Catalog (GSWLC): Star Formation Rates, Stellar Masses, and Dust Attenuations of 700,000 Low-redshift Galaxies. ApJS 227.1, 2, p. 2. DOI: `10.3847/0067-0049/227/1/2`. arXiv: `1610.00712 [astro-ph.GA]`.

Salim, Samir et al. (May 2018). Dust Attenuation Curves in the Local Universe: Demographics and New Laws for Star-forming Galaxies and High-redshift Analogs. ApJ 859.1, 11, p. 11. DOI: `10.3847/1538-4357/aabf3c`. arXiv: `1804.05850 [astro-ph.GA]`.

Salpeter, Edwin E. (Jan. 1955). The Luminosity Function and Stellar Evolution. ApJ 121, p. 161. DOI: `10.1086/145971`.

Sánchez Almeida, J. et al. (Mar. 2016). Search for Extremely Metal-poor Galaxies in the Sloan Digital Sky Survey. (II). High Electron Temperature Objects. ApJ 819.2, 110, p. 110. DOI: `10.3847/0004-637X/819/2/110`. arXiv: `1601.01631 [astro-ph.GA]`.

Sanders, Ryan L. et al. (Feb. 2015). The MOSDEF Survey: Mass, Metallicity, and Star-formation Rate at z $\sim$2.3. ApJ 799.2, 138, p. 138. DOI: `10.1088/0004-637X/799/2/138`. arXiv: `1408.2521 [astro-ph.GA]`.

— (Jan. 2016). The MOSDEF Survey: Electron Density and Ionization Parameter at z $\sim$2.3. ApJ 816.1, 23, p. 23. DOI: `10.3847/0004-637X/816/1/23`. arXiv: `1509.03636 [astro-ph.GA]`.

Sanders, Ryan L. et al. (May 2018). The MOSDEF Survey: A Stellar Mass-SFR-Metallicity Relation Exists at z $\sim$ 2.3. ApJ 858.2, 99, p. 99. DOI: `10.3847/1538-4357/aabcbd`. arXiv: `1711.00224 [astro-ph.GA]`.

Sanders, Ryan L. et al. (June 2021). The MOSDEF Survey: The Evolution of the Mass-Metallicity Relation from z = 0 to z 3.3. ApJ 914.1, 19, p. 19. DOI: `10.3847/1538-4357/abf4c1`. arXiv: `2009.07292 [astro-ph.GA]`.

Savaglio, S. et al. (Dec. 2005). The Gemini Deep Deep Survey. VII. The Redshift Evolution of the Mass-Metallicity Relation. ApJ 635.1, pp. 260–279. DOI: 10.1086/497331. arXiv: astro-ph/0508407 [astro-ph].

Schaerer, D. (Jan. 2003). The transition from Population III to normal galaxies: Lyalpha and He II emission and the ionising properties of high redshift starburst galaxies. A&A 397, pp. 527–538. DOI: 10.1051/0004-6361:20021525. arXiv: astro-ph/0210462 [astro-ph].

Schlegel, David J. et al. (June 1998). Maps of Dust Infrared Emission for Use in Estimation of Reddening and Cosmic Microwave Background Radiation Foregrounds. ApJ 500.2, pp. 525–553. DOI: 10.1086/305772. arXiv: astro-ph/9710327 [astro-ph].

Schreiber, C. et al. (Mar. 2015). The Herschel view of the dominant mode of galaxy growth from $z = 4$ to the present day. A&A 575, A74, A74. DOI: 10.1051/0004-6361/201425017. arXiv: 1409.5433 [astro-ph.GA].

Scodeggio, M. et al. (Jan. 2018). The VIMOS Public Extragalactic Redshift Survey (VIPERS). Full spectroscopic data and auxiliary information release (PDR-2). A&A 609, A84, A84. DOI: 10.1051/0004-6361/201630114. arXiv: 1611.07048 [astro-ph.GA].

Scoville, N. et al. (Apr. 2016). ISM Masses and the Star formation Law at Z = 1 to 6: ALMA Observations of Dust Continuum in 145 Galaxies in the COSMOS Survey Field. ApJ 820.2, 83, p. 83. DOI: 10.3847/0004-637X/820/2/83. arXiv: 1511.05149 [astro-ph.GA].

Scudder, Jillian M. et al. (Oct. 2012). Galaxy pairs in the Sloan Digital Sky Survey - V. Tracing changes in star formation rate and metallicity out to separations of 80 kpc. MNRAS 426.1, pp. 549–565. DOI: 10.1111/j.1365-2966.2012.21749.x. arXiv: 1207.4791 [astro-ph.CO].

Searle, L. et al. (Oct. 1978). Composition of halo clusters and the formation of the galactic halo. ApJ 225, pp. 357–379. DOI: 10.1086/156499.

Shapley, Alice E. et al. (Dec. 2005). Chemical Abundances of DEEP2 Star-forming Galaxies at z~1.0-1.5. ApJ 635.2, pp. 1006–1021. DOI: 10.1086/497630. arXiv: astro-ph/0509102 [astro-ph].

Shapley, Alice E. et al. (Mar. 2015). The MOSDEF Survey: Excitation Properties of $z \sim 2.3$ Star-forming Galaxies. ApJ 801.2, 88, p. 88. DOI: 10.1088/0004-637X/801/2/88. arXiv: 1409.7071 [astro-ph.GA].

Shivaei, Irene et al. (Nov. 2020). Dependence of the IRX-β Dust Attenuation Relation on Metallicity and Environment. ApJ 903.2, L28, p. L28. DOI: 10.3847/2041-8213/abc1ef. arXiv: 2010.10538 [astro-ph.GA].

Silk, J. et al. (Dec. 2014). Galaxy Formation. *Proceedings of the International School of Physics 'Enrico Fermi' Course 186 'New Horizons for Observational Cosmology' Vol. 186*. Vol. 186, pp. 137–187. DOI: 10.3254/978-1-61499-476-3-137. arXiv: 1312.0107 [astro-ph.CO].

Silk, Joseph et al. (Aug. 2012). The current status of galaxy formation. *Research in Astronomy and Astrophysics* 12.8, pp. 917–946. DOI: 10.1088/1674-4527/12/8/004. arXiv: 1207.3080 [astro-ph.CO].

Siudek, M. et al. (Sept. 2018). The VIMOS Public Extragalactic Redshift Survey (VIPERS). The complexity of galaxy populations at $0.4 < z < 1.3$ revealed with unsupervised machine-learning algorithms. A&A 617, A70, A70. DOI: 10.1051/0004-6361/201832784. arXiv: 1805.09904 [astro-ph.GA].

Skillman, E. D. et al. (May 1988). The extremely low oxygen abundance of GR 8 : a very low luminosity dwarf irregular galaxy. A&A 196, pp. 31–38.

Somerville, Rachel S. et al. (Aug. 2015). Physical Models of Galaxy Formation in a Cosmological Framework. ARA&A 53, pp. 51–113. DOI: 10.1146/annurev-astro-082812-140951. arXiv: 1412.2712 [astro-ph.GA].

Speagle, J. S. et al. (Oct. 2014). A Highly Consistent Framework for the Evolution of the Star-Forming "Main Sequence" from z ∼0-6. ApJS 214.2, 15, p. 15. DOI: 10.1088/0067-0049/214/2/15. arXiv: 1405.2041 [astro-ph.GA].

Steidel, Charles C. et al. (July 2010). The Structure and Kinematics of the Circumgalactic Medium from Far-ultraviolet Spectra of z ∼= 2-3 Galaxies. ApJ 717.1, pp. 289–322. DOI: 10.1088/0004-637X/717/1/289. arXiv: 1003.0679 [astro-ph.CO].

Steidel, Charles C. et al. (Nov. 2014). Strong Nebular Line Ratios in the Spectra of z ∼2-3 Star Forming Galaxies: First Results from KBSS-MOSFIRE. ApJ 795.2, 165, p. 165. DOI: 10.1088/0004-637X/795/2/165. arXiv: 1405.5473 [astro-ph.GA].

Stott, John P. et al. (Dec. 2013). A fundamental metallicity relation for galaxies at z = 0.84-1.47 from HiZELS. MNRAS 436.2, pp. 1130–1141. DOI: 10.1093/mnras/stt1641. arXiv: 1309.0506 [astro-ph.CO].

Strom, Allison L. et al. (Dec. 2018). Measuring the Physical Conditions in High-redshift Star-forming Galaxies: Insights from KBSS-MOSFIRE. ApJ 868.2, 117, p. 117. DOI: 10.3847/1538-4357/aae1a5. arXiv: 1711.08820 [astro-ph.GA].

Suzuki, Tomoko L. et al. (Nov. 2017). The Interstellar Medium in [O III]-selected Star-forming Galaxies at $z \sim 3.2$. ApJ 849.1, 39, p. 39. DOI: 10.3847/1538-4357/aa8df3. arXiv: 1709.06731 [astro-ph.GA].

Tacchella, Sandro et al. (Apr. 2016). The confinement of star-forming galaxies into a main sequence through episodes of gas compaction, depletion and replenishment. MNRAS 457.3, pp. 2790–2813. DOI: 10.1093/mnras/stw131. arXiv: 1509.02529 [astro-ph.GA].

Tacconi, L. J. et al. (Feb. 2010). High molecular gas fractions in normal massive star-forming galaxies in the young Universe. Nature 463.7282, pp. 781–784. DOI: 10.1038/nature08773. arXiv: 1002.2149 [astro-ph.CO].

Takeuchi, T. T. et al. (Sept. 2005). The evolution of the ultraviolet and infrared luminosity densities in the universe at $0 < z < 1$. A&A 440.2, pp. L17–L20. DOI: 10.1051/0004-6361:200500158. arXiv: astro-ph/0508124 [astro-ph].

Talent, David Leroy (Jan. 1981). A spectrophotometric study of H II regions in chemically young galaxies. PhD thesis. Rice University, Texas.

Taylor, Philip et al. (Dec. 2016). Time evolution of galaxy scaling relations in cosmological simulations. MNRAS 463.3, pp. 2465–2479. DOI: 10.1093/mnras/stw2157. arXiv: 1608.06685 [astro-ph.GA].

Telford, O. Grace et al. (Aug. 2016). Exploring Systematic Effects in the Relation Between Stellar Mass, Gas Phase Metallicity, and Star Formation Rate. ApJ 827.1, 35, p. 35. DOI: 10.3847/0004-637X/827/1/35. arXiv: 1606.08850 [astro-ph.GA].

Tomczak, Adam R. et al. (Feb. 2016). The SFR-M* Relation and Empirical Star-Formation Histories from ZFOURGE* at $0.5 < z < 4$. ApJ 817.2, 118, p. 118. DOI: 10.3847/0004-637X/817/2/118. arXiv: 1510.06072 [astro-ph.GA].

Topping, Michael W. et al. (Sept. 2021). The MOSDEF survey: the mass-metallicity relationship and the existence of the FMR at z 1.5. MNRAS 506.1, pp. 1237–1249. DOI: 10.1093/mnras/stab1793. arXiv: 2103.09245 [astro-ph.GA].

Torrey, Paul et al. (June 2018). Similar star formation rate and metallicity variability time-scales drive the fundamental metallicity relation. MNRAS 477.1, pp. L16–L20. DOI: 10.1093/mnrasl/sly031. arXiv: 1711.11039 [astro-ph.GA].

Torrey, Paul et al. (Apr. 2019). The evolution of the mass-metallicity relation and its scatter in IllustrisTNG. MNRAS 484.4, pp. 5587–5607. DOI: 10.1093/mnras/stz243. arXiv: 1711.05261 [astro-ph.GA].

Trager, S. C. et al. (July 2000). The Stellar Population Histories of Early-Type Galaxies. II. Controlling Parameters of the Stellar Populations. AJ 120.1, pp. 165–188. DOI: 10.1086/301442. arXiv: astro-ph/0004095 [astro-ph].

Tremonti, Christy A. et al. (Oct. 2004). The Origin of the Mass-Metallicity Relation: Insights from 53 000 Star-forming Galaxies in the Sloan Digital Sky Survey. ApJ 613.2, pp. 898–913. DOI: 10.1086/423264. arXiv: astro-ph/0405537 [astro-ph].

Troncoso, P. et al. (Mar. 2014). Metallicity evolution, metallicity gradients, and gas fractions at z ~3.4. A&A 563, A58, A58. DOI: 10.1051/0004-6361/201322099. arXiv: 1311.4576 [astro-ph.CO].

Tumlinson, J. et al. (Nov. 2011). The Large, Oxygen-Rich Halos of Star-Forming Galaxies Are a Major Reservoir of Galactic Metals. *Science* 334.6058, p. 948. DOI: 10.1126/science.1209840. arXiv: 1111.3980 [astro-ph.CO].

Turner, Sebastian et al. (May 2021). Synergies between low- and intermediate-redshift galaxy populations revealed with unsupervised machine learning. MNRAS 503.2, pp. 3010–3031. DOI: 10.1093/mnras/stab653. arXiv: 2102.05056 [astro-ph.GA].

van Zee, Liese et al. (Jan. 2006). Oxygen and Nitrogen in Isolated Dwarf Irregular Galaxies. ApJ 636.1, pp. 214–239. DOI: 10.1086/498017. arXiv: astro-ph/0509677 [astro-ph].

Vazdekis, A. et al. (June 2010). Evolutionary stellar population synthesis with MILES - I. The base models and a new line index system. MNRAS 404.4, pp. 1639–1671. DOI: 10.1111/j.1365-2966.2010.16407.x. arXiv: 1004.4439 [astro-ph.CO].

Ventou, E. et al. (Dec. 2017). The MUSE Hubble Ultra Deep Field Survey. IX. Evolution of galaxy merger fraction since $z \approx 6$. A&A 608, A9, A9. DOI: 10.1051/0004-6361/201731586. arXiv: 1711.00423 [astro-ph.GA].

Vergani, D. et al. (Aug. 2008). The VIMOS VLT Deep Survey. Tracing the galaxy stellar mass assembly history over the last 8 Gyr. A&A 487.1, pp. 89–101. DOI: 10.1051/0004-6361:20077910. arXiv: 0705.3018 [astro-ph].

Vietri, G. et al. (Mar. 2022). The Type II AGN-host galaxy connection. Insights from the VVDS and VIPERS surveys. A&A 659, A129, A129. DOI: 10.1051/0004-6361/202141072. arXiv: 2111.08730 [astro-ph.GA].

Vincenzo, F. et al. (Feb. 2016). Modern yields per stellar generation: the effect of the IMF. MNRAS 455.4, pp. 4183–4190. DOI: 10.1093/mnras/stv2598. arXiv: 1503.08300 [astro-ph.GA].

Weiner, Benjamin J. et al. (Feb. 2009). Ubiquitous Outflows in DEEP2 Spectra of Star-Forming Galaxies at $z = 1.4$. ApJ 692.1, pp. 187–211. DOI: 10.1088/0004-637X/692/1/187. arXiv: 0804.4686 [astro-ph].

Whitaker, Katherine E. et al. (July 2011). The NEWFIRM Medium-band Survey: Photometric Catalogs, Redshifts, and the Bimodal Color Distribution of Galaxies out to z ~3. ApJ 735.2, 86, p. 86. DOI: 10.1088/0004-637X/735/2/86. arXiv: 1105.4609 [astro-ph.CO].

Whitaker, Katherine E. et al. (Aug. 2012). The Star Formation Mass Sequence Out to $z = 2.5$. ApJ 754.2, L29, p. L29. DOI: 10.1088/2041-8205/754/2/L29. arXiv: 1205.0547 [astro-ph.CO].

Whitaker, Katherine E. et al. (Nov. 2014). Constraining the Low-mass Slope of the Star Formation Sequence at $0.5 < z < 2.5$. ApJ 795.2, 104, p. 104. DOI: 10.1088/0004-637X/795/2/104. arXiv: 1407.1843 [astro-ph.GA].

Whitaker, Katherine E. et al. (Dec. 2017). The Constant Average Relationship between Dust-obscured Star Formation and Stellar Mass from $z = 0$ to $z = 2.5$. ApJ 850.2, 208, p. 208. DOI: 10.3847/1538-4357/aa94ce. arXiv: 1710.06872 [astro-ph.GA].

White, S. D. M. et al. (May 1978). Core condensation in heavy halos: a two-stage theory for galaxy formation and clustering. MNRAS 183, pp. 341–358. DOI: `10.1093/mnras/183.3.341`.

Wilkinson, David M. et al. (Dec. 2017). FIREFLY (Fitting IteRativEly For Likelihood analYsis): a full spectral fitting code. MNRAS 472.4, pp. 4297–4326. DOI: `10.1093/mnras/stx2215`. arXiv: `1711.00865 [astro-ph.GA]`.

Wright, Shelley A. et al. (July 2009). Dynamics of Galactic Disks and Mergers at z ~1.6: Spatially Resolved Spectroscopy with Keck Laser Guide Star Adaptive Optics. ApJ 699.1, pp. 421–440. DOI: `10.1088/0004-637X/699/1/421`. arXiv: `0810.5599 [astro-ph]`.

Wu, Yu-Zhong et al. (Apr. 2016). Mass-metallicity relation for local star-forming galaxies. MNRAS 457.3, pp. 2929–2935. DOI: `10.1093/mnras/stw113`. arXiv: `1601.03527 [astro-ph.GA]`.

Wuyts, Eva et al. (Aug. 2012). Constraints on the Low-mass End of the Mass-Metallicity Relation at z = 1-2 from Lensed Galaxies. ApJ 755.1, 73, p. 73. DOI: `10.1088/0004-637X/755/1/73`. arXiv: `1202.5267 [astro-ph.CO]`.

Wuyts, Eva et al. (July 2014). A Consistent Study of Metallicity Evolution at 0.8 < z < 2.6. ApJ 789.2, L40, p. L40. DOI: `10.1088/2041-8205/789/2/L40`. arXiv: `1405.6590 [astro-ph.GA]`.

Wuyts, Eva et al. (Aug. 2016). The Evolution of Metallicity and Metallicity Gradients from z = 2.7 to 0.6 with KMOS^{3D}. ApJ 827.1, 74, p. 74. DOI: `10.3847/0004-637X/827/1/74`. arXiv: `1603.01139 [astro-ph.GA]`.

Wuyts, Stijn et al. (Jan. 2007). What Do We Learn from IRAC Observations of Galaxies at 2 < z < 3.5? ApJ 655.1, pp. 51–65. DOI: `10.1086/509708`. arXiv: `astro-ph/0609548 [astro-ph]`.

Xia, Lifang et al. (July 2012). Metallicities of Emission-line Galaxies from HST ACS PEARS and HST WFC3 ERS Grism Spectroscopy at $0.6 < z < 2.4$. AJ 144.1, 28, p. 28. DOI: `10.1088/0004-6256/144/1/28`. arXiv: `1205.3172 [astro-ph.CO]`.

Xiao, Lin et al. (June 2018). Emission-line diagnostics of nearby H II regions including interacting binary populations. MNRAS 477.1, pp. 904–934. DOI: `10.1093/mnras/sty646`. arXiv: `1801.07068 [astro-ph.GA]`.

Yabe, Kiyoto et al. (June 2012). NIR Spectroscopy of Star-Forming Galaxies at z $\sim$ 1.4 with Subaru/FMOS: The Mass-Metallicity Relation. PASJ 64, 60, p. 60. DOI: `10.1093/pasj/64.3.60`. arXiv: `1112.3704 [astro-ph.CO]`.

Yabe, Kiyoto et al. (Feb. 2014). The mass-metallicity relation at z $\sim$ 1.4 revealed with Subaru/FMOS. MNRAS 437.4, pp. 3647–3663. DOI: `10.1093/mnras/stt2185`. arXiv: `1311.2624 [astro-ph.CO]`.

Yabe, Kiyoto et al. (Dec. 2015). The Subaru FMOS Galaxy Redshift Survey (FastSound). III. The mass-metallicity relation and the fundamental metallicity relation at z $\sim$ 1.4*. PASJ 67.6, 102, p. 102. DOI: `10.1093/pasj/psv079`. arXiv: `1508.01512 [astro-ph.GA]`.

Yang, G. et al. (Jan. 2020). X-CIGALE: Fitting AGN/galaxy SEDs from X-ray to infrared. MNRAS 491.1, pp. 740–757. DOI: `10.1093/mnras/stz3001`. arXiv: `2001.08263 [astro-ph.GA]`.

Yang, Guang et al. (Mar. 2022). Fitting AGN/Galaxy X-Ray-to-radio SEDs with CIGALE and Improvement of the Code. ApJ 927.2, 192, p. 192. DOI: `10.3847/1538-4357/ac4971`. arXiv: `2201.03718 [astro-ph.GA]`.

Yates, Robert M. et al. (May 2012). The relation between metallicity, stellar mass and star formation in galaxies: an analysis of observational and model data. MNRAS 422.1, pp. 215–231. DOI: `10.1111/j.1365-2966.2012.20595.x`. arXiv: `1107.3145 [astro-ph.CO]`.

Zahid, H. J. et al. (Apr. 2011a). The Mass-Metallicity and Luminosity-Metallicity Relations from DEEP2 at z ∼0.8. ApJ 730.2, 137, p. 137. DOI: `10.1088/0004-637X/730/2/137`. arXiv: `1006.4877 [astro-ph.CO]`.

— (Apr. 2011b). The Mass-Metallicity and Luminosity-Metallicity Relations from DEEP2 at z ∼0.8. ApJ 730.2, 137, p. 137. DOI: `10.1088/0004-637X/730/2/137`. arXiv: `1006.4877 [astro-ph.CO]`.

Zahid, H. J. et al. (Sept. 2014a). The FMOS-COSMOS Survey of Star-forming Galaxies at z ∼1.6. II. The Mass-Metallicity Relation and the Dependence on Star Formation Rate and Dust Extinction. ApJ 792.1, 75, p. 75. DOI: `10.1088/0004-637X/792/1/75`. arXiv: `1310.4950 [astro-ph.CO]`.

Zahid, H. Jabran et al. (July 2013). The Chemical Evolution of Star-forming Galaxies over the Last 11 Billion Years. ApJ 771.2, L19, p. L19. DOI: `10.1088/2041-8205/771/2/L19`. arXiv: `1303.5987 [astro-ph.CO]`.

Zahid, H. Jabran et al. (Aug. 2014b). The Universal Relation of Galactic Chemical Evolution: The Origin of the Mass-Metallicity Relation. ApJ 791.2, 130, p. 130. DOI: `10.1088/0004-637X/791/2/130`. arXiv: `1404.7526 [astro-ph.GA]`.

Zaritsky, Dennis et al. (Jan. 1994). H II Regions and the Abundance Properties of Spiral Galaxies. ApJ 420, p. 87. DOI: `10.1086/173544`.